

# **Searches for New Physics using Pairs of Jets Containing $b$ -quarks at the ATLAS Detector**

*Laurie Iain M<sup>c</sup>Clymont*

A dissertation submitted in partial fulfillment  
of the requirements for the degree of  
**Doctor of Philosophy**  
of  
**University College London.**

Department of Physics and Astronomy,  
University College London

1st July 2018

I, Laurie Iain McClymont, confirm that the work presented in this thesis is my own. Where information has been derived from other sources, I confirm that this has been indicated in the work.

Laurie McClymont

## Abstract

Two searches for Beyond Standard Model resonances are performed using 13 TeV proton–proton collision data collected by the ATLAS detector in 2015 and 2016 using the invariant mass distribution of pairs of jets, where at least one or both jets are identified as containing a  $b$ -quark. The searches are sensitive to resonances decaying to a pair of  $b$ -quarks or a  $b$ -quark and a gluon. A high-mass search probes the mass region 1.4 – 6 TeV using a data-set corresponding to an integrated luminosity of  $13.3 \text{ fb}^{-1}$ . A low-mass search utilises real-time  $b$ -jet identification to probe the mass region 0.6 – 1.5 TeV using a data-set corresponding to an integrated luminosity of  $24.3 \text{ fb}^{-1}$ . No evidence of a resonance is found. Excited  $b^*$  quarks with masses from 1.4 to 2.3 TeV and a set of  $Z'$  boson models with masses from 0.6 to 1.25 TeV or at 1.5 TeV are excluded at the 95% credibility-level. In addition, 95% credibility-level upper limits are set on generic signals with a Gaussian distribution in the mass range 0.65 – 6 TeV.

# Acknowledgements

I would like to thank Andreas for always being eager to provide advice, support and macchiatos. Your supervision has made this thesis possible and is greatly appreciated.

Thanks to Rui, Andrea, Bing, Nishu, Sergei, Jeff, Jimmy and all those I worked with in the di-*b*-jet analysis team; I hope that your hard work is given justice in this thesis.

I would also like to thank all the students, fellows and post-docs at ATLAS and UCL who provided help throughout my PhD; the way that so many are always willing to drop what they are doing to aid another is something that makes ATLAS a great collaboration to be a part of. Particular thanks go to Tim, Kate, John and Gabriel for always providing help and guidance when I needed it. Also thanks to Andy and Jiggins for putting up with me in the office for so long and answering every one of my inane questions.

Thanks to my family and friends in Manchester, Glasgow, London and Geneva who have made the last three and a bit years an enjoyable experience.

Finally, a huge thanks to my parents who have always supported and encouraged me; without you this wouldn't have been possible.

# Contents

<b>1</b>	<b>Introduction</b>	<b>18</b>
1.1	Personal Contributions . . . . .	20
<b>2</b>	<b>An Incomplete Theory</b>	<b>22</b>
2.1	The Standard Model . . . . .	22
2.1.1	Particles . . . . .	22
2.1.2	Forces . . . . .	24
2.2	QCD: Hadronic Jet Formation and Dijet Production . . . . .	25
2.2.1	Renormalisation and the Running of $\alpha_S$ . . . . .	25
2.2.2	Hadronic Jet Formation . . . . .	28
2.2.3	Dijet Production in $p p$ Collisions . . . . .	29
2.2.4	$t\bar{t}$ Production . . . . .	33
2.3	Beyond Standard Model Physics . . . . .	34
2.3.1	Motivations . . . . .	34
2.3.2	Beyond Standard Model Theories . . . . .	36
<b>3</b>	<b>The LHC and the ATLAS Detector</b>	<b>39</b>
3.1	The Large Hadron Collider (LHC) . . . . .	39
3.1.1	LHC running conditions in 2015 and 2016 . . . . .	39
3.2	The ATLAS Detector . . . . .	40
3.2.1	Co-ordinate System . . . . .	41
3.2.2	Inner Detector . . . . .	42
3.2.3	Calorimeter System . . . . .	45
3.2.4	Muon Spectrometer . . . . .	49
3.2.5	Magnets . . . . .	51

<b>4 Object Definition and Reconstruction</b>	<b>52</b>
4.1 Tracks . . . . .	52
4.1.1 Primary Vertex Identification . . . . .	53
4.2 Jets . . . . .	53
4.2.1 Hadronic Topocluster Reconstruction . . . . .	54
4.2.2 Jet Reconstruction . . . . .	55
4.2.3 Jet Calibration . . . . .	57
4.2.4 Jet Energy Uncertainties . . . . .	59
4.3 $b$ -Jets . . . . .	61
4.3.1 Truth Flavour Label . . . . .	61
4.3.2 Baseline $b$ -Tagging Algorithms . . . . .	61
4.3.3 Multi-Variate $b$ -Tagging Algorithm . . . . .	63
4.3.4 Calibration and Uncertainties . . . . .	66
4.3.5 $b$ -Jet Energy Scale . . . . .	67
4.4 Electrons and Muons . . . . .	68
<b>5 The ATLAS Trigger System</b>	<b>69</b>
5.1 Jet Triggers . . . . .	70
5.2 $b$ -Jet Triggers . . . . .	71
5.3 Measurement of the $b$ -Jet Trigger Efficiency in 2016 Data . . . . .	74
5.3.1 Description of Event Selection and Data-Sets . . . . .	75
5.3.2 Investigation of Data-Simulation Discrepancies . . . . .	77
5.3.3 $b$ -Jet Trigger Aware Good Run List (GRL) . . . . .	83
5.3.4 Efficiency Measurement Results and Associated Uncertainties . . . . .	86
<b>6 Di-<math>b</math>-Jet Search: Analysis Introduction</b>	<b>96</b>
6.1 Analysis Outline . . . . .	96
6.2 List of Data-Sets Used . . . . .	98
6.3 Background and Signals . . . . .	99
<b>7 Di-<math>b</math>-Jet Search: Event Selection</b>	<b>102</b>
7.1 Jet Selection . . . . .	102
7.2 Event-Level Selection . . . . .	104
7.3 $b$ -Tagging . . . . .	106
7.3.1 Effect of $b$ -Jet Trigger Matching in the <i>Full16_LowMass</i> Data-Set .	109
7.4 Summary of Event Selection . . . . .	112

<b>8 Di-<i>b</i>-Jet Search: Search Phase</b>	<b>116</b>
8.1 Dijet Mass Spectrum . . . . .	116
8.2 Background Estimation . . . . .	117
8.2.1 Functional Form . . . . .	118
8.2.2 Wilks' Test Statistic . . . . .	119
8.3 Resonance Search Strategy . . . . .	120
8.4 <i>Summer16_HighMass</i> Search Phase . . . . .	122
8.4.1 Validation Studies: Background-Only Data-Set . . . . .	122
8.4.2 Validation Studies: Dijet Mass Range Studies . . . . .	123
8.4.3 Fit Function Selection . . . . .	127
8.4.4 Validation Studies: Spurious Signal . . . . .	129
8.4.5 Validation Studies: Signal Injection . . . . .	132
8.4.6 Search Phase Results . . . . .	132
8.5 <i>Full16_LowMass</i> Search Phase . . . . .	134
8.5.1 Background-Only Samples . . . . .	134
8.5.2 Global Fit Strategy . . . . .	137
8.5.3 Sliding Window Fit Background Estimation (SWiFt) . . . . .	139
8.5.4 Window Selection Strategy . . . . .	140
8.5.5 SWiFt Validation Studies: Window Selection . . . . .	142
8.5.6 SWiFt Validation Studies: Spurious Signal . . . . .	143
8.5.7 SWiFt Validation Studies: Signal Injection . . . . .	148
8.5.8 Results of Window Selection Procedure . . . . .	154
8.5.9 Search Phase Results . . . . .	156
<b>9 Di-<i>b</i>-Jet Search: Limit Setting Phase</b>	<b>157</b>
9.1 Limit Setting Methodology . . . . .	157
9.2 Description of Systematic Uncertainties . . . . .	160
9.3 <i>Summer16_HighMass</i> Data-Set Limits . . . . .	162
9.4 <i>Full16_LowMass</i> Data-set Limits . . . . .	165
9.4.1 Signal Morphing . . . . .	165
9.4.2 Summary of Systematic Uncertainties . . . . .	166
9.4.3 Signal Subtracted Background Estimation . . . . .	167
9.4.4 Results . . . . .	171

<b>10 Future Prospects of Di-<i>b</i>-Jet Searches</b>	<b>175</b>
10.1 Di- <i>b</i> -Jet Searches at Higher Luminosities . . . . .	175
10.2 Combination of <i>b</i> -Tagging Categories . . . . .	176
10.3 Improvement of <i>b</i> -Jet Trigger Efficiency Measurement . . . . .	177
10.4 Signal Plus Background Fit in the Search Phase . . . . .	178
<b>11 Conclusions</b>	<b>179</b>
<b>Appendices</b>	<b>181</b>
<b>A Dijet Mass Binning</b>	<b>181</b>
<b>B Single Jet Trigger Threshold <math>p_T</math> Fit</b>	<b>182</b>
<b>C Additional Plots for <i>Full16_LowMass</i> Data-Set Fit Validation Studies</b>	<b>184</b>
<b>Bibliography</b>	<b>192</b>

# List of Figures

2.1	A schematic showing the gluon propagator with additional first order loops.	26
2.2	Summary of measurements of $\alpha_S$ as a function of the energy scale, $Q$ .	27
2.3	A Feynman diagram showing dijet production in a proton–proton collision through the $qg \rightarrow qg$ channel.	29
2.4	MMHT2014 NNLO PDFs at $Q^2 = 10 \text{ GeV}^2$ and $Q^2 = 10^4 \text{ GeV}^2$ , with associated 68% confidence-level uncertainty bands.	31
2.5	A Feynman diagram showing an example of a di-lepton $t\bar{t}$ event.	33
2.6	The leading-order Feynman diagram of the process $q\bar{q} \rightarrow Z' \rightarrow b\bar{b}$ .	37
2.7	The leading-order Feynman diagram of the process $bg \rightarrow b^* \rightarrow bg$	38
3.1	A cut-away schematic of the ATLAS detector.	41
3.2	A schematic showing a slice of the barrel components of the ATLAS Inner Detector including the Insertable <i>B</i> -Layer.	43
3.3	A schematic showing the barrel and end cap components of the ATLAS Inner Detector.	43
3.4	A cut-away schematic of the ATLAS calorimeter system.	45
3.5	A cut-away of the ATLAS Muon Spectrometer.	50
3.6	The layout of the ATLAS magnet system.	51
4.1	A schematic illustrating the algorithm used to form a topocluster.	55
4.2	A comparison of the jets built using the $k_T$ and anti- $k_T$ algorithm.	56
4.3	The fractional jet energy scale uncertainty as a function of jet- $p_T$ and $\eta$ .	59
4.4	The fractional jet energy resolution uncertainty as a function of jet- $p_T$ and $\eta$ .	60
4.5	The key features of a <i>b</i> -jet utilised by the base <i>b</i> -tagging algorithms.	62
4.6	An illustration of how the three base flavour tagging algorithms are combined in the MV2 algorithm.	63
4.7	The expected <i>b</i> -jet efficiency of the <i>b</i> -tagging algorithm, MV2, with respect to light-jet and <i>c</i> -jet rejection in simulated $t\bar{t}$ events.	64

4.8	The $b$ -tagging efficiency for $b$ -jets, $c$ -jets and light-jets as a function of jet- $p_T$ for the MV2c20 algorithm at the 70% operating point in the 2015 configuration. . . . .	65
4.9	The ratio of $b$ -tagging efficiency in data and simulation for MV2c10 at the 77% operating point as a function of jet- $p_T$ in di-lepton $t\bar{t}$ events. . . . .	66
5.1	The expected $b$ -jet efficiency of $b$ -jet triggers in Run-2 compared to the set-up used in 2012 data-taking. . . . .	72
5.2	The $b$ -jet trigger efficiency in data and simulation when the $b$ -jet trigger aware GRL is not applied and offline–online jet matching is not required. . . . .	77
5.3	The $b$ -jet trigger efficiency for data from Epoch 1 and simulation against jet- $p_T$ and online beamspot $z$ -position. The $b$ -jet trigger aware GRL is not applied. . . . .	79
5.4	The $b$ -jet trigger efficiency and the number of offline jets against vertex class for data from Epoch 1 and simulation. The $b$ -jet trigger aware GRL is not applied. . . . .	80
5.5	The $b$ -jet trigger efficiency for data from Epoch 1 and simulation against jet- $p_T$ and online beamspot $z$ -position when a $xPrmVtx$ vertex has been found. The $b$ -jet trigger aware GRL is not applied. . . . .	80
5.6	The $b$ -jet trigger efficiency for data from Epoch 2 and simulation against jet- $p_T$ and online beamspot $z$ -position. The $b$ -jet trigger aware GRL is not applied. . . . .	81
5.7	The online primary vertex efficiency for data from Epoch 2 and simulation against leading-jet $p_T$ , online beamspot $z$ -position and leading jet- $\eta$ . The $b$ -jet trigger aware GRL is not applied. . . . .	82
5.8	The $b$ -jet trigger efficiency for data from Epoch 3 and simulation. . . . .	83
5.9	The $b$ -jet trigger efficiency for data from Epoch 2 and simulation. The $b$ -jet trigger aware GRL is applied. . . . .	84
5.10	The online primary vertex efficiency for data in Epoch 2 and simulation. The $b$ -jet trigger aware GRL is applied. . . . .	84
5.11	The $b$ -jet trigger efficiency for the full 2016 data-set and simulation. The $b$ -jet trigger aware GRL is applied. . . . .	85
5.12	The online primary vertex efficiency for the full 2016 data-set and for simulation. The $b$ -jet trigger aware GRL is applied. . . . .	85
5.13	The $b$ -jet purity and $b$ -jet trigger efficiency when the size of the non- $b$ -jet contamination is systematically varied. . . . .	87

5.14	The $b$ -jet trigger efficiency for non- $b$ -jets and inclusive jets for systematic variations of the non- $b$ -jet efficiency. . . . .	88
5.15	A figure to demonstrate the stages of the high- $p_{\text{T}}$ extrapolation procedure for the $b$ -jet trigger efficiency measurement. . . . .	90
5.16	The $b$ -jet trigger efficiency measured in data and the corrected simulation as a function of offline jet- $p_{\text{T}}$ . The extrapolation uncertainties and total uncertainty are shown. . . . .	90
5.17	The $b$ -jet trigger efficiency measured in data and the associated data/simulation scale factors as a function of offline jet- $p_{\text{T}}$ . . . . .	91
5.18	The measured online primary vertex efficiency as a function of offline leading jet- $\eta$ . . . . .	94
6.1	A cartoon illustrating the use of the dijet mass distribution in the search phase of a di- $b$ -jet search. . . . .	97
7.1	Derivations of the leading jet- $p_{\text{T}}$ and $m_{jj}$ cuts for the <i>Summer16_HighMass</i> data-set event selection using events that pass an unprescaled L1_J75 trigger compared to events that pass a range of single-jet triggers in one run of 2016 data. . . . .	103
7.2	Derivations of the dijet mass cut for the <i>Full16_LowMass</i> data-set event selection. . . . .	106
7.3	The dijet flavour composition of simulated QCD dijet production as a function of dijet mass for the <i>Summer16_HighMass</i> data-set. . . . .	108
7.4	The dijet flavour composition of simulated QCD dijet production as a function of dijet mass for the <i>Full16_LowMass</i> data-set. . . . .	108
7.5	A comparison of the dijet mass spectra created using the <i>EXOT2</i> derivation and the <i>FTAG1</i> derivation and a comparison of the dijet mass spectra of all events and $b$ -jet trigger matched events using the <i>FTAG1</i> derivation. For both plots the full <i>Full16_LowMass</i> event selection is applied. . . . .	111
7.6	Event displays of high dijet mass events in the <i>Summer16_HighMass</i> data-set. . . . .	113
7.7	Plots to show the acceptance of the <i>Summer16_HighMass</i> data-set event selection for the $b^*$ quark and SSM $Z'$ boson signal models. . . . .	114
7.8	Plots to show the acceptance of the <i>Full16_LowMass</i> data-set event selection for the SSM and DM $Z'$ boson signal models. . . . .	114
8.1	The scaled and effective entries dijet mass spectra from QCD dijet simulation when the <i>Summer16_HighMass</i> data-set event selection has been applied. . . . .	123

8.2	The scaled dijet mass spectrum from QCD dijet simulation fitted to using the 4 parameter dijet fit function, with the lower edge of the dijet mass spectrum at 1100 GeV. The <i>Summer16_HighMass</i> data-set event selection has been applied. . . . .	124
8.3	The scaled dijet mass spectrum from QCD dijet simulation fitted to using the 4 parameter dijet fit function, with the lower edge of the dijet mass spectrum at 1378 GeV. The <i>Summer16_HighMass</i> data-set event selection has been applied. . . . .	125
8.4	The BumpHunter, DeficitHunter and $\chi^2$ $p$ -values for search phases performed to the scaled dijet mass spectrum from QCD dijet simulation as a function of the lower edge of the dijet mass spectrum. The <i>Summer16_HighMass</i> data-set event selection has been applied. . . . .	126
8.5	The Wilks' $p$ -value as a function of luminosity for a $8.8 \text{ fb}^{-1}$ subset of the <i>Summer16_HighMass</i> data-set in the 2 and $\geq 1$ $b$ -tag category. . . . .	128
8.6	The scaled and effective entries dijet mass spectra overlaid with a data-like dijet mass spectrum from QCD dijet simulation when the <i>Summer16_HighMass</i> data-set event selection has been applied. . . . .	129
8.7	A data-like dijet mass spectrum from QCD dijet simulation for the 2 and $\geq 1$ $b$ -tag category, fitted to using the 3 parameter dijet fit function. . . . .	130
8.8	An illustration of the calculation of the BumpHunter $p$ -value for the search phase applied to data-like dijet mass spectra from QCD dijet simulation. The <i>Summer16_HighMass</i> data-set event selection has been applied. . . . .	130
8.9	The normalised distributions of BumpHunter, DeficitHunter and $\chi^2$ $p$ -values for the search phase performed on 200 data-like dijet mass spectra from QCD dijet simulation. The <i>Summer16_HighMass</i> data-set event selection has been applied. . . . .	131
8.10	The dijet mass spectrum of the <i>Summer16_HighMass</i> data-set in the 2 and the $\geq 1$ $b$ -tag category compared to the background estimation created using the 3 parameter dijet fit function. The most discrepant excess found by the BumpHunter algorithm and the associated $p$ -value are shown. . . . .	133
8.11	The dijet mass spectrum of the full <i>Full16_LowMass</i> data-set and a $3 \text{ fb}^{-1}$ subset. . . . .	135
8.12	A figure showing the process of obtaining the fit control region dijet mass spectrum used for the <i>Full16_LowMass</i> data-set fit studies. . . . .	136
8.13	The smooth dijet mass spectrum from the <i>Full16_LowMass</i> fit control region fitted to using the 3, 4 and 5 parameter global fits. . . . .	138

8.14 The global fit performed on the smooth dijet mass spectrum from the <i>Full16_LowMass</i> fit control region using the 4 and 5 parameter dijet fit functions. . . . .	138
8.15 The windows used by the SWiFt background estimate in the <i>Full16_LowMass</i> data-set analysis for a range of window half-widths. . . . .	139
8.16 The window selection procedure for a $3 \text{ fb}^{-1}$ subset of <i>Full16_LowMass</i> data. . . . .	143
8.17 The SWiFt search phase run on a $3 \text{ fb}^{-1}$ subset of the <i>Full16_LowMass</i> data-set. . . . .	144
8.18 The SWiFt search phase run on the smooth dijet mass spectrum from the <i>Full16_LowMass</i> fit control region. . . . .	145
8.19 The SWiFt search phase run on a data-like dijet mass spectrum of the <i>Full16_LowMass</i> fit control region. . . . .	146
8.20 The normalised distributions of BumpHunter $p$ -values from performing the SWiFt background estimate on an ensemble of data-like dijet mass spectra from the <i>Full16_LowMass</i> fit control region. . . . .	148
8.21 The SWiFt search phase run on a data-like dijet mass spectrum from the fit control region with a simulated SSM $Z'$ boson of mass 800 GeV injected. . . . .	150
8.22 The SWiFt search phase run on a data-like dijet mass spectrum from the fit control region with a simulated SSM $Z'$ boson of mass 800 GeV injected when a region of 705–834 GeV has been excluded from the SWiFt background estimation. . . . .	151
8.23 An illustration of the window selection procedure for a data-like dijet mass spectrum when a simulated SSM $Z'$ boson of mass 800 GeV has been injected and a region of 705–834 GeV has been excluded from the SWiFt background estimation. . . . .	152
8.24 The window selection procedure for the full <i>Full16_LowMass</i> data-set. . . . .	155
8.25 The $\chi^2$ $p$ -value and Wilks' $p$ -value for each window fit in the SWiFt background estimate performed on the full <i>Full16_LowMass</i> data-set. . . . .	155
8.26 The dijet mass spectrum of the <i>Full16_LowMass</i> data-set and the SWiFt background estimation. The most discrepant excess found by the BumpHunter algorithm and the associated $p$ -value are shown. . . . .	156
9.1 The background systematic uncertainties as a function of dijet mass in the <i>Summer16_HighMass</i> data-set analysis. . . . .	162
9.2 95% credibility level upper limits on the product of cross-section, detector acceptance and tagging efficiency for the $Z'$ boson and $b^*$ quark as a function of generated mass using the <i>Summer16_HighMass</i> data-set. . . . .	163

9.3	95% credibility observed upper limits on the product of cross-section, detector acceptance, tagging efficiency and branching ratio for Gaussian signals using the <i>Summer16_HighMass</i> data-set. . . . .	164
9.4	Simulated SSM $Z'$ boson dijet mass signal templates and dijet mass signal templates created using the signal morphing technique used in the <i>Full16_LowMass</i> data-set limit setting phase. . . . .	166
9.5	The $b$ -jet trigger and background systematic uncertainties for the <i>Full16_LowMass</i> data-set as a function of dijet mass. . . . .	167
9.6	The nominal SWiFt background and signal subtracted background estimations for a data-like dijet mass spectrum from the fit control region with a SSM $Z'$ boson injected as a ratio to the nominal SWiFt background estimation performed on the same data-like dijet mass spectrum when no signal is injected. . . . .	169
9.7	The ratio of signal subtracted background estimations and the SWiFt background estimate performed on the full <i>Full16_LowMass</i> data-set. . . . .	170
9.8	95% credibility level upper limits on the product of cross-section and branching ratio for the SSM, leptophobic and DM $Z'$ boson and as a function of generated mass using the <i>Full16_LowMass</i> data-set. . . . .	172
9.9	95% credibility upper limits on the product of cross-section, detector acceptance, tagging efficiency and branching ratio for Gaussian signals using the <i>Full16_LowMass</i> data-set. . . . .	174
B.1	A plot showing the threshold jet- $p_T$ of a single jet trigger as a function of the trigger-level jet- $p_T$ requirements. . . . .	183
C.1	Figure 8.20 for all SWiFt configurations using the 4 parameter dijet fit function. . . . .	184
C.2	Figure 8.20 for all SWiFt configurations using the 5 parameter dijet fit function. . . . .	185
C.3	Figure 8.18 for all SWiFt configurations using the 4 parameter dijet fit function. . . . .	186
C.4	Figure 8.18 for all SWiFt configurations using the 5 parameter dijet fit function. . . . .	187
C.5	Figure 8.19 for all SWiFt configurations using the 4 parameter dijet fit function. . . . .	188
C.6	Figure 8.19 for all SWiFt configurations using the 5 parameter dijet fit function. . . . .	189

C.7	Figure 8.21 for all SWiFt configurations using the 4 parameter dijet fit function. . . . .	190
C.8	Figure 8.21 for all SWiFt configurations using the 5 parameter dijet fit function. . . . .	191

# List of Tables

2.1	The key properties of the particles in the Standard Model . . . . .	23
3.1	Summary of the main characteristics of the components of the ATLAS Inner Detector. . . . .	42
3.2	A summary of the stochastic, noise and constant terms of the intrinsic energy resolution of components of the ATLAS calorimeter. . . . .	49
4.1	The MV2c10 $b$ -tagging algorithm operating points; with the corresponding $b$ -jet efficiency, $c$ -jet rejection, light-jet rejection and $\tau$ rejection. . . . .	65
5.1	A table summarising the three epochs of data, showing the constituent run numbers, the integrated luminosity after a $b$ -jet trigger GRL is applied and the effect of not finding a $xPrmVtx$ primary vertex. . . . .	78
5.2	A table showing the systematic uncertainty assigned for the high- $p_T$ extrapolation. . . . .	89
5.3	The jet-level $b$ -jet trigger efficiency data/simulation scale factors as a function of jet- $p_T$ with total uncertainty and the contributions from the different sources of uncertainty considered. . . . .	92
5.4	A comparison of the uncertainty on the jet-level $b$ -jet trigger efficiency for various offline operating points. . . . .	93
5.5	A table showing the event-level online primary vertex efficiency as a function of leading jet- $\eta$ with total uncertainty and the contributions from the different sources of uncertainty considered. . . . .	95
7.1	The estimated $S/\sqrt{B}$ at $3 \text{ fb}^{-1}$ for 3 different MV2c10 operating points for the <i>Full16.LowMass</i> data-set analysis. . . . .	107
7.2	A summary of the key details of the di- $b$ -jet event selection applied. . . . .	112
8.1	The functional form of the dijet fit functions. . . . .	118

8.2	The fraction of data-like spectra that pass the fit quality requirements when the SWiFt background estimation procedure is performed for 100 data-like dijet mass spectra taken from the <i>Full16_LowMass</i> fit control region. . . . .	143
8.3	The fraction of data-like dijet mass spectra with a BumpHunter <i>p</i> -value less than 0.05 and 0.01, for the SWiFt search phase performed on an ensemble of data-like spectra taken from the <i>Full16_LowMass</i> fit control region. . . . .	147
8.4	The BumpHunter <i>p</i> -value when performing the SWiFt search phase to a data-like dijet mass spectrum that has been injected with a SSM $Z'$ boson with a variety of generated masses and normalisation factors. . . . .	153
9.1	The signal systematic uncertainties used in the <i>Summer16_HighMass</i> data-set analysis. . . . .	162
9.2	The signal systematic uncertainties used in the <i>Full16_LowMass</i> data-set analysis. . . . .	166
10.1	A summary of the integrated luminosity of data-sets used by the di- <i>b</i> -jet analyses performed at ATLAS and the expected integrated luminosities at key points in the LHC schedule . . . . .	176
10.2	A comparison of the observed 95% credibility level upper mass limits set by the <i>Summer16_HighMass</i> data-set analysis and a di- <i>b</i> -jet search performed by the CMS collaboration . . . . .	177

## Chapter 1

# Introduction

The Standard Model is the current best description of the fundamental particles of the universe and their interactions. However, inconsistencies within the Standard Model indicate that there must be Beyond Standard Model (BSM) physics. Many proposed BSM models predict the existence of new particles which preferentially decay to a pair of  $b$ -quarks or a  $b$ -quark and a gluon. The observation of such a BSM particle would provide crucial experimental evidence in the development of a more complete theory of particle physics.

One experimental technique to discover a BSM particle is to search for the dominant resonant production of that particle using a particle collider. Resonant production occurs when the invariant mass of the colliding partons is equal to the mass of the BSM particle. The experimental signature of resonant production is known as a resonance.

Many searches for resonances of BSM particles decaying to a pair of quarks or gluons have been performed using the invariant mass distribution of pairs of hadronic jets created by high-energy hadron collisions [1], such searches are known as inclusive dijet searches. Inclusive dijet searches have been performed using 13 TeV proton–proton ( $pp$ ) collisions at the Large Hadron Collider (LHC) by the ATLAS and CMS collaborations; the searches have probed the mass ranges 1.1 – 8 TeV [2, 3, 4] and 0.1 – 1.5 TeV [5, 6, 7], no evidence of a BSM resonance has yet been found.

The sensitivity of dijet searches to BSM particles decaying to one or two  $b$ -quarks can be increased using  $b$ -jets, where a  $b$ -jet is a hadronic jet containing a  $b$ -quark. Such searches are known as di- $b$ -jet searches. Di- $b$ -jet searches have previously been performed by the CDF collaboration using 1.8 TeV  $p\bar{p}$  collisions at the Tevatron [8] and by the CMS collaboration using 8 TeV  $pp$  collisions at the LHC [9]; no evidence of a BSM resonance was found by either collaboration.

Di-*b*-jet searches have been performed using the ATLAS experiment with higher-energy  $pp$  collisions than any previous di-*b*-jet search, representing an unprecedented opportunity to search for BSM particles decaying to *b*-quarks. This thesis presents two di-*b*-jet searches performed using 13 TeV  $pp$  collision data collected in 2015 and 2016 by the ATLAS detector. A high-mass di-*b*-jet search probes the mass region 1.4 – 6 TeV using an integrated luminosity of  $13.3 \text{ fb}^{-1}$ ; the analysis has been published as a conference note [10]. A low-mass di-*b*-jet search probes the mass region 0.6 – 1.5 TeV using an integrated luminosity of  $24.3 \text{ fb}^{-1}$ ; the analysis has been submitted to Phys. Rev. D. [11].

For the low-mass di-*b*-jet search, real-time identification of *b*-jets is used to collect data, this data-acquisition tool is known as the ATLAS *b*-jet trigger. Therefore, for the low mass di-*b*-jet search, a detailed understanding of the performance of the ATLAS *b*-jet trigger is required. The measurement of the ATLAS *b*-jet trigger efficiency in 2016 data is also presented in this thesis.

The thesis presents the di-*b*-jet searches in the following structure.

Firstly, the theoretical and experimental background to the di-*b*-jet searches is discussed.

- **Chapter 2** presents a description of the Standard Model, a summary of the motivations for BSM physics and an outline of some BSM models that predict particles decaying to one or two *b*-quarks.
- **Chapter 3** presents a description of the LHC accelerator and the ATLAS detector.
- **Chapter 4** presents the reconstructed physics objects used in the di-*b*-jet searches.
- **Chapter 5** presents a description of the triggers used in the di-*b*-jet searches and the measurement of the ATLAS *b*-jet trigger efficiency in 2016 data.

Then, the two di-*b*-jet searches are presented.

- **Chapter 6** presents an introduction to the analysis strategy used in the di-*b*-jet searches.
- **Chapter 7** presents the event selection utilised by the di-*b*-jet searches.
- **Chapter 8** presents the search phase of the di-*b*-jet searches; which is a search for evidence of resonances in the di-*b*-jet events selected. The strategy and results from the search phase for both di-*b*-jet searches are shown.
- **Chapter 9** presents the limit setting phase of the di-*b*-jet searches. The strategy and results of the limit setting phase for both di-*b*-jet searches are shown.

Finally, the work presented in this thesis is summarised.

- **Chapter 10** presents an outlook of the future prospects of di-*b*-jet searches.
- **Chapter 11** presents the conclusions of the research presented in this thesis

## 1.1 Personal Contributions

In modern experimental particle physics, most research is performed as part of large collaborations, such that the experimental challenges of construction, operation and data-analysis can be shared amongst many. One such of these collaborations is the ATLAS experiment at the LHC, comprised of over 3,000 physicists and engineers.

This thesis presents research performed between September 2014 and December 2017 carried out as part of the ATLAS collaboration. To present the research in a complete form, the work must be presented within the context of the research carried out by the ATLAS collaboration. Furthermore, only the most significant contributions of the work are presented such that this thesis forms a coherent and consistent document without repetition or the presentation of superseded studies.

For clarity, this section summarises my personal contributions to the research activities of the ATLAS collaboration and highlights where these are presented in the thesis. In addition, all figures and tables that I did not produce are indicated using a citation in the caption; only figures that I produced do not have a citation.

- ***b*-Tagging:**

I was a member of the *b*-tagging group between September 2014 and September 2015. I investigated improvements to *b*-tagging at high jet- $p_T$  and performed the first data/simulation comparisons of *b*-tagging performance in 13 TeV data using dijet events collected between May and July 2015 by the ATLAS detector. This work is not presented in this thesis.

- **Di-*b*-Jet Search with the *Full15\_HighMass* data-set:**

Between September 2015 and February 2016 I was a member of the analysis team that performed the first ever di-*b*-jet search at ATLAS. This analysis searched the mass range 1.2 – 5 TeV using  $3.2 \text{ fb}^{-1}$  of 13 TeV  $pp$  collision data collected in 2015 by the ATLAS detector. The analysis has been published in Physics Letters B [12]. I performed validation studies for the background estimation procedure. This work is not presented in this thesis.

- **Di-*b*-Jet Search with the *Full15\_LowMass* data-set:**

Between February 2015 and June 2016 I was a member of the analysis team that performed the first ever di-*b*-jet search at ATLAS using a *b*-jet trigger. This analysis searched the mass range 0.6 – 1.2 TeV using  $3.2 \text{ fb}^{-1}$  of 13 TeV  $pp$  collision data collected in 2015 by the ATLAS detector. This analysis has been published as a conference note [13]. I performed validation studies for the background estimation procedure. This work is not

presented in this thesis.

- **Di-*b*-Jet Search with the *Summer16\_HighMass* data-set:** (Presented in Chapters 6 – 9)

Between June 2015 and September 2016 I was a member of the analysis team for the *Summer16\_HighMass* data-set analysis. This analysis is presented in Chapters 6 – 9. The analysis has been published as a conference note [10]. I was responsible for:

- Validating the background estimation and search phase (presented in Section 8.4).
- Selection of the mass range of the analysis (Section 7.2).
- Creation of event displays (Section 7.4).

- ***b*-Jet Trigger Efficiency Measurement in 2016 data:** (Presented in Section 5.3)

Between September 2016 and March 2017, as part of the *b*-jet trigger group, I performed the *b*-jet trigger efficiency measurement in 2016 data which is presented in Section 5.3. I was responsible for all aspects of the analysis, using a framework and strategy developed jointly with John Alison.

- **Di-*b*-Jet Search with the *Full16\_LowMass* data-set:** (Presented in Chapters 6 – 9)

Between September 2016 and December 2017 I was a member of the analysis team for the *Full16\_LowMass* data-set analysis. From May 2017, I co-lead the analysis team as analysis contact. The analysis is presented in Chapters 6 – 9. The analysis has been submitted to Phys. Rev. D. [11]. I was responsible for:

- All aspects of event selection, except *b*-tagging optimisation (Chapter 7).
- Validation and results of the search phase (Section 8.5).
- Adapting the data processing framework for the use of the *b*-jet trigger.
- Derivation of the *b*-jet trigger and background systematic uncertainties, creation of the background templates used in the limit-setting phase (both Section 9.4).
- Organising and representing the analysis within the ATLAS collaboration.

- **Di-*b*-Jet Search with the *Full16\_HighMass* data-set:**

Between September 2016 and December 2017 I was a member of the analysis team for the *Full16\_HighMass* data-set analysis. This analysis has been submitted jointly with the *Full16\_LowMass* data-set analysis to Phys. Rev. D. [11]. The analysis is not presented in this thesis. I contributed towards the validation of the background estimation and search phase. This work is not presented in this thesis.

- **Event Display:**

Between July 2015 and December 2016 I carried out maintenance of the ATLANTIS Event Display used in the ATLAS control room and performed shifts as on-call expert.

## Chapter 2

# An Incomplete Theory

One of the great questions that humans have always tried to answer is what are the fundamental building blocks of the universe and what are the rules that govern them? The current best answer to this question is the ‘*Standard Model of Particle Physics*’, a mathematical description of a finite set of fundamental particles and their interactions. The Standard Model has been found to agree with experimental data at great precision [14] and, as a result, is the foundation of the field of particle physics. However, it is known that this is not a complete theory and there must be a deeper underlying theory that lies beyond the Standard Model.

This chapter will describe the Standard Model and possible Beyond Standard Model (BSM) physics in the context of di- $b$ -jet searches. Section 2.1 briefly describes the particles and forces of the Standard Model. Section 2.2 describes hadronic jet formation and the production of the dominant Standard Model background to di- $b$ -jet searches. Section 2.3 will discuss BSM physics; specifically the problems in the Standard Model that require BSM physics and proposed BSM models that predict resonances preferentially decaying to one or two  $b$ -quarks.

## 2.1 The Standard Model

The Standard Model is a quantum field theory, meaning that the theory describes a finite set of particles and their interactions in terms of a set of fields.

### 2.1.1 Particles

The Standard Model consists of a set of fundamental particles, where fundamental means that they are not composed of other constituent particles. Full details of the Standard Model particles are found in [15].

The particles of the Standard Model form three groups of particles with similar properties. The particle groups are:

- **Quarks:** There are 6 different types of quarks, known as flavours, arranged in 3 generations. For each quark there is also an anti-quark, which has identical mass and spin, but opposite charge and quantum numbers.
- **Leptons:** There are 6 different types of leptons, arranged into 3 generations, each containing a charge  $-1$  particle and a charge 0 neutrino. For each lepton there is also an anti-lepton.
- **Bosons:** There are a set of integer-spin particles known as bosons. The bosons act as the mediators of the forces that will be described below.

Table 2.1 summarises the key properties of the particles in the Standard Model.

Particle Group	Particle Name	Symbol	Charge	Spin	Mass [GeV]
Quark	Up	$u$	$+2/3$	$1/2$	0.0022
	Down	$d$	$-1/3$	$1/2$	0.0047
	Charm	$c$	$+2/3$	$1/2$	1.3
	Strange	$s$	$-1/3$	$1/2$	0.096
	Top	$t$	$+2/3$	$1/2$	173
	Bottom	$b$	$-1/3$	$1/2$	4.2
Lepton	Electron	$e$	$-1$	$1/2$	$5.1 \times 10^{-4}$
	Electron Neutrino	$\nu_e$	0	$1/2$	$<2 \times 10^{-9}$
	Muon	$\mu$	$-1$	$1/2$	0.11
	Muon Neutrino	$\nu_\mu$	0	$1/2$	$<1.9 \times 10^{-4}$
	Tau	$\tau$	$-1$	$1/2$	1.8
	Tau Neutrino	$\nu_\tau$	0	$1/2$	$<1.8 \times 10^{-2}$
Boson	Photon	$\gamma$	0	1	0
	W boson	$W^\pm$	$\pm 1$	1	80
	Z boson	$Z_0$	0	1	91
	Gluon	$g$	0	1	0
	Higgs Boson	$H$	0	0	125

**Table 2.1:** The key properties of the particles in the Standard Model, organised by particle group and then by generation. Values taken from [15].

### 2.1.2 Forces

The Standard Model combines three key quantum field theories. The first is the electro-weak theory [16] which describes the electro-magnetic force and the weak force. The second is Quantum Chromodynamics (QCD) [15] which describes the strong force. Finally, the Higgs Mechanism<sup>1</sup> [17, 18] describes the origin of mass in the Standard Model<sup>2</sup>. Each of the forces is discussed below.

- **Electro-magnetic (EM) Force:**

The EM force is an interaction between electrically charged particles and is mediated by the photon. The strength of the EM coupling is proportional to the EM coupling constant,  $\alpha_{EM}$ , multiplied by the product of the charges of the two particles, where  $\alpha_{EM} \sim 1/137$ <sup>3</sup>.

- **Weak Force:**

The weak force is composed of two interactions described by the electro-weak theory: the neutral current interaction and the charged current interaction.

- The ‘*neutral current interaction*’ is mediated by the  $Z_0$  boson, interacts with all fermions, and does not allow flavour changing interactions.
- The ‘*charged current interaction*’ is mediated by the  $W^+$  and  $W^-$  bosons, has a universal interaction with all fermions, and flavour changing interactions are allowed. In the quark sector, the charged current interaction couples with weak eigenstates of fermions rather than their flavour eigenstates, allowing for interactions that change the generation of the quark’s flavour. The relative amplitudes of each flavour changing interaction is described by the CKM matrix [19]; the values of this matrix highly suppress generational changing interactions involving the 3rd generation of quarks.

At low energies ( $Q < m_W$ ) the weak force is less strong than the EM force due to the large mass of the  $W/Z$  boson (Weak/EM  $\sim 10^{-4}$ ). At large energies ( $Q \gtrsim m_W$ ) the EM force and weak force become comparable in strength.

- **Strong Force:**

QCD describes the strong force. The strong force is mediated by gluons and interacts with particles that have colour charge; which are quarks and gluons. QCD has 3 colour charges: known as red, green and blue. A quark has a colour charge, an anti-quark has an anti-colour charge and a gluon has a colour charge and an anti-colour charge, leading to 8 independent gluon colour states. A colour neutral object can be formed if all three colour charges are present (i.e. in a baryon containing three quarks) or if a colour and the

<sup>1</sup>Also known as the Englert-Brout-Higgs mechanism.

<sup>2</sup>With the exception of the neutrinos, whose mass is not described by the Standard Model.

<sup>3</sup> $\alpha_{EM}$  depends on the energy scale of the collision;  $\alpha_{EM} \sim 1/137$  is the zero energy value.

corresponding anti-colour is present (i.e. in a meson that contains  $q\bar{q}$ ). As QCD describes hadronic jet formation and the largest background in a di- $b$ -jet search, QCD is discussed further in Section 2.2.

- **Higgs Mechanism:**

The Higgs mechanism introduces an extra scalar field to the Standard Model with a Higgs potential given by the so-called ‘Mexican-hat potential’. This allows for spontaneous symmetry breaking which gives mass to the Standard Model bosons. In addition, a Yukawa coupling term between the scalar field and the fermions gives rise to the mass of the fermions<sup>4</sup>. A final prediction of the Higgs mechanism is the existence of the Higgs boson. The first observation of the Higgs boson by the ATLAS [20] and CMS [21] experiments in 2012 confirms the Higgs mechanism, a great triumph of the Standard Model.

## 2.2 QCD: Hadronic Jet Formation and Dijet Production

As described above, Quantum Chromodynamics (QCD) is a theory that describes the strong interaction between quarks and gluons. Section 2.2.1 will describe the renormalisation of QCD, which is important for understanding how QCD works. Then Section 2.2.2 will describe the formation of hadronic jets and Section 2.2.3 will describe the production of dijet events through QCD in  $pp$  collisions, which is the dominant background in di- $b$ -jet searches; these two elements of QCD are critical to the analyses being presented in this thesis. Quarks and gluons can often fill similar roles in hadronic jet formation and dijet production, hence I will refer to them collectively as ‘partons’ in this section.

### 2.2.1 Renormalisation and the Running of $\alpha_S$

To perform calculations of cross-sections using QCD, or indeed any quantum field theory, one must consider higher-order loop diagrams; for example a simple gluon propagator has additional first-order diagrams as shown in Figure 2.1.

The first-order diagrams shown in Figure 2.1 are loop diagrams, meaning that they contain an internally connected virtual quark or gluon. Therefore, when calculating a cross-section by integrating over all possible phase space; the contribution from loop diagrams becomes divergent because the virtual quark/gluon can take an infinite range of energy values without violating conservation of energy.

---

<sup>4</sup>With the exception of the neutrinos, whose mass is not described by the Standard Model.

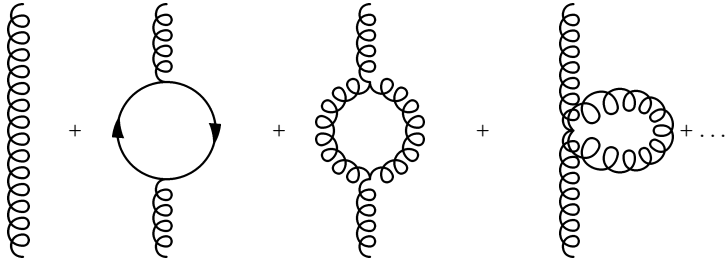


**Figure 2.1:** A schematic showing the gluon propagator with additional first order loops [22].

To avoid these divergences, there is a well accepted mathematical procedure [15, 23]. The first step of the procedure, known as regularisation, separates the divergent and non-divergent terms of the cross-section calculation. One method of regularisation introduces an arbitrarily large upper limit,  $\Lambda$ , to the energy that the internal gluon/quark can have such that cross-section calculations involving an integral over all phase space no longer contain divergent terms, however the cross-section will now depend on some unknown and large parameter  $\Lambda$ .

In the second step of the procedure, known as renormalisation, the parameters of QCD are redefined such that  $\Lambda$  is absorbed into the redefined parameters. To ensure that the parameters maintain a physical dimension in this process a new arbitrary energy must be introduced, known as the renormalisation scale,  $\mu_R$ . The result is that the cross-section can be calculated using the renormalised parameters of QCD, where each parameter depends on  $\mu_R$ . This is a powerful statement as if, through experimental measurement, we know the parameters of the renormalised QCD theory for a specific value of  $\mu_R$  then we are able to calculate the parameters of QCD, and hence physical observables such as cross-sections, at any value of  $\mu_R$  without having any knowledge of the value of  $\Lambda$ .

When applying the renormalised QCD theory to a specific process the renormalisation scale is chosen to be the momentum transfer,  $Q$ , of the process being considered. This is because the cross-section of the process is typically calculated by performing perturbative expansions of the renormalised QCD theory, and by setting  $\mu_R = Q$  we ensure that higher-order contributions cannot become large due to a dependence on  $\mu_R$ .

Now let's consider the strong coupling constant,  $\alpha_S$ , which is the parameter of QCD that describes the strength of the strong interaction. In the renormalised QCD theory  $\alpha_S$  effectively depends on the momentum scale of the process being considered, this effect is known as the '*running of  $\alpha_S$* '. The running of  $\alpha_S$  can be measured through experimental observation; Figure 2.2 shows the measured values of  $\alpha_S$  as a function of the energy scale,  $Q$ , in a range of experiments.

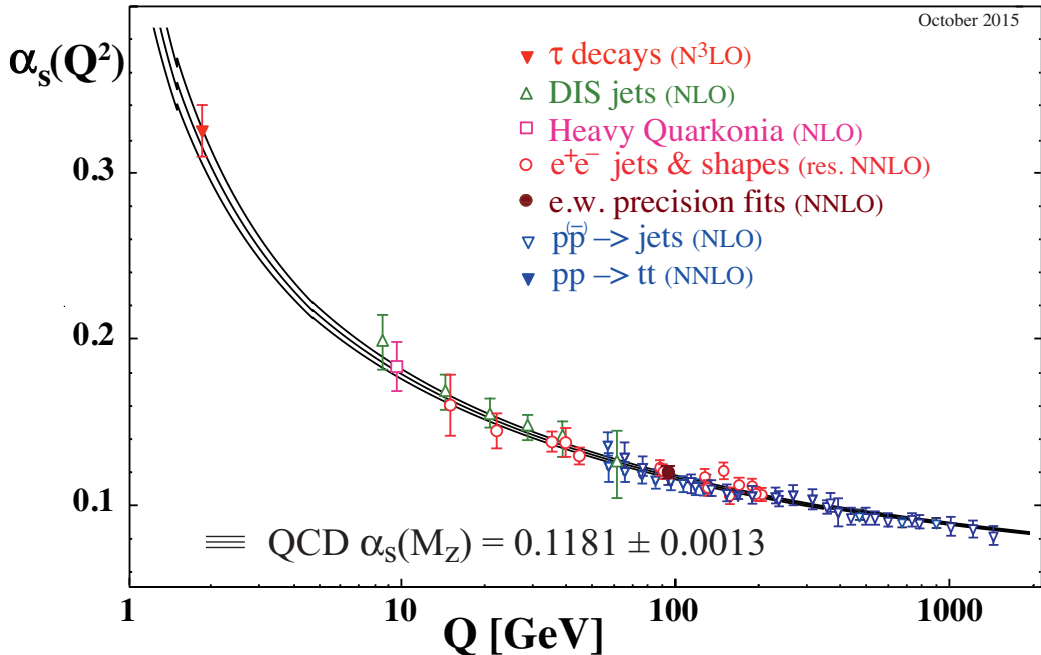


**Figure 2.2:** Summary of measurements of  $\alpha_s$  as a function of the energy scale,  $Q$ . The respective degree of QCD perturbation theory used in the extraction of  $\alpha_s$  is indicated in brackets (NLO: next-to-leading order; NNLO: next-to-next-to leading order; res. NNLO: NNLO matched with resummed next-to-leading logs; N3LO: next-to-NNLO) [15].

There are three features of Figure 2.2 that should be noted. Firstly, the size of  $\alpha_s$  is generally large compared to  $\alpha_{EM}$  ( $\sim 1/137$ ); this means that, depending on the energy scale, the strong force is typically stronger than the EM force by one or two orders of magnitude. Secondly, at high energies/small distances the strong force becomes relatively weak, this phenomenon is known as ‘asymptotic freedom’. At these energy scales, perturbative expansions of QCD are possible. Finally, at low energies/large distances the strong force is exceptionally strong. As a result, if two interacting quarks are separated by a large distance then it is energetically favourable to pair-produce  $q\bar{q}$  pairs from the vacuum until a colour neutral object can be formed. Therefore, quarks are not observed in isolation, but instead quarks form colour neutral hadrons; this feature of QCD is known as ‘confinement’. At low-energy scales perturbative expansions of QCD are not possible.

## 2.2.2 Hadronic Jet Formation

It is common in hadronic colliders that a high-momentum quark or gluon will be produced in the final-state<sup>5</sup>. However, due to the effect of quark confinement described above, an isolated quark or gluon will not be observed. Instead a stream of energetic, collimated hadrons will be formed, known as a hadronic jet. Hadronic jet formation occurs through two distinct processes; parton shower and hadronisation.

- **Parton Shower:**

The high-energy final-state quark or gluon will split into a  $qg$  or  $q\bar{q}$  pair respectively. The resulting quarks and gluons will also undergo splitting to form more partons, which in turn can split. This process repeats to form the parton shower. Due to relativistic effects, each splitting will generally be at a small opening angle in the lab-frame and as such the partons will be highly collimated in the direction of the initial parton. The parton shower process occurs at high energy where the value of  $\alpha_S$  is small and thus perturbative expansions of QCD can be used to perform calculations. However, at each step of the splitting, the energy of the partons decreases and thus the value of  $\alpha_S$  increases.

- **Hadronisation:**

When the energy scale becomes small<sup>6</sup>,  $\alpha_S$  becomes large such that the dominant QCD effect is quark confinement. Therefore, the quarks and anti-quarks produced in the parton shower form hadrons. The hadrons are colour neutral objects, meaning that stable hadrons that do not decay through QCD will be formed<sup>7</sup>. The hadronisation process occurs at large values of  $\alpha_S$  so cannot be calculated using perturbative expansions; models such as the string model [24] and the cluster model [25] are used to simulate hadronisation.

The end result of the hadronisation process is a set of collimated stable hadrons, known as a hadronic jet, which can be observed in an experiment. Note that our understanding of how one goes from an initial parton to a hadronic jet is model dependant, for example there is a choice of hadronisation model. Hence, in experiments this dependence is removed by defining a jet in terms of observables, such that the experimental results are model-independent and results can be reinterpreted when improved models become available<sup>8</sup>. The details of the experimental definition of a hadronic jet is discussed in Section 4.2.

<sup>5</sup>An example of this is dijet production, as will be described in Section 2.2.3.

<sup>6</sup>This is generally defined as small relative to the hadronic scale,  $\Lambda$ , which is typically a few hundred MeV

<sup>7</sup>Some unstable hadrons, such as a  $\Delta^{++}$ , may be initially formed in the process but these will decay rapidly through the strong interaction. In addition, some hadrons might not be stable under the weak or EM interaction, such as a Kaon, but the time-scale of their decays will be much larger.

<sup>8</sup>A good explanation of why model-independent jets are desirable is found in [26].

### 2.2.3 Dijet Production in $pp$ Collisions

QCD dijet production is one of the most common processes that occurs in  $pp$  colliders. QCD dijet production occurs when the two protons interact through QCD to produce two quarks or gluons in the final state. The free partons will then form hadronic jets through the processes described in Section 2.2.2. Figure 2.3 shows the Feynman diagram of dijet production in a  $pp$  collision through the  $qg \rightarrow qg$  channel.

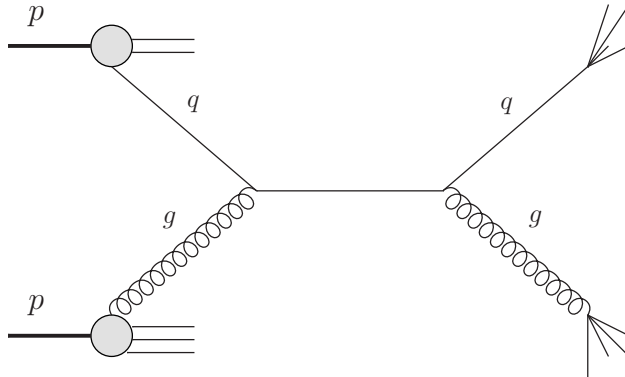


**Figure 2.3:** A Feynman diagram showing dijet production in a proton–proton collision through the  $qg \rightarrow qg$  channel. Adapted from [27].

The cross-section of QCD dijet production from a  $pp$  collision is described by the hadronic cross-section,  $\sigma_{had}$ . To calculate the hadronic cross-section, two elements are separated out in a process known as ‘factorisation’.

The first element is the ‘parton-level cross-section’,  $\hat{\sigma}$ , which is the cross-section of two partons from the proton ( $p_i$  and  $p_j$ ) scattering to give two final state partons ( $p_k$  and  $p_l$ ). In Figure 2.3,  $p_i$  and  $p_j$  represent the incoming  $q$  and  $g$  whilst  $p_k$  and  $p_l$  represent the outgoing  $q$  and  $g$ . The parton-level cross section is discussed further in Section 2.2.3.1.

The second element is the *Parton Distribution Function* (PDF),  $F_i(x_i)$ , which gives the number density of a specific parton,  $p_i$ , with momentum fraction,  $x_i$ , in a proton. Momentum fraction is defined as the fraction of the proton’s total momentum that the parton is carrying,  $x = p_{\text{parton}}/p_{\text{proton}}$ . This part of the interaction is indicated by the circles on the left of the Feynman diagram in Figure 2.3. Further details on PDFs is found in Section 2.2.3.2.

The elements are combined to calculate  $\sigma_{had}$ :

$$\sigma_{had} = \sum_{i,j,k,l} \int dx_i dx_j F_i(x_i, Q^2) F_j(x_j, Q^2) \hat{\sigma}(p_i, p_j \rightarrow p_k p_l) \quad (2.1)$$

where there is an integral over all possible values of momentum fractions  $x_i$  and  $x_j$ , a sum

over all possible initial partons from the two protons labelled  $i$  and  $j$ , and a sum over all possible final-state partons labelled by  $k$  and  $l$ <sup>9</sup>.  $Q^2$  is the energy scale of the collision.

With the two elements separated we can discuss each separately.

### 2.2.3.1 Parton-Level Cross-Section

To describe the parton-level cross-section, some useful variables must be defined. The first is the invariant mass of the outgoing partons,  $m_{kl}$ , which is given in terms of the four-momentum of the two partons;

$$m_{kl}^2 = (p_k^\mu + p_l^\mu)^2 \quad (2.2)$$

Then there are two related angular variables,  $y^*$  and  $\theta^*$ , defined in terms of the rapidities of the outgoing partons,  $y_k$  and  $y_l$ ;

$$y^* = \left( \frac{y_k - y_l}{2} \right) \quad (2.3)$$

$$\cos(\theta^*) = \tanh(y^*) \quad (2.4)$$

Finally the Mandelstam variables are defined as,

$$\hat{s} = m_{kl}^2, \quad \hat{t} = -\frac{1}{2} \hat{s} (1 - \cos \theta^*), \quad \hat{u} = -\frac{1}{2} \hat{s} (1 + \cos \theta^*) \quad (2.5)$$

The Mandelstam variables represent the square of the 4-momentum of the propagator in a 2→2 particle scatter event for an s, t or u-channel Feynman diagram respectively.

The parton-level differential cross-section of incoming partons  $i$  and  $j$  scattering to give outgoing partons  $k$  and  $l$  is given in terms of the variables  $\theta^*$  and  $m_{kl}$  [28];

$$\frac{d^2\hat{\sigma}(p_i p_j \rightarrow p_k p_l)}{dm_{kl}^2 d\cos\theta^*} = \frac{\pi\alpha_s^2}{2m_{kl}^2} \delta(x_i x_j s - m_{kl}^2) S(ij \rightarrow kl) \quad (2.6)$$

where  $\sqrt{s}$  is the centre-of-mass energy and  $S(ij \rightarrow kl)$  is the process dependant kinematics of a  $ij \rightarrow kl$  parton scatter. The  $\delta(x_i x_j s - m_{kl}^2)$  term requires that the invariant mass of the incoming partons is same as the invariant mass of the propagator.

The  $S(ij \rightarrow kl)$  for each process is given in Table 1 in [1]. All but one process can occur through a t-channel diagram and therefore the  $S(ij \rightarrow kl)$  for those processes contains a  $1/\hat{t}$  or  $(1/\hat{t})^2$  term. The importance of this will be discussed in Section 2.2.3.3.

---

<sup>9</sup>The final state sums do not include top-quarks because, as will be discussed in Section 2.2.4, they do not form regular jets. In addition, due to its heavy mass, the top-quark is heavily suppressed in the PDFs so can be ignored in the sum over initial partons.

### 2.2.3.2 Parton Distribution Functions

The proton contains two  $u$ -quarks and a  $d$ -quark, known as valence quarks, and a sea of quarks and gluons created through QCD interactions, such as gluons being emitted from the valence quarks and  $q\bar{q}$  pairs being produced from the emitted gluons.

Parton Distribution Functions (PDFs) give the number density of a specific parton,  $p_i$ , in a proton for a given momentum fraction,  $x_i$ , and energy scale,  $Q$ . Due to the large value of  $\alpha_S$  in the proton, QCD cannot be considered in perturbative expansions and as such the PDFs cannot be calculated directly. Instead, the PDFs can be measured by combining a range of experimental scattering results. In particular, strong constraints on the PDFs come from deep inelastic scattering using  $ep$  colliders, such as HERA [29]; the strong constraints are due, in part, to there only being one parton in the collision allowing direct access to the PDFs in a cross-section measurement.

Figure 2.4 shows the  $xF(x, Q^2)$  for a  $Q^2$  of 10 and  $10^4$   $\text{GeV}^2$  from the MMHT2014 PDF set [30]. The various coloured lines represent the PDF for each of the different partons. It shows that as  $x$  increases the values of the PDF for the sea quarks and gluons will fall smoothly; this is because it is energetically unfavourable to produce high momentum gluons or  $q\bar{q}$  pairs. The fall in the PDFs with respect to  $x$  is particularly notable for the gluon which is the dominant contribution at large  $Q^2$  and at low  $x$ . The PDFs of the valence quarks,  $u_v$  and  $d_v$ , have a peak value around  $x \sim \frac{1}{3}$ , and then fall off rapidly at higher  $x$ . This shape is caused as at leading-order the quarks share the momentum equally, but higher-order QCD effects smear this distribution.

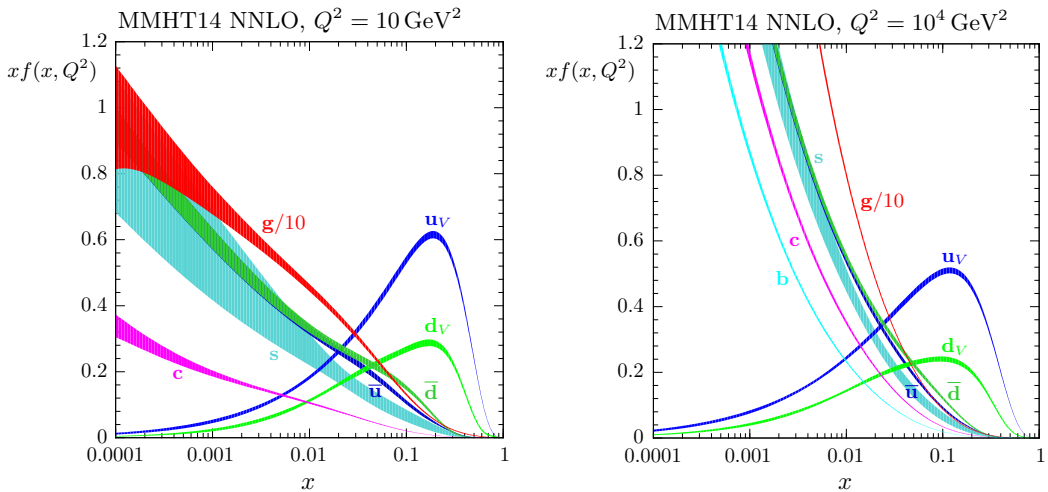


**Figure 2.4:** MMHT2014 NNLO PDFs at  $Q^2 = 10 \text{ GeV}^2$  and  $Q^2 = 10^4 \text{ GeV}^2$ , with associated 68% confidence-level uncertainty bands [30].

### 2.2.3.3 Features of QCD Dijet Production

From the two factorised elements discussed above, there are four important features of the dijet hadronic cross-section that are significant when forming the di-*b*-jet search strategy.

- **Large cross-section :**

The strong coupling constant,  $\alpha_s$ , is large meaning that the dijet cross-section is large. Therefore QCD dijet production is the dominant background in di-*b*-jet searches.

- **Smoothly falling with respect to  $m_{kl}$  :**

QCD dijet production will be smooth and monotonically decreasing with respect to  $m_{kl}$  as a result of three factors. Firstly, the cross section has a  $1/m_{kl}^2$  term. Secondly, as shown in Section 2.2.1,  $\alpha_S$  will smoothly decrease with increasing  $Q$ , which in this case is correlated with  $m_{kl}$ . Finally, as  $m_{kl}$  increases then the momentum fraction of the proton,  $x$ , required to create the dijet event will also increase. As shown in Figure 2.4, the parton distribution functions are generally falling with respect to  $x$ , which will lead to falling behaviour in the hadronic cross-section.

- **Increased production at large values of  $|y^*|$  :**

As discussed in Section 2.2.3.1, all but one of the  $S(ij \rightarrow kl)$  terms contain a  $1/\hat{t}$  or  $(1/\hat{t})^2$  contribution from t-channel Feynman diagrams. These terms will become large when  $\hat{t} \rightarrow 0$  which, from the definition of  $\hat{t}$  in Equation 2.5, occurs when  $\cos \theta^* \rightarrow 1$ . This means that QCD dijet production is increased at large values of  $|y^*|$ .

- **Preference of light-flavour quarks:**

Most  $ij \rightarrow kl$  processes that produce heavy flavour quarks ( $c$  or  $b$ ), with the exception of  $q\bar{q} \rightarrow b\bar{b}$  (or  $c\bar{c}$ ) and  $gg \rightarrow b\bar{b}$  (or  $c\bar{c}$ ), require a heavy flavour quark to be one of the initial partons. Figure 2.4 shows the heavy flavour quarks are suppressed in the PDFs relative to the other partons. Therefore, dijet events will be dominated by jets initiated by gluons or light-quarks ( $u$ ,  $d$  or  $s$ ).

Finally, it should be noted that the above description of QCD dijet production is not complete; only tree-level diagrams have been considered, but there are also higher-order diagrams. Related to that issue is the occurrence of initial state and final state radiation, known as ISR and FSR respectively. ISR is when an additional parton is radiated off the incoming parton and FSR is when an additional parton is radiated off an outgoing parton. ISR and FSR can lead to additional jets in an event, creating a multi-jet event.

In addition, there is the Underlying Event (UE) which consists of the remnants of the proton not used in dijet production and  $pp$  collisions other than the collision creating the dijet event. The UE can lead to additional jets in the event, again creating a multi-jet event.

### 2.2.4 $t\bar{t}$ Production

The top-quark is a special case when discussing the formation of jets from quarks, due to two properties of the top-quark which are distinctive. Firstly, the top-quark decays to a  $b$ -quark and a  $W$  boson with a branching ratio of close to 1 because generational changing interactions involving the 3rd generation of quarks are strongly suppressed in the charged current weak interaction<sup>10</sup>. Secondly, the top-quark is much heavier than the  $b$ -quark meaning that the decay to a  $b$ -quark is energetically favourable. Therefore, the top-quark decays on a shorter time-scale than parton shower processes resulting in two separate objects; the  $W$  boson and the hadronic jet containing a  $b$ -quark.

As in dijet production,  $t\bar{t}$  pairs can be pair-produced in  $pp$  collisions through QCD interactions. The two top-quarks will both decay into a  $W$  boson and a jet containing a  $b$ -quark. In the di-lepton decay mode of  $t\bar{t}$ , one  $W$  boson decays into a  $l^+ \nu_l$  pair and the other into a  $l^- \bar{\nu}_l$  pair. A Feynman diagram showing an example of a di-lepton  $t\bar{t}$  event is shown in Figure 2.5<sup>11</sup>.

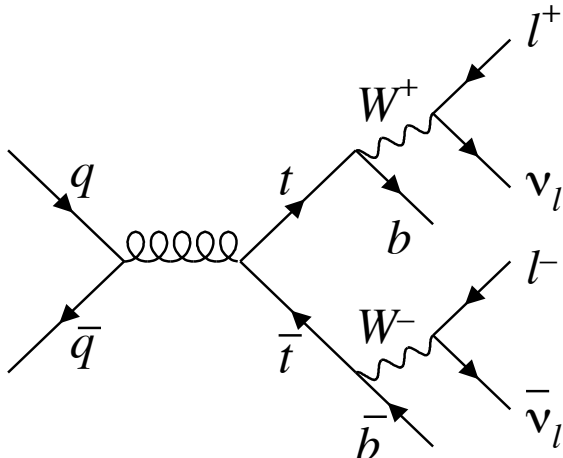


**Figure 2.5:** A Feynman diagram showing an example of a di-lepton  $t\bar{t}$  event [31].

Di-lepton  $t\bar{t}$  events provide a distinct experimental signature. In particular, the  $e\mu$  di-lepton  $t\bar{t}$  decay mode, where the leptons are an electron and a muon, is very distinct as this can only be caused by two separate weak-decays. In addition we have two jets formed from  $b$ -quarks, which can be observed. The distinct signature of di-lepton  $t\bar{t}$  events and the fact that the top-quark nearly always decays to a  $b$ -quark means that this decay topology is used to obtain a pure sample of jets containing  $b$ -quarks, as will be shown in Section 4.3.4 and 5.3.

<sup>10</sup> Section 2.1.2 contains further details of the charged current weak interaction.

<sup>11</sup> This figure shows the  $q\bar{q}$  production mode of  $t\bar{t}$  production; the  $gg$  mode is dominant at the LHC.

## 2.3 Beyond Standard Model Physics

The preceding sections of this chapter described the Standard Model and some of its successes. However, the Standard Model is known to be an incomplete picture of the universe. This section will present some of the key deficiencies of the Standard Model demonstrating that Beyond Standard Model (BSM) physics is required and will discuss some proposed BSM models that motivate the analyses shown in this thesis.

### 2.3.1 Motivations

The motivations for BSM physics listed in this section describe only a subset of deficiencies of the Standard Model, with a focus on the most important missing parts and those that motivate models searched for in this thesis.

#### 2.3.1.1 Gravity

When listing forces in Section 2.1.2, there was no reference to gravity. This is because the description of gravity, Einstein’s General Theory of Relativity, has not been successfully merged with the Standard Model in a so-called ‘Quantum Theory of Gravity’. It is a clear inadequacy of the Standard Model that there is no description of gravity.

#### 2.3.1.2 Dark Matter

Astronomers have made the remarkable observation that  $\sim 80\%$  of the matter in universe must be so-called ‘dark matter’ [32]. Dark matter is not described by the Standard Model, so is clear evidence of Beyond Standard Model physics. It is assumed that dark matter interacts through gravity and can only interact weakly, if at all, with the Standard Model, otherwise we would have already observed it through interactions with Standard Model particles.

The evidence for dark matter comes from many separate astronomical observations, such as studies of galaxy rotation curves, the cosmic microwave background and a collision of two clusters of galaxies, known as the bullet cluster. A wider summary of the evidence for dark matter can be found in [33].

Furthermore, it is assumed the dark matter couples to the Standard Model. This is required in many models of dark matter [34] to explain the observed relative abundance of dark matter particles in the universe. As a result, this means that there may be some unknown particle that couples to both dark matter and Standard Model particles; this particle is referred to as a dark matter mediator.

### 2.3.1.3 Hierarchy Problem

The Hierarchy problem [35] is the fact that the energy scale of the Higgs mechanism ( $M_H = 125$  GeV) is much smaller than the energy scale of gravity, known as the Planck scale ( $M_{Planck} \sim 10^{19}$  GeV) [15]. This means that the energy scale of the Standard Model is very far from the energy scale of the next known interaction, gravity.

The Hierarchy problem leads to complications in theoretical calculations, such as that of the Higgs boson mass [35]. When calculating the Higgs boson mass, one must consider radiative contributions from additional loop diagrams, similar to the corrections considered for a gluon propagator shown in Figure 2.1. However, these contributions are found to be of the order  $\delta m_H^2 \sim \frac{1}{16\pi^2} M_{Planck}^2$ , orders of magnitude larger than the observed mass of the Higgs boson. This means that some mechanism must either cancel the contributions or reduce their size. Whilst the free parameters of the Standard Model can be chosen such that these different contributions approximately cancel out, such fine-tuning of the parameters is hard to believe without some underlying explanation.

Instead, there are two solutions typically proposed to stabilise the effect of the loop corrections. Firstly, one can introduce BSM physics that has loop contributions that cancel the Standard Model contributions. For example this occurs in theories of supersymmetry [36]. Secondly, one can introduce some BSM physics at a new energy scale such that the loop diagram contributions are cut off at  $\delta m_H^2 \sim \frac{1}{16\pi^2} M_{BSM}^2$ . If the BSM physics is on the TeV scale then this would reduce the size of the loop corrections to the scale of the Higgs boson mass, giving some prior belief that new physics could be found at the TeV energy scale.

### 2.3.1.4 Generational Structure of Quarks

The quarks of the Standard Model have a well ordered generational symmetry. However the generational symmetry is not perfect; each generation is heavier than the previous one and within the generations quarks have different masses. In particular, the third generation of quarks is somewhat special; the top-quark is much heavier than the  $b$ -quark and is the heaviest particle of the Standard Model. Furthermore, as the mass of the top-quark is close to the mass of the Higgs boson, the 3rd generation of quarks have a role in symmetry breaking within the Higgs mechanism for some BSM models [37].

There is no good explanation of why there is generational structure in the Standard Model, why the mass hierarchy is unsymmetric or why the third generation has one quark with such a large mass. The generational structure could be a result of some underlying broken symmetry which forms a part of a deeper theory of particle physics. Any deeper

theory explaining the generational structure could contain observable BSM particles, and, given the special nature of the third generation, the BSM particles could couple strongest with the third generation of quarks.

Unlike the case of dark matter, the generational structure of quarks and the special nature of the third generation is not concrete evidence of BSM physics. But it does mean that there are motivations to be particularly interested in searches for resonances decaying to the third generation of quarks.

### 2.3.2 Beyond Standard Model Theories

The previous section discussed a list of deficiencies of the Standard Model, which makes us confident that Beyond Standard Model physics must exist. This leads us to ask what the new theory of physics could be and how can one obtain evidence of such a theory.

Many proposed theories of BSM physics include the addition of a new particle and, in particular, the special nature of the third generation<sup>12</sup> means that some BSM models predict new particles that preferentially decay to two  $b$ -quarks or a  $b$ -quark and a gluon. Furthermore, the Hierarchy Problem suggests that BSM physics may exist at the TeV energy-scale. The observation of such a particle would be evidence of BSM physics.

Two such models that predict particles that preferentially decay to  $b$ -quarks are discussed below. These are used as ‘*benchmark models*’ in the analyses presented in this thesis, where a benchmark model is a plausible signal model that is used to form and optimise a search strategy. Furthermore the benchmark models are used to represent many models that decay to one or two  $b$ -quarks.

#### 2.3.2.1 $Z'$ Boson

One of the most simple additions to the Standard model is that of a  $U(1)'$  gauge symmetry which would result in an additional spin-1 boson, known as the  $Z'$  boson. An additional  $U(1)'$  symmetry appears in many different BSM models and is therefore a well motivated BSM extension [38]. The  $Z'$  boson can decay to a pair of  $b$ -quarks, as shown in Figure 2.6.

Three different  $Z'$  boson models are considered. The first is known as the ‘*Sequential Standard Model*’ (SSM)  $Z'$  boson in which the couplings of the new  $Z'$  boson are the same as the Standard Model  $Z$  boson. The strongest limits on the SSM  $Z'$  boson at the TeV scale are set by searching for a  $Z'$  boson decaying to lepton pairs [39]<sup>13</sup>.

---

<sup>12</sup>Discussed in Section 2.3.1.4.

<sup>13</sup>Because a di-lepton signature is distinct to the large QCD dijet backgrounds produced in  $pp$  collisions.

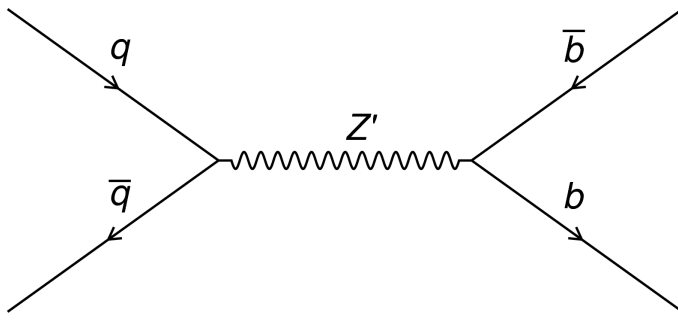


**Figure 2.6:** The leading-order Feynman diagram of the process  $q\bar{q} \rightarrow Z' \rightarrow b\bar{b}$ .

The second model is a ‘*leptophobic*’  $Z'$  boson that does not couple to the lepton sector but has the same coupling to each of the quarks as the Standard Model  $Z$  boson [40]. This model is therefore not strongly constrained by di-lepton searches.

The final model is a ‘*Dark Matter inspired*’ (DM)  $Z'$  model; in which the DM  $Z'$  boson acts as a dark matter mediator which can couple to both the dark matter sector and the Standard Model quark sector [41]. The motivation for a dark matter mediator was discussed in Section 2.3.1.2. This model introduces an additional  $U(1)'$  symmetry and a Dirac fermion dark matter particle that only interacts through the new gauge group. The resulting DM  $Z'$  boson does not couple with the lepton sector and couples with the DM fermion and the Standard Model quark sector with couplings  $g_\chi$  and  $g_{SM}$ , respectively.

It is worth noting in the models considered that the  $Z'$  boson does not preferentially decay to  $b$ -quarks, but rather with similar branching ratio as the other quarks. However, this can still be considered as preferential decay to  $b$ -quarks with respect to the dijet background which is dominated by gluons and quarks from the first two generations, as discussed in Section 2.2.3. Furthermore, there exist  $Z'$  models that do not couple to all generations equally [42], such that a  $Z'$  boson preferentially decaying to  $b$ -quarks is possible.

### 2.3.2.2 Excited Third-Generation Quark

To explain the generational and mass structure of the quark sector, discussed in Section 2.3.1.4, quark compositeness models describe quarks not as fundamental particles, but instead constructed of other fundamental particles. One consequence of quark compositeness models is the prediction of excited quarks,  $q^*$ , which can be observed as heavy resonances.

In particular we consider an excited 3rd generation quark, the  $b^*$  quark [43]. In the regime that the mass of the  $b^*$  quark is much larger than the sum of the masses of the top-quark and the  $W$  boson, as considered by the searches for the  $b^*$  quark presented in this thesis, the dominant decay mode of a  $b^*$  quark is to  $bg$  with a branching ratio of 85% while the remaining decay modes are to  $Wt$ ,  $bZ$  and  $b\gamma$  with branching ratios of 10%, 4.5% and 0.5% respectively<sup>14</sup>. A Feynman diagram showing the dominant production and decay mode of a  $b^*$  quark is shown in Figure 2.7.

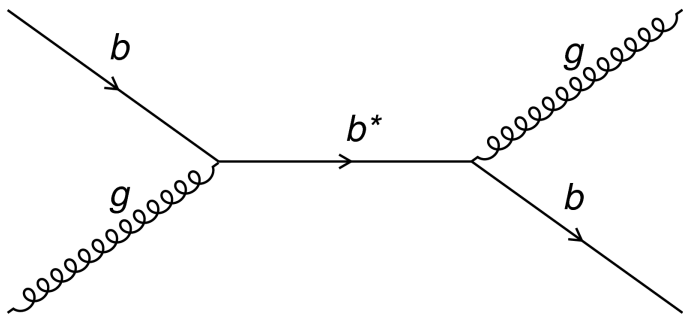


**Figure 2.7:** The leading-order Feynman diagram of the process  $bg \rightarrow b^* \rightarrow bg$

### 2.3.2.3 Model Independence

The two benchmark models demonstrate that searching for particles decaying to one or two  $b$ -quarks is well motivated. However, it is important to note that the prior belief in any specific model of BSM is small. This is because there are many BSM theories proposed and there is little evidence to prefer one model over another. In addition, one must also consider that the true theory may not have been anticipated, such that experiments might be able to see evidence of something truly unexpected.

This means that the di- $b$ -jet searches should be constructed to be sensitive to as many BSM models as possible and allow for the unexpected gifts that nature might throw up.

---

<sup>14</sup>The branching ratios quoted use the assumptions outlined in [43].

## Chapter 3

# The LHC and the ATLAS Detector

### 3.1 The Large Hadron Collider (LHC)

High-energy particle colliders have been an essential tool in high-energy physics research for over 50 years, with a rich history of discovering new particles as each generation of collider pushes the energy frontier; including the discovery of the  $Z$  and  $W$  bosons using the Super Proton Synchotron at CERN in 1983 [44, 45, 46, 47] and the discovery of the top-quark at the Tevatron in 1995 [48, 49].

The Large Hadron Collider (LHC) is the highest energy collider ever built, operated by the *Conseil Européen pour la Recherche Nucléaire (CERN)*. Lying in a tunnel 100 m beneath the Swiss/French border near Geneva, the LHC is a 27 km circumference ring of superconducting magnets and accelerating structures, which accelerate beams of protons to a maximum energy of 6.5 TeV. The proton beams are collided in four different locations on the LHC ring and around each collision point a different detector is constructed to observe these collisions; one of these detectors is the ATLAS detector.

#### 3.1.1 LHC running conditions in 2015 and 2016

Since May 2015 the LHC has been colliding bunches of protons at a centre-of-mass energy of 13 TeV, the highest energy collisions ever obtained by a particle collider<sup>1</sup>. In 2015 and 2016 at the LHC, the time interval between colliding bunches, known as the bunch spacing, was 25 ns<sup>2</sup>.

*Integrated luminosity*,  $L$ , is the quantity that describes the size of a data-set from a collider experiment. Integrated luminosity is defined as  $L = N_{evt}/\sigma$ , where  $\sigma$  is the cross-

---

<sup>1</sup>The period of data-taking starting in 2015 and scheduled to continue until the end 2018 is known as Run-2.

<sup>2</sup>A small amount of data in 2015 was collected with a bunch spacing of 50 ns

section of a particular process occurring at that collider experiment and  $N_{\text{evt}}$  is the number of events in the data-set that occur through that process. Instantaneous luminosity, defined as  $dL/dt$ , is the rate of data-collection. An integrated luminosity of  $3.9 \text{ fb}^{-1}$  and  $35.6 \text{ fb}^{-1}$  was recorded by ATLAS in 2015 and 2016 respectively [50].

To achieve high instantaneous luminosity at the LHC, bunches of protons are collided resulting in many collisions per bunch-crossing. The mean number of collisions per bunch-crossing ( $\langle\mu\rangle$ ) depends on the running conditions of the LHC. For ATLAS, the luminosity weighted average of  $\langle\mu\rangle$  is 13.7 in 2015 data and 24.9 in 2016 data [50]. Collisions in addition to the collision of interest<sup>3</sup> are collectively referred to as ‘pile-up’ [51]. Pile-up presents a challenge to physics analyses at the LHC as the resulting particles from pile-up collisions can affect the measurement of particles from the collision of interest.

Pile-up collisions are then further categorised as ‘*in-time pile-up*’, which are defined as collisions caused by the same bunch crossing as the collision of interest, and ‘*out of time pile-up*’, defined as collisions that occurred in a different bunch crossing than the collision of interest.

## 3.2 The ATLAS Detector

The ATLAS (A Toroidal Large Hadron Collider ApparatuS) detector design, construction and performance has been described in detail in [52, 53, 54]. Therefore this chapter provides a general description of the detector with a focus on the needs of di-*b*-jet searches.

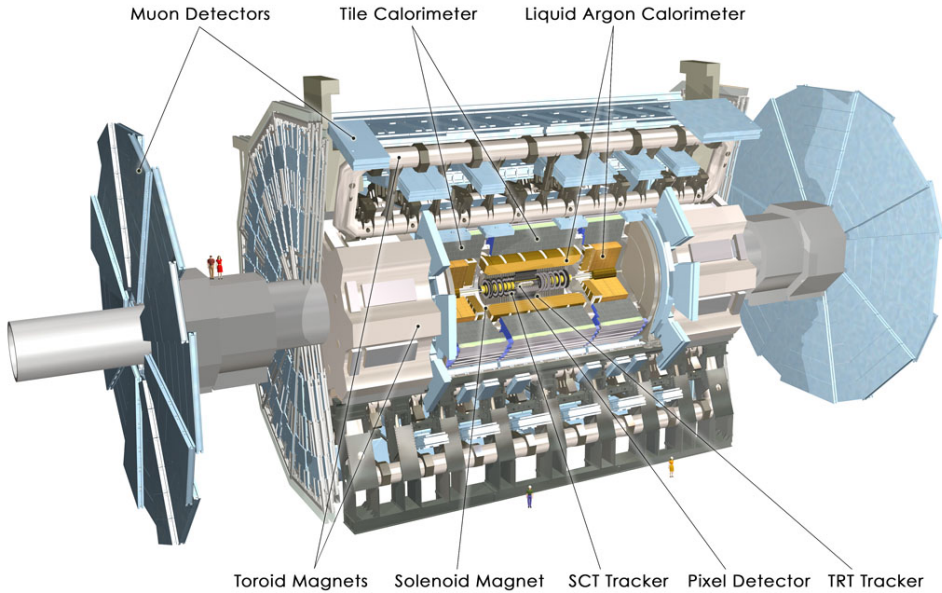
The ATLAS detector is a large closed cylindrical detector, consisting of a system of magnets and three sub-detectors; the Inner Detector, the Calorimeter system and the Muon Spectrometer. The magnets and sub-detectors sit in concentric rings around the interaction point, where the proton bunches collide. Combining the measurements from each of the sub-detectors allows the ATLAS detector to identify and measure the key properties<sup>4</sup> of particles that pass through its volume. Each component of the ATLAS detector is described in further detail below.

Figure 3.1 shows a cut-away schematic of the ATLAS detector.

---

<sup>3</sup> The position of the collision of interest is known as the hard-scatter primary vertex; the experimental definition of hard-scatter primary vertex (and therefore the collision of interest) is discussed in Section 4.1.1.

<sup>4</sup> For example four-momentum.



**Figure 3.1:** A cut-away schematic of the ATLAS detector [52].

### 3.2.1 Co-ordinate System

ATLAS uses a right-handed coordinate system, in which the origin lies at the interaction point. The  $x$ -axis points towards the centre of the LHC ring parallel to the surface of the earth, the  $y$ -axis points vertically upwards towards the surface of the earth and the  $z$ -axis runs along the beam-pipe, pointing anti-clockwise along the LHC beam-pipe. The azimuthal angle,  $\phi$ , is defined right-handedly around the  $z$ -axis starting at the  $x$ -axis.

The polar angle,  $\theta$ , is defined as the angle measured from the  $z$ -axis, such that along the  $z$ -axis corresponds to  $\theta = 0$  and anti-aligned with the  $z$ -axis corresponds to  $\theta = \pi$ . From that pseudorapidity,  $\eta$ , is defined as:

$$\eta = -\ln \left[ \tan \left( \frac{\theta}{2} \right) \right] \quad (3.1)$$

Thus,  $\eta = 0$  corresponds to a particle travelling perpendicular to the beam-pipe, where a positive value of  $\eta$  corresponds to a particle travelling with a tilt towards the positive  $z$ -axis. The quantity is called pseudorapidity as in the massless limit (when  $|\vec{p}| \rightarrow E$ ) it can be shown that  $\eta$  converges to rapidity,  $y$ , where rapidity is defined as,

$$y = \frac{1}{2} \ln \left( \frac{E + p_z}{E - p_z} \right) \quad (3.2)$$

A key property of rapidity is that differences in rapidity,  $\Delta y$ , are invariant against Lorentz boosts along the  $z$ -axis. This is important in  $pp$  colliders as each collision has a differ-

ent Lorentz boost along the  $z$ -axis, due to the effects of the Parton Distribution Functions described in Section 2.2.3.2. This implies that, in the massless limit,  $\Delta\eta$  is also invariant against Lorentz boosts along the  $z$ -axis. Therefore  $\eta$  is used to define the angular direction with respect to the  $z$ -axis in the ATLAS co-ordinate system. The final important quantity of the ATLAS co-ordinate system is  $\Delta R$ , which is defined as  $\Delta R = \sqrt{\Delta\eta^2 + \Delta\phi^2}$ .  $\Delta R$  represents the angular separation between two vectors.

### 3.2.2 Inner Detector

The innermost ATLAS sub-detector is the Inner Detector (ID) which measures the trajectory of charged particles. The ID is constructed from many concentric layers of detectors. As a charged particle passes through the ID, each of the layers provide a position measurement known as a hit. A particle passing through the whole ID at  $\eta = 0$  will typically cause 44 hits. The trajectory of the particle is determined using the hits from each of the layers, the measured trajectory is known as a track. Track reconstruction will be discussed further in Section 4.1. The ID is immersed in a 2 T magnetic field which bends the trajectories of charged particles; the sign of the charge and the momentum of the particle is inferred from the sign and magnitude of the track's curvature.

The ID consists of four components; the Insertable B-Layer (IBL), the pixel detector, the Semi-Conductor Tracker (SCT) and the Transition Radiation Tracker (TRT). The ID measures the position of particles in the angular range  $|\eta| < 2.5$ ; to achieve this the ID components are organised into the barrel, which are cylinders around the beam-pipe in the central region of the detector, and the end caps, which are disks that lie perpendicular to beam-pipe on either end of the barrel. Table 3.1 summarises the key properties of the components of the ID in both the barrel and the end cap.

Component of ID	$\eta$ Coverage	Element Size ( $\mu\text{m}$ )	Intrinsic Resolution ( $\mu\text{m}$ )		# Layers or Disks
IBL	$ \eta  < 2.5$	50 x 250	8 ( $R\text{-}\phi$ )	40 ( $z$ )	1
Pixel	Barrel	$ \eta  < 1.7$	50 x 400	10 ( $R\text{-}\phi$ )	115 ( $z$ )
	End Cap	$1.7 <  \eta  < 2.5$		10 ( $R\text{-}\phi$ )	115 ( $R$ )
SCT	Barrel	$ \eta  < 1.4$	80	17 ( $R\text{-}\phi$ )	580 ( $z$ )
	End Cap	$1.4 <  \eta  < 2.5$		17 ( $R\text{-}\phi$ )	580 ( $R$ )
TRT	Barrel	$ \eta  < 0.7$	4000	130 ( $R\text{-}\phi$ )	
	End Cap	$0.7 <  \eta  < 2.0$		$\sim 36$ hits per track	

**Table 3.1:** Summary of the main characteristics of the components of the ATLAS Inner Detector (ID). For the SCT and TRT the element sizes refer to the spacing of the readout strips and the diameter of the straw tubes respectively [52, 55].

Figure 3.2 shows the components of the ID in the barrel and the radial positions of each of the layers. Figure 3.3 shows the layout of the barrel and end cap components of the ID (except the IBL) in one half of the detector.

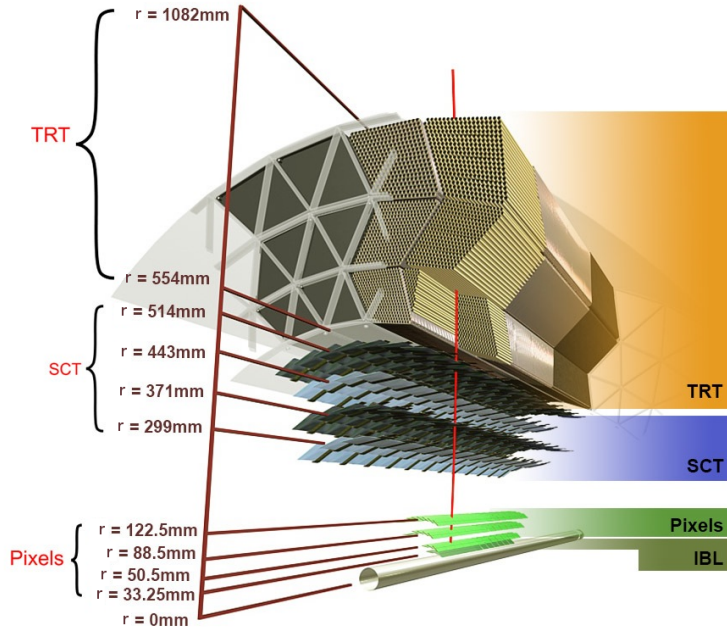


**Figure 3.2:** A schematic showing a slice of the barrel components of the ATLAS Inner Detector (ID) including the Insertable  $B$ -Layer (IBL). Each component is labelled and the radial distance from the beam-pipe ( $r$ ) is shown [56].

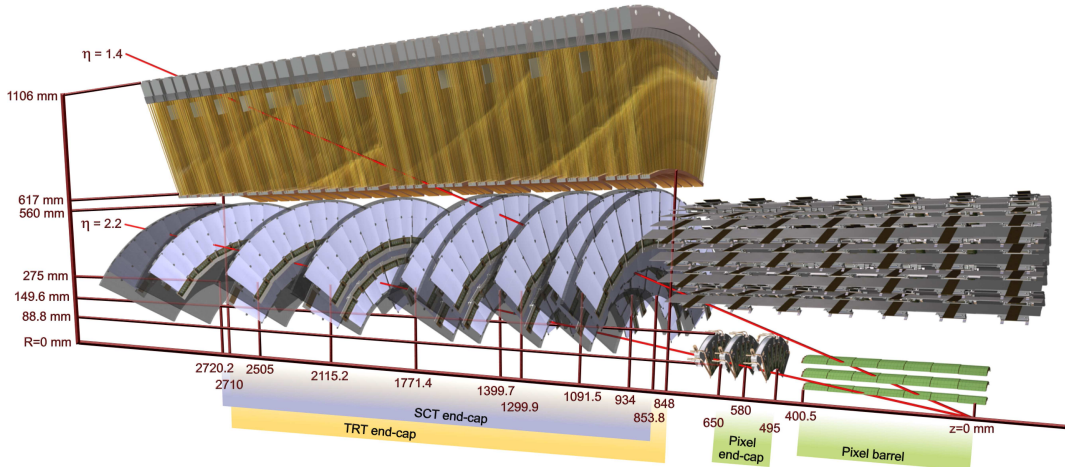


**Figure 3.3:** A schematic showing the barrel and end cap components of the ATLAS Inner Detector (ID); the Insertable  $B$ -Layer and the barrel TRT components are not shown. The axial distance from the beam-pipe ( $z$ ) is indicated. The red lines indicate the trajectory of a particle at  $\eta = 1.4$  and  $2.2$  with  $p_T = 10\text{ GeV}$  [52].

The components of the ID closest to the beam-pipe are the IBL and the pixel detector, which are both made out of silicon based pixel modules. As shown in Table 3.1, the high-granularity of the IBL and pixel detector allow for high precision position measurements close to the beam-pipe, the importance of this will be outlined below. The pixel detector consists of 3 barrel layers and 3 end cap disks at either end of the ID. The IBL was added to the ID in 2014 to provide an extra position measurement close to the beam-pipe and to improve tracking efficiency, which had been degraded by damage to the other layers of the pixel detector in data-taking before 2014. The IBL is a single layer of pixel modules in the barrel only, which provides an angular coverage of  $|\eta| < 2.5$ .

Moving radially outwards, the next component of the ID is the Semi-Conductor Tracker (SCT). The SCT modules are made from two parallel layers of semi-conducting strips. The strips are  $\sim 120$  mm in length<sup>5</sup> and have a strip pitch (spatial separation between strips) of  $80\text{ }\mu\text{m}$ . The parallel strip layers within each module have a 40 mrad angular offset along their common normal such that each module can produce a 3D position measurement.

The outermost component of the ID is the Transition Radiation Tracker (TRT). The TRT is constructed of many 4 mm radius cylindrical tubes filled with a xenon based gas mixture<sup>6</sup> with an anode wire through the central axis. A charged particle passing through the gas causes ionisation allowing for a measurement of its position using drift-time. In addition, the space between the straws is filled with polymer fibres (barrel) and foils (end caps) to create transition radiation, which is emitted by relativistic charged particles as they pass a boundary between materials with different refractive indices. The intensity of the transition radiation is inversely proportional to the mass of the charged particle, which is used to discriminate between electrons and pions [58].

The trajectory, momentum and transition radiation measurements provided by the Inner Detector are essential for particle identification at ATLAS. In particular, the high precision position measurements close to the beam-pipe from the IBL and pixel detector are used to identify tracks originating from hadrons containing  $b$ -quarks, which are then used to identify  $b$ -jets.  $b$ -jet identification is important for di- $b$ -jet searches and is described in Section 4.3.

---

<sup>5</sup> This number varies for the various parts of the SCT.

<sup>6</sup> 70% Xe, 27% CO<sub>2</sub> and 3% O<sub>2</sub> [57].

### 3.2.3 Calorimeter System

The ATLAS calorimeter system is located on the outside of the solenoid magnet surrounding the ID and is designed to provide an energy measurement of the traversing particles. The ATLAS calorimeter is particularly important for di-*b*-jet searches as it measures the energy of hadronic jets which are used to calculate the invariant mass of jet pairs.

The ATLAS calorimeter consists of two different systems built in concentric rings; the innermost is the ‘*Electromagnetic Calorimeter system*’ (ECAL) used to measure electromagnetic objects such as photons and electrons. Outside of that is the ‘*Hadronic Calorimeter system*’ (HCAL) that, in addition to the ECAL, is used to measure the energy of hadronic jets. The HCAL consists of the Tile and Hadronic Endcap calorimeters. Both the ECAL and HCAL have barrel and end cap components to make energy measurements at a large range of  $\eta$  values. Figure 3.4 shows a cut-away of the ATLAS calorimeter.

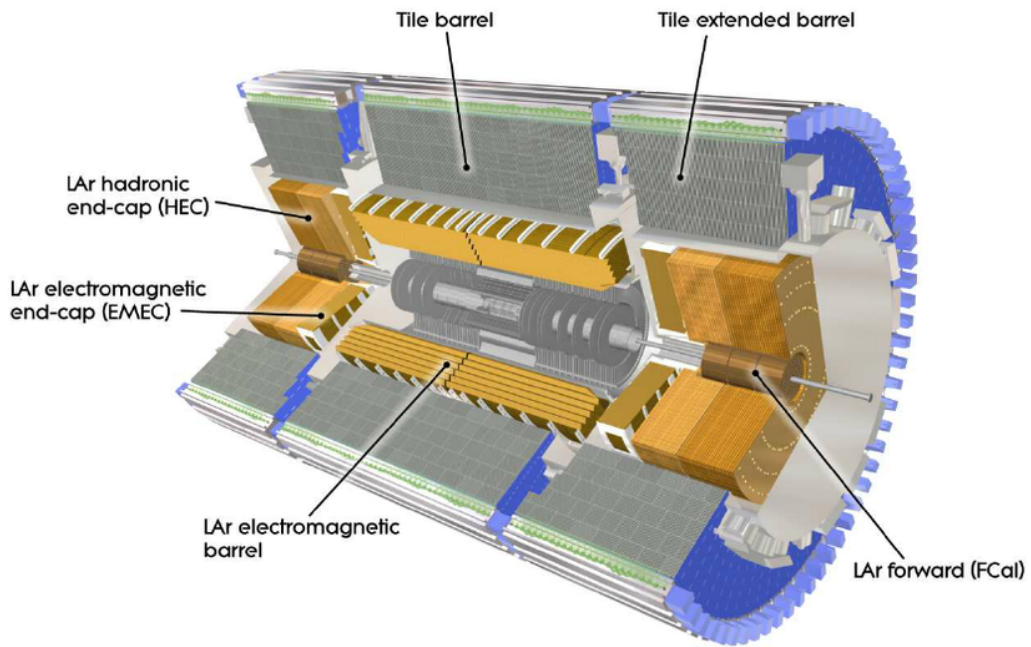


**Figure 3.4:** A cut-away schematic of the ATLAS calorimeter system [52].

A more detailed description of the calorimeter components will follow; however, the principle behind each component of the calorimeter is common so is described first. The calorimeters at ATLAS are sampling calorimeters, which means that they consist of alternating layers of absorber and active material. The role of the ‘*absorber layer*’ is to force the particle, whose energy we want to measure, to emit secondary particles. These secondary

particles will again emit further particles and so on such that a particle cascade is formed, the many resulting particles from the cascade are known as the cascade particles. The role of the ‘*active material layer*’ is to measure the energy of the cascade particles by counting electrons released by ionisation or photons emitted by excited atoms. The ATLAS calorimeter is designed such that as much as possible of the full particle shower of the initial particle will occur within its volume, meaning that the total energy of the initial particle can be determined.

### 3.2.3.1 Electromagnetic Calorimeter (ECAL)

For the electromagnetic interaction, at energies above the critical energy (7 MeV for lead [15]) the particle cascade process is dominated by two processes; bremsstrahlung, ( $e^\pm \rightarrow e^\pm + \gamma$ ) and pair production ( $\gamma \rightarrow e^+ + e^-$ ). Below the critical energy the particle cascade process is dominated by ionisation. As the energy loss per ionisation interaction is approximately the ionisation energy of the active material, the number of electrons released through ionisation is proportional to the energy of the initial particle.

The electromagnetic calorimeter at ATLAS is known as the ‘*Liquid Argon (LAr) calorimeter*’. The absorber material used in the LAr calorimeter is lead; lead is chosen because the EM coupling of a charged particle to a nucleus of an atom in the absorber material is proportional to  $Z^2$ , where  $Z$  is the atomic number of the material, meaning that the high atomic number of lead will increase the rate of the cascade processes and reduce the shower depth. The active material is liquid argon (LAr); the electrons released through ionisation in the LAr are captured by an electric field and counted such that the energy of the initial particle can be calculated.

As discussed above the LAr calorimeter is split up into two sections; the barrel section covers a region of  $|\eta| < 1.475$  and two end cap components cover  $1.375 < |\eta| < 3.2$ . The depth of an electromagnetic calorimeter is often expressed in units of radiation length,  $X_0$ , which is both the mean distance that an electron loses all but  $1/e$  of its energy through bremsstrahlung and 7/9 of the mean free path for a photon to produce an  $e^+e^-$  pair. High-Z materials have a shorter radiation length; in lead  $X_0 = 0.6$  cm [15]. The LAr calorimeter has a depth of  $> 22 X_0$  in the barrel and  $> 24 X_0$  in the end caps, meaning that almost all of the particle shower from a high-energy photon or electron is contained within the electromagnetic calorimeter. The finest granularity of the LAr calorimeter in the  $\eta-\phi$  plane is  $0.025 \times 0.025$  for the Barrel and  $0.025 \times 0.1$  for the end cap<sup>7</sup>.

---

<sup>7</sup>Full details on the granularity of all components of the ATLAS calorimeter is found in Table 1.3 of [52].

### 3.2.3.2 Hadronic Calorimeter (HCAL)

For particles that interact through the strong force, such as the components of a hadronic jet, the particle cascade is a more complicated process. A hadronic cascade is dominated by processes such as ionisation, nuclear spallation and neutron generation [22, 59]. For a chargeless hadron, for example a neutron, strong processes, such as spallation, are the only processes that contribute to its cascade. During both the parton shower (described in Section 2.2.2) and hadronic cascade processes many  $\pi_0$  mesons are created, which can decay to a pair of photons causing an electromagnetic cascade.

For hadronic interactions, the depth of detector is given in units of the interaction length,  $\lambda$ , defined as the distance required to reduce the number of relativistic hadrons by  $1/e$ . By the end of the LAr calorimeter there is  $2.3 \lambda$  of active material in the barrel. Therefore the hadronic shower depth is larger than the depth of the LAr calorimeter. For a full measurement of the hadronic energy, the Hadronic Calorimeter system (HCAL) is required.

The central regions of the HCAL consist of the ‘*Tile Calorimeter*’, which is constructed from absorber layers of steel and active material layers of scintillating tiles. The cascade particles produced by the absorber will excite atoms in the scintillating tiles which will then produce photons at a constant mean energy; therefore by measuring the intensity of the scintillating light (number of photons produced) the energy of the cascade particle can be determined. The Tile Calorimeter has a depth of  $7.4 \lambda$ , meaning the majority of the hadronic shower is captured by the LAr and Tile calorimeter. The Tile Calorimeter consists of barrel and extended barrel components; the barrel covers the region  $|\eta| < 1.0$  and the extended barrel covers the region  $0.8 < |\eta| < 1.7$ . The finest granularity of the Tile calorimeter in the  $\eta-\phi$  plane is  $0.1 \times 0.1$  for both the barrel and the extended barrel<sup>8</sup>.

The next component of the HCAL is the ‘*Hadronic Endcap Calorimeter*’ (HEC) which is housed in two large wheels at either end of the ATLAS detector and covers a region of  $1.5 < |\eta| < 3.2$ . The HEC is constructed using copper as the absorber layers and liquid argon as the active material and has a depth of  $\sim 12 \lambda$ . The finest granularity of the HEC calorimeter in the  $\eta-\phi$  plane is  $0.1 \times 0.1$ .

Finally, the ‘*Forward Calorimeter*’ (FCAL) covers the very forward region of  $3.1 < |\eta| < 4.9$ . It is constructed from absorber layers of copper (for EM interactions) and tungsten (for hadronic interactions) with liquid argon for the active material layers. The finest granularity of the LAr calorimeter in the  $x-y$  plane is  $3.0 \text{ cm} \times 2.6 \text{ cm}$ .

---

<sup>8</sup>Full details on the granularity of all components of the ATLAS calorimeter is found in Table 1.3 of [52].

The ATLAS calorimeter is a non-compensating calorimeter; which means that the response of the detector to an electromagnetic particle (such as an electron) is larger than the response to a hadronic particle (for example a pion). This is because some energy is lost in the hadronic cascade process; mainly due to the energy required to release nucleons from calorimeter nuclei during spallation [60, 61]. The ATLAS calorimeter is initially calibrated to the EM-scale, meaning that the initial energy measurement of a calorimeter assumes that the particle is only EM-interacting. For hadronic objects a jet energy scale correction is applied, this is described in Section 4.2.3.

### 3.2.3.3 Energy Resolution of a Calorimeter

The intrinsic energy resolution of a calorimeter is given by three terms:

$$\left(\frac{\Delta E}{E}\right)^2 = \left(\frac{c_s}{\sqrt{E}}\right)^2 + \left(\frac{c_n}{E}\right)^2 + c_c^2 \quad (3.3)$$

In more detail the three terms are:

- **Stochastic Term ( $c_s$ ):** This term represents random fluctuations in the cascade shower process.  $\Delta E_s$  is proportional to the square root of the number of photons/electrons counted in the active layer, which means that  $\Delta E_s \propto \sqrt{E}$ .
- **Noise Term ( $c_n$ ):** This term represents uncertainties that are a constant size in units of energy, such that  $\Delta E_n = c_n$ . Contributions to the noise term include electronic noise and effects from pile-up.
- **Constant Term ( $c_c$ ):** This term represents uncertainties that are independent of the energy measurement, such that  $\Delta E_c/E = c_c$ . This uncertainty is mainly caused by the geometry of the calorimeter such as regions of inactive material (detector cracks, material before the calorimeter) and dead modules.

Table 3.2 shows approximate values of  $c_s$ ,  $c_n$  and  $c_c$  for the components of the ATLAS calorimeter. The noise term depends strongly on  $\eta$  and pile-up conditions, so an approximate order of magnitude is given. For high- $p_T$  objects ( $> 100$  GeV), such as the jets used in di- $b$ -jet searches, the constant term is the dominant term, as the other terms are suppressed by the large values of  $E$ .

Calorimeter Component	Stochastic ( $c_s$ ) [ $\sqrt{\text{GeV}}$ ]	Noise ( $c_n$ ) [GeV]	Constant ( $c_c$ )
EM Barrel	10%	~ 1%-10%	0.7%
EM End Cap	10%	~ 1%-10%	0.7%
Tile	50%	~ 10%-100%	3%
HEC	50%	~ 10%-100%	3%
FCAL	100%	~ 10%-100%	10%

**Table 3.2:** A summary of the stochastic, noise and constant terms of the intrinsic energy resolution of components of the ATLAS calorimeter. The noise term depends on  $\eta$  and pile-up conditions so only an approximate order of magnitude is given [52, 61]

### 3.2.4 Muon Spectrometer

The Muon Spectrometer (MS) is the outermost part of the ATLAS detector and is designed to measure the trajectory of charged particles that are not stopped by the calorimeter system. As the muon is the only charged particle that can pass through the calorimeter system, measurements in the MS are used to identify muons. The MS consists of layers of detector providing positional measurements (or hits) in the presence of a magnetic field, similar to the concept used for the Inner Detector (ID). Therefore, the trajectory and momentum of muons can be calculated using hits from the MS. Details of muon reconstruction are discussed further in Section 4.4.

In the barrel region ( $|\eta| < 1.4$ ) a large barrel toroid provides the magnetic field, in the end cap region ( $1.6 < |\eta| < 2.7$ ) two smaller end cap magnets provide the magnetic field and finally in the transition region ( $1.4 < |\eta| < 1.6$ ) both sets of magnets contribute to the magnetic field. A further description of the magnets used in ATLAS is found in the next section.

Muon chambers are the detectors that measure the position of the muon. In the barrel region, muon chambers are arranged in three concentric cylindrical layers of chambers formed around the beam-pipe, whilst in the transition and end cap regions there are three disks of chambers perpendicular to the beam-pipe either side of the barrel.

There are two types of muon chambers; trigger and precision. The trigger muon chambers provide a position measurement in 3-dimensions within 15–25 ns which is used to reconstruct muons in the ATLAS trigger system, the trigger will be discussed in Chapter 5. The trigger muon chambers comprise of Resistive Plate Chambers (RPCs) in the barrel and Thin Gap Chambers (TGCs) in the end cap regions. The precision muon chambers provide a precise measurement of the muon position in the  $R$ - $z$  plane, the plane in which trajectory curvature occurs in the MS, allowing for precise measurements of the muon track- $p_T$ . In the

region  $|\eta| < 2.0$ , the precision muon chambers are entirely Monitored Drift Tubes (MDTs), whilst at large pseudorapidity ( $2.0 < |\eta| < 2.7$ ) Cathode Strip Chambers (CSCs) are used in addition to MDTs. A schematic of the MS is shown in Figure 3.5, the types of muon chambers are labelled.

There is an additional use of the MS that relates to high-energy jets. Whilst for most jets the shower is fully contained within the calorimeter there are some jets, particularly at high- $p_T$ , where a non-negligible amount of energy is not deposited in the calorimeter. This effect, known as ‘*punch-through*’, is estimated using energy deposits in the MS.

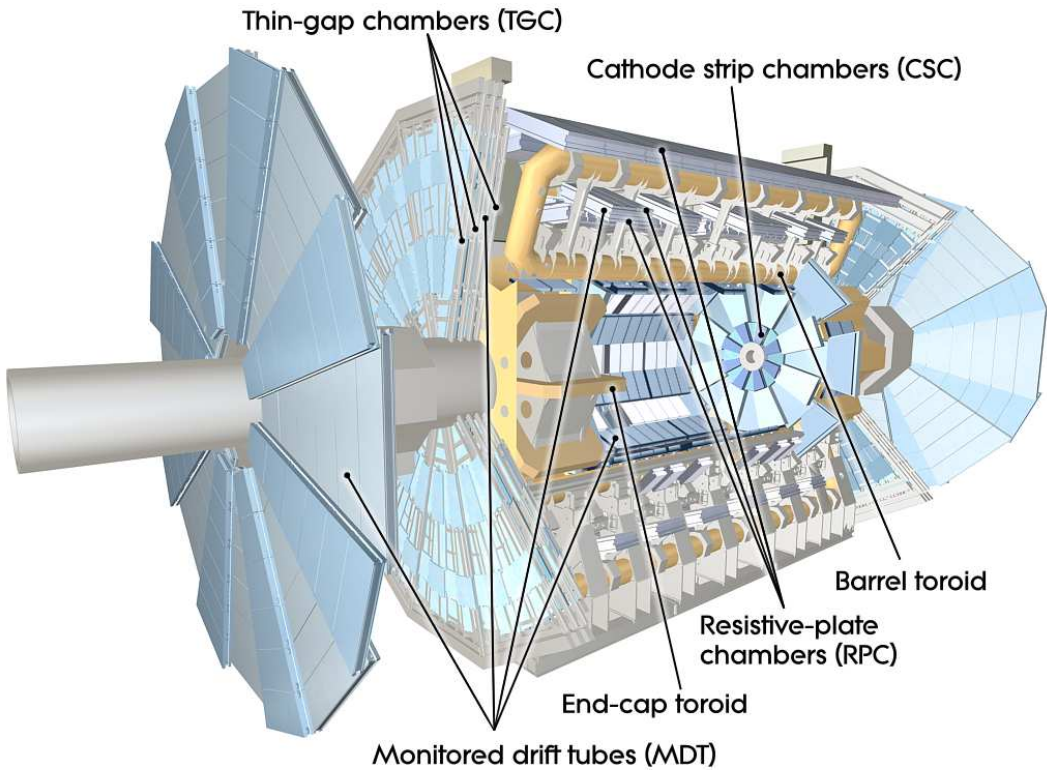


**Figure 3.5:** A cut-away of the ATLAS Muon Spectrometer (MS). The types of muon chamber used in each part of the MS are labelled on the figure. [52].

### 3.2.5 Magnets

In ATLAS, magnetic fields are important for obtaining the momentum of particles from their observed trajectories in the ID and MS. The ATLAS magnet system consists of four large superconducting magnets. The inner solenoid surrounds the ID and provides a 2 T magnetic field within the ID, the barrel toroid magnet provides a magnetic field of  $\sim 0.5$  T in the central regions of the MS and the two end cap toroid magnets produce a magnetic field of  $\sim 1$  T in the forward regions of the MS. Figure 3.6 shows the layout of the ATLAS magnet system [62].

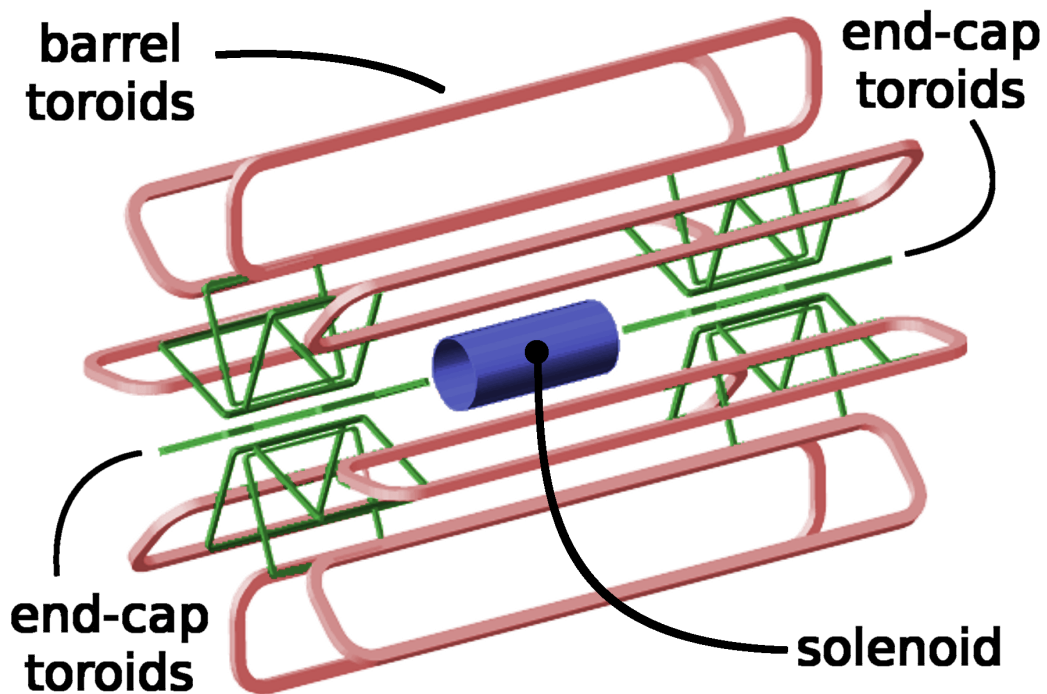


**Figure 3.6:** The layout of the ATLAS magnet system [62].

## Chapter 4

# Object Definition and Reconstruction

As described in the previous chapter, the ATLAS detector consists of many sub-detectors that each provide a different set of measurements. The measurements from the sub-detectors are combined to reconstruct physics objects, which are physically meaningful and are used to study the hard-scatter process; examples are electrons and hadronic jets containing  $b$ -quarks. This chapter will define the physics objects used in the analyses presented in this thesis and describe how each physics object is identified and their 4-momenta reconstructed.

### 4.1 Tracks

The trajectory of charged particles that pass through the Inner Detector (ID) can be reconstructed using hits from the IBL, pixel detector, SCT and TRT which are described in Section 3.2.2. The reconstructed trajectories are known as tracks. The momentum of the charged particle can be determined from the magnitude of track curvature caused by the solenoid magnet. Track reconstruction is important to identify and reconstruct many other physics objects at ATLAS for example:  $b$ -jets, electrons and muons.

The tracking reconstruction procedure [56] follows these steps:

- **Track Candidates:** Initial track candidates are formed using hits from the IBL, pixel detector and SCT because they have a higher precision and granularity than the TRT. Track candidates are built in three steps. Firstly, for each layer of the ID, adjacent hits are converted into a 3D ‘space-point’ that represents the position of a charged particle. Secondly, track seeds are then formed from three space-points in consecutive layers of the ID consistent with the trajectory of a charged particle. Finally, from the track seeds, track candidates are built by iteratively adding space-points from the remaining IBL, pixel and SCT detector layers.

- **Track Selection / Ambiguity Resolving:** Each track candidate is assigned a ‘track-score’ that represents the track quality based on the compatibility of hits to the track candidate and the  $p_T$  of the track. The self-consistent set of track candidates with the highest combined track-score is selected. Details of the track selection algorithm are found in [56].
- **Add TRT Information:** Finally, track candidates are updated such that hits in the TRT consistent with the track candidates are included. Including hits from the TRT means that tracks are measured over a larger radial distance which improves momentum resolution.

The momentum resolution of reconstructed tracks,  $\sigma(p_T)/p_T$ , as a function of track  $p_T$  is given by [52]:

$$\frac{\sigma(p_T)}{p_T} = 0.05\% \frac{p_T}{\text{GeV}} \oplus 1\% \quad (4.1)$$

#### 4.1.1 Primary Vertex Identification

As described in Section 3.1, to achieve a high instantaneous luminosity, the LHC collides bunches of protons leading to multiple collisions per bunch crossing; in  $pp$  collision data collected in 2015 and 2016 by ATLAS, the average number collisions per bunch crossing is 13.7 and 24.9 respectively [50].

A primary vertex is the position where a  $pp$  collision occurred. The position of primary vertices in a bunch-crossing is calculated by performing an iterative fit using the positions that tracks intersect the centre of the region where the proton beams interact (known as the beam-spot) [63]. In the iterative fit procedure, tracks are associated to primary vertices. The hard-scatter primary vertex is defined as the primary vertex with the highest sum of the squared transverse momenta ( $\sum p_T^2$ ) of associated tracks. This is because a vertex with a large number of high- $p_T$  tracks associated is likely to have been caused by a hard-scatter collision, which is defined as a collision in which the momentum transfer is large compared to the proton mass [64]. Hard-scatter collisions are of interest as, for example, such a collision is required to produce a TeV scale BSM particle.

## 4.2 Jets

Quarks or gluons created in a proton-proton scatter event will form a stream of high-energy hadrons, known as a hadronic jet. Section 2.2.2 described the formation of a hadronic jet in detail. The high-energy hadrons that form the hadronic jet will then deposit their energy in the cells of the ATLAS calorimeter through the processes described in Section 3.2.3. Therefore, the ATLAS calorimeter has an energy and positional measurement of the components

of the hadronic jet.

This section describes the jet building procedure utilised by ATLAS to convert energy deposits in calorimeter cells into well defined and calibrated hadronic jets. Only hadronic jets built from calorimeter cells are described, as this is the jet object used in di-*b*-jet searches. Other types of jets used are, for example, jets constructed from tracks [65].

### 4.2.1 Hadronic Topocluster Reconstruction

The first step of jet building at ATLAS is the formation of 3D clusters, known as topoclusters, from groups of energy deposits in neighbouring calorimeter cells [66]. Each topocluster represents a hadron or a set of collimated hadrons within a hadronic jet. The calorimeter cells can be from either the EM or hadronic calorimeter systems which are described in Section 3.2.3. The topocluster building algorithm uses the variable ‘*cell signal significance*’,  $S_{\text{cell}}$ , defined as:

$$S_{\text{cell}} = \frac{E_{\text{cell}}}{\sigma_{\text{noise},\text{cell}}} \quad (4.2)$$

where  $E_{\text{cell}}$  is the energy deposited in a cell and  $\sigma_{\text{noise},\text{cell}}$  is the background noise in a cell. A value of  $S_{\text{cell}} > 1$  indicates that the energy deposit is likely due to a real particle rather than noise in the calorimeter.

Using the value of  $S_{\text{cell}}$ , each calorimeter cell is labelled as follows

- If  $(|S_{\text{cell}}| > 4)$ : the cell is labelled as a **seed** cell.
- If  $(2 < |S_{\text{cell}}| < 4)$ : the cell is labelled as a **growth** cell.
- If  $(0 < |S_{\text{cell}}| < 2)$ : the cell is labelled as a **boundary** cell.

Topoclusters are then built using the following steps

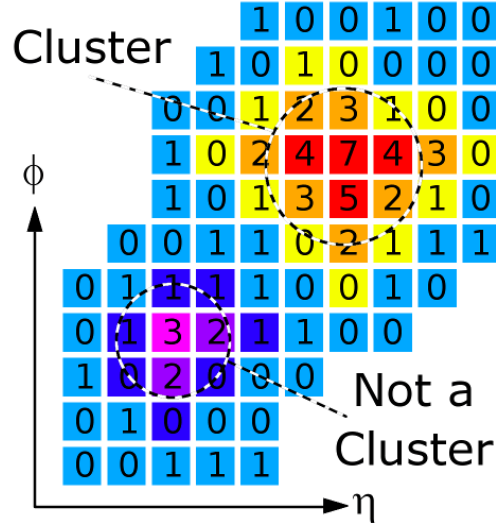
1. A seed cell forms the centre of a new topocluster.
2. Neighbouring seed cells are added together to form one topocluster seed.
3. Then, growth cells neighbouring the topocluster are added.
4. Finally, boundary cells neighbouring the topocluster are added.

Figure 4.1 shows an illustration of a set of energy deposits that would form a topocluster and a set of energy deposits that would not form a topocluster, as no seed cell is present.

The topoclusters are treated as massless objects<sup>1</sup> such that the four-momentum of each topocluster is determined from the  $\eta - \phi$  position and the sum of energy deposited.

---

<sup>1</sup> As no particle identification is possible in the hadronic calorimeter an assumption of the mass is required.



**Figure 4.1:** A schematic illustrating the algorithm used to form a topocluster. The numbers on the grid represent  $|S_{\text{cell}}|$  and the colours represent the cell label [62].

### 4.2.2 Jet Reconstruction

In the next step of jet building, jet reconstruction algorithms are employed to build jets from the four-momenta of the topoclusters. Each jet built by the algorithm has a well defined four-momentum and set of constituents. A detailed discussion of jet reconstruction algorithms is found in [67].

ATLAS analyses use a type of jet reconstruction algorithm known as sequential recombination algorithms, which selectively add together the calorimeter topoclusters to form the jet; these are specifically the  $k_t$ , anti- $k_t$  and Cambridge-Aachen (CA) algorithms.

The sequential recombination algorithms consider a set of four-momenta which are referred to as clusters; the initial set of clusters are the topoclusters described above. The algorithm makes use of two distances: the inter-jet distance between clusters  $i$  and  $j$  ( $d_{ij}$ ) and the particle-beam distance for cluster  $i$  ( $d_{iB}$ ). The distances are defined as

$$d_{ij} = \min[(p_{Ti})^a, (p_{Tj})^a] \left( \frac{\Delta R_{ij}}{R} \right)^2, \quad d_{iB} = (p_{Ti})^a \quad (4.3)$$

where  $p_T$  is transverse momentum (component of momentum perpendicular to the beam-pipe) and  $\Delta R_{ij} = \sqrt{(y_i - y_j)^2 + (\phi_i - \phi_j)^2}$ .  $R$  is the jet width parameter, a free parameter of the algorithm. The parameter  $a$  takes the value  $a = 2$  for the  $k_t$  algorithm,  $a = -2$  for the anti- $k_t$  algorithm and  $a = 0$  for the Cambridge-Aachen algorithm. If  $d_{ij} < d_{iB}$  for a pair of clusters then it is likely that the two clusters are from the same jet. In contrast, if  $d_{ij} > d_{iB}$  then it is unlikely that the two clusters are from the same jet.

Sequential reclustering algorithms then proceed using the following steps:

1. Calculate  $d_{ij}$  and  $d_{iB}$  for all combinations of clusters and find the minimum.
2. If the minimum is a  $d_{ij}$  combine cluster  $i$  and  $j$  to form a new cluster.
3. If the minimum is a  $d_{iB}$  declare cluster  $i$  as a final-state jet and remove it from the set.
4. Repeat until all clusters have been declared as final-state jets.

The four-momentum of a final-state jet is the sum of the four-momenta of the topoclusters assigned to that jet. The jet width parameter,  $R$ , effectively gives the maximum width of a reconstructed jet because if  $\Delta R_{ij} > R$  for a pair of clusters then  $d_{iB} < d_{ij}$  for one of the clusters and so the two cluster cannot be merged.

The sequential reclustering algorithms described above are used as they satisfy two important criteria: infrared and collinear safety<sup>2</sup>. Infrared safety requires that the jet reconstruction algorithm result should be invariant against soft gluon emission<sup>3</sup> and collinear safety requires that the result should be invariant against a parton splitting into two partons with small angular separation. If the jet reconstruction algorithm is not infrared and collinear safe, two different sets of jets could be built from identical hard-scatter processes due to an additional emission process in the parton shower.

$\text{Anti-}k_T$  is the standard jet reconstruction algorithm used at ATLAS. This is because the anti- $k_T$  algorithm provides regular jet shapes around the centre of the jet as the algorithm reconstructs the high- $p_T$  core of the jets first and then adds in the lower  $p_T$  suburbs. To illustrate this point, Figure 4.2 shows the jets built by the  $k_T$  and anti- $k_T$  algorithm using the same set of input clusters; the anti- $k_T$  algorithm creates a more regular jet shape.

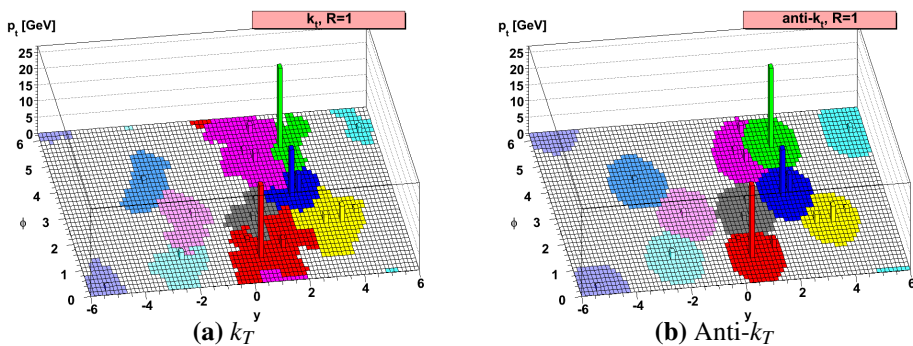


**Figure 4.2:** A comparison of the jets built using the (a)  $k_T$  and (b) anti- $k_T$  algorithm from the same simulated event. The constituent clusters of each of the jets built is indicated using various colours [69].

<sup>2</sup> Cone-based jet reconstruction algorithms used at some previous collider experiments, such as UA2 [68], do not satisfy infrared and collinear safety.

<sup>3</sup> Soft means low momentum.

To choose the jet width parameter,  $R$ , one must balance the effects that a narrow jet will not contain all the energy from the jet formation process whilst a wide jet will include energy from the underlying event. The standard choice at ATLAS is  $R=0.4$  to minimise the two effects described above; Section 5 of [67] provides a numerical calculation to justify this choice.

### 4.2.3 Jet Calibration

The jets initially built from the topoclusters will not represent the true energy of the hadronic jet. The key factors for the unrepresentative hadronic jet energy measurement are [22, 70]:

- **Jet Energy Scale:** As discussed in Section 3.2.3.2, the response of the ATLAS calorimeter is different for an EM-object and a hadronic object. The calorimeter energy response is initially calibrated for an EM-object. Therefore energy measurements of hadronic objects must be corrected using a jet energy scale correction.
- **Detector Effects:** Some of the jet energy may be deposited either in an inactive region within the ATLAS detector, outside of the angular acceptance of the calorimeter or beyond the calorimeter, an effect known as ‘punch-through’.
- **Jet Reconstruction:** Jet energy can be lost either in topocluster formation due to the cell signal significance thresholds or from inaccuracies in the jet reconstruction algorithm.
- **Pile-Up:** In Section 3.1 pile-up was defined as proton collisions other than the hard-scatter primary vertex. Particles from pile-up collisions can be included in the jet reconstruction and hence effect the jet energy measurement.

As a result, a calibration procedure is performed to correct the energy of a jet [71].

For a calibration, one must decide what to correct with respect to. Naively one could choose the truth initial parton, however the correction would then strongly depend on the theoretical modelling of the parton shower and hadronisation process. The resulting corrected jets would then not be model-independent<sup>4</sup>. Instead, jets are corrected with respect to a ‘truth jet’; where a truth jet is constructed by running the anti- $k_T$  algorithm on the set of stable truth particles in a simulated event. A stable particle is required to have a lifetime  $c\tau > 10$  mm and muons, neutrinos, and particles from pile-up collisions are ignored. Truth jets are a good choice as they are well-defined and model-independent objects representing the jets that would have been reconstructed if one had a perfect detector.

---

<sup>4</sup> An explanation of why model-independent jets are desirable is found in [26].

The calibration process uses Monte-Carlo simulation and data to correct the jets initially built from the EM-scale topoclusters using a number of steps:

1. **Origin Correction:** This step changes the direction of the jets such that the four-momentum is pointing at the hard-scatter primary vertex rather than the centre of the detector. This calculation conserves the jet energy.
2. **Jet Area-Based Pile-Up Correction:** This step removes unwanted energy contributions from pile-up. This correction subtracts the area of the jet,  $A$ , multiplied by the average energy density due to pile-up,  $\rho$ .  $\rho$  is calculated for each event using the median ( $p_T/A$ ) of a set of jets reconstructed from positive-energy topo-clusters in the range  $|\eta| < 2$  using the  $k_T$  algorithm with  $R = 0.4$ .
3. **Residual Pile-Up Correction:** This step further reduces effects from pile-up utilising the linear dependence of pile-up effects on the number of primary vertices,  $N_{PV}$ , and the mean number of  $pp$  collisions per bunch crossing,  $\langle\mu\rangle$ . This correction can hence be written as  $p_T^{\text{Pile-up Corrected}} = p_T^{\text{Initial}} - \alpha * (N_{PV} - 1) - \beta * \mu$ , where  $\alpha$  and  $\beta$  are constants derived using simulated events.
4. **Absolute JES Correction:** This step corrects the jet four-momentum from the EM-scale, at which they were initially built, to the truth jet energy. This correction is derived using truth jets and reconstructed jets in Monte-Carlo simulated dijet events.
5. **Global Sequential Calibration:** This step uses information from the calorimeter, muon spectrometer and track-based variables to refine the reconstructed energy and reduce the overall uncertainties.
6. **In-situ calibration:** All previous steps use simulation to correct detector-level jets to truth jets. This step corrects for differences between simulation and data using events containing a jet to be calibrated and a reference object; the reference object is a photon, a  $Z$  boson, or a set of calibrated jets. The reference objects used have been calibrated such that they have a well measured  $p_T$ ; therefore, from conservation of momentum, the true  $p_T$  of the jet to be calibrated can be inferred. One can then calculate a correction factor, which is applied to the jet four-momentum in data only.

$$\text{Correction Factor } (p_T, \eta) = \frac{\langle p_T^{\text{jet}} / p_T^{\text{ref}} \rangle_{\text{MC}}}{\langle p_T^{\text{jet}} / p_T^{\text{ref}} \rangle_{\text{Data}}} \quad (4.4)$$

This calibration scheme is called ‘EM+JES’, as the topoclusters are at the EM-scale. There are other schemes used for calibrating jets at ATLAS, for example, some analyses [72] correct each topocluster to the hadronic scale before clustering the jet, in a scheme called Local Cluster Weighted (LCW) [66]. EM+JES is generally used in ATLAS analyses as it is a simpler calibration scheme than LCW, but provides similar results.

The end result of the processes described in this section is a jet reconstructed from EM-scale topoclusters using an anti- $k_T$  algorithm with a jet width parameter  $R=0.4$  that is calibrated using the EM+JES calibration scheme. This is the definition of a jet used throughout this thesis.

#### 4.2.4 Jet Energy Uncertainties

There are two components of uncertainty on the jet energy measurement; jet energy scale and jet energy resolution.

Jet energy scale (JES) uncertainties arise from the calibration procedure to correct jets from the EM-scale to the hadronic-scale, outlined above. 80 separate uncertainties are derived to cover each step of the calibration, the dominant uncertainties arise from the data-driven in-situ step [71]. Figure 4.3 shows the fractional JES uncertainty as a function of jet- $p_T$  and jet- $\eta$ . The increased uncertainty in the region  $2 < |\eta| < 2.6$  is caused by localised data/simulation discrepancies caused by mismodelling of the detector response in the EM end-cap calorimeters.

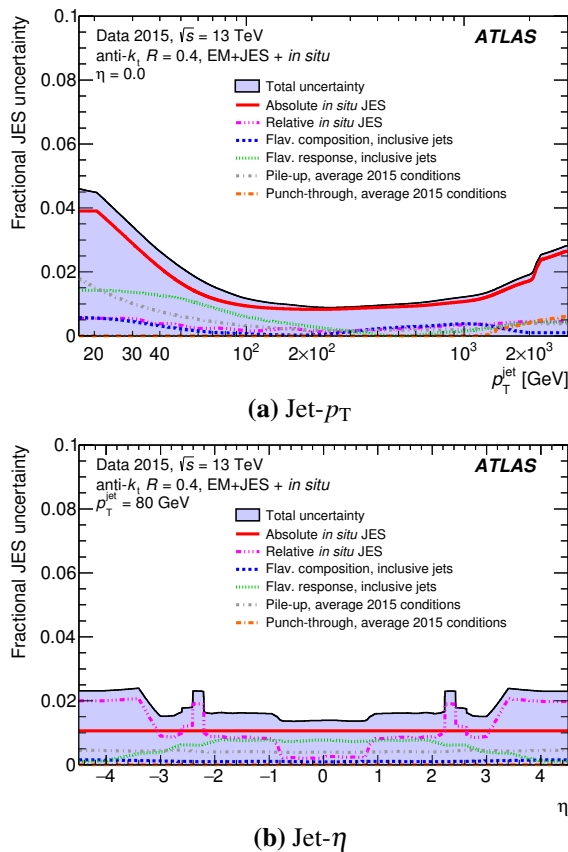


**Figure 4.3:** The fractional jet energy scale uncertainty as a function of jet- $p_T$  and  $\eta$ . The total uncertainty is shown with the contributions from the various sources of uncertainty [71].

Jet energy resolution (JER) is defined as  $\sigma(E)/E$ , and JER uncertainties account for the imperfect simulation of detector resolution in Monte-Carlo simulation. The uncertainty is measured using an in-situ technique from the balancing of jets in 8 TeV collision data which is extrapolated for 13 TeV data; the final uncertainty accounts for this extrapolation. Figure 4.4 shows the fractional JER uncertainty as a function of jet- $p_T$  and jet- $\eta$ . Full details on the derivation of this uncertainty can be found in [70] and [73].

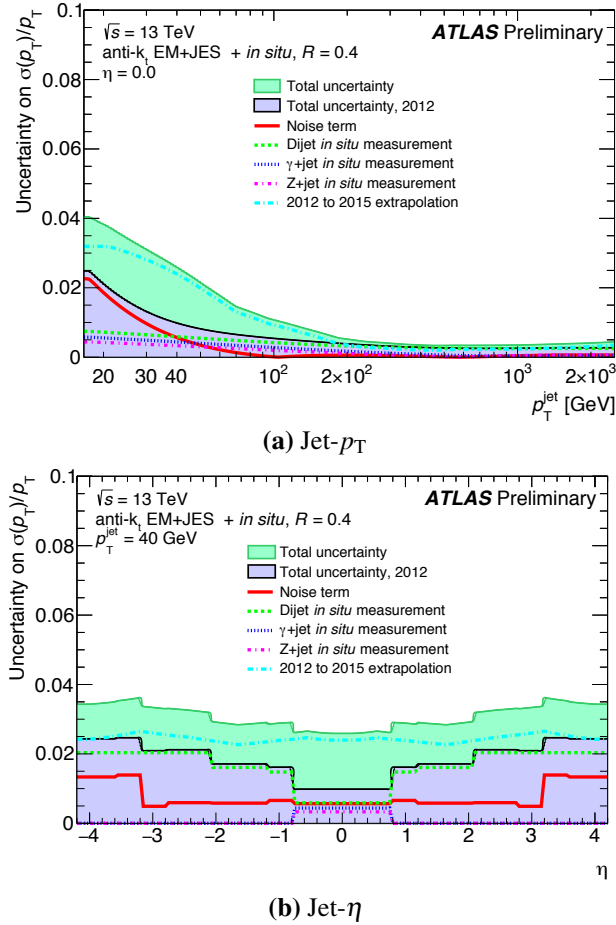


**Figure 4.4:** The fractional jet energy resolution uncertainty as a function of jet- $p_T$  and  $\eta$ . The total uncertainty is shown with the contributions from the various sources of uncertainty [70].

### 4.3 *b*-Jets

There are three flavour categories of hadronic jets based on the flavour of the constituent quarks. *b*-jets are defined as jets containing one or more *b*-hadrons, where a *b*-hadron is any hadron containing a *b*-quark. *c*-jets are defined as jets containing one or more *c*-hadrons but no *b*-hadrons and light jets consist of only light hadrons (formed of *u*, *d* and *s* quarks).

The identification of *b*-jets, known as *b*-tagging, is an essential tool in a range of ATLAS collaboration results [74, 75]; *b*-tagging is used in di-*b*-jet searches to reduce the light jet dominated background and increase sensitivity to BSM models that decay preferentially to 1 or 2 *b*-jets in their final state.

The process of *b*-tagging at ATLAS in Run-2 is described in great detail in [76, 77], so what follows is a summary of the key features of the process.

#### 4.3.1 Truth Flavour Label

In simulation, the particle-level truth information is known, and hence a truth flavour label of a jet can be defined. Truth-level hadrons with  $p_T > 5$  GeV are matched to jets if  $\Delta R < 0.3$  between the reconstructed jet and the hadron; the matching is exclusive meaning each hadron is assigned to the jet with the smallest  $\Delta R$  separation. If a *b*-hadron is matched to a jet, the jet is then declared a *b*-jet; this process is then repeated for *c*-hadrons and  $\tau$  leptons. If no match between *b*, *c* or  $\tau$  is achieved, the jet is labelled as a light jet. This definition of truth flavour label in simulation is used generally within this thesis.

#### 4.3.2 Baseline *b*-Tagging Algorithms

To identify *b*-jets in data, *b*-tagging algorithms utilise the long lifetimes of the heavy-hadrons that decay through the flavour changing weak interaction. Weakly decaying *b*-hadrons produced at the LHC have an average lifetime of  $\sim 1.6$  ps [15]<sup>5</sup>. A *b*-jet decay chain will typically contain two of these flavour changing interactions as, at the quark level, the *b*-quark contained in the jet will decay to a *c*-quark, which will then decay into a *s* or *d* quark. Due to their long lifetimes, *b*-hadrons decay a measurable distance from the hard-scatter primary vertex; for example, a  $B_0$  meson with a  $p_T$  of 100 GeV will travel approximately 10 mm. Hence, the flavour of a jet can be inferred from the presence of particles that originate from a point offset from the hard-scatter primary vertex.

The *b*-tagging algorithms use tracks and jets as described in Section 4.1 and 4.2. To

---

<sup>5</sup> There are also excited *b*-hadron states that decay rapidly to other *b*-hadrons through the strong force.

perform *b*-tagging, tracks are associated to jets if there is a small angular separation,  $\Delta R$ , between the two objects. Tracks are exclusively matched, meaning each track is only associated to the jet with the smallest  $\Delta R$  separation. The maximum value of  $\Delta R$  for association decreases as jet- $p_T$  increases because high- $p_T$  jets are more collimated;  $\Delta R_{\max}$  is 0.45 for a jet- $p_T$  of 20 GeV whilst  $\Delta R_{\max}$  is 0.26 for a jet- $p_T$  of 150 GeV.

Three baseline *b*-tagging algorithms are utilised to produce flavour discriminating variables [77], which are described in the next three sections. The flavour discriminating variables are then combined in a multi-variate algorithm described in Section 4.3.3. Figure 4.5 shows a schematic illustrating how tracks are used by the baseline *b*-tagging algorithms to identify a *b*-jet, the details of this figure are referred to in the following three sections.

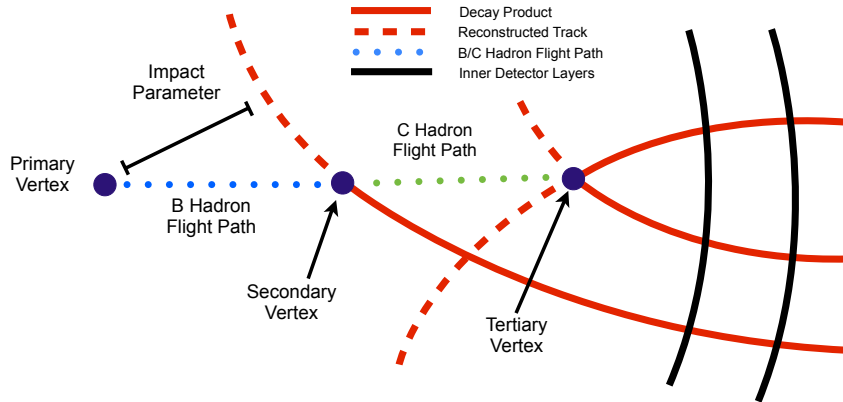


**Figure 4.5:** An illustration of the key features of a *b*-jet utilised by the base *b*-tagging algorithms.

#### 4.3.2.1 Impact Parameter Based Algorithm

The IP3D and IP2D algorithms utilise the impact parameter, which is defined as the shortest distance between a track and the hard-scatter primary vertex. A track corresponding to a particle from the offset decay vertex of a heavy-hadron is likely to have a large impact parameter, meaning that the distribution of track impact parameter is different for each of the jet-flavours. The impact parameter of a track coming from the decay of a heavy hadron is indicated in Figure 4.5. For all tracks associated to a jet, the impact parameter is calculated in both the transverse (perpendicular to beam-line) and longitudinal (parallel to beam-line) direction, which are referred to as  $d_0$  and  $z_0$ . The IP3D algorithm calculates a likelihood of the jet having a specific flavour, based on the distributions of the impact parameters ( $d_0, z_0$ ) and their significances ( $d_0/\sigma_{d0}$  and  $z_0/\sigma_{z0}$ ). The IP2D algorithm calculates the jet flavour likelihood from just the transverse distributions, ( $d_0$  and  $d_0$  significance), which is more robust to pile-up because tracks originating from a pile-up primary vertex that occurred at a different position on the  $z$ -axis are likely to have large  $z_0$  significance values.

### 4.3.2.2 Secondary Vertex Based Algorithm

The SV1 algorithm aims to reconstruct a secondary vertex of two or more intersecting tracks, corresponding to the decay of a heavy-flavour hadron; the secondary vertex within a *b*-jet's decay chain is illustrated in Figure 4.5. The SV1 algorithm calculates a set of flavour discriminating variables using the properties of the reconstructed secondary vertex. Examples of flavour discriminating variables are the invariant mass of tracks associated to a vertex, which will be larger for *b*-jets due to the heavy mass of the *b*-hadron<sup>6</sup>, the distance in the transverse plane between the hard-scatter primary vertex and the secondary vertex, which will be larger for *b*-jets due to the long lifetime of the *b*-hadron, and the number of tracks at the secondary vertex, which will be larger for reliable secondary vertices.

### 4.3.2.3 Jet Fitter Algorithm

The JetFitter algorithm (JF) attempts to reconstruct the full decay chain of the *b*-hadron into a *c*-hadron and then into light-hadrons. This is done by assuming that all vertices lie on a common *b*-flight axis, and constructing vertices from the intersection of one or more tracks and the flight axis. The aim is to reconstruct the secondary and tertiary vertices which correspond to the decays of the *b* and *c*-hadron, as illustrated in Figure 4.5. Similar to SV1, the JetFitter algorithm then calculates a number of flavour discriminating variables: for example, vertex mass and number of vertices with two or more tracks.

### 4.3.3 Multi-Variate *b*-Tagging Algorithm

The three base algorithms are combined in a Boosted Decision Tree (BDT) [78], a machine-learning technique for combining the many flavour discriminating variables, resulting in the MV2 algorithm. A BDT is able to use the complex correlations between the input variables to maximise *b*-tagging performance. As shown in Figure 4.6, MV2 combines the likelihood output of IP3D and IP2D with the flavour discriminating variables of SV1 and JF discussed

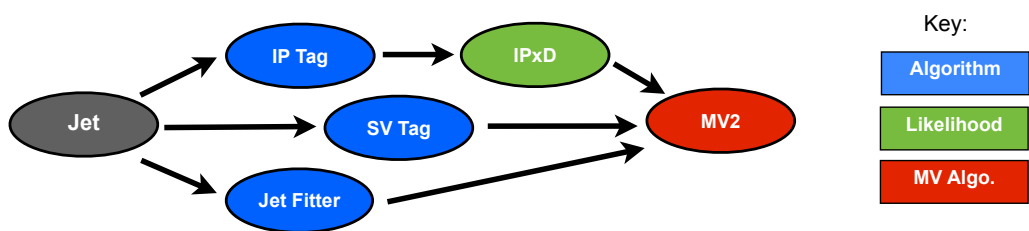


**Figure 4.6:** An illustration of how the three base flavour tagging algorithms are combined in the MV2 algorithm. The figure shows that the flavour discriminating variables from SV1 and Jet Fitter are combined with the likelihood outputs from IP2D and IP3D.

<sup>6</sup> The mass of a  $B_0$  or  $B^\pm$  meson is  $\sim 5$  GeV, which are the most common *b*-hadrons in a *b*-jet [15].

in the preceding sections. The MV2 output is a variable between -1 and 1, where 1 indicates that the jet is likely to be a *b*-jet and -1 indicates the inverse.

The BDT is trained using a simulated sample of  $t\bar{t}$  events that will contain a mix of *b*-, *c*- and light-jets, in addition to a sample containing a  $Z'$  boson decaying to *b*-quarks to increase statistics in the high jet- $p_T$  region. The training makes use of the truth jet flavour label scheme described in Section 4.3.1. Subtly different MV2 algorithms are created using samples containing different fractions of light and *c*-jets; the fraction of *c*-jets used is labelled in the algorithm name. For example, the MV2c10 algorithm has been trained on a sample containing 10% charm-jets, which gives strong light- and *c*-jet rejection.

A *b*-tagged jet is required to have a MV2 output above a specific cut value, such that *b*-tagged jets are likely to be *b*-jets. The choice of cut value will vary the *b*-jet efficiency, light-jet rejection and *c*-jet rejection: where *b*-jet efficiency is defined as the probability of *b*-tagging a *b*-jet, light-jet rejection is defined as 1 divided by the probability of *b*-tagging a light-jet, and *c*-jet rejection is defined as 1 divided by the probability of *b*-tagging a *c*-jet. Figure 4.7 shows the *b*-jet efficiency against (a) light jet rejection and (b) *c*-jet rejection of the MV2 algorithm for a continuous range of cut values. The different lines show the performance of the algorithm in the 2015 configuration [76] and in the 2016 configuration [77] where different fractions of *c*-jets are used in the training; 2016 MV2c10 is the configuration used throughout this thesis as recommended in [77].

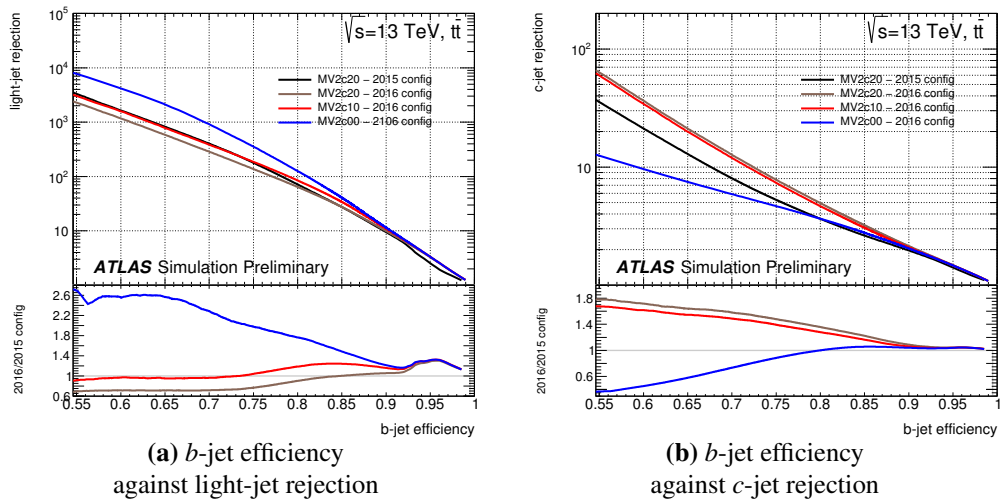


**Figure 4.7:** The expected *b*-jet efficiency of the *b*-tagging algorithm, MV2, with respect to (a) light-jet and (b) *c*-jet rejection in simulated  $t\bar{t}$  events. The various lines show the performance of the algorithm for different configurations and training setups [77].

There are four standard choices of MV2c10 cut value used in ATLAS analyses, these standard choices are known as *b*-tagging operating points. Table 4.1 shows the MV2c10

cut value of the four operating points and the corresponding values of *b*-jet efficiency, *c*-jet rejection, light-jet rejection and  $\tau$  rejection measured using simulated  $t\bar{t}$  events for jets with  $p_T$  greater than 20 GeV.

MV2c10 Cut Value	<i>b</i> -jet efficiency	<i>c</i> -jet rejection	Light-jet rejection	$\tau$ rejection
0.9349	60%	34	1538	184
0.8244	70%	12	381	55
0.6459	77%	6	134	22
0.1758	85%	3.1	33	8.2

**Table 4.1:** The MV2c10 *b*-tagging algorithm operating points; with the corresponding *b*-jet efficiency, *c*-jet rejection, light-jet rejection and  $\tau$  rejection. These values have been derived using simulated  $t\bar{t}$  events for jets with  $p_T$  above 20 GeV [77].

The *b*-jet efficiencies given in Table 4.1 are used to name the corresponding *b*-tagging operating points, as such the operating points are known as the 60%, 70%, 77% and 85% *b*-tagging operating points. To be specific, for a jet to be *b*-tagged at the 70% operating point the output of the MV2c10 algorithm performed on that jet must be greater than 0.8244.

*b*-tagging performance is known to decrease at high jet- $p_T$ . To illustrate this trend, Figure 4.8 shows the *b*-tagging efficiency for *b*-jets, *c*-jets and light-jets in  $t\bar{t}$  simulation as a function of jet- $p_T$  for the MV2c20 algorithm in the 2015 configuration [76]. A similar trend is also found for the MV2c10 using the 2016 configuration [77].

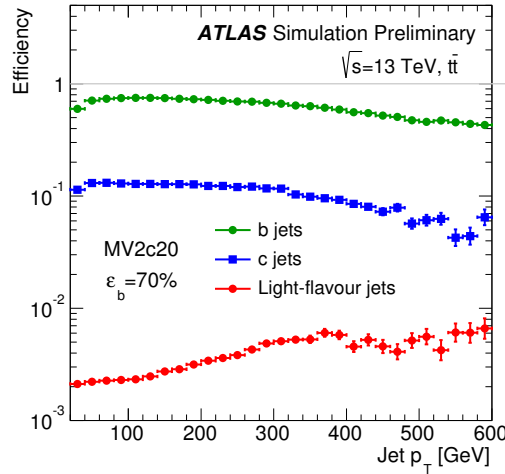


**Figure 4.8:** The *b*-tagging efficiency for *b*, *c* and light-jets against jet- $p_T$  for the MV2c20 algorithm at the 70% operating point using the 2015 configuration in simulated  $t\bar{t}$  events [76].

The decrease *b*-tagging performance at high  $p_T$  is due to a number of factors. Firstly, high- $p_T$  jets are more collimated meaning that reconstructed vertices will have a larger positional uncertainty and fake vertices become more common. Secondly, the fraction of tracks in a *b*-jet that do not come from the decay of a *b*-hadron increases, meaning that the

flavour discriminating variables are diluted. Finally, at high- $p_{\text{T}}$  the *b*-hadron can decay on the far side of the IBL, leading to a reduced vertex and impact parameter resolution.

#### 4.3.4 Calibration and Uncertainties

A calibration is performed to correct the modelling of *b*-tagging in simulation to the *b*-tagging performance in data. The *b*-tagging calibration uses di-lepton  $t\bar{t}$  events which, as described in Section 2.2.4, have a distinctive signature for event selection and provide a high-purity sample of *b*-jets [79, 80]. From the high-purity *b*-jet sample one can perform a likelihood fit to extract the *b*-jet efficiency,  $\epsilon_{b\text{Tag}}$ , which is defined as:

$$\epsilon_{b\text{Tag}} = \frac{N(\text{*b*-tagged jets})}{N(\text{*b*-jets})} \quad (4.5)$$

where *b*-tagged means above the cut on the MV2 output for a given operating point. By measuring  $\epsilon_{b\text{Tag}}$  in both data and in Monte-Carlo simulation one can derive a correction to simulation, known as a data/simulation scale factor ( $SF_{b\text{Tag}}$ ):

$$SF_{b\text{Tag}} = \epsilon_{b\text{Tag}}^{\text{Data}} / \epsilon_{b\text{Tag}}^{\text{MC}} \quad (4.6)$$

Uncertainties are derived for the scale factors to account for uncertainties in the modelling of the Standard Model processes and the detector response to electrons, muons and jets in simulation. The dominant source of uncertainty is the modelling of  $t\bar{t}$  in simulation. Figure 4.9 shows the data/simulation scale factor measured in 2015 and 2016 data as a function of jet  $p_{\text{T}}$ .

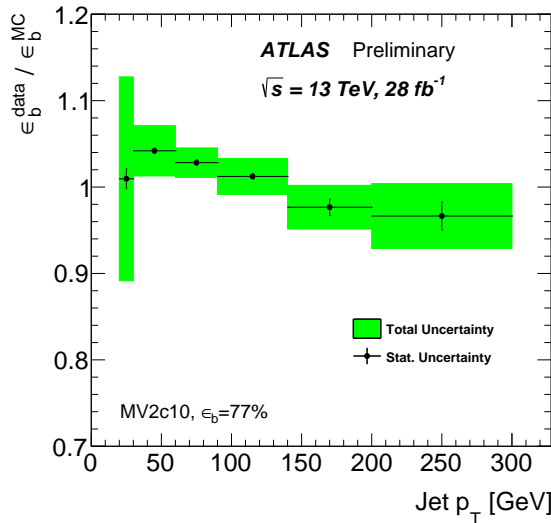


**Figure 4.9:** The ratio of *b*-tagging efficiency in data and Monte Carlo for MV2c10 at the 77% operating point as a function of jet- $p_{\text{T}}$  in di-lepton  $t\bar{t}$  events. Statistical uncertainties (black lines) and total uncertainties (green shaded region) are shown [80].

The *b*-tagging calibration using di-lepton  $t\bar{t}$  events described above is unable to measure a data/simulation scale factor for jets with  $p_T$  greater than 300 GeV, due to low data statistics in the high- $p_T$  region. Thus, the measured scale factors are extrapolated to cover the high jet- $p_T$  region. To derive an uncertainty for the high- $p_T$  extrapolation;  $\varepsilon_{b\text{Tag}}$  is measured in Monte-Carlo simulations of high- $p_T$  *b*-jets when variables known to affect the performance of *b*-tagging are varied to represent the modelling uncertainties of high- $p_T$  *b*-jets [81]. The dominant extrapolation uncertainty is from variations of the impact parameter resolution.

### 4.3.5 *b*-Jet Energy Scale

Section 4.2.3 described the jet energy scale correction applied to hadronic jets. For *b*-jets this correction may be different due to differences in the parton shower and hadronisation processes for a *b*-jet; for example, during the decay of the *b*-hadron, muons and neutrinos can be produced that will not deposit all/any of their energy in the calorimeter.

As a result, an additional *b*-jet energy scale (*b*JES) uncertainty has been specifically derived in a previous di-*b*-jet search at ATLAS [12]. The *b*JES uncertainty is found to be within 2.6% for all jets with a  $p_T$  greater than 60 GeV. The dominant source of the *b*JES uncertainty is from the modelling of the detector response to *b*-jets in simulation; other contributions to the *b*JES uncertainty considered are the modelling of *b*-jet formation in simulation, *b*-tagging calibration and jet energy resolution. In addition, an uncertainty is applied to cover a bias in the number of charged tracks associated to a *b*-jet with respect to a light jet, which is necessary because, as is described below, tracks are used to validate the *b*JES uncertainty.

The *b*JES uncertainty is validated by comparing jet energy measurements to independently calibrated objects, in this case tracks that are associated to the jets. It is found that the energy of *b*-tagged jets is consistent with the energy of jets with no *b*-tagging applied within the 2.6% *b*JES uncertainty considered. Therefore no additional *b*JES correction is required.

## 4.4 Electrons and Muons

Reconstruction of electrons and muons is important for a number of analyses at ATLAS; including the selection of di-lepton  $t\bar{t}$  events which is used in the calibration of the  $b$ -jet trigger, described in Section 5.3.

Electron<sup>7</sup> reconstruction at ATLAS [82] uses the matching of narrow clusters of energy deposits in the EM calorimeter to a track from the ID (described in Section 4.1), from which the four-momentum of the electron can be determined. Information such as the calorimeter shower shape, properties of the matched track and TRT transition radiation (described in Section 3.2.2) are used to identify electrons. Three different operating points are provided for electron identification which are, in order of increasing background rejection: *Loose*, *Medium* and *Tight*.

Muons<sup>8</sup> are the only charged particle not to be stopped by the ATLAS calorimeter. Therefore muons are identified at ATLAS using hits in the sub-detector outside of the calorimeter, the Muon Spectrometer (MS), which is described in Section 3.2.4. Two of the techniques used for muon reconstruction are combined muons and extrapolated muons. Combined muons are reconstructed by extrapolating tracks formed in the MS inwards to match tracks formed in the ID; if a match is found then a muon track is reconstructed from the associated ID and MS hits. By using both ID and MS hits, a higher precision muon track is created and the muon tracks can be accurately assigned to a primary vertex, which is used to identify muons from pile-up. Extrapolated muons are muon tracks formed using only hits in the MS with a loose requirement on the track pointing to the hard-scatter primary vertex to reduce effects from pile-up; extrapolated muons are important in the range  $2.5 < |\eta| < 2.7$  for which there is no ID coverage. The four-momentum of the reconstructed muons is determined from the direction and curvature of the muon tracks.

The muon identification operating points are *Loose*, *Medium*, *Tight* and *High- $p_T$* . Medium muons, used in Section 5.3, are combined or extrapolated muons that pass a quality criteria based on number of MS hits, track fit quality and, where relevant, compatibility between the ID and MS tracks.

---

<sup>7</sup> For the purposes of reconstruction positrons are included as a subset of electrons.

<sup>8</sup> Similar to positrons, in reconstruction anti-muons are included as a subset of muons.

## Chapter 5

# The ATLAS Trigger System

In 2015 and 2016, the LHC has been colliding proton bunches every 25 ns, meaning that the ATLAS experiment has been collecting data at a rate of 40 MHz. Due to the large computing resources required to process and store each event, it is not possible to record all events. The most interesting events to study contain a hard-scatter collision<sup>1</sup> as these are the collisions that, for example, can produce a TeV scale BSM particle. Therefore, the ATLAS experiment uses a trigger system to select events that contain a high- $p_T$  physics object which indicates that a hard-scatter collision has occurred.

The ATLAS trigger-system used in Run-2<sup>2</sup> consists of two levels; the first level trigger (L1) and the higher level trigger (HLT) [83, 84, 85].

The L1 trigger is hardware based and reduces the rate from 40 MHz to 100 kHz within a time window of 2.5  $\mu$ s. The L1 trigger uses custom electronics to rapidly process information directly from the calorimeter and Muon Spectrometer, searching for high- $p_T$  muon tracks and large energy deposits in the calorimeter. If the observed muon tracks and calorimeter deposits pass a set of pre-defined conditions, a L1 trigger accept is given. At the same time Regions of Interests (RoIs) are constructed around the high- $p_T$  objects identified by the L1 trigger, which are utilised by the HLT.

If the L1 trigger is passed the event is processed by the HLT, a software based trigger, which further reduces the event rate to 1 kHz within a time window of 0.2 s. The HLT uses the information from the full detector to perform a more complete reconstruction of the physics objects within the event; the most time consuming reconstruction algorithms are only run within the RoIs taken from L1. The more complex event analysis

---

<sup>1</sup>Defined in Chapter 4.

<sup>2</sup> The period of data-taking starting in 2015 and scheduled to continue until the end of 2018 is known as Run-2.

within the software-based trigger includes track reconstruction and therefore allows for  $b$ -jet identification. If the content of the event reconstruction passes pre-set criteria, a HLT accept is issued meaning that the events are passed on for processing and storage.

In the ATLAS trigger system there is an additional process known as pre-scaling that can be applied. If a trigger is pre-scaled, only a fraction of the events that pass the trigger are recorded. Pre-scaling is applied to maintain the output rate of the L1 and HLT trigger systems at 100 and 1 kHz respectively as the instantaneous luminosity of the LHC collisions is increased. An unprescaled trigger is defined as a trigger that has no pre-scale applied to it. Most analyses at ATLAS use unprescaled triggers to maximise the acceptance of the trigger.

This chapter describes triggers used in the two di- $b$ -jet searches presented in this thesis. Section 5.1 describes jet triggers used in the high-mass di- $b$ -jet search, Section 5.2 describes  $b$ -jet triggers used in the low-mass di- $b$ -jet search and finally Section 5.3 presents the measurement of the  $b$ -jet trigger efficiency, an essential input to the low-mass search.

There are two important definitions used in this chapter, and throughout this thesis. ‘*Online*’ refers to any algorithms run or objects reconstructed at the trigger level. ‘*Offline*’ refers to algorithms run after events have passed the trigger at the data-processing level. Offline algorithms and objects used in this thesis are described in Chapter 4.

## 5.1 Jet Triggers

Section 4.2 described that hadronic jets are built from energy deposits in the ATLAS calorimeter. Jet triggers select events that contain one or more high- $p_T$  jets; in Run-2 jet triggers are used at both the L1 and HLT level [86, 87].

The L1 trigger is a hardware based trigger which accepts or rejects an event within  $2.5\ \mu\text{s}$ . Due to this time constraint, the L1 jet trigger uses coarser jet reconstruction techniques than are used by offline reconstruction. The L1 jet trigger uses trigger towers which are defined as energy deposits in a region of  $0.1 \times 0.1$  in the  $\eta - \phi$  plane integrated radially over all layers of the EM and hadronic calorimeter. The L1 jet trigger accepts an event if a neighbouring group of  $4 \times 4$  trigger towers containing energy deposits above some pre-set threshold is found.

The HLT jet trigger is able to use more complex algorithms to reconstruct jets due to the longer time allowed for a trigger decision. Similar to offline jet reconstruction, in the HLT jets are reconstructed using hadronic topoclusters formed from EM or hadronic

calorimeter cells and the anti- $k_T$  jet-reconstruction algorithm with  $R=0.4$  (see Section 4.2). The HLT jet trigger is passed if the reconstructed jets meet pre-set criteria that depend on the number and  $p_T$  of the jets. The  $b$ -jet triggers described in the following section also use the L1 and HLT jet trigger procedures to reconstruct jets.

For the high-mass di- $b$ -jet search the HLT\_j380 trigger is used, which requires that at least one jet is found with a  $p_T > 380$  GeV. This is chosen as it is the unprescaled single jet trigger with the lowest cut on jet- $p_T$  in 2016 data-taking.

However, as will be shown in Section 7, the online jet  $p_T$  threshold limits the mass region that the high-mass di- $b$ -jet can probe to  $m > 1.1$  TeV. In the mass region  $m < 1.1$  TeV a kinematic bias from the online jet  $p_T$  threshold is introduced such that the backgrounds from the Standard Model cannot be modelled. Therefore, for a di- $b$ -jet search to probe lower masses a different trigger strategy is required.

## 5.2 *b*-Jet Triggers

As described in Section 4.3,  $b$ -jets, defined as jets containing a  $b$ -hadron, can be identified from the topology of tracks in a process known as  $b$ -tagging.  $b$ -tagging can be utilised online to reduce rates of jets significantly<sup>3</sup> allowing for a lower jet- $p_T$  threshold than is used by the single jet trigger. Hence, using a  $b$ -jet trigger in di- $b$ -jet searches means that a lower mass range can be probed.

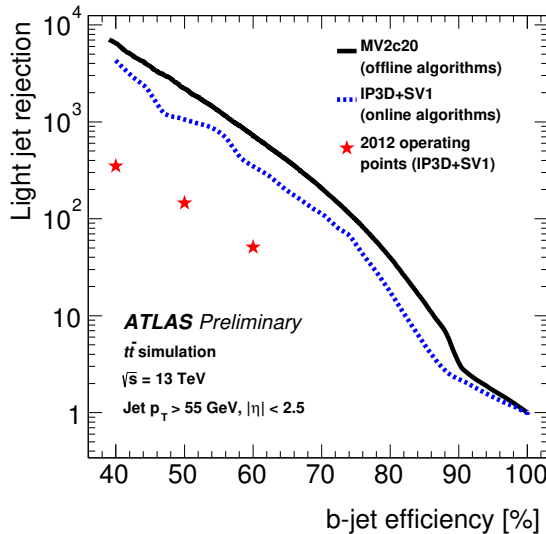
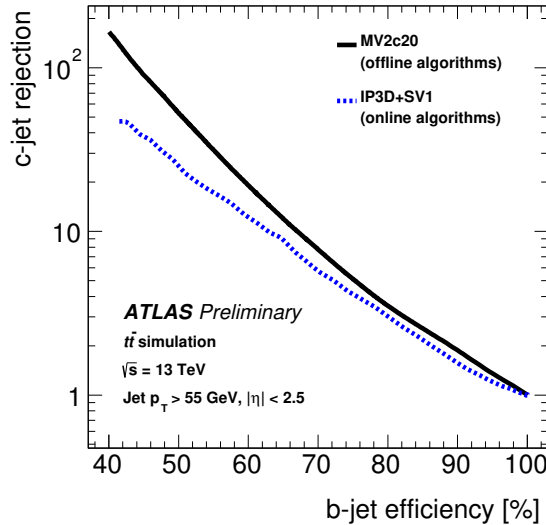
Due to the complexity of the algorithms used in  $b$ -tagging, the  $b$ -jet trigger is only available in the HLT. The  $b$ -jet trigger utilises the regions of interest (RoI) defined by the jets reconstructed in the L1 jet trigger. The  $b$ -jet trigger procedure for 2016 data-taking contains three steps [87]. Firstly, a fast-tracking algorithm is run in the RoIs and the reconstructed tracks are used to identify the hard-scatter primary vertex (PV) in the event. Secondly, precision tracking is performed within each jet RoI. Finally, the precision tracks are used by the MV2c20  $b$ -tagging algorithm, described in Section 4.3.3, to identify  $b$ -jets.

Figure 5.1 shows the  $b$ -jet efficiency against light-jet and  $c$ -jet rejection for online  $b$ -tagging in a variety of  $b$ -jet trigger configurations in simulated  $t\bar{t}$  events. The black line represents the MV2c20 algorithm used in 2016 data as described in Section 4.3.3<sup>4</sup>. The blue line represents the IP3D+SV1 algorithm that combines two of the base  $b$ -tagging algorithms described in Section 4.3.2; IP3D+SV1 was used by the  $b$ -jet trigger in 2015 data.

---

<sup>3</sup> As described in Section 2.2.3.3, QCD dijet production is dominated by light-jets.

<sup>4</sup> In Figure 5.1 the MV2c20 algorithm is referred to as an ‘offline algorithm’ as it was initially developed by the offline  $b$ -tagging group.

(a) *b*-jet efficiency against light-jet rejection.(b) *b*-jet efficiency against *c*-jet rejection.

**Figure 5.1:** The expected *b*-jet efficiency of *b*-jet triggers with respect to (a) light-jet and (b) *c*-jet rejection in the case where the *b*-tagging algorithm used is MV2c20 (black), IP3D+SV1 (blue) and, in panel (a) only, for the set-up used in 2012 data-taking (red stars) [87].

There are several *b*-jet triggers available with a variety of requirements on the jet multiplicity, number of tagged jets and *b*-tag operating point used. As the signal considered in the low mass di-*b*-jet search is a BSM particle decaying to two *b*-quarks, a double *b*-jet trigger is used. The double *b*-jet trigger requires that there are two online jets with  $p_T > 150$  and  $50$  GeV respectively, which have been *b*-tagged at the 60% efficiency operating point<sup>5</sup>. It will be shown in Chapter 7 that the low mass di-*b*-jet search is able to probe the mass range  $m > 570$  GeV.

<sup>5</sup> The trigger is known as *HLT\_j150\_bmv2c2060\_split\_j50\_bmv2c2060\_split*.

There are significant differences in the *b*-jet trigger configurations used in 2016 and 2015 data-taking. Firstly, the online *b*-tagging algorithm is MV2c20 in 2016 data-taking whilst IP3D+SV1 was used in 2015 data-taking; MV2c20 is used in 2016 due to improved *b*-tagging performance, as shown in Figure 5.1. Secondly, different algorithms are used to identify the hard-scatter primary vertex in 2015 and 2016 data. 2016 data-taking employs the `xPrmVtx` algorithm, which is based on the hard-scatter primary vertex finding algorithm used offline, as described in Section 4.1.1. In 2015 data-taking the `EFHist` algorithm is employed [88]; which groups all tracks in a histogram based on the *z* position of the track intersection with the centre of the region where the proton beams interact (known as the beam-spot); the centre of the bin containing the largest sum of track- $p_T$  is the hard-scatter primary vertex. Because of these significant differences, data taken in 2015 and 2016 by the *b*-jet trigger are not easily combined in a di-*b*-jet search. Therefore, the low mass di-*b*-jet search presented in this thesis uses only the 2016 data-set; the 2016 data-set has an improved online *b*-tagging performance, as shown in Figure 5.1, and contains 88% of the integrated luminosity collected by the *b*-jet trigger in 2015 and 2016.

Furthermore, there are also significant differences between the *b*-tagging procedure used online and offline. Firstly, coarser tracking information is available online; notably online tracks are only reconstructed within the jet RoIs. Secondly, a different fraction of *c*-jets were present in the sample used to train the MV2 algorithm in online and offline *b*-tagging; specifically 10% were used offline (MV2c10) and 20% were used online (MV2c20). The training samples used by the MV2 algorithm are discussed in Section 4.3.3. The reason that MV2c20, which was recommended for analyses using only 2015 data [76], is used online in 2016 data-taking is that the *b*-jet trigger configuration had to be determined before the start of data-taking in March 2016, whilst the recommendation to use MV2c10 was announced internally in May 2016 [77]. As offline and online *b*-tagging are significantly different, online *b*-tagging must have an independent calibration, which is described in the following section.

## 5.3 Measurement of the $b$ -Jet Trigger Efficiency in 2016 Data

The trigger is critical in the event selection of any analysis, therefore the performance of the triggers utilised must be understood and calibrated. This section describes the  $b$ -jet trigger efficiency measurement in 2016 data, which is an important input to the low-mass di- $b$ -jet search presented in this thesis.

The  $b$ -jet trigger is always used in tandem with offline  $b$ -tagging, which is calibrated independently of the  $b$ -jet trigger, as described in Section 4.3.4. Therefore, the  $b$ -jet trigger efficiency,  $\epsilon_{b\text{Trig}}$ , is defined with respect to offline  $b$ -tagging; specifically,  $\epsilon_{b\text{Trig}}$  is defined as the number of  $b$ -jets that are offline  $b$ -tagged and match an online  $b$ -tagged trigger-jet divided by the number of  $b$ -jets that are offline  $b$ -tagged and match a trigger jet. Or to put this in an equation;

$$\epsilon_{b\text{Trig}} = \frac{N(\text{Offline } b\text{-tagged, online } b\text{-tagged, } b\text{-jets})}{N(\text{Offline } b\text{-tagged, trigger-matched, } b\text{-jets})} \quad (5.1)$$

A  $b$ -jet is defined as a jet containing a  $b$ -hadron. The process used to match trigger jets and offline jets is described in Section 5.3.1.

The  $b$ -jet trigger efficiency is measured in both data and Monte-Carlo simulated samples. Then a  $b$ -jet trigger data/simulation scale factor ( $SF_{b\text{Trig}}$ ), is derived, where:

$$SF_{b\text{Trig}} = \epsilon_{b\text{Trig}}^{\text{Data}} / \epsilon_{b\text{Trig}}^{\text{Simulation}} \quad (5.2)$$

The data/simulation scale-factor is applied to Monte-Carlo simulation to correct for mis-modelling of the  $b$ -jet trigger performance. The scale-factors for the  $b$ -jet trigger are to be applied in addition to the offline  $b$ -tagging scale factors described in Section 4.3.4.

The  $b$ -jet trigger efficiency and data/simulation scale factors are measured for all combinations of offline and online  $b$ -tagging operating points. Only the 70% offline and 60% online operating point combination is presented in this section, as this is set of operating points used in the low mass di- $b$ -jet search; Chapter 7 contains full details of the  $b$ -tagging operating points used in di- $b$ -jet searches.

### 5.3.1 Description of Event Selection and Data-Sets

Di-lepton  $t\bar{t}$  events containing a muon and an electron are selected to provide a high purity sample of  $b$ -jets to measure the  $b$ -jet trigger efficiency. As discussed in Section 2.2.4,  $e\mu$  di-lepton  $t\bar{t}$  events provide a distinctive signature for selection and a high purity sample of  $b$ -jets required for the efficiency measurement. Furthermore, the electron and muon provide a signature that can be used to select events at the trigger-level without using a  $b$ -jet trigger such that no bias is introduced from online  $b$ -tagging.

For this measurement, the triggers deployed are  $b$ -performance triggers, which are special triggers used in data-taking specifically for monitoring the  $b$ -jet trigger performance. They are passed if there is an electron or a muon in the event. The  $b$ -performance triggers then run and record the output of the online  $b$ -tagging algorithms for all online jets with  $|\eta| < 2.5$  and  $p_T > 35$  GeV, without placing any requirements on the output of the MV2c20 algorithm. Therefore,  $b$ -performance triggers can select di-lepton  $t\bar{t}$  events at the trigger-level and thus provide an unbiased source of online  $b$ -tagged jets to measure the  $b$ -jet trigger efficiency.

Furthermore, using a  $b$ -performance trigger allows us to monitor and accurately measure the actual online  $b$ -jet trigger performance in real time. This is important as if there is unexpected behaviour at any point in the  $b$ -jet trigger procedure, for instance if there is a hardware outage, then we are able firstly to identify that there is an issue and later to apply corrections to any affected regions of data.

For an event to be selected it is required to:

- Pass one of two single lepton  $b$ -performance triggers<sup>6</sup> that require
  - An online reconstructed medium muon with  $p_T > 26$  GeV.
  - Or an online reconstructed electron with  $p_T > 26$  GeV.
- Contain an offline medium muon with  $p_T > 30$  GeV and no jet within  $\Delta R$  of 0.4.
- Contain an offline medium electron with  $p_T > 30$  GeV.
- Contain  $\geq 2$  offline  $b$ -tagged jets, defined as:
  - Offline  $R=0.4$  anti- $k_T$  jets.
  - $p_T > 35$  GeV and  $|\eta| < 2.5$ .
  - Offline  $b$ -tagged at the 85% operating point.
  - The offline jet must be matched to an online jet.

Details of muon, electron, jet and  $b$ -tagged jet object definition are in Chapter 4.

---

<sup>6</sup> Known as *HLT\_mu26\_imedium\_2j35\_boffperf\_split* and *HLT\_e26\_tight\_iloose\_2j35\_boffperf\_split*.

As specified in the list above, for selecting di-lepton  $t\bar{t}$  events 2 offline jets must be  $b$ -tagged at the 85% operating point; the loose operating point is chosen as this provides the largest number of events. However, it is important to note that for a jet to be included in the set of jets to calculate of  $\varepsilon_{b\text{Trig}}$  it must also be  $b$ -tagged at the offline operating point be calibrated, which in the studies being presented in this thesis is the 70% operating point.

The offline leptons are required to have a  $p_T > 30$  GeV such that there is no kinematic bias from the online lepton  $p_T$  requirement. The muon used for event selection is required to have no jet within  $\Delta R$  of 0.4 to exclude events where the only muon is caused by the decay of the  $b$ -hadron within a  $b$ -jet, which would increase the fraction of non- $t\bar{t}$  backgrounds.

Offline jets are matched to online jets if  $\Delta R < 0.4$ , the matching is exclusive meaning that online jets are only matched to offline jets with the smallest  $\Delta R$  separation. Matching is required such that the  $b$ -jet trigger efficiency measurement does not have a kinematic bias from the online jet- $p_T$  requirement used in the  $b$ -performance trigger. The 85% operating point is chosen for offline  $b$ -tagging as a tighter event selection cannot be used to calibrate the 85% operating point.

The data-set used is 13 TeV  $pp$  collision data collected by the ATLAS detector between March and December 2016; the same data-set is used by the low mass di- $b$ -jet search presented in this thesis.

For any data-set, a Good Run List (GRL) is applied to remove events of low data-quality, which is typically caused by an element of the detector not operating optimally. For example, data-taking periods where the inner-most layer of the inner detector, the IBL, was not operating are removed as this data-taking period has a lower  $b$ -tagging performance.

In this section it will be shown that when using data collected by ATLAS in 2016 using a  $b$ -jet trigger it is necessary to apply a  $b$ -jet trigger aware GRL; Section 5.3.2 will describe the observations that lead the a requirement of a  $b$ -jet trigger aware GRL and Section 5.3.3 describes the details of the  $b$ -jet trigger aware GRL. After the application of the  $b$ -jet trigger aware GRL the data-set corresponds to an integrated luminosity of  $24.3 \text{ fb}^{-1}$ .

Events that pass the event selection are dominated by  $t\bar{t}$  production with a small contribution from single-top production [89]; the remaining backgrounds are negligible and are not considered in this efficiency measurement. For the simulated sample, a Monte-Carlo simulated  $t\bar{t}$  sample is produced using the Powheg-Box v2 [90] generator with the CT10 PDF sets [91] in the matrix element calculations. For the simulated single-top sample electro-weak  $t$ -channel,  $s$ -channel and  $Wt$ -channel single top-quark events are generated

using the Powheg-Box v1 generator and CT10 PDF sets. For both processes the parton shower, fragmentation and the underlying event are simulated using the PYTHIA6 [92] generator with the CTEQ6L1 [93] PDF sets and the corresponding Perugia 2012 tune [94]. The top mass is set to 172.5 GeV. The EVTGEN v1.2.0 program [95] is used to model the decays of  $b$  and  $c$  hadrons.

### 5.3.2 Investigation of Data-Simulation Discrepancies

This section will present the initial observation and investigation of discrepancies between the  $b$ -jet trigger efficiency measured in 2016 data and simulation. To replicate the event selection used during the discrepancy and investigation studies the  $b$ -jet trigger aware GRL is not applied in this section.

Figure 5.2 shows the measured  $b$ -jet trigger efficiency in data and simulation against jet- $p_T$  and  $\eta$ . To accurately reflect the total  $b$ -jet trigger efficiency, offline jets are not required to match online jets in the denominator of the  $b$ -jet trigger efficiency for this figure. The reason for relaxing this requirement is described later in this section.

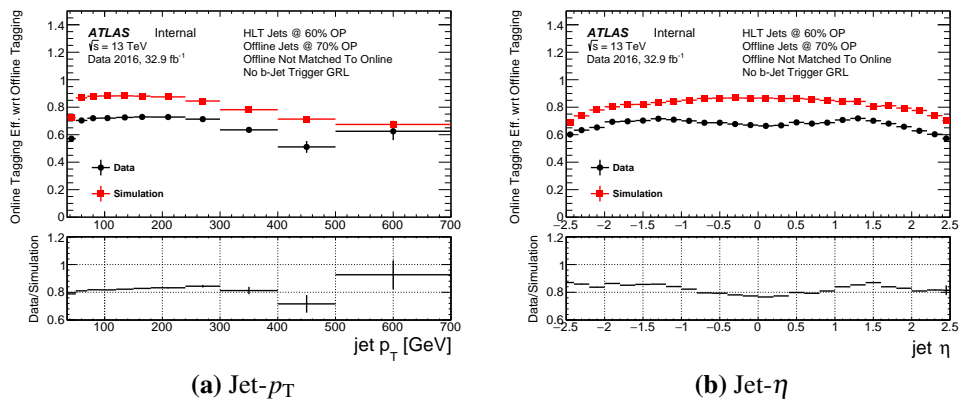


**Figure 5.2:** The 60% operating point  $b$ -jet trigger efficiency with respect to the offline 70% operating point for data (black) and simulation (red) against (a) jet- $p_T$  and (b) jet- $\eta$ . The  $b$ -jet trigger aware GRL is not applied and offline–online jet matching is not required.

In Figure 5.2 the efficiency in data is substantially lower than the efficiency expected from simulation and has a different distribution with respect to jet- $\eta$ . The substantial differences need to be investigated and understood. The drop in efficiency in the lowest  $p_T$  bin (35–50 GeV) is because not all offline jets with a  $p_T < 50$  GeV will have an equivalent online jet with  $p_T > 35$  GeV required to be considered by the  $b$ -performance trigger. This bias is removed when offline–online jet matching is required.

A number of cross-checks were performed to investigate the discrepancy between data and simulation shown in Figure 5.2: including checking for a dependence of the  $b$ -jet trigger efficiency on the ATLAS detector conditions and the number of pile-up collisions. It has been discovered that the problem causing the large data-simulation discrepancies was related to hard-scatter primary vertex finding.

As described in Section 5.2, in 2016 data the  $xPrmVtx$  algorithm is used to find the hard-scatter primary vertex (PV) in the  $b$ -jet trigger. It has since been uncovered that there was an error in the implementation of this algorithm that relates to the online beam-spot position. The beam-spot position is defined as the centre of the region where the two proton bunches cross in the ATLAS detector. The beam-spot position is estimated at the trigger-level using the average position of reconstructed primary vertices over many events, this is known as the online beam-spot position [96]. Online tracks use positions with respect to the online beam-spot whilst the  $xPrmVtx$  algorithm assumes track positions with respect to the origin. As a result of this mismatch, if the online beamspot  $z$ -position is far from the origin then a  $xPrmVtx$  PV is often not found and a dummy PV with position at the origin is used by the  $b$ -jet trigger. The evidence for this hypothesis is discussed in the remainder of this section. For brevity, online beamspot  $z$ -position is henceforth referred to as  $z_{bs}^{\text{online}}$ .

The exact configuration of the  $b$ -jet trigger has changed over time to respond to performance issues as they are observed. The 2016 data-set is therefore split into 3 different ‘epochs’ of data, which are defined by the effect on  $b$ -jet trigger performance of not finding a  $xPrmVtx$  PV. The epochs are summarised in Table 5.1. The  $b$ -jet trigger efficiency is investigated in each epoch independently.

Epoch	Range of Run Numbers	Integrated Luminosity	Effect if no $xPrmVtx$ PV is found
1	296939-300571, 300655	$0.8 \text{ fb}^{-1}$	An invalid primary vertex is used in online $b$ -tagging.
2	300600, 300784-308084	$15.2 \text{ fb}^{-1}$	The $b$ -jet trigger will not pass the event.
3	309331-311481	$8.3 \text{ fb}^{-1}$	A back-up primary vertex finding algorithm is used.

**Table 5.1:** A table summarising the three epochs of data, showing the constituent run numbers, the integrated luminosity after a  $b$ -jet trigger GRL is applied and the effect of not finding a  $xPrmVtx$  primary vertex (PV).

Firstly, let's consider Epoch 1; Figure 5.3(a) shows that the  $b$ -jet trigger efficiency measured in data is 80-90% of the efficiency in simulation. Figure 5.3(b) shows that the  $b$ -jet trigger efficiency in Epoch 1 has a strong dependence on  $z_{\text{bs}}^{\text{online}}$ ; when  $z_{\text{bs}}^{\text{online}}$  is close to zero the  $b$ -jet trigger efficiency in data and simulation are comparable<sup>7</sup> but as  $|z_{\text{bs}}^{\text{online}}|$  increases efficiency falls off steeply.

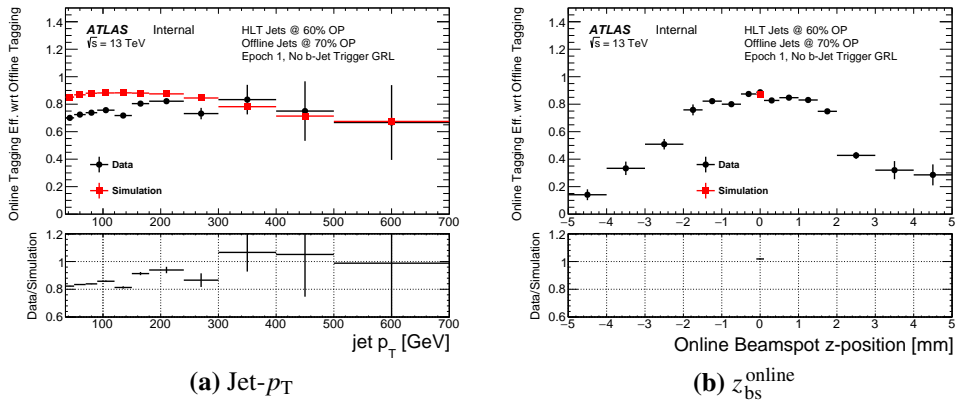


**Figure 5.3:** The 60% operating point  $b$ -jet trigger efficiency with respect to the offline 70% operating point for data from Epoch 1 (black) and simulation (red) against (a) jet- $p_T$  and (b) online beamspot  $z$ -position. The  $b$ -jet trigger aware GRL is not applied.

To understand this performance the variable ‘*vertex class*’ is studied, which is defined as 0 when a  $\chi_{\text{PrmVtx}}^2/\text{PV}$  is found and 1 if not. Figure 5.4(a) shows that when a  $\chi_{\text{PrmVtx}}^2/\text{PV}$  is found the  $b$ -jet trigger efficiency is reasonably high ( $\sim 0.8$ ) and is comparable between data and simulation (within 5%), whilst if no  $\chi_{\text{PrmVtx}}^2/\text{PV}$  is found then efficiency is close to zero in both simulation and data. However, Figure 5.4(b) shows that a  $\chi_{\text{PrmVtx}}^2/\text{PV}$  is found in simulation for  $> 99\%$  of the jets, whilst in data there is  $\sim 16\%$  of events where no  $\chi_{\text{PrmVtx}}^2/\text{PV}$  is found.

It is also useful to study the subset of events where a  $\text{xPrmVtx}$  PV has been found. Figure 5.5 shows the  $b$ -jet trigger efficiency against jet- $p_T$  and  $z_{\text{bs}}^{\text{online}}$  when a  $\text{xPrmVtx}$  PV is found. It is shown that when a  $\text{xPrmVtx}$  PV is found, the measured  $b$ -jet trigger efficiency in data and simulation are in agreement and there is no strong dependence on  $z_{\text{bs}}^{\text{online}}$ .

Hence, using the information in Table 5.1 and Figures 5.3 – 5.5 it can be concluded that for events in Epoch 1 where the  $|z_{\text{bs}}^{\text{online}}|$  is far from zero, a  $\chi \text{P} \text{rmVt} \times \text{PV}$  is often not found resulting in a low  $b$ -jet trigger efficiency. This is the cause of the data/simulation differences observed in Epoch 1, as shown in Figure 5.3.

<sup>7</sup> Simulation is produced with  $z_{\text{bs}}^{\text{online}}$  equal to zero.

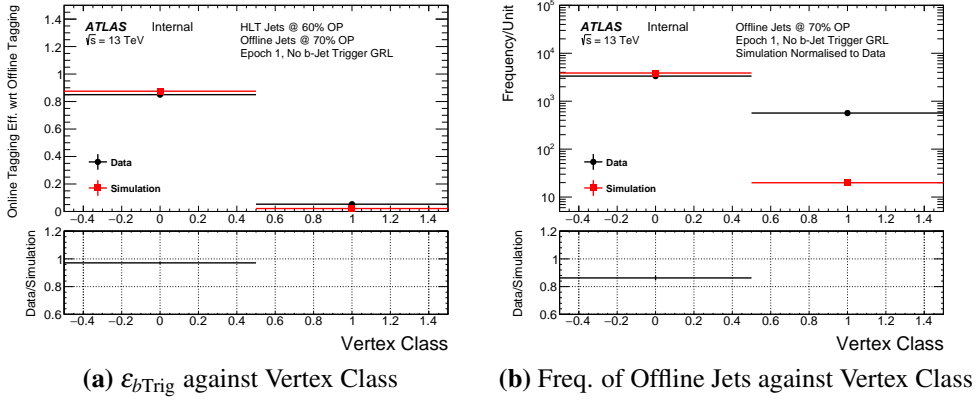


**Figure 5.4:** (a) The 60% operating point  $b$ -jet trigger efficiency with respect to the offline 70% operating point and (b) the number of offline jets  $b$ -tagged at the 70% operating point that match a HLT trigger jet against vertex class for data from Epoch 1 (black) and simulation (red). Vertex class is defined as 0 when a  $xPrmVtx$  vertex is found and 1 if not. The  $b$ -jet trigger aware GRL is not applied.

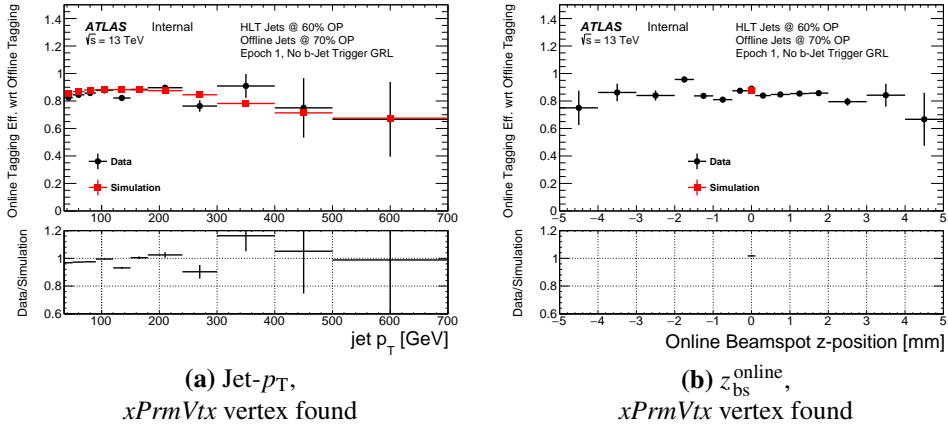


**Figure 5.5:** The 60% operating point  $b$ -jet trigger efficiency with respect to the offline 70% operating point for data from Epoch 1 (black) and simulation (red) against (a) jet- $p_T$  and (b) online beamspot  $z$ -position in the case where an  $xPrmVtx$  vertex has been found. The  $b$ -jet trigger aware GRL is not applied.

In Epoch 2 if a  $xPrmVtx$  PV is not found, the  $b$ -jet trigger procedure terminates whilst processing the event and therefore the trigger does not pass the event. As the  $b$ -jet trigger procedure terminates, the  $b$ -performance triggers will also not be passed when no  $xPrmVtx$  PV is found. This means that events with no  $xPrmVtx$  PV are lost in both numerator and denominator when calculating the  $b$ -jet trigger efficiency, defined in Equation 5.1. Therefore, by using the  $b$ -performance triggers one is effectively measuring the  $b$ -jet trigger efficiency when a  $xPrmVtx$  PV is found. Figure 5.6 shows that the  $b$ -jet trigger efficiency measured in Epoch 2 is in agreement with simulation within 5%. This is the reason it was necessary to relax the offline–online jet matching to accurately represent the full data-simulation discrepancy in Figure 5.2.

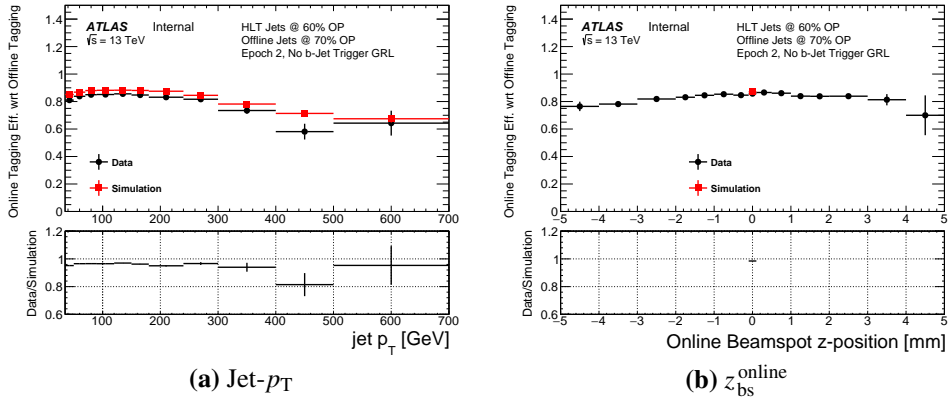


**Figure 5.6:** The 60% operating point  $b$ -jet trigger efficiency with respect to the offline 70% operating point for data from Epoch 2 (black) and simulation (red) against (a) jet- $p_T$  and (b) online beamspot  $z$ -position. The  $b$ -jet trigger aware GRL is not applied.

Therefore, in Epoch 2 it is necessary to account for the cases when a `xPrmVtx` PV is not found by measuring the online primary vertex efficiency,  $\epsilon_{\text{PV}}$ , which is the efficiency that there is a primary vertex in the event.  $\epsilon_{\text{PV}}$  is calculated in Epoch 2 by dividing the number of events that pass the single muon  $b$ -performance trigger by the number of events that pass the equivalent single muon trigger with no  $b$ -performance functionality<sup>8</sup>. The denominator of  $\epsilon_{\text{PV}}$  has no  $b$ -jet trigger dependency so is unaffected by the `xPrmVtx` algorithm.  $\epsilon_{\text{PV}}$  is an event level quantity that must be measured with respect to other event level quantities, such as leading jet- $p_T$ .

Figure 5.7(a) shows that  $\varepsilon_{\text{PV}}$  has a data/simulation ratio of around 80% which is similar to that shown in Figure 5.3. Figure 5.7(b) shows that  $\varepsilon_{\text{PV}}$  has a similar shape with respect to  $z_{\text{bs}}^{\text{online}}$  as observed in Epoch 1, shown in Figure 5.3(b). Furthermore, in Figure 5.7(c) it is shown that there is a reduced online primary vertex efficiency at smaller values of leading jet- $|\eta|$ ; this shows that the inefficiency in finding a  $\times \text{PrmVtx} \times \text{PV}$  causes a kinematic bias with respect to leading jet- $\eta$ .

<sup>8</sup> Specifically  $\varepsilon_{\text{PV}} = \text{Number of events that pass } HLT\_mu26\_imedium\_2j35\_boffper\_split \text{ divided by the number that pass } HLT\_mu26\_imedium.$

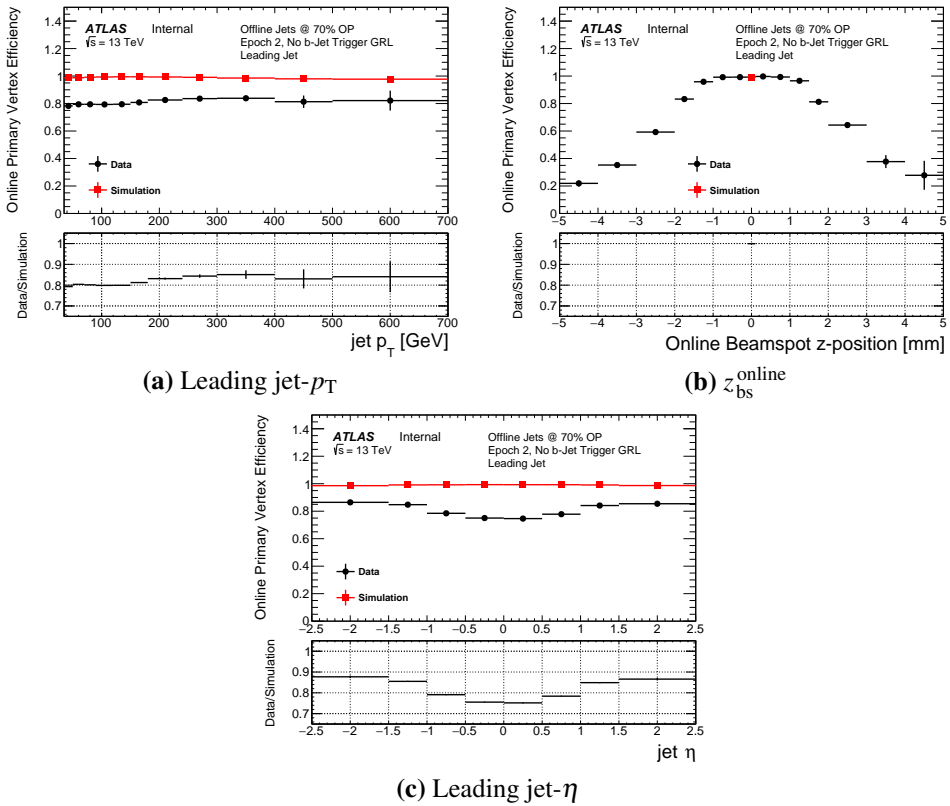


**Figure 5.7:** The online primary vertex efficiency,  $\epsilon_{\text{PV}}$ , for data from Epoch 2 (black) and simulation (red) against (a) leading-jet  $p_T$ , (b) online beamspot  $z$ -position and (c) leading jet- $\eta$ . The  $b$ -jet trigger aware GRL is not applied.

For Epoch 3, when no `xPrmVtx` PV is found a backup PV finding algorithm is used. The backup algorithm, known as `EFHist`, is the PV finding algorithm used in 2015 data and finds the PV through a basic histogramming of the tracks. The simplicity of the `EFHist` algorithm means that a PV is always found. Figure 5.8 shows the  $b$ -jet trigger efficiency in Epoch 3 against jet- $p_T$ , jet- $\eta$ ,  $z_{\text{bs}}^{\text{online}}$  and vertex class (as defined above). In Epoch 3 the  $b$ -jet trigger efficiency measured in data is within 5% of simulation and there is no shape difference between the two with respect to jet- $\eta$ . In addition, it is shown that in Epoch 3 there is no dependence of the  $b$ -jet trigger efficiency on  $z_{\text{bs}}^{\text{online}}$  or vertex class. This demonstrates that the use of a backup finding algorithm alleviates the  $b$ -jet trigger performance issues observed in Epoch 1 and Epoch 2.

To summarise, it is shown that at large values of absolute online beamspot  $z$ -position the measured  $b$ -jet trigger efficiency in Epoch 1 and  $b$ -jet performance efficiency in Epoch 2 is lower in data than in simulation due to poor  $\text{xPrmVtx}$  PV finding performance. In Epoch 3 there is reasonable data/simulation agreement due to the use of a backup vertex finding algorithm.

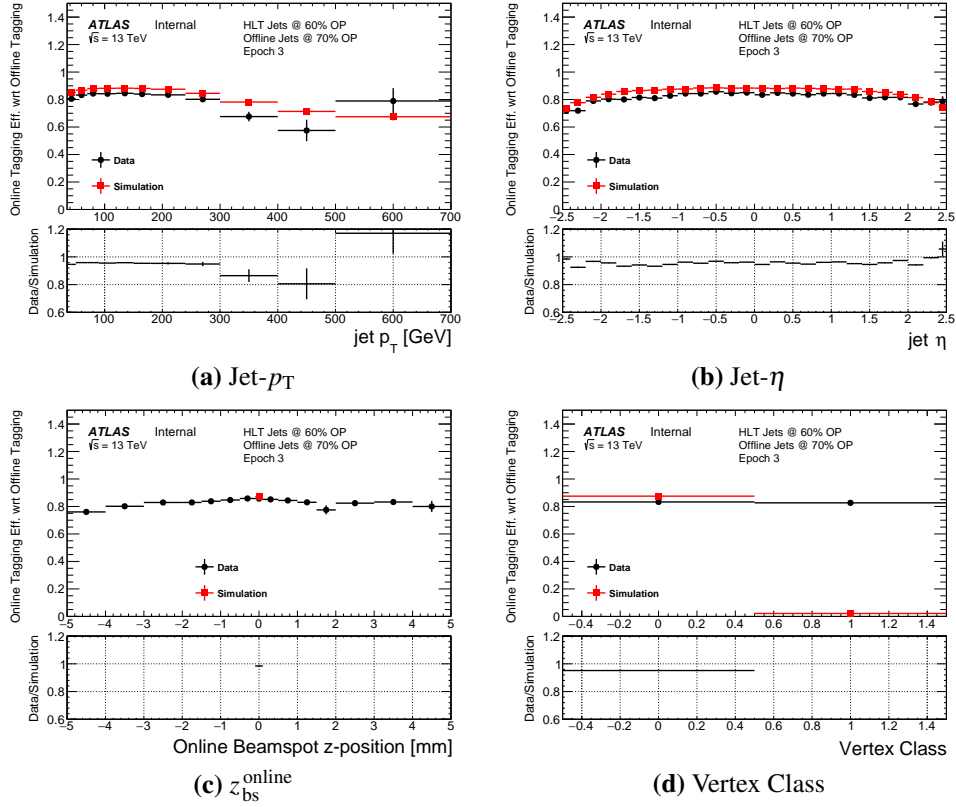


**Figure 5.8:** The 60% operating point  $b$ -jet trigger efficiency with respect to the offline 70% operating point for data from Epoch 3 (black) and simulation (red) against (a) jet- $p_T$ , (b) jet- $\eta$ , (c) online beamspot  $z$ -position and (d) vertex class. Vertex class is defined as 0 when a  $xPrmVtx$  vertex is found and 1 if not.

### 5.3.3 $b$ -Jet Trigger Aware Good Run List (GRL)

To resolve the large data-simulation discrepancies shown in the previous section, a  $b$ -jet trigger aware GRL is applied to remove events with  $|z_{bs}^{\text{online}}| > 2 \text{ mm}$  in Epoch 1 and 2, such that the events with low efficiency are removed. No such requirement is necessary for Epoch 3 due to the use of a backup primary vertex finding algorithm. To retain as much data as possible, the cut value is chosen to be the widest value of  $|z_{bs}^{\text{online}}|$  that corresponds to an efficiency not significantly reduced by the  $xPrmVtx$  algorithm performance issue. A 2 mm cut is selected using Figure 5.3(b) and Figure 5.7(b).

It was decided to use a  $b$ -jet trigger aware GRL instead of deriving a correction factor with respect to  $z_{bs}^{\text{online}}$  for the full data-set. The cost of using a  $b$ -jet trigger aware GRL is a reduction in the integrated luminosity of the data-set from  $32.9 \text{ fb}^{-1}$  to  $24.3 \text{ fb}^{-1}$ . The reasons for using a  $b$ -jet trigger aware GRL are threefold. Firstly, as there is no online beamspot position distribution in simulation, it is not clear that kinematics of events at high  $|z_{bs}^{\text{online}}|$  can be well understood and modelled; the sculpting of the efficiency with respect to

$\text{jet-}\eta$  shown in Figure 5.7(c) is an example of this. Secondly, the efficiencies are low at high beamspot  $z$ -position, so the loss in luminosity  $\times$  acceptance is relatively small. Finally, using a GRL means that the stated value of integrated luminosity is a more accurate representation of the size of the data-set.

The application of the GRL significantly improves data-simulation agreement in Epoch 1 and 2. Figure 5.9 shows that the  $b$ -jet trigger efficiency for Epoch 1 becomes approximately 90–95% of the efficiency measured in simulation. Figure 5.10 shows that the  $b$ -performance trigger efficiency measured in Epoch 2 becomes approximately 95% of the efficiency in simulation.

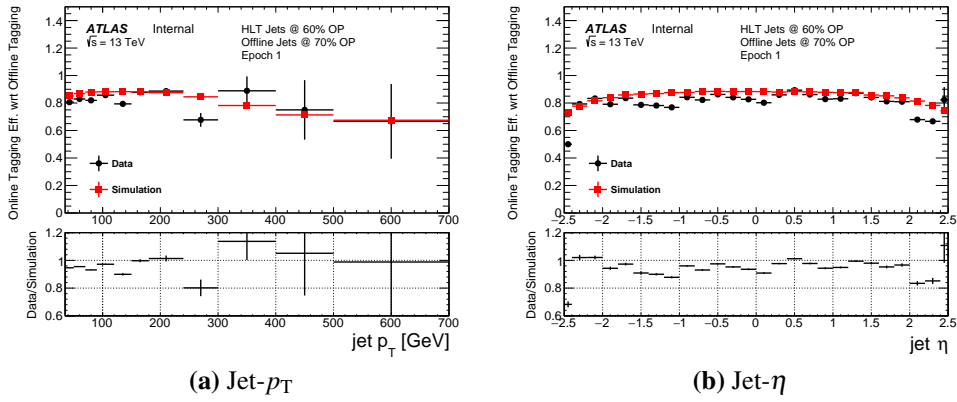


**Figure 5.9:** The 60% operating point  $b$ -jet trigger efficiency with respect to the offline 70% operating point for data from Epoch 1 (black) and simulation (red) against (a) jet- $p_T$  and (b) jet- $\eta$ . The  $b$ -jet trigger aware GRL is applied.

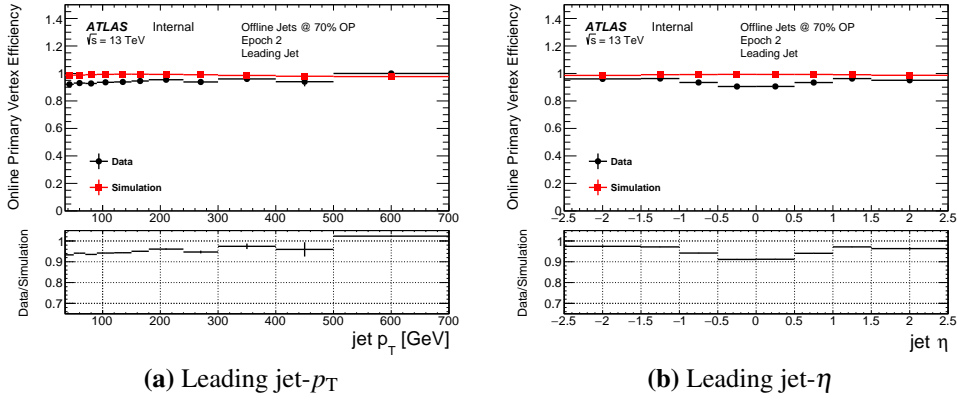


**Figure 5.10:** The online primary vertex efficiency,  $\epsilon_{\text{PV}}$ , for data from Epoch 2 (black) and simulation (red) against leading jet (a)  $p_T$  and (b)  $\eta$ . The  $b$ -jet trigger aware GRL is applied.

Figures 5.11 and 5.12 show the measured  $b$ -jet trigger efficiency and online primary vertex efficiency for the full 2016 data-set, combining Epochs 1, 2 and 3, with the  $b$ -jet trigger aware GRL applied. Data agrees with simulation within 5%. A residual kinematic

bias with respect to leading jet- $\eta$  is still present in Figure 5.12(b); a correction for this effect is derived in Section 5.3.4.2.

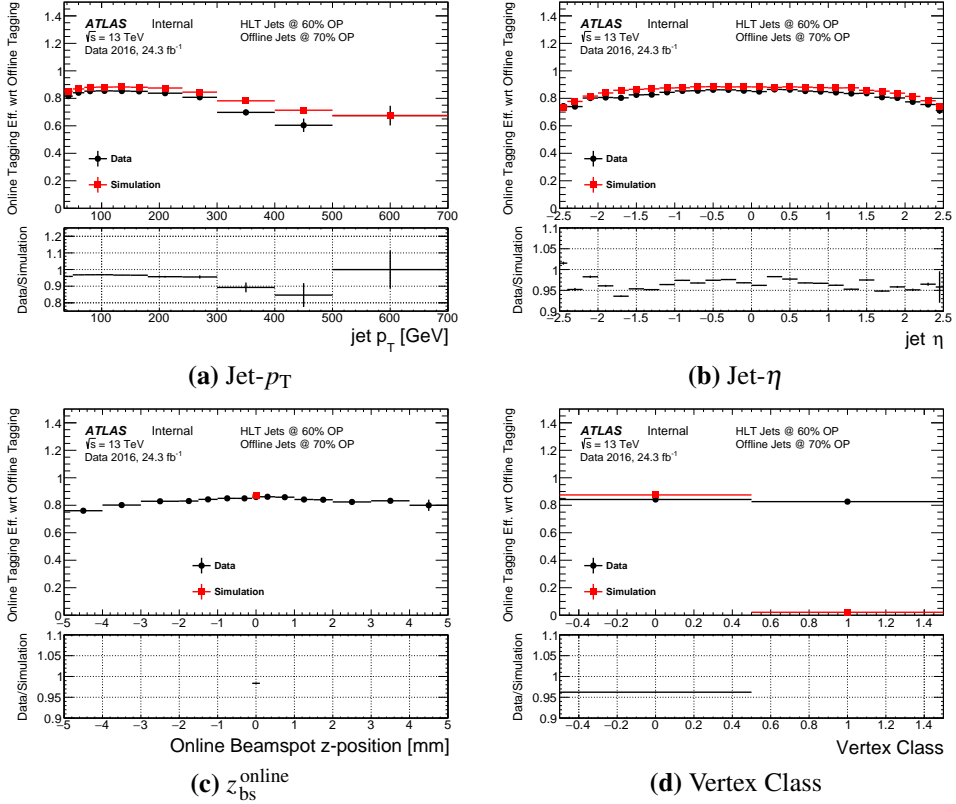


**Figure 5.11:** The 60% operating point  $b$ -jet trigger efficiency with respect to the offline 70% operating point for the full 2016 data-set (black) and simulation (red) against (a) jet- $p_T$ , (b) jet- $\eta$ , (c) online beamspot  $z$ -position and (d) vertex class. Vertex class is defined as 0 when a  $xPrmVtx$  vertex is found and 1 if not. The  $b$ -jet trigger aware GRL is applied.

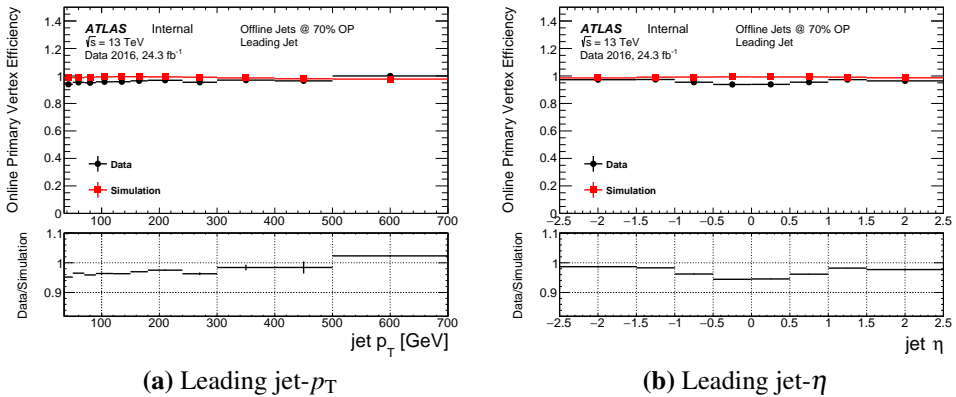


**Figure 5.12:** The online primary vertex efficiency,  $\epsilon_{PV}$ , for the full 2016 data-set (black) and simulation (red) against leading jet (a)  $p_T$  and (b)  $\eta$ . The  $b$ -jet trigger aware GRL is applied.

### 5.3.4 Efficiency Measurement Results and Associated Uncertainties

In the previous two sections it has been shown that after a  $b$ -jet trigger aware GRL is applied the  $b$ -jet trigger performance is understood and the data/simulation agreement is within 5%. The remaining data/simulation differences are corrected by applying a jet-level and an event-level data/simulation scale factor. The jet-level correction accounts for differences between data and simulation in events where a valid primary vertex is found. The event level correction accounts for events that don't contain a valid primary vertex, which have a near zero probability of passing the  $b$ -jet trigger. Jet-level and event-level efficiencies are separated such that  $b$ -jet triggers that place requirements on different multiplicities of  $b$ -jets can use the same efficiencies.

#### 5.3.4.1 Jet-Level Efficiency and Scale Factor Measurement

The jet-level correction uses the  $b$ -jet trigger efficiency,  $\varepsilon_{b\text{Trig}}$  which has been defined in Equation 5.1. The  $b$ -jet trigger efficiency is measured in data and simulation and the resulting data/simulation scale factor ( $SF_{b\text{Trig}}$ ) is applied as a jet-level correction to simulation. The  $b$ -jet trigger efficiency is measured in events where a valid primary vertex is found, either by the `xPrmVtx` algorithm or by the backup vertex algorithm used in Epoch 3.

For the jet-level efficiency measurement the statistical uncertainties of data and simulation are considered in addition to three sets of systematic uncertainties: a  $b$ -jet purity uncertainty, a non- $b$ -jet efficiency uncertainty and a high- $p_T$  extrapolation uncertainty.

##### (1) $b$ -Jet Purity Uncertainty

Despite the strict event selection there are jets that are not  $b$ -jets included in the sample of jets used. The effect of this non- $b$ -jet contamination on the measured  $b$ -jet trigger efficiency is corrected for using simulation and an uncertainty on this correction is derived.

Jets used in the denominator of the  $b$ -jet trigger efficiency are referred to as inclusive jets. The  $b$ -jet purity is defined as the fraction of inclusive jets that are true  $b$ -jets, where in simulation a jet is categorised as a true  $b$ ,  $c$  or light jet using the truth labelling scheme described in Section 4.3.1. For this measurement true  $c$  and light jets are grouped together in a single non- $b$ -jet category. The black line of Figure 5.13(a) shows the  $b$ -jet purity for inclusive jets showing that the  $b$ -jet purity is  $> 95\%$  up to jet- $p_T$  of  $\sim 300$  GeV and  $> 90\%$  for higher values of jet- $p_T$ .

An uncertainty on the modelling of  $b$ -jet purity in simulation is derived by considering systematic variations where the size of non- $b$ -jet contamination is set to zero or doubled.

To illustrate the systematic variation considered, Figure 5.13(a) shows the  $b$ -jet purity for inclusive jets and for each of the systematic variations. Wide variations are chosen as uncertainties in the modelling of both offline  $b$ -tagging and the standard model processes affects the  $b$ -jet purity.

Figure 5.13(b) shows the  $b$ -jet trigger efficiency for inclusive jets (black) and for the systematic variations (red and blue), the lower panel shows a ratio of the efficiencies for systematic variations to the efficiency for inclusive jets. Statistical uncertainties are not shown in the figure, such that one can distinguish between the systematic variations of the efficiency. The ratio of efficiency for true  $b$ -jets to that of inclusive jets (red ratio line) is applied as a correction to the final efficiency measured in data to account for the effect of non- $b$ -jet contamination. The bin-by-bin maximum fractional difference in efficiency due to systematic variations (red or blue ratio line) is taken as symmetric uncertainty.

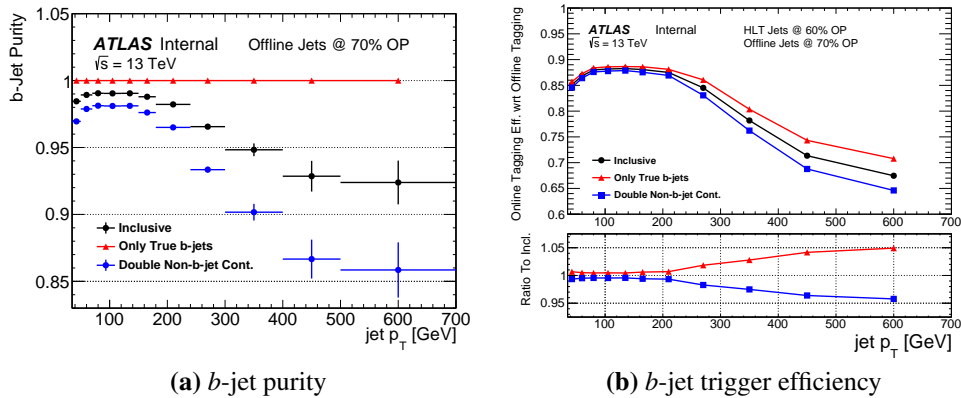


**Figure 5.13:** Panel (a) shows the  $b$ -jet purity of the sample of inclusive jets (black) used in the  $b$ -jet trigger efficiency measurement and the  $b$ -jet purity in the systematic variations of true  $b$ -jets only (red) and when non- $b$ -jet contamination is doubled (blue). Panel (b) shows the 60% operating point  $b$ -jet trigger efficiency with respect to an offline 70% operating point for inclusive jets (black) and the systematic variations of true  $b$ -jets only (red) and double non- $b$ -jet contamination (blue). The lower panel shows a ratio of the efficiencies in the systematic variations to the efficiency for inclusive jets. Statistical uncertainties are not shown in panel (b). Both panels use simulated events.

## (2) Non- $b$ -jet efficiency uncertainty

The efficiency of the  $b$ -jet trigger for non- $b$ -jets is not measured and could be mismodelled in simulation. To derive a non- $b$ -jet efficiency systematic uncertainty; up and down systematic variations are created by doubling and halving the non- $b$ -jet efficiency respectively. For the up variation, the non- $b$ -jet efficiency is limited to be no greater than the efficiency of true  $b$ -jets, which avoids unrealistic results. To illustrate the systematic variations, Figure 5.14(a) shows the  $b$ -jet trigger efficiency in simulation for non- $b$ -jets in the

nominal case and in the two systematic variations considered.

Figure 5.14(b) shows the  $b$ -jet trigger efficiency in simulation for inclusive jets in the nominal case and for the two systematic variations. Again statistical uncertainties are not shown in the figure. The maximum fractional bin-by-bin difference in efficiency for inclusive jets between the nominal and the systematic variations, as shown in the ratio plot of Figure 5.14(b), is taken as a symmetric uncertainty.

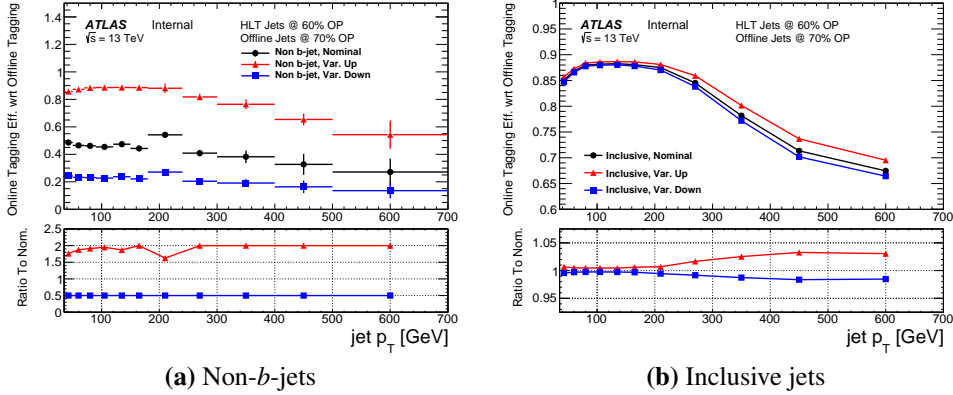


**Figure 5.14:** The 60% operating point  $b$ -jet trigger efficiency with respect to the offline 70% operating point for (a) non- $b$ -jets and (b) inclusive jets in simulated events for the nominal case (black) and the systematic variations where the non- $b$ -jet efficiency has been halved (blue) and doubled (red). The lower panel in both plots show the ratio of the efficiency of the systematic variations to the nominal efficiency. Statistical uncertainties are not shown in panel (b).

### (3) High- $p_T$ extrapolation

There is a limited number of high- $p_T$  inclusive jets in the data-set which causes large statistical fluctuations in the  $b$ -jet trigger efficiency in data, as shown in Figure 5.11(a). Therefore, the  $b$ -jet trigger efficiency shape from simulation is used to extrapolate the efficiency for jet- $p_T > 240$  GeV. This  $p_T$  range is chosen for extrapolation as in this region the data statistical uncertainty is the dominant uncertainty.

The extrapolation procedure uses three fits to produce a “corrected simulation”  $b$ -jet trigger efficiency. The three fits are:

- **Normalisation Fit:** A ‘normalised simulation’ efficiency is created by applying a normalisation factor derived by performing a single-constant fit to the ratio of the  $b$ -jet trigger efficiency in data and simulation. This accounts for the normalisation difference between the  $b$ -jet trigger efficiency in data and simulation for the full jet- $p_T$  range. The lowest  $p_T$  bin has an inconsistent data/simulation ratio compared to other low- $p_T$  bins, so is ex-

cluded from the fit<sup>9</sup>. The normalisation fit is shown in Figure 5.15(a), the uncertainty on the fit-parameter is used as a systematic uncertainty.

- **Linear Correction Fit:** A ‘*corrected simulation*’ efficiency is created by applying a linear correction factor to the normalised simulation efficiency. This correction accounts for a difference in slope between the  $b$ -jet trigger efficiency in data and simulation for the high jet- $p_T$  region. The correction is derived by performing a linear fit to the ratio of the  $b$ -jet trigger efficiency in data and the normalised simulation for jet- $p_T > 240$  GeV, as shown in Figure 5.15(b). To estimate an uncertainty on the linear correction the gradient of the fit is varied within uncertainties whilst the point at which the fit crosses 1 is kept constant. The maximum difference between the nominal fit and the systematic variations is used as a symmetric uncertainty. Figure 5.15(c) shows the  $b$ -jet trigger efficiency in data compared to the corrected simulation, in the lower panel the blue lines represent the linear correction uncertainties.
- **Quadratic Systematic Fit:** To estimate an uncertainty on the choice of the linear functional form as the correction factor, a quadratic function is used to fit the data and corrected simulation ratio as shown in Figure 5.15(d). The difference of the quadratic fit from one is considered as the functional form systematic uncertainty.

For jet- $p_T > 240$  GeV the  $b$ -jet trigger efficiency in data and thus the numerator of the data/simulation scale factors is given by the corrected simulation. The systematic uncertainty on the extrapolation is defined as the uncertainty from the normalisation fit added to the bin-by-bin maximum of the uncertainty from the linear correction fit and the uncertainty from the quadratic systematic fit. The uncertainties on the high- $p_T$  extrapolation procedure are summarised in Table 5.2.

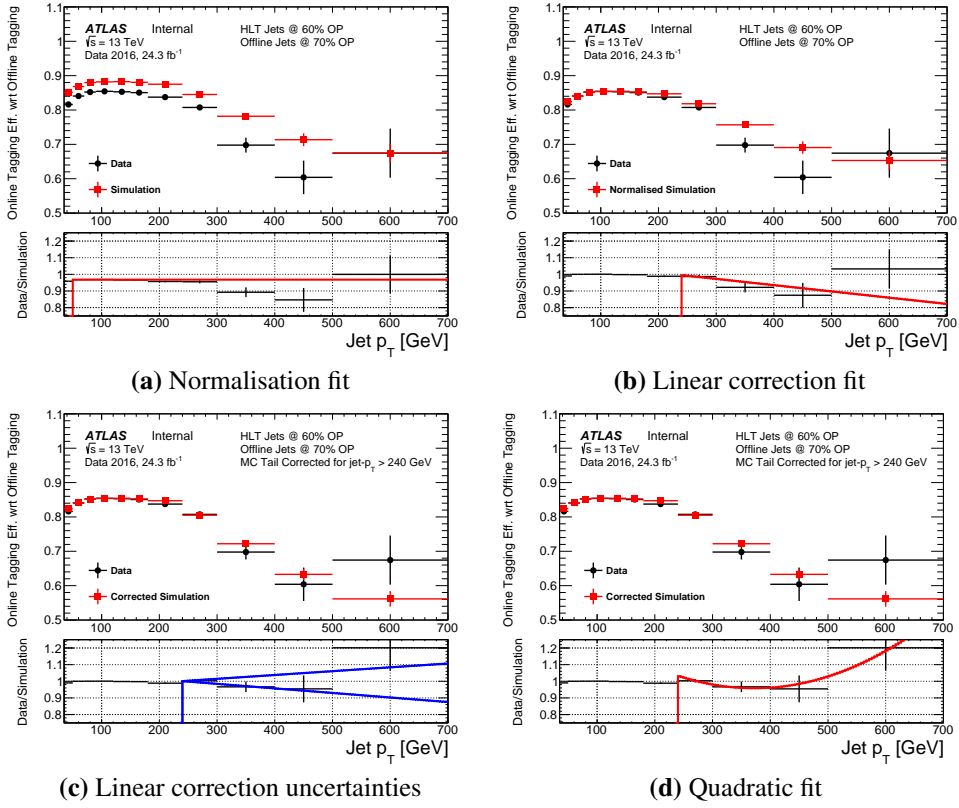
Jet $p_T$ [GeV]	MC Extrap.	Normalisation	Linear Fit	Quadratic Fit
240-300	0.8%	<0.1%	0.8%	0.3%
300-400	4.0%	<0.1%	2.9%	4.0%
400-500	5.6%	<0.1%	5.6%	1.7%
500-700	18.0%	<0.1%	9.6%	18.0%

**Table 5.2:** A table showing the systematic uncertainty assigned for the high- $p_T$  extrapolation.

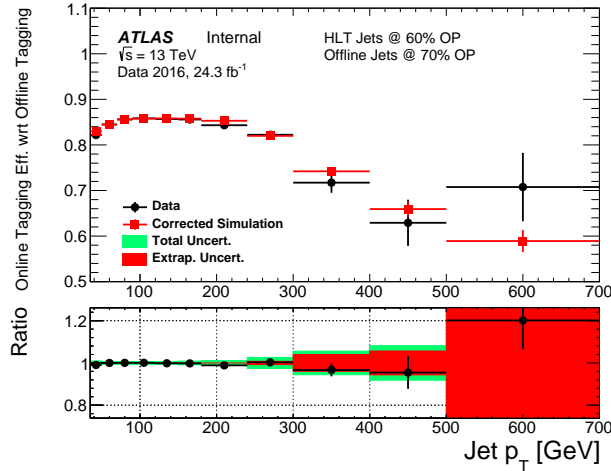
As a closure test of the high- $p_T$  extrapolation procedure, Figure 5.16 shows the  $b$ -jet trigger efficiency in data and corrected simulation, the lower panel shows the ratio with extrapolation and total uncertainties overlaid. For jet- $p_T > 240$  GeV, the data and corrected simulation are consistent within the extrapolation uncertainties.

---

<sup>9</sup> The discrepancy is shown below in Table 5.3. The difference is within purity uncertainties.

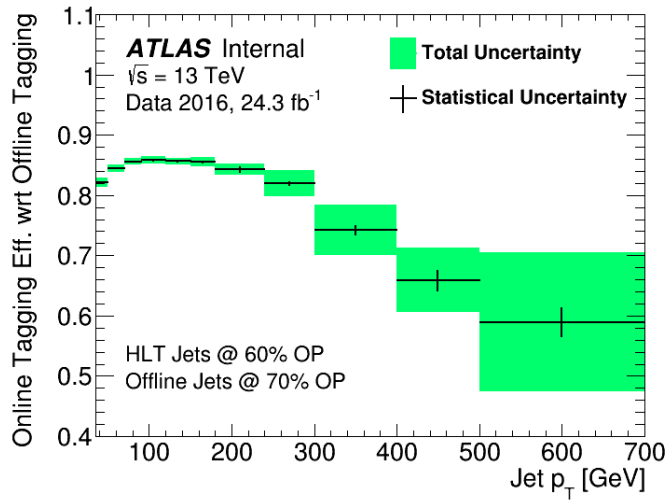
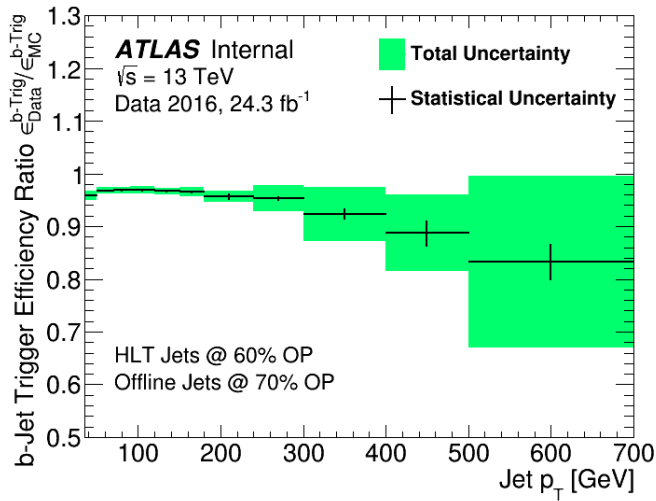


**Figure 5.15:** A figure to demonstrate the stages of the high- $p_T$  extrapolation procedure for the 60% operating point  $b$ -jet trigger efficiency with respect to the offline 70% operating point. The  $b$ -jet trigger efficiency as a function of jet- $p_T$  is shown for data (black) and simulation after corrections have been applied (red); the corrections used are labelled and are described in the text. Panel (a) shows the normalisation fit, panel (b) shows the linear correction fit, panel (c) shows linear correction uncertainties (blue lines) and panel (d) shows the quadratic fit.



**Figure 5.16:** The 60% operating point  $b$ -jet trigger efficiency with respect to the offline 70% operating point as measured in data (black) and the corrected simulation (red) as a function of offline jet- $p_T$ . In the ratio plot in the lower panel the extrapolation uncertainties (red band) and total uncertainty (green band) are overlaid.

The raw measurements of the  $b$ -jet trigger efficiency from Figure 5.11 and the additional corrections and systematic uncertainties described above can be brought together. In Figure 5.11(b) it is shown that, whilst efficiency does depend on jet- $\eta$ , the data to simulation ratio is flat with respect to jet- $\eta$ . Therefore the  $b$ -jet trigger efficiency and data/simulation scale factors are derived as a function of jet- $p_T$  only. The jet-level  $b$ -jet trigger efficiency measurement is shown in Figure 5.17(a), the jet-level data/simulation scale factors are shown in Figure 5.17(b).

(a)  $b$ -jet trigger efficiency measured in data

(b) Data/simulation scale factor

**Figure 5.17:** (a) The measured 60% operating point  $b$ -jet trigger efficiency with respect to the offline 70% operating point and (b) the associated data/simulation scale factors as a function of offline jet- $p_T$ . The central values and statistical uncertainties are shown in black and the green bands represent the total uncertainty.

Table 5.3 summarises the uncertainties on the jet-level data/simulation scale factor. Purity, non- $b$ -jet efficiency and simulation statistical uncertainties are considered for the full  $p_T$  range. The statistical uncertainty of data is considered for jet- $p_T < 240$  GeV whilst the high- $p_T$  extrapolation uncertainty is applied for jet- $p_T > 240$  GeV. The  $b$ -jet purity and non- $b$ -jet efficiency uncertainties dominate for jet- $p_T < 300$  GeV and the high- $p_T$  extrapolation uncertainty dominates for jet- $p_T > 300$  GeV.

Jet $p_T$ [GeV]	Scale Factor	Total Uncertainty	Sources of Uncertainty			
			Stat.	Extrap.	Purity	Non- $b$ Trig. Eff.
35-50	95.9%	1.0%	0.1%	-	0.7%	0.7%
50-70	96.8%	0.7%	0.1%	-	0.5%	0.5%
70-90	96.9%	0.6%	0.1%	-	0.5%	0.5%
90-120	96.9%	0.7%	0.1%	-	0.5%	0.5%
120-150	96.7%	0.6%	0.2%	-	0.4%	0.4%
150-180	96.6%	0.9%	0.2%	-	0.6%	0.6%
180-240	95.7%	1.1%	0.5%	-	0.7%	0.7%
240-300	95.3%	2.6%	0.4%	0.8%	1.8%	1.7%
300-400	92.4%	5.6%	1.1%	4.0%	2.8%	2.5%
400-500	88.8%	8.1%	2.6%	5.6%	4.2%	3.3%
500-700	83.4%	19.4%	4.0%	18.0%	4.9%	3.1%

**Table 5.3:** The jet-level  $b$ -jet trigger efficiency data/simulation scale factors as a function of jet- $p_T$  with total uncertainty and the contributions from the different sources of uncertainty considered; specifically statistical, high- $p_T$  extrapolation,  $b$ -jet purity and non- $b$ -jet trigger efficiency.

Although only the 70% offline operating point has been shown in this section, jet-level efficiencies and uncertainties are calculated for all combinations of online and offline operating points. Table 5.4 shows a comparison of the jet level uncertainties for the 60% online operating point with respect to the 70%, 77% and 85% offline operating point. For looser offline operating points the uncertainty becomes larger, due to increased non- $b$ -jet contamination.

Jet $p_T$ [GeV]	Total Uncertainty for Offline OP		
	70% OP	77% OP	85% OP
35-50	1.0%	2.3%	6.2%
50-70	0.7%	1.6%	4.6%
70-90	0.6%	1.3%	3.7%
90-120	0.7%	1.3%	3.7%
120-150	0.6%	1.4%	3.7%
150-180	0.9%	1.8%	4.6%
180-240	1.1%	2.6%	6.4%
240-300	2.6%	4.4%	10.2%
300-400	5.6%	7.5%	17.6%
400-500	8.1%	10.9%	22.2%
500-700	19.4%	19.0%	36.6%

**Table 5.4:** A comparison of the uncertainty on the jet-level  $b$ -jet trigger efficiency for the 60% online operating point with respect to the various offline operating points (OP). The increase in uncertainty for looser offline operating points is caused by larger non- $b$ -jet contamination.

### 5.3.4.2 Event-Level Efficiency and Uncertainties

The online primary vertex efficiency,  $\epsilon_{\text{PV}}$ , is defined as the efficiency that there is a valid primary vertex in an event. If a valid primary vertex is not found, the probability that the event will pass the  $b$ -jet trigger is effectively zero<sup>10</sup>. Figure 5.12 shows that the online primary vertex efficiency after the  $b$ -jet trigger aware GRL is applied is flat with respect to leading jet- $p_T$  and has kinematic bias with respect to leading jet- $\eta$ .

To correct for the kinematic bias the online primary vertex efficiency is measured in data as a function of leading jet- $\eta$  and is applied as a correction to simulation. As the online primary vertex efficiency is one in simulation, the data/simulation scale factor and efficiency measured in data are identical.

The online primary vertex efficiency is measured using a different technique in each epoch. In Epoch 1 it is the number of events with vertex class = 0 divided by the number of events. In Epoch 2 it is defined as the number of events that pass a single muon  $b$ -performance trigger divided by the number that pass the equivalent single muon trigger<sup>11</sup>. In Epoch 3 online primary vertex efficiency is one, as the back-up vertex finding algorithm will always find a vertex. The online primary vertex efficiency is measured in each of the three regions separately and is then combined using a luminosity weighted average.

The uncertainty of the online primary vertex efficiency is the combination of the stat-

---

<sup>10</sup> Specifically it is exactly zero in Epoch 2 and very close to zero in Epoch 1.

<sup>11</sup> Specifically  $\epsilon_{\text{PV}} = \text{Number of events that pass } HLT\_mu26\_imed\_2j35\_boffperf\_split \text{ divided by the number that pass } HLT\_mu26\_imed}$ .

istical uncertainties from data and simulation and a shape systematic uncertainty. The shape systematic uncertainty accounts for possible variations in the shape of the online primary vertex efficiency with respect to jet- $\eta$ . It is defined as half of the difference between the maximum efficiency and the minimum efficiency in any jet- $\eta$  bin; such that the uncertainty covers the case where the online primary vertex efficiency is flat with respect to jet- $\eta$  and the case where the bias is twice as large as observed.

Figure 5.18 and Table 5.5 show the event-level efficiency and the associated systematic uncertainties. The uncertainty is dominated by the shape systematic uncertainty.

The  $b$ -jet trigger aware GRL and  $b$ -jet trigger efficiencies presented in this section are used by all analyses at ATLAS utilising the  $b$ -jet trigger in 2016 data as recommended by the ATLAS  $b$ -jet trigger group.

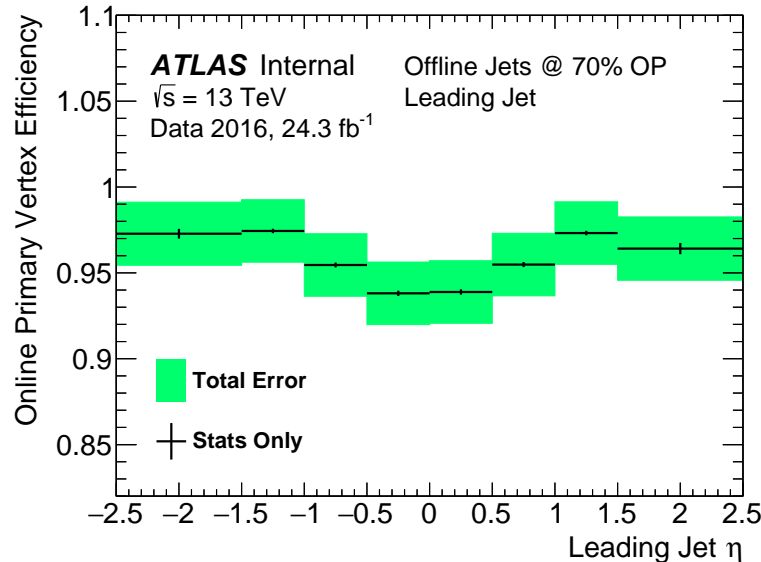


**Figure 5.18:** The measured online primary vertex efficiency as a function of offline leading jet- $\eta$ . The central values and statistical uncertainties are shown in black and the green bands represent the total uncertainty.

Leading Jet $\eta$	Event-level Efficiency	Total Uncertainty	Sources of Uncertainty		
			Data Stat.	MC Stat.	Shape Syst.
-2.5–1.5	97.3%	1.9%	0.3%	0.1%	1.9%
-1.5–1.0	97.4%	1.9%	0.1%	0.0%	1.9%
-1.0–0.5	95.5%	1.9%	0.1%	0.0%	1.9%
-0.5–0.0	93.8%	1.9%	0.2%	0.0%	1.9%
0.0–0.5	93.9%	1.9%	0.2%	0.0%	1.9%
0.5–1.0	95.5%	1.9%	0.2%	0.0%	1.9%
1.0–1.5	97.3%	1.9%	0.1%	0.0%	1.9%
1.5–2.5	96.4%	1.9%	0.3%	0.1%	1.9%

**Table 5.5:** A table showing the event-level online primary vertex efficiency as a function of leading jet- $\eta$  with total uncertainty and the contributions from the different sources of uncertainty considered.

## Chapter 6

# Di-*b*-Jet Search: Analysis Introduction

In Chapter 2 it was shown that many Beyond Standard Model theories predict new particles decaying to one or two *b*-quarks that could be produced by the LHC. Chapters 3, 4 and 5 described the detectors and reconstruction techniques used to observe such events in the ATLAS detector. Hence the motivation and tools required to perform a search for resonances decaying to one or two *b*-jets has been outlined. Such analyses are known as di-*b*-jet searches.

This thesis will present two di-*b*-jet searches performed at the ATLAS detector using a high-mass data-set and a low-mass data-set. As the analysis structure for both di-*b*-jet searches is similar the analyses are presented together in Chapters 6, 7, 8 and 9.

This chapter is organised as follows: Section 6.1 contains an outline of the analysis strategy and describes how the analysis will be presented within this thesis, Section 6.2 outlines the data-sets used in the two di-*b*-jets searches and Section 6.3 will describe the backgrounds and benchmark signal models considered.

### 6.1 Analysis Outline

The strategy used for both di-*b*-jet searches can be split up into three parts, which form the three proceeding chapters. A brief outline of the parts is given here, and full detail can be found in the relevant chapter.

- **Di-*b*-Jet Event Selection:** (*Chapter 7*)

The first step is to select events that are consistent with a resonance decaying to one or two *b*-quarks in a way such that the number of background events is minimised. Briefly, two high-momentum jets are required and two *b*-tag categories are considered; a category

in which both jets have been  $b$ -tagged (2  $b$ -tag) and a category where at least one jet has been  $b$ -tagged ( $\geq 1$   $b$ -tag). Chapter 7 will provide details on the event selection used in the two di- $b$ -jet searches.

- **Search Phase:** (*Chapter 8*)

Once events have been selected the next part of the analysis aims to determine if there is evidence of a new particle in the selected events; this step is known as the ‘search phase’. This step uses the dijet mass ( $m_{jj}$ ) spectrum, where dijet mass is the invariant mass of the two highest  $p_T$  jets; note that the two highest  $p_T$  jets are selected before  $b$ -tagging is applied. A new particle will appear as a resonance (or ‘bump’) on the smoothly falling background dijet mass distribution from QCD dijet production, as illustrated in Figure 6.1. The background is modelled using a smoothly falling function and a model-independent search for resonances is performed using the BUMPHUNTER algorithm [97]. Chapter 8 contains a full description of the search phase strategy and the results of the search phase for both di- $b$ -jet searches, including studies that validate the background estimation strategy used.

It is useful to note that as part of the search phase validation studies, it is shown that some regions of phase space cannot be adequately described by the background estimation strategy. As a result, the validation studies shown in Chapter 8 have an impact on the event selection used in Chapter 7, this will be clearly noted in the text.

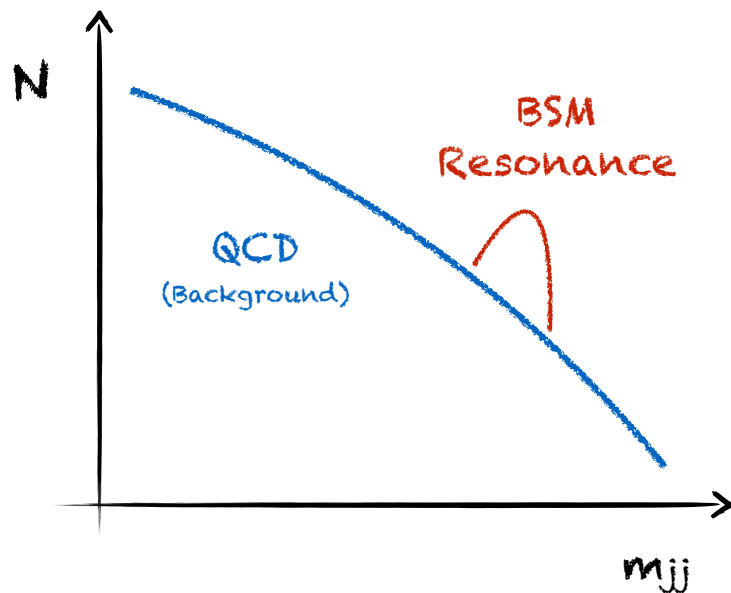


**Figure 6.1:** A cartoon illustrating the use of the dijet mass ( $m_{jj}$ ) distribution in the search phase of a di- $b$ -jet search. Shown is the smoothly falling distribution from QCD dijet production and a resonance shape caused by a Beyond Standard Model (BSM) particle.

- **Limit Setting:** (*Chapter 9*)

If, in the search phase of the analysis, no significant evidence of a resonance is found then 95% credibility level limits are set on the cross-section of the benchmark signal models as a function of mass. Chapter 9 presents the limit setting methodology, a description of the systematic uncertainties and the limit setting results for both di-*b*-jet searches.

## 6.2 List of Data-Sets Used

Di-*b*-jet searches are performed in several iterations as data is being collected, where each iteration uses a different data-set. This is done for two reasons; firstly it is important to know as soon as possible if there is evidence of a new resonance as this would affect the strategy of future di-*b*-jet searches and that of other analyses at ATLAS. Secondly, this allows us to incrementally expand, adapt and improve the analysis in each iteration.

In this thesis two different data-sets are considered; one for a high-mass di-*b*-jet search and one for a low-mass di-*b*-jet search. The overall analysis strategy is the same for each data-set so the analyses are described together. However, there are some significant differences in the details; as such during the analysis description it will be clearly labelled which data-set is being referred to.

For each data-set considered in this analysis a Good Run List (GRL) is applied to remove events of low data quality; a further discussion of GRLs is found in Section 5.3.1.

The data-sets are listed below, the trigger used in each data-set is described. All quoted luminosities are given after the GRL has been applied.

- ***Summer16\_HighMass*:**

The *Summer16\_HighMass* data-set contains 13 TeV  $pp$  collision data collected between May 2015 and July 2016 corresponding to an integrated luminosity  $13.3\text{ fb}^{-1}$ . The trigger used in this data-set is `HLT_j380`, which requires an online<sup>1</sup> jet with  $p_T > 380\text{ GeV}$ , and is chosen as it is the lowest unprescaled single jet trigger<sup>2</sup>. Section 5.1 contains further details on single jet triggers. The analysis on this data-set has been published as a conference note [10].

---

<sup>1</sup> Online refers to reconstructed objects used in the trigger decision whilst offline refers to objects reconstructed after events have passed the trigger at the data-processing level, from the definition in Section 5.3.

<sup>2</sup> Unprescaled means that the trigger accepts every event passing the trigger selection criteria.

- ***Full16\_LowMass*:**

The *Full16\_LowMass* data-set contains 13 TeV  $pp$  collision data collected between March 2016 and December 2016, corresponding to an integrated luminosity of  $24.3 \text{ fb}^{-1}$ . The trigger used in this data-set is a double  $b$ -jet trigger which requires two online jets with  $p_T > 150 \text{ GeV}$  and  $p_T > 50 \text{ GeV}$  where both online jets have been  $b$ -tagged at the 60% operating point. Section 5.2 contains further details of  $b$ -jet triggers and the particular trigger used in this analysis. The *Full16\_LowMass* data-set uses a  $b$ -jet trigger as the lower  $p_T$  thresholds allow the analysis to probe a lower range of dijet mass. This analysis does not combine data collected in 2015 and 2016, as the  $b$ -jet trigger configurations used in 2015 and 2016 are significantly different. The *Full16\_LowMass* data-set uses a  $b$ -jet trigger aware GRL which additionally removes periods of data where the  $b$ -jet trigger was performing in a sub-optimal way; the  $b$ -jet trigger aware GRL is described in Section 5.3.3. As a double  $b$ -jet trigger is used only the 2  $b$ -tag category is considered. The analysis on this data-set has been submitted to Phys. Rev. D. [11].

In addition there is another relevant data-set being analysed that is not described in this thesis.

- ***Full16\_HighMass*:**

The *Full16\_HighMass* data-set contains 13 TeV  $pp$  collision data collected between May 2015 and December 2016, corresponding to an integrated luminosity of  $36.1 \text{ fb}^{-1}$ . A single jet trigger is used. The analysis on this data-set has been submitted together with the *Full16\_LowMass* data-set analysis to Phys. Rev. D. [11]. This analysis is not presented in this thesis. However, as this analysis has been submitted together with the *Full16\_LowMass* data-set, some analysis decisions in the *Full16\_LowMass* data-set analysis are affected by the *Full16\_HighMass* data-set analysis.

### 6.3 Background and Signals

In the di- $b$ -jet analyses two benchmark signal models and one dominant background are considered. The background and signal models are used in optimisation and validation studies for the event selection and search phase of the analyses (presented in Chapters 7 and 8 respectively). The signal models are also used in the limit setting phase presented in Chapter 9.

Monte-Carlo simulations of the considered background and signal processes are produced. Unless specified, all Monte-Carlo simulations are produced using the PYTHIA8 [98] program for event generation, the EVTGEN package [95] to model the decays of the  $b$  and  $c$  hadrons, and the A14 parameter set [99] to model the parton shower, hadronisation and un-

derlying event. The NNPDF23LO PDF set [100] is used to describe the Parton Distribution Function (PDF) and the detector response is modelled using the ATLAS detector simulation package [101].

- **Background: QCD Dijet Production:**

Section 2.2 discussed the details of QCD dijet production. In particular in Section 2.2.3.3 it was noted that the relative strength of the strong force compared to other forces of the Standard Model means that QCD dijet production dominates all other backgrounds in a di- $b$ -jet event selection. A simulated QCD dijet sample is also used in this analysis for background studies and background modelling validation.

Before describing the signal models used it is useful to clearly differentiate between the two definitions of mass used in this analysis. The ‘*dijet mass*’ is the invariant mass of the two leading jets, and is denoted by  $m_{jj}$ . The ‘*generated mass*’ is defined as the pole mass of the signal model used in the generator. The two differ due to uncertainties in jet energy measurements.

- **Signal:  $Z'$  Boson:**

The  $Z'$  boson is an additional gauge boson that can decay to two  $b$ -quarks. The  $Z'$  boson models considered are described in detail in Section 2.3.2.1. The  $Z'$  boson provides a benchmark model in the 2  $b$ -tag category.

In the *Summer16\_HighMass* and *Full16\_LowMass* data-set analyses the Sequential Standard Model (SSM)  $Z'$  and the leptophobic  $Z'$  models are considered. The intrinsic width of the  $Z'$  boson has been set to 3% of the generated mass; this width is chosen as it is not significantly larger than the dijet mass resolution, which ranges from 3% at 1.5 TeV to 2% at 5 TeV [2], and as such the model is narrow enough to produce a signal distinguishable from the background. Monte-Carlo simulation is used to produce dijet mass signal templates at leading order (LO). Only decays to  $b\bar{b}$  are simulated; other decays of the  $Z'$  boson are ignored such that the results are easier to interpret for other signal models decaying to pairs of  $b$ -quarks. It has been shown that for a  $Z'$  boson model the cross-sections can increase by up to 30% from the addition of next-to-leading order (NLO) diagrams [102]. Therefore the signal template normalisation is corrected to account for NLO effects, the correction factors have been derived by comparing the LO and NLO matrix calculations performed using the MADGRAPH generator [103] and are found to be between 1.2 and 1.3 depending on the generated mass. Simulated SSM and leptophobic  $Z'$  boson templates are produced at generated mass points of 600, 800, 1000, 1250, 1500, 1750, 2000, 2500, 3000, 4000 and 5000 GeV.

Further to this, for the *Full16\_LowMass* data-set the Dark Matter inspired (DM)  $Z'$  boson is also considered. For this model the DM  $Z'$  boson signal generation is performed at next-to-leading order using the `MADGRAPH5_AMC@NLO` generator [104], whilst all other aspects of event modelling, including parton shower and hadronisation, are performed using the configuration with `PYTHIA8` as described above. The coupling of the DM  $Z'$  boson to the dark matter fermion ( $g_\chi$ ) is set to 1 and the mass of the dark matter fermion ( $m_\chi$ ) is set to 10 TeV, the large value of  $m_\chi$  means that decays of the  $Z'$  boson to the dark matter fermion are suppressed. The coupling to quarks ( $g_{SM}$ ) is set to 0.1, decays to  $b$ ,  $c$  and light flavour quarks are considered, and the generated mass points are 600, 800 and 1000 GeV. This configuration is chosen to be consistent with recommendations in [41] and to be consistent with other dijet searches at ATLAS [2].

- **Signal:  $b^*$  Quark:**

The  $b^*$  quark is a third generation excited quark which results from quark compositeness models. The dominant decay mode of the  $b^*$  quark is to  $bg$ . The model considered is described in detail in Section 2.3.2.2. The  $b^*$  quark provides a benchmark model in the  $\geq 1$   $b$ -tag category.

For the *Summer16\_HighMass* data-set the same  $b^*$  quark model is considered. Monte-Carlo simulation is used to produce a  $b^*$  quark dijet mass signal template. Only leading order calculations are considered. Decays to  $bg$ ,  $b\gamma$ ,  $bZ_0$  and  $tW^-$  are considered<sup>3</sup>. Simulated  $b^*$  quark signal templates are produced at generated mass points of 1250, 1500, 1750, 2000, 2500, 3000, 4000 and 5000 GeV. In the *Full16\_LowMass* data-set the  $b^*$  quark model is not considered as only the 2  $b$ -tag category is used.

---

<sup>3</sup> Using the branching ratios described in Section 2.3.2.2.

## Chapter 7

# Di-*b*-Jet Search: Event Selection

Event selection is the first part of the di-*b*-jet analysis strategy. The aim of the event selection is to select events that are consistent with a BSM particle decaying to one or two *b*-quarks whilst minimising the number of background events selected, such that the sensitivity of the di-*b*-jet search to a new resonance is maximised.

The event selection of the di-*b*-jet analyses is designed with two specific objectives. Firstly, the event selection is constructed to maximise sensitivity to signal; in the event selection optimisation studies shown in this chapter the sensitivity is approximated in terms of  $S/\sqrt{B}$ , where  $S$  is the number of benchmark signal events and  $B$  is the number of background events. Secondly, the smoothly falling nature of the background needs to be maintained as this is the underlying assumption of the background estimation strategy, which will be described in Chapter 8. Here, smooth means that the spectrum is monotonically decreasing with no discontinuities.

The di-*b*-jet event selection is split up into three parts, with each part described in a separate section. Firstly, a pair of jets are selected (Section 7.1), then a set of event-level kinematic cuts are applied using the selected jets (Section 7.2) and finally *b*-tagging is applied to the jets (Section 7.3). In Section 7.4 the full event selection is summarised and the signal acceptance is evaluated.

The event selection is different for the two data-sets considered, these differences will be noted and discussed in the text.

## 7.1 Jet Selection

Jets are reconstructed using the anti- $k_T$  algorithm [69] with  $R = 0.4$  and calibrated using the EM+JES scheme; a full description of jets used in this analysis is in Section 4.2.

At least two jets are required in an event. The two highest  $p_T$  jets, referred to as the leading and subleading jet, are the jets used throughout this analysis. To reduce the number of fake jets from sources such as calorimeter noise both jets are required to pass *loose* jet cleaning cuts based on the properties and distributions of the energy deposits in the calorimeter associated to the jet; details can be found in [105].

Requirements are placed on the leading and subleading jet- $p_T$  such that events are on the trigger plateau; the kinematic region where all events that pass the offline jet- $p_T$  requirements also pass the online jet- $p_T$  requirements of the trigger. To be on the trigger plateau of a single jet trigger the offline jet- $p_T$  must be above some threshold value, which is referred to as the threshold jet- $p_T$ .

For the *Summer16\_HighMass* data-set; it is required that the leading jet has  $p_T > 430$  GeV to be on the trigger plateau of HLT\_j380. This cut is derived by comparing the leading jet- $p_T$  distributions of jets that pass the trigger, HLT\_j380, relative to a reference trigger with a lower jet- $p_T$  threshold, L1\_J75. Figure 7.1(a) shows the leading jet- $p_T$  of events that pass the single jet triggers HLT\_j360 (red), HLT\_j380 (green) and HLT\_j400 (blue) compared to events that pass the reference trigger L1\_J75 (black), in one run of data where L1\_J75 is unprescaled. In the ratio it is shown that for leading jet- $p_T > 430$  GeV events are on the trigger plateau of HLT\_j380. The subleading jet is

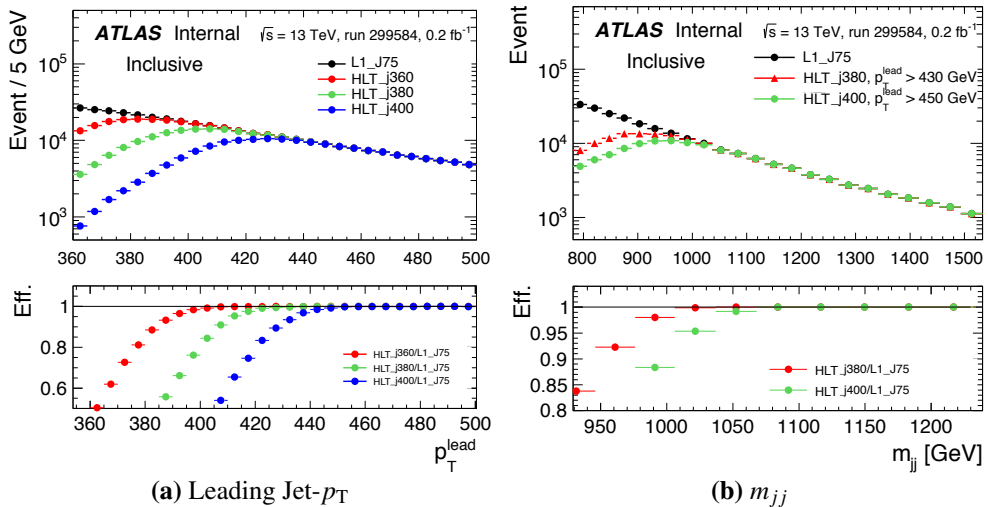


**Figure 7.1:** The distributions of (a) leading jet- $p_T$  ( $p_T^{\text{lead}}$ ) and (b) dijet mass ( $m_{jj}$ ) of events that pass an unprescaled L1\_J75 trigger (black) compared to events that pass a range of single-jet triggers (coloured) in one run of 2016 data. As shown in the legend, the single-jet triggers considered are HLT\_j380, HLT\_j400 and, in plot (a), HLT\_j360. In plot (b) the *Summer16\_HighMass* event selection (excluding  $b$ -tagging) is applied with a leading jet- $p_T$  cut as described in the legend. The ratio with respect to L1\_J75 is shown in the lower panel [10].

required to have jet- $p_T > 60$  GeV to reduce contamination from pile-up jets<sup>1</sup>. Both jets are required to have  $|\eta| < 2.4$  such that the jets lie within the volume of the ATLAS pixel detector, which is essential for optimal  $b$ -tagging performance.

For the *Full16\_LowMass* data-set a double  $b$ -jet trigger is used; which requires that there is one online jet with  $p_T > 150$  GeV and another online jet with  $p_T > 50$  GeV. Therefore, to be on the trigger plateau the leading jet- $p_T$  is required to be above the threshold jet- $p_T$  of a single jet trigger that requires an online jet with  $p_T > 150$  GeV and the subleading jet- $p_T$  is required to be above the threshold jet- $p_T$  of a single jet trigger that requires online jet- $p_T > 50$  GeV. To find the threshold jet- $p_T$  of the two single-jet triggers, a linear fit to the threshold jet- $p_T$  of a range of single jet triggers is used, details are in Appendix B. Using the results of the linear fit the leading jet is required to have  $p_T > 200$  GeV and the subleading jet is required to have  $p_T > 80$  GeV. Both jets are required to have  $|\eta| < 2.0$ ; the tighter cut on  $|\eta|$  (relative to the *Summer16\_HighMass* data-set) is selected as the  $b$ -jet energy scale uncertainty is significantly increased at large values of jet- $|\eta|$ .

## 7.2 Event-Level Selection

The next part of the event selection is a set of event-level requirements using the two selected jets. Firstly, the primary vertex must have at least two tracks associated with it to ensure good primary vertex reconstruction,

Secondly, there is a cut applied to the variable  $y^*$ , defined as

$$y^* = \frac{(y_1 - y_2)}{2} \quad (7.1)$$

where  $y_1$  and  $y_2$  are the rapidities of the leading and subleading jet respectively. As discussed in Section 2.2.3.3, QCD dijet production can occur through  $t$ -channel processes leading to more background events at large values of  $|y^*|$ , whilst signal production occurs only through  $s$ -channel processes so will have no dependence on  $y^*$ . Therefore, requiring that  $|y^*|$  is below some threshold value will lead to increased sensitivity.

For both the *Summer16\_HighMass* and *Full16\_LowMass* data-sets it is required that  $|y^*| < 0.6$ . This value has been shown to maximise  $S/\sqrt{B}$  when no  $b$ -tagging is applied in previous inclusive dijet searches at ATLAS [2]<sup>2</sup>, where  $S$  is the number of benchmark signal events and  $B$  is the number of background events. The effect of  $b$ -tagging on the

<sup>1</sup>Specifically, if jets have  $p_T < 60$  GeV then it is recommended that a pile-up suppression algorithm known as Jet Vertex Tagger (JVT) is used [106]. There is little gain in acceptance from the addition of low  $p_T$  subleading jets and complications from implementing the recommendations so the jets are removed.

<sup>2</sup>Inclusive dijet analysis means a dijet analysis where no  $b$ -tagging is applied.

optimal value of this cut is assumed to be small, as  $t$ -channel processes still dominate the background.

The dijet mass,  $m_{jj}$ , is required to be above a threshold value to ensure that two conditions are met. Firstly it is required that there is no kinematic bias on the dijet mass distribution caused by the trigger or jet- $p_T$  requirements described in Section 7.1. Secondly, it is also required that the background is smooth in the dijet mass region chosen such that it can be described using our background modelling strategy.

In the *Summer16\_HighMass* data-set it is required that  $m_{jj} > 1378$  GeV; which ensures the two conditions listed above are met. Firstly, Figure 7.1(b) shows the dijet mass spectra for events that pass the trigger `HLT_j380` and the *Summer16\_HighMass* jet- $p_T$  requirements compared to events that pass a reference trigger, `L1_J75`, in one run of data where `L1_J75` is unprescaled. For both spectra events are required to pass the jet- $|\eta|$  and  $|y^*|$  requirements of the *Summer16\_HighMass* event selection. The ratio plot demonstrates that for  $m_{jj} > 1100$  GeV there is no kinematic bias from the trigger or event selection. Secondly, it has been shown using simulated events that  $m_{jj} > 1378$  GeV is required such that the dijet mass distribution from QCD dijet production can be described by our background modelling strategy; this study is presented in Section 8.4.2. Hence,  $m_{jj} > 1378$  GeV is the loosest cut that meets both of the conditions.

For the *Full16\_LowMass* data-set it is found that for  $m_{jj} > 500$  GeV there is no kinematic bias from the jet- $p_T$  cuts used in the *Full16\_LowMass* data-set event selection. Figure 7.2 compares the dijet mass distribution of events that pass the event selection requirements that the leading (subleading) jet- $p_T > 200$  (80) GeV, labelled as ‘analysis cuts’, compared to events that pass lower requirements that the leading (subleading) jet- $p_T > 150$  (50) GeV, labelled as ‘low cuts’. Events are required to pass the `L1_J75` trigger and are taken from a run of 2016 data where `L1_J75` was unprescaled. The events are additionally required to pass the jet- $|\eta|$  and  $|y^*|$  requirements of the *Full16\_LowMass* data-set event selection. For  $m_{jj} > 500$  GeV there is no kinematic bias from the *Full16\_LowMass* event selection, this includes a one dijet mass bin buffer that is used as a safety measure.

However, for the *Full16\_LowMass* data-set there is an additional kinematic bias on dijet mass due to the effect of jets other than the leading or subleading jet that was discovered as the analysis progressed. To account for this effect it is required that  $m_{jj} > 566$  GeV. The studies showing this effect are described below in Section 7.3.1 as the  $b$ -tagging selections used in the *Full16\_LowMass* event selection must be introduced first.

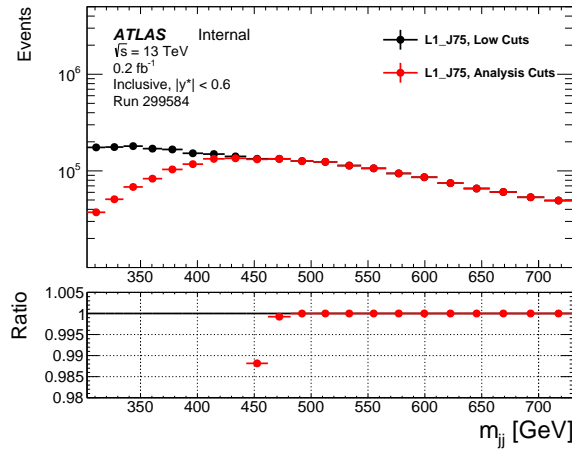


**Figure 7.2:** The dijet mass ( $m_{jj}$ ) spectra of events that pass the analysis jet- $p_T$  cuts of leading (subleading) jet- $p_T > 200$  (80) GeV (red) compared to events that pass a set of low jet- $p_T$  cuts of leading (subleading) jet- $p_T > 150$  (50) GeV (black). The events are required to pass the L1\_J75 trigger and are taken from one run of 2016 data where the trigger L1\_J75 is unprescaled. Events are required to have  $|y^*| < 0.6$  and no *b*-tagging requirements have been applied.

For the *Full16\_LowMass* data-set the upper bound of the dijet mass range considered by the search phase is 1533 GeV. This value is chosen such that there is no gap in the mass range searched by the low-mass and high mass di-*b*-jet searches.

### 7.3 *b*-Tagging

The selection of *b*-jets, known as *b*-tagging, forms an essential technique in the di-*b*-jet event selection. A detailed description of *b*-tagging is found in Section 4.3. *b*-Tagging is performed using a multi-variate algorithm known as MV2c10 which has been described in Section 4.3.3.

Two *b*-tagging categories are used for the two different types of signal model considered. The 2 *b*-tag category requires that both jets are *b*-tagged, and is used to search for resonances decaying to 2 *b*-quarks such as the  $Z'$  boson. The  $\geq 1$  *b*-tag category requires that at least one jet is *b*-tagged, and is used to search for resonances decaying to 1 *b*-quark and a quark/gluon, such as the  $b^*$  quark. The exclusive 1 *b*-tag category was also considered but was found to be less sensitive to the  $b^*$  quark model. For the *Full16\_LowMass* data-set analysis, only the 2 *b*-tag category is considered as the double *b*-jet trigger used applies online *b*-tagging to the leading and subleading jet.

In the *Summer16\_HighMass* data-set, *b*-tagging is performed using the 85% operating point of the MV2c10 algorithm; details on the operating points of MV2c10 are found in

Section 4.3.3. This operating point is chosen as it was found to maximise  $S/\sqrt{B}$  for a range of generated mass points in a previous di-*b*-jet search at ATLAS [12], where  $S$  is the number of signal events and  $B$  is number of background events.

In the *Full16\_LowMass* data-set offline *b*-tagging is performed using the 70% operating point of the MV2c10 algorithm. This operating point was chosen to maximise  $S/\sqrt{B}$  for a range of generated mass points.  $S$  is estimated in a narrow dijet mass window around each generated mass point considered using the simulated SSM  $Z'$  boson signal template described in Section 6.3 scaled to  $3 \text{ fb}^{-1}$ .  $B$  is estimated in the same narrow dijet mass windows using a  $3 \text{ fb}^{-1}$  subset of *Full16\_LowMass* data<sup>3</sup>. The full *Full16\_LowMass* event selection has been applied. The 85% operating point is not considered because the associated *b*-jet trigger systematic uncertainties are significantly larger, as shown in Table 5.4. Table 7.1 summarises  $S/\sqrt{B}$  for each operating point; the 70% operating point is selected as it performs well across the full range of mass points considered and, as shown in Table 5.4, has a smaller *b*-jet trigger uncertainty associated than the 77% operating point. The conclusions of this study are luminosity independent.

Generated Mass [GeV]	800	1000	1250
Mass window [GeV]	657-861	861-1068	1068-1269
$S/\sqrt{B}$ for 77% OP	$4.30 \pm 0.20$	$2.09 \pm 0.21$	$0.86 \pm 0.19$
$S/\sqrt{B}$ for 70% OP	$4.57 \pm 0.21$	$1.97 \pm 0.22$	$0.77 \pm 0.21$
$S/\sqrt{B}$ for 60% OP	$4.50 \pm 0.23$	$1.57 \pm 0.23$	$0.52 \pm 0.20$

**Table 7.1:** The estimated  $S/\sqrt{B}$  at  $3 \text{ fb}^{-1}$  for 3 different MV2c10 operating points (OP).  $S$  is estimated using a simulated SSM  $Z'$  boson sample and  $B$  is estimated using a  $3 \text{ fb}^{-1}$  subset of data. The *Full16\_LowMass* data-set event selection has been applied. Three different generated mass points are considered and the mass windows used to estimate  $S$  and  $B$  for each mass point are shown in the table [11].

To further understand the effect of *b*-tagging in this analysis the flavour composition of the background is studied. The dijet flavour composition is defined as the truth flavour of the jets used in the di-*b*-jet search, using the definition of truth flavour from Section 4.3.1, and is estimated using the Monte Carlo simulated QCD dijet sample, described in Section 6.3. Figure 7.3 shows the dijet flavour composition of the QCD background for the *Summer16\_HighMass* data-set in the case where no *b*-tagging has been applied (inclusive) and in the  $\geq 1$  and 2 *b*-tag categories. Figure 7.4 shows the dijet flavour composition of the QCD dijet background when the *Full16\_LowMass* data-set event selection has been applied.

---

<sup>3</sup>A subset of data was used such that the studies were not biased if signal is present in the final data-set.

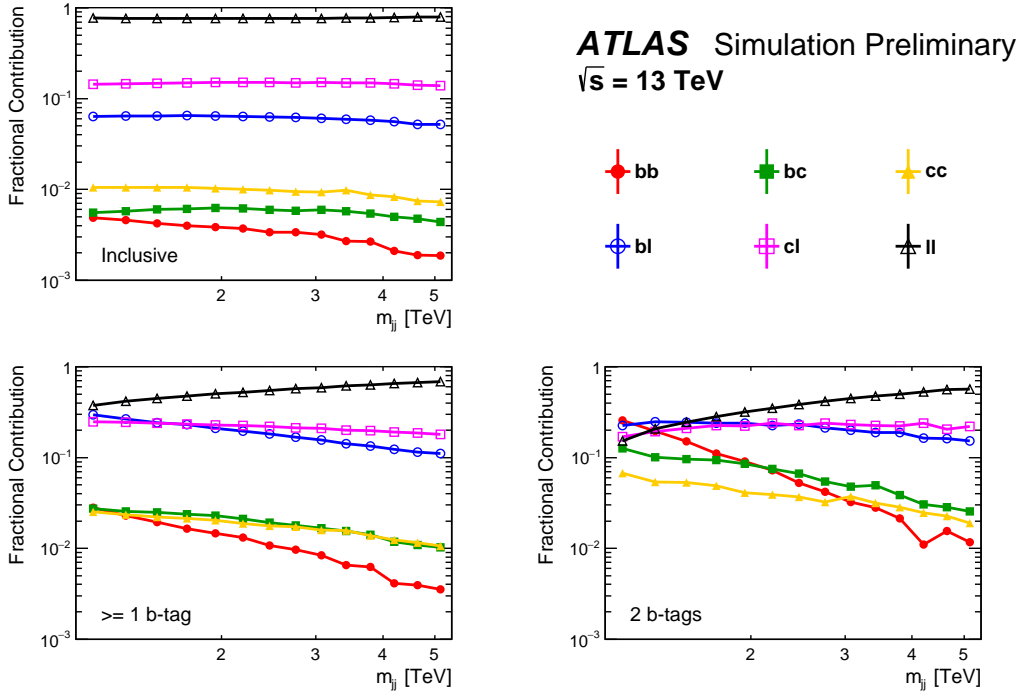


**Figure 7.3:** The dijet flavour composition of simulated QCD dijet production as a function of dijet mass ( $m_{jj}$ ) for the *Summer16\_HighMass* data-set shown without applying *b*-tagging (inclusive) and for the  $\geq 1$  *b*-tag and 2 *b*-tag categories. In the legend *b*, *c* and *l* refer to a truth matched *b*-jet, *c*-jet and light jet respectively. The *Summer16\_HighMass* data-set event selection has been applied.

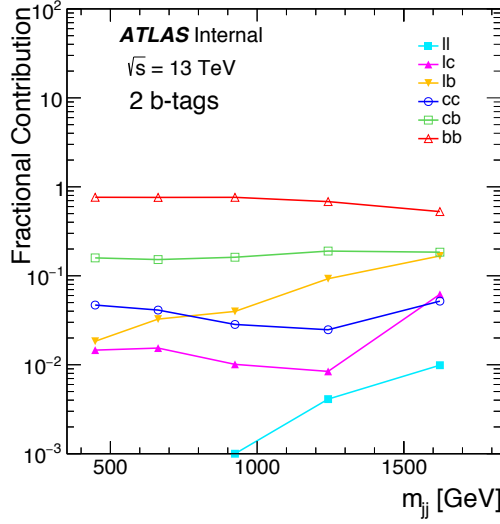


**Figure 7.4:** The dijet flavour composition of simulated QCD dijet production as a function of dijet mass for the *Full16\_LowMass* data-set shown after the application of online and off-line *b*-tagging requirements. In the legend *b*, *c* and *l* refer to a truth matched *b*-jet, *c*-jet and light jet respectively. The *Full16\_LowMass* data-set event selection has been applied [11].

There are a few features of the dijet flavour composition that should be noted. Firstly, the background before *b*-tagging is dominated by light-jets for the reasons outlined in Section 2.2.3.3. As the background is dominated by light-jets, the application of *b*-tagging can increase background rejection and thus increase sensitivity to signal models that decay to *b*-quarks. This motivates the use of *b*-tagging in the analysis.

Secondly, in the *Summer16\_HighMass* data-set analysis, even after the application of *b*-tagging, the largest contribution to the background is from light jets except for a small region at low mass in the 2 *b*-tag category. This shows that the sensitivity of the analysis is limited by the light-jet rejection of *b*-tagging at high jet- $p_{\mathrm{T}}$ . In the *Full16\_LowMass* data-set the background is dominated by *b*-jets due to the tighter *b*-tagging operating point used and improved *b*-tagging performance at low jet- $p_{\mathrm{T}}$ .

Finally, in all four cases the dijet flavour fractions are smoothly changing, where smooth means monotonically changing with no discontinuities. This is evidence that the effect of *b*-tagging on the background does not produce a non-smooth feature in the background dijet mass spectra.

### 7.3.1 Effect of *b*-Jet Trigger Matching in the *Full16\_LowMass* Data-Set

As discussed in Section 5.2, the double *b*-jet trigger used in the *Full16\_LowMass* data-set requires that there is one online jet with  $p_{\mathrm{T}} > 150 \text{ GeV}$ , another online jet with  $p_{\mathrm{T}} > 50 \text{ GeV}$  and that both jets are *b*-tagged at the 60% online operating point.

As described in Section 7.1, it is required that the leading and subleading offline jet have a jet  $p_{\mathrm{T}}$  above 200 GeV and 80 GeV respectively such that events are on the trigger plateau. Then, in Section 7.2 it was shown that in the *Full16\_LowMass* data-set there is no kinematic bias in the dijet mass distribution due to the leading and subleading offline jet  $p_{\mathrm{T}}$  cuts for  $m_{jj} > 500 \text{ GeV}$ .

However, it has been discovered that one must also consider the effect of offline jets other than the leading and subleading jet, these jets I will refer to as ‘non-leading jets’. As online and offline *b*-tagging are different processes<sup>4</sup>, it is possible to have an event where the leading and subleading offline jet pass the *Full16\_LowMass* data-set event selection but one or both of the leading or subleading jets do not pass the online *b*-tagging requirements. Such an event can still pass the double *b*-jet trigger if a non-leading jet passes the online jet- $p_{\mathrm{T}}$  requirements and is online *b*-tagged. In this case different jets are used at the trigger level than are used in the offline analysis. Therefore, it must be additionally shown that in

---

<sup>4</sup> The differences are described in Section 5.2.

the dijet mass range considered there is not a kinematic bias due to events where a non-leading jet is used by the trigger.

A study is performed to determine the effect of the *b*-jet trigger using non-leading jets on the dijet mass spectrum. For this study offline jets are matched to online jets in a process known as trigger matching. An offline jet is matched to an online jet if  $\Delta R$  between the jets is less than 0.4; the matching is exclusive meaning that online jets are only matched to offline jets with the smallest  $\Delta R$  separation.

Then one can define ‘*b*-jet trigger matched events’ as events where the leading and subleading offline jets have successfully been matched to online jets and that these online jets pass the double *b*-jet trigger requirements described above. In *b*-jet trigger matched events it is known that the leading and subleading jet are used to pass the double *b*-jet trigger. In events that are not *b*-jet trigger matched events, a non-leading jet has been used by the double *b*-jet trigger.

To study *b*-jet trigger matched events an additional complication has to be overcome. To perform trigger matching the  $p_T$ ,  $\eta$ ,  $\phi$  and MV2c20 output of the online jets is required. Data from the ATLAS collaboration is processed and stored in containers known as ‘derivation containers’<sup>5</sup>. To reduce the computer resources required to analyse a derivation container there are many types of derivation containers, where each contains only the events and the reconstructed object information required to perform an analysis. For the di-*b*-jet search a derivation called *EXOT2* is used, however the online jet information required for trigger matching is not present in the *EXOT2* derivation containers. Instead, a derivation container called *FTAG1* is used, in which the online jet information is present. However, in the *FTAG1* derivation not all events that pass the double *b*-jet trigger are included. Therefore, neither derivation container contains the full information required to do *b*-jet trigger matching on the full *Full16\_LowMass* data-set.

To overcome this problem the effect of *b*-jet trigger matching can be studied using the *FTAG1* derivation to test if there is a kinematic bias. Firstly, one can consider the dijet mass spectrum of all events in the *FTAG1* derivation that pass the *Full16\_LowMass* data-set event selection before *b*-jet trigger matching is applied. I will refer to this as the dijet mass spectrum from *FTAG1*. Figure 7.5(a) shows the dijet mass spectrum from *FTAG1* compared to the full dijet mass spectrum from the *EXOT2* derivation, where all events are present. The full *Full16\_LowMass* data-set event selection has been applied to both. The ratio shows that there is a deficit of events in the dijet mass spectrum from *FTAG1* at low mass.

---

<sup>5</sup>Formally the ‘derivation containers’ are known as Derived Analysis Object Data (DAODs)

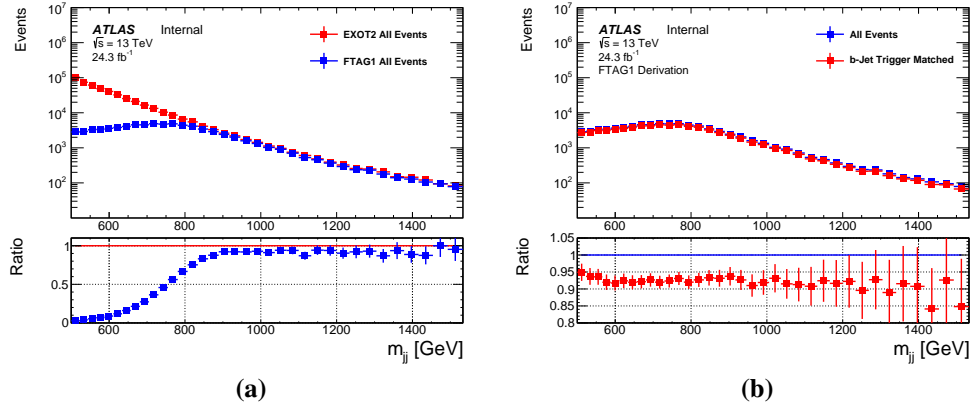


**Figure 7.5:** (a) A comparison of the dijet mass ( $m_{jj}$ ) spectra created using the *EXOT2* derivation and the *FTAG1* derivation. (b) A comparison of the dijet mass spectra of all events and *b*-jet trigger matched events using the *FTAG1* derivation. For both plots the full *Full16\_LowMass* event selection is applied. Details of the derivation containers is given in the text.

Figure 7.5(b) shows the comparison of the dijet mass spectrum from *FTAG1* before and after the application of *b*-jet trigger matching. The full *Full16\_LowMass* data-set event selection has been applied in both cases. A ratio of the two spectra is in the lower panel; the ratio shows that  $\sim 8\%$  of events that pass the *Full16\_LowMass* event selection do not pass *b*-jet trigger matching requirement. In these events it can be concluded that a non-leading jet is used by the double *b*-jet trigger. For  $m_{jj} > 566$  GeV the ratio is smooth with respect to dijet mass. However in the region  $500 < m_{jj} < 566$  GeV, which is shown by the first three  $m_{jj}$  bins, there is a clear discontinuity in the ratio plot which indicates that there is a kinematic bias due to the double *b*-jet trigger in the final data-set.

The background estimation strategy (described in Section 8) requires that the dijet mass spectrum must be smooth, therefore it is required that there is no effect that can cause a non-smooth feature in the dijet mass spectrum. It has been shown that for  $m_{jj} > 566$  GeV there is no effect from non-leading jets being used in the double *b*-jet trigger that can cause an unsmooth feature in the final data-set. Therefore, for the *Full16\_LowMass* data-set it is required that  $m_{jj} > 566$  GeV.

Finally it should be noted that for future iterations of the di-*b*-jet search the full information required for *b*-jet trigger matching will be included in the *EXOT2* derivation, and as such trigger matching can be applied such that analyses can search a dijet mass range beginning at 500 GeV.

## 7.4 Summary of Event Selection

A summary of the key components of the di- $b$ -jet event selection for each of the data-sets considered is listed in Table 7.2.

Data-Set	<i>Summer16_HighMass</i>	<i>Full16_LowMass</i>
Integrated Luminosity	$13.3 \text{ fb}^{-1}$	$24.3 \text{ fb}^{-1}$
Trigger	Single jet	Double $b$ -jet (60% OP)
Online LJ $p_T$	$> 380 \text{ GeV}$	$> 150 \text{ GeV}$
Online SLJ $p_T$	-	$> 50 \text{ GeV}$
Leading Jet- $p_T$	$> 430 \text{ GeV}$	$> 200 \text{ GeV}$
Subleading Jet- $p_T$	$> 60 \text{ GeV}$	$> 80 \text{ GeV}$
Jet- $ \eta $	$< 2.4$	$< 2.0$
$m_{jj}$	$> 1378 \text{ GeV}$	$566 - 1533 \text{ GeV}$
$ y^* $	$< 0.6$	$< 0.6$
$b$ -Tagging OP	85%	70%
$b$ -Tag Categories	2 and $\geq 1$	2

**Table 7.2:** A summary of the key details of the di- $b$ -jet event selection applied in the two data-sets considered. LJ refers to leading jet and SLJ refers to subleading jet. For full details refer to the text.

To visualise events that pass the event selection, Figure 7.6 show events displays for high dijet mass events that pass the  $\geq 1$  and 2  $b$ -tag event selection respectively. The figure was made using the VP1 event display package [107]. These events pass the *Summer16\_HighMass* data-set event selection.

With the event selection now defined, the signal acceptance of the di- $b$ -jet event selection is studied to understand the performance of the analysis selection. The signal acceptance is also a required input to the limit setting phase of the analysis, described in Chapter 9. The signal acceptance multiplied by trigger efficiency is defined as the fraction of signal events that pass the analysis' trigger and event selection. In addition, as  $b$ -tagging is a unique selection in our analysis relative to other dijet searches, the event-tagging efficiency is also considered, which is defined as the fraction of signal events that pass the  $b$ -tagging requirements given that the event has passed all other aspects of the event selection. Signal acceptance and event tagging efficiency are estimated using the Monte-Carlo signal templates discussed in Section 6.3.

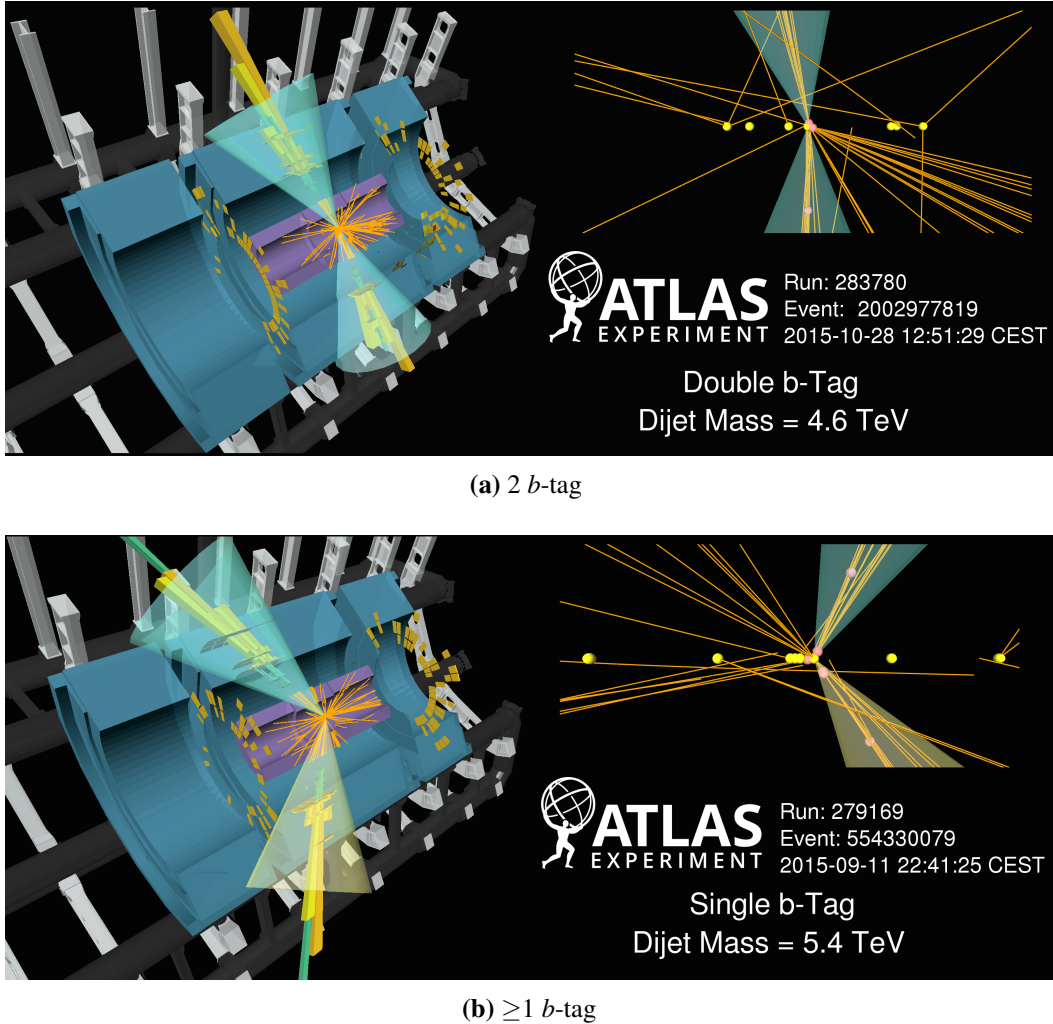


**Figure 7.6:** Event displays showing high dijet mass ( $m_{jj}$ ) events that pass the (a) 2 and (b)  $\geq 1$   $b$ -tag di- $b$ -jet event selection in the *Summer16\_HighMass* data-set analysis. The left section of the figures show a cut-away of the ATLAS detector; the inner detector is shown in purple, the hadronic calorimeter is shown in blue and the toroid magnet and supporting structure is shown in black and grey. The upper right section of the figures show a close-up view of the inner detector in the  $r - z$  plane. In both sections tracks inside the inner detector are shown in orange and energy deposits in the EM and hadronic calorimeter are shown in green and yellow respectively. The two leading jets are indicated by the cones, a blue cone indicates that the jet has been  $b$ -tagged and a yellow cone indicates that it has not. In the upper right panel the yellow spheres show the reconstructed primary vertices and the red spheres show the reconstructed secondary vertices.

For the *Summer16\_HighMass* data-set event selection; Figure 7.7(a) shows the signal acceptance multiplied by trigger efficiency for the  $b^*$  quark and SSM  $Z'$  boson signal models as a function of the generated mass with and without the application of  $b$ -tagging. Figure 7.7(b) shows the event tagging efficiency for the  $b^*$  quark and SSM  $Z'$  boson for a range of generated mass points as a function of the dijet mass. For the SSM  $Z'$  boson only decays to  $b$ -quarks are considered. In both plots the  $b$ -tagging category used is labelled.

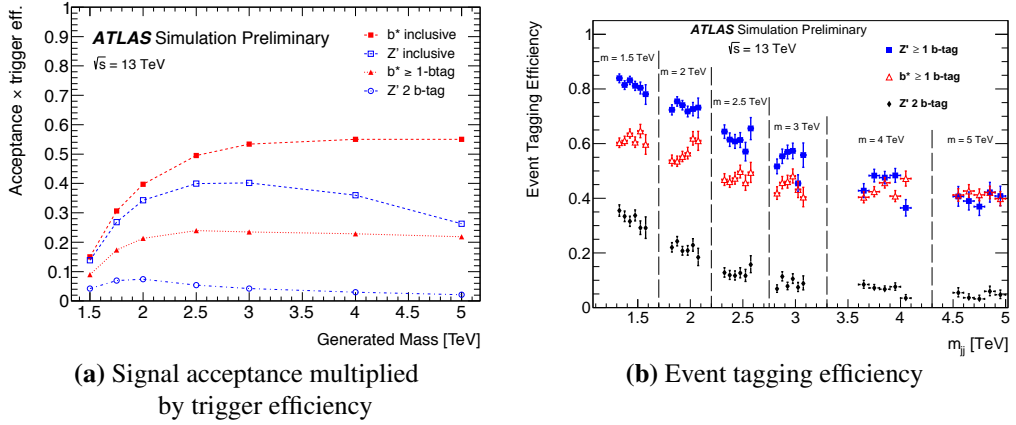


**Figure 7.7:** Plots to show the acceptance of the *Summer16\_HighMass* data-set event selection for the  $b^*$  quark and SSM  $Z'$  boson signal models. Panel (a) shows the signal acceptance multiplied by trigger efficiency as a function of the generated mass of the signal model, in the case where  $b$ -tagging has been applied and not. Panel (b) shows the event tagging efficiency as a function of the dijet mass ( $m_{jj}$ ) for a range of generated masses,  $m$ , as indicated on the plot. In both figures the  $b$ -tagging categories used are indicated in the legend. Figures taken from [10].

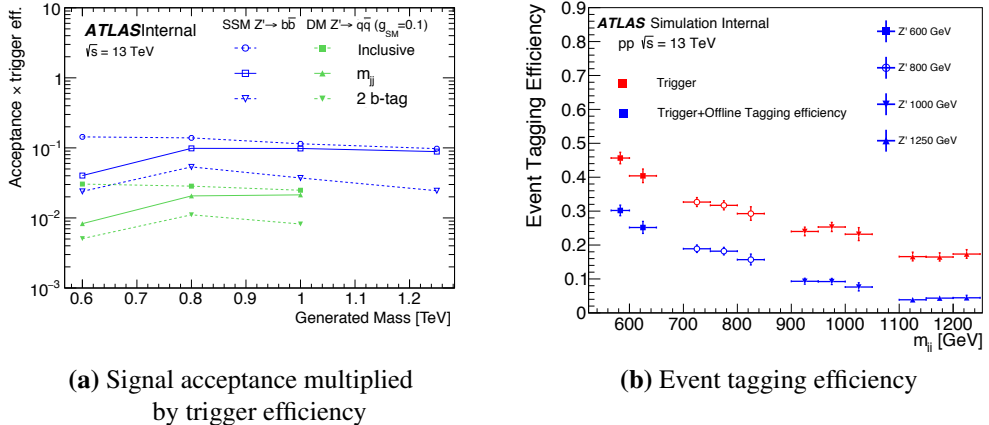


**Figure 7.8:** Plots to show the acceptance of the *Full16\_LowMass* data-set event selection for the Sequential Standard Model (SSM)  $Z'$  boson and Dark Matter inspired (DM)  $Z'$  boson signal models. Panel (a) shows the signal acceptance multiplied by trigger efficiency as a function of the generated mass of the signal model, before and after the dijet mass and offline  $b$ -tagging requirements are applied. Panel (b) shows the event tagging efficiency of just online  $b$ -tagging and the combination of online and offline  $b$ -tagging as a function of the dijet mass,  $m_{jj}$ , for the SSM  $Z'$  boson at a range of generated masses,  $m$ , as indicated in the legend. Figures taken from [11].

For the *Full16\_LowMass* data-set event selection; Figure 7.8(a) shows the signal acceptance multiplied by trigger efficiency for the SSM  $Z'$  boson and Dark Matter inspired (DM)  $Z'$  boson signal models as a function of the generated mass. For both models the signal acceptance is shown before and after the dijet mass and offline  $b$ -tagging requirements are applied. The signal acceptance is considerably lower for the DM  $Z'$  boson model in the

*Full16\_LowMass* data-set as decays to light,  $c$  and  $b$  quarks are considered whilst for the SSM model only decays to  $b$ -quarks are considered. Figure 7.8(b) shows the event tagging efficiency of just online  $b$ -tagging and the combination of online and offline  $b$ -tagging for the SSM  $Z'$  boson for a range of generated mass points as a function of the dijet mass,  $m_{jj}$ .

There are a few features of the signal acceptance and tagging efficiency that should be commented on. Firstly, the event tagging efficiency decreases at high values of dijet mass due to a lower performance of  $b$ -tagging at high jet- $p_T$ , which has been discussed in Section 4.3.3. Secondly, there is a reduced signal acceptance at lower generated masses due to the dijet mass requirement of the event selection.

Thirdly, for the  $Z'$  boson model, even before  $b$ -tagging is applied, there is a reduced signal acceptance at large generated masses; this can be seen using the ‘ $Z'$  inclusive’ line in Figure 7.7(a). This occurs because the high generated mass signal templates have a bias towards low dijet mass events caused by a preference for low masses by the PDFs; these low dijet mass events can be rejected by the dijet mass requirements of the event selection. This effect is not observed for the  $b^*$  quark as these low mass events were removed by the program used to generate the events. It is important to note that this feature does not affect the analysis as, for the high generated mass signals being discussed, the low dijet mass events do not contribute to the signal peak and hence are indistinguishable from the background in a resonance search.

Finally, in Figure 7.7 the  $b^*$  quark has a similar tagging efficiency as the  $Z'$  boson in the  $\geq 1$   $b$ -tag category when  $m_{jj} > 3$  TeV, whilst naively one would expect that the SSM  $Z'$  boson should have a higher event tagging efficiency as it decays to two  $b$ -quarks; this is because the gluon from the  $b^*$  quark decay can split into a pair of lower  $p_T$   $b$ -quarks which can often be  $b$ -tagged.

## Chapter 8

# Di-*b*-Jet Search: Search Phase

The role of the search phase is to determine if there is any evidence of Beyond Standard Model (BSM) physics in the form of a resonance (or a bump) in the dijet mass spectra of the di-*b*-jet events selected. This is performed in two parts; firstly a background fit is used to estimate the dijet mass spectrum of the QCD dijet background. Then, the difference between the data and the background estimation is used to search for a significant excess that would be evidence of BSM physics.

This chapter presents the details of the dijet mass spectra used in the analysis (Section 8.1), the background estimation strategy (Section 8.2) and the technique used to search for excesses (Section 8.3). Then the specific details, validation and results of the search phase for each of the data-sets are then shown in Section 8.4 and 8.5.

## 8.1 Dijet Mass Spectrum

The dijet mass ( $m_{jj}$ ) spectrum is the distribution of the invariant mass of the leading and subleading jet of events that have passed the di-*b*-jet event selection. The dijet mass spectrum is analysed in a binned histogram, the bin width is chosen to be approximately the same size as the dijet mass resolution whilst still giving a smooth dijet mass spectrum [2]. The exact bins chosen are shown in Appendix A.

Searching for resonances using the dijet mass spectrum is effective for narrow resonances where the majority of signal events have a narrow distribution in dijet mass, such that a significant excess will be created. The benchmark models considered for this analysis are examples of narrow resonances. For signals that are much wider than the dijet mass resolution, signal is hard to distinguish from the background using a dijet mass spectrum. Inclusive dijet searches for wide signals have been performed using angular distributions [2]<sup>1</sup>.

---

<sup>1</sup>Inclusive dijet analysis means a dijet analysis where no *b*-tagging is applied.

## 8.2 Background Estimation

A di-*b*-jet search requires an estimation of the dijet mass spectrum of events from background processes, which, as discussed in Section 6.3, is totally dominated by QCD dijet production. Many analyses at ATLAS use Monte-Carlo simulation to provide a background estimation [75]. However, simulation is not used to estimate the background in the di-*b*-jet search due to three problems [1]. Firstly, due to the large cross-section of QCD dijet production it is difficult to produce Monte-Carlo simulation with the required statistical precision. Secondly, there are large theoretical uncertainties associated with simulations of QCD dijet production, such as hadronisation modelling and PDF uncertainties. Finally, there are experimental uncertainties affecting data-simulation comparisons, such as jet energy scale and *b*-tagging uncertainties.

Instead, the background is estimated using a smooth fit function. This approach utilises the fact that the dijet mass spectrum from QCD dijet production is smoothly falling, as discussed in Section 2.2.3.3. Smoothly falling functions have been widely used to model smoothly falling backgrounds in a wide range of searches for resonances: including inclusive dijet, di-*b*-jet and di-photon searches [2, 12, 108].

This approach sets two requirements on a fit function; firstly the fit function must be able to describe the dijet mass spectrum from QCD dijet production including the impact of any detector or reconstruction effects that could change the dijet mass spectrum, such as *b*-tagging. If the fit function is unable to adequately describe QCD dijet production then the background estimate may create false signal or hide a true signal, neither of these occurrences are allowed. Secondly, the fit function used must be constrained enough such that there is not a significant change in the background estimate if a resonance is present in the dijet mass spectrum, such a change is referred to as a signal induced fit bias. As evidence of such a resonance is found when the data diverges from the background estimate, a signal induced fit bias would reduce the sensitivity to signal. The fit functions considered in this analysis will be described in the following section.

For any given fit function, the parameters of the function are chosen to maximise the likelihood; where the likelihood is defined as the probability of obtaining the observed dijet mass spectrum under the assumption that the number of observed events in each dijet mass bin follows a Poisson probability distribution about the background estimation. Hence, the likelihood is calculated as:

$$\mathcal{L} = \prod_i \left( \frac{b_i^{n_i} e^{-b_i}}{n_i!} \right) \quad (8.1)$$

where  $n_i$  is the number of data events observed in bin  $i$ ,  $b_i$  is the number events predicted

by the background estimation in bin  $i$ , and the product is over all bins in the dijet mass spectrum.

### 8.2.1 Functional Form

The dijet mass spectrum of the di- $b$ -jet events will be described by dijet fit functions, a family of functions with a varying number of parameters. The dijet fit functions used in this analysis are listed in Table 8.1.

Function Name	Equation	$x$
3 parameter	$f(x) = p_1 (1-x)^{p_2} x^{p_3}$	$m_{jj}/\sqrt{s}$
4 parameter	$f(x) = p_1 (1-x)^{p_2} x^{p_3+p_4 \ln x}$	$m_{jj}/\sqrt{s}$
5 parameter	$f(x) = p_1 (1-x)^{p_2} x^{p_3+p_4 \ln x+p_5 (\ln x)^2}$	$m_{jj}/\sqrt{s}$
6 parameter	$f(x) = p_1 (1-x)^{p_2} x^{p_3+p_4 \ln x+p_5 (\ln x)^2}$	$m_{jj}/p_6$

**Table 8.1:** The functional form of the dijet fit functions. The fit functions are named by the number of free parameters used.  $p_i$  are the free parameters of the fit function.  $\sqrt{s}$  is the centre-of-mass energy of the collisions.

The dijet fit functions are motivated using a theoretical understanding of QCD dijet production and experience from previous dijet searches [1]. The 3 parameter dijet fit function has been used in dijet searches beginning with CDF [109] and the three components are motivated as follows: the  $p_1$  term gives the normalisation, the  $(1-x)^{p_2}$  term is a common parameterisation for the behaviour of the PDFs with the property of vanishing as  $x$  approaches unity, and the  $x^{p_3}$  term is motivated by the  $1/m_{kl}^2$  term in the matrix element (shown in Equation 2.6). The  $\sqrt{s}$  term is the centre-of-mass energy of the  $pp$  collisions, which is 13 TeV for the analyses in this thesis. Additional parameters of  $x^{p_4 \ln x}$  and  $x^{p_5 (\ln x)^2}$  have been considered in dijet searches to give an adequate description of high dijet mass region when large mass ranges are considered [2, 110]. Finally, the  $x = m_{jj}/p_6$  term is added as an additional degree of freedom [22].

The dijet fit functions are ‘nested functions’, which are defined as a sequence of functions where each function can be formed from the next function in the sequence by fixing the value of one parameter. For example, the 3 parameter dijet fit function can be formed from the 4 parameter dijet fit function by setting  $p_4 = 0$  and so on.

The dijet fit functions have been developed for and used in inclusive dijet analyses [1], using the dijet mass spectrum of events with no requirements on  $b$ -tagging. The effect of  $b$ -tagging on the dijet mass spectrum has been found to be smooth, therefore the dijet mass spectrum of di- $b$ -jet events can still be described by the dijet fit functions [12]. Validation studies are performed to show that dijet fit functions are able to adequately describe the dijet

mass spectrum of the data-sets considered in this thesis; the search phase validation studies are presented in Sections 8.4 and 8.5.

Functions with higher numbers of parameters may be required to describe the dijet mass spectrum from QCD dijet production; especially in large data-sets where small statistical uncertainties reveal finer details of the dijet mass shape and large mass ranges where stronger constraints are applied to the fit function. However, additional parameters also allow for more flexibility in the background estimation, which may allow a signal induced fit bias to occur. Hence, the dijet fit function with the fewest number of parameters that can adequately describe the background is used, such that sensitivity to signal is maximised.

### 8.2.2 Wilks' Test Statistic

To determine if a dijet fit function has a sufficient number of parameters to adequately describe the dijet mass spectrum an approach using the Wilks' test statistic is used, as employed in previous inclusive dijet and di-*b*-jet searches at ATLAS [2, 12].

For this test one considers the null hypothesis that a nominal dijet fit function is the true parameterisation of the dijet mass spectrum and the alternative hypothesis that a dijet fit function with an additional parameter is required.

The Wilks' test statistic,  $t_W$ , is defined as

$$t_W = -2 \ln \left( \frac{\mathcal{L}_{\text{Nom}}}{\mathcal{L}_{\text{Alt}}} \right) \quad (8.2)$$

where  $\mathcal{L}_{\text{Nom}}$  and  $\mathcal{L}_{\text{Alt}}$  are the maximised likelihoods of the nominal and alternative function respectively, using the definition of likelihood given in Equation 8.1. A Wilks' test statistic close to zero indicates that the observed data is compatible with the null hypothesis.

Wilks' theorem states that for nested functions, such as the dijet fit functions, in the null hypothesis the Wilks' test statistic will follow a  $\chi^2$  distribution with 1 degree of freedom [111]. As a result the Wilks' *p*-value can be calculated, which is defined as the probability of obtaining a Wilks' test statistic of the same value or larger than the one observed in data under the assumption of the null hypothesis. If the *p*-value  $< 0.05$  it is concluded that the nominal dijet fit function does not have sufficient parameters to provide an adequate description of the data.

The Wilks' *p*-value is employed to determine the background estimation strategy in both the *Summer16\_HighMass* and *Full16\_LowMass* data-set analyses in different ways, which will be described below in Sections 8.4.3 and 8.5.4 respectively.

### 8.3 Resonance Search Strategy

After a background estimation is created, the next step is to determine if there is evidence of a resonance in the dijet mass spectra of the selected di-*b*-jet events. A resonance can be observed if there is a discrepant excess in the dijet mass spectrum, as illustrated in Figure 6.1; an excess is defined as any set of consecutive bins that contains more events in data than the background estimation, and discrepant describes how inconsistent an excess is with the background estimation.

To put this in terms of hypothesis testing, the null hypothesis states that the dijet mass spectrum contains only events created by QCD dijet production which are modelled by the background estimation, this is referred to as the background-only hypothesis. The alternate hypothesis states that there is also a resonance at some unknown mass point causing an excess in the dijet mass spectrum.

Due to statistical fluctuations in the number of background events, excesses in the dijet mass spectrum are expected in the background-only hypothesis. Therefore, to discover a new resonance a significant excess is required, which is an excess that is highly unlikely to have occurred from such a fluctuation. A *p*-value is used to quantify the significance of an excess, where a *p*-value is defined as the probability of an excess which is at least as discrepant as the excess found in data occurring in the background-only hypothesis. Hence, a small *p*-value indicates that the excess is inconsistent with the background-only hypothesis and that new physics might be present; in particle physics it is conventional to consider a *p*-value below  $\sim 0.001$  ( $3\sigma$ ) as evidence of new physics whilst a *p*-value below 1 in  $\sim 3.5$  million ( $5\sigma$ ) is considered as the discovery of new physics.

In this analysis the BumpHunter algorithm [97] is employed; this algorithm uses the BumpHunter test statistic to search for the most discrepant excess in the data and calculate the *p*-value of such an excess. The BumpHunter test statistic gives a quantitative measure of how discrepant any given excess is. To derive the test statistic let's consider a set of consecutive bins in which a total of  $d$  data events are found and  $b$  background events are expected. As this is a search for excesses we will consider the case where  $d > b$ . Using Poisson statistics one can calculate the probability that an excess which is at least as discrepant would occur in the background-only hypothesis in this set of bins:

$$P(d, b) = \sum_{n=d}^{\infty} \left( \frac{b^n e^{-b}}{n!} \right) \quad (8.3)$$

From this probability, the BumpHunter test statistic,  $t$ , is defined such that its size

represents how discrepant an excess is. The BumpHunter test statistic is defined as:

$$t = -\ln(P(b, d)) \quad (8.4)$$

The BumpHunter algorithm calculates the value of  $t$  for all excesses in the dijet mass spectrum by scanning over all possible combinations of consecutive bins. The narrowest excess allowed is two bins and the widest excess allowed contains half the number of bins in the spectrum. The excess with the largest BumpHunter test-statistic is the most discrepant excess and the value of  $t$  observed is labelled  $t_{obs}$ .

To calculate the  $p$ -value of the most discrepant excess, Poisson fluctuations are applied to the background estimation to create pseudo-experiments which represent the range of dijet mass spectra possible under the background-only hypothesis. In each pseudo-experiment the BumpHunter scan is performed to find the most discrepant excess and corresponding value of  $t$ . This is done for many pseudo-experiments to estimate the probability density function of  $t$  under the assumption of the null hypothesis,  $f_{PE}(t|H_{Bkg})$ . The BumpHunter  $p$ -value of the most discrepant excess in data is then calculated using

$$\text{BumpHunter } p\text{-value} = \int_{t_{obs}}^{\infty} f_{PE}(t|H_{Bkg}) \quad (8.5)$$

An example of this calculation is illustrated in Figure 8.8, the details of this example will be described in Section 8.4.4. Using the same logic, except requiring that  $d < b$ , it is possible to also search for deficits, this is referred to as the DeficitHunter  $p$ -value throughout this thesis.

The BumpHunter algorithm is chosen to search for excesses due to two important features. Firstly, the BumpHunter  $p$ -value is model independent; the algorithm makes no prior assumptions about the nature of the new physics model that could be present other than it would produce extra di- $b$ -jet events and that the extra events would occur in consecutive dijet mass bins. Secondly, the BumpHunter  $p$ -value is naturally global; this means that the  $p$ -value accounts for the fact that under the background-only hypothesis an excess such as the one observed could have occurred at any mass point in the dijet mass spectrum. The BumpHunter  $p$ -value is global due to the fact that in the BumpHunter scan for each of the pseudo-experiments, there is no prior assumption on the location of the most discrepant excess.

The combined process of creating a background estimate and then finding the most discrepant excess and associated  $p$ -value using the BumpHunter algorithm is referred to as the search phase throughout this Chapter.

## 8.4 *Summer16\_HighMass* Search Phase

This section presents strategy, validation and results of the search phase for the *Summer16\_HighMass* data-set. As described in Chapter 7 there are two  $b$ -tag categories considered for the *Summer16\_HighMass* data-set (2  $b$ -tag and  $\geq 1$   $b$ -tag) giving two dijet mass spectra. Hence, an independent search phase is performed for both categories.

For the *Summer16\_HighMass* data-set, the background estimate is created using a single dijet fit function (described in Table 8.1) for the full range of the dijet mass spectra. This strategy, known as the global fit strategy, has been used in previous inclusive dijet and di- $b$ -jet searches at ATLAS [2, 12].

The *Summer16\_HighMass* data-set search phase will be presented as follows: Section 8.4.1 describes the data-sets used for validation studies, Section 8.4.2 presents the selection of the dijet mass range, Section 8.4.3 presents the selection of the dijet fit function, Sections 8.4.4 and 8.4.5 present validation studies of the search phase using the chosen fit function and dijet mass range, and Section 8.4.6 presents the results of the search phase.

### 8.4.1 Validation Studies: Background-Only Data-Set

It is important to perform search phase validation studies to demonstrate that the dijet fit functions are a valid description of the background dijet mass spectrum caused by QCD dijet production. In this and the following sections the validation studies for the *Summer16\_HighMass* data-set are presented.

To perform the validation studies a dijet mass spectrum that represents the shape of the background with no signal contamination is required. The simulated QCD dijet sample described in Section 6.3 is used as the representative background-only data-set. The simulation sample is produced in several slices of leading jet  $p_T$ , where each slice contains the same number of events. A weight is applied to each event such that the dijet mass spectrum from the merged slices is representative of the smoothly falling dijet mass spectrum that is expected, whilst still maintaining the same statistical precision across the full mass range. The weighted dijet mass spectrum is then scaled to  $10 \text{ fb}^{-1}$ <sup>2</sup>, this is referred to as the ‘scaled’ dijet mass spectrum, and is the expected number of background events in a specific dijet mass bin. The statistical precision of the scaled spectrum in each dijet mass bin is represented by the number of ‘effective entries’; defined as the number of events in data that would be required to give the same statistical precision.

---

<sup>2</sup> The search phase validation studies were performed during data-taking and as such the final integrated luminosity of the data-set had to be estimated,  $10 \text{ fb}^{-1}$  was used in the validation studies whereas the final data-set is  $13.3 \text{ fb}^{-1}$ .

The number of effective entries,  $N_{\text{eff}}$ , can be calculated from the event weights:

$$N_{\text{eff}} = (\sum w_i)^2 / \sum w_i^2 \quad (8.6)$$

Figure 8.1 shows the scaled and effective entries distributions of the simulated QCD dijet sample as a function of dijet mass for the 2  $b$ -tag and  $\geq 1$   $b$ -tag categories. The number of effective entries is larger than the number of scaled entries, meaning that the scaled spectrum contains smaller statistical fluctuations than are present in the final data-set. The oscillating pattern in the effective entry distribution is caused by the merging of the different jet- $p_T$  slices of the simulated sample.

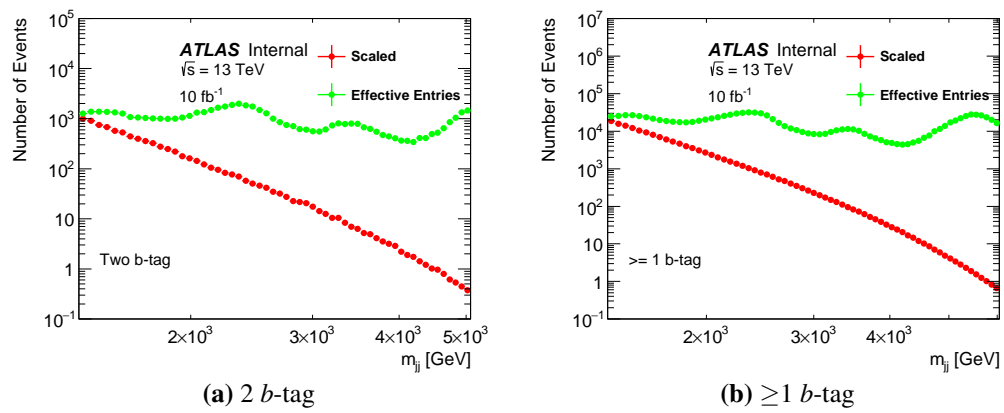


**Figure 8.1:** The scaled dijet mass spectrum (red) compared to the effective entries dijet mass spectrum (green) from QCD dijet simulation for the (a) 2 and (b)  $\geq 1$   $b$ -tag category. The *Summer16\_HighMass* data-set event selection has been applied.

## 8.4.2 Validation Studies: Dijet Mass Range Studies

The first validation study performed is to show that the dijet fit functions are able to describe the dijet mass spectra in the mass range considered. To perform this study the search phase is applied to the scaled dijet mass spectra from simulation, as described in the previous section.

For this validation study the dijet mass spectrum uses the statistical uncertainties of the simulated sample, which are given by the square root of the number of effective entries. 10,000 pseudo-experiments are used to calculate BumpHunter and DeficitHunter  $p$ -values, as will be done in all *Summer16\_HighMass* search phase validation studies. The initial dijet mass spectra are considered with the lower edge of the dijet mass spectrum at  $m_{jj} = 1100$  GeV, selected such that there is no kinematic bias from the single jet trigger, and an upper mass edge at the lowest dijet mass bin which contains less than one entry.

When performing the dijet mass range validation studies, the dijet fit function that would be used in the final data-set was not known. Therefore, it was necessary to select a dijet fit function to perform this study; the 4 dijet fit function was chosen. The 3 parameter dijet fit function was not selected as it represents a special case of the 4 parameter dijet fit function when one parameter ( $p_4$ ) is set to zero; hence if the 4 parameter dijet fit function cannot adequately describe the background neither can the 3 parameter dijet fit function. The 5 parameter dijet fit function was not chosen as, at the time, it had not been used or validated at previous di- $b$ -jet searches.

Figure 8.2 shows the search phase for both  $b$ -tag categories, using the 4 parameter dijet fit function and the lower edge of the dijet mass spectrum at  $m_{jj} = 1100$  GeV. The most discrepant excess is indicated by the blue lines and the BumpHunter  $p$ -value of the excess is shown on the plot. The lower panel shows the significance in each dijet mass bin, defined as the difference between the data and the background estimate divided by the statistical uncertainty of number of data events.

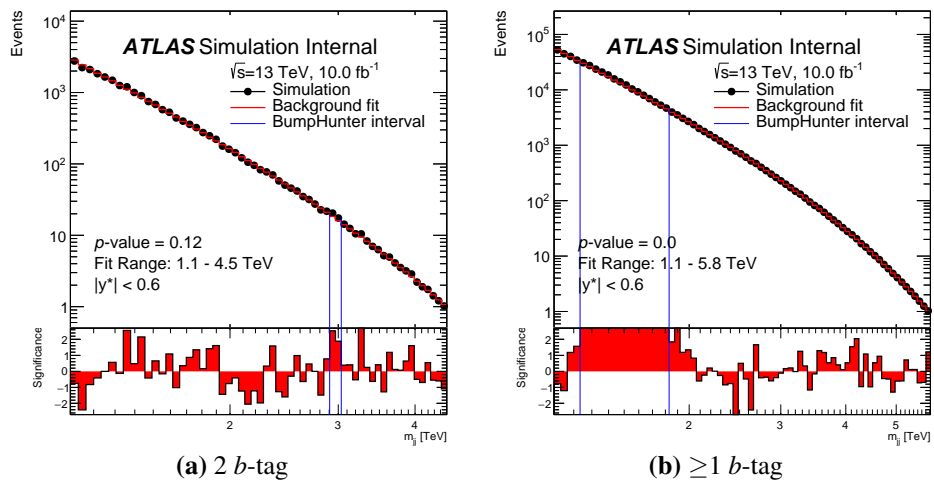


**Figure 8.2:** The scaled dijet mass spectrum from QCD dijet simulation for the (a) 2 and (b)  $\geq 1$   $b$ -tag category, fitted to using the 4 parameter dijet fit function, with the lower edge of the dijet mass spectrum at 1100 GeV. The most discrepant excess as found by the BumpHunter algorithm is indicated by the vertical blue lines and the  $p$ -value of this excess is printed on the plot. The *Summer16\_HighMass* data-set event selection has been applied.

In Figure 8.2 it is shown that, in the  $\geq 1$   $b$ -tag category, a discrepant excess is observed which has been assigned a BumpHunter  $p$ -value of  $<0.0001$ <sup>3</sup>. The search phase was also performed using the 5 parameter dijet fit function to confirm that this would not produce a significantly different result, again a BumpHunter  $p$ -value of  $<0.0001$  is found. This shows that the 4 and 5 parameter dijet fit functions provide a poor description of the background

<sup>3</sup>This means that the observed BumpHunter test-statistic was greater than in all 10,000 pseudo-experiments.

dijet mass spectrum in the  $\geq 1 b$ -tag category. It can also be concluded that the 3 parameter dijet fit function will also be inadequate, as it is a subset of the 4 parameter dijet fit function.

However, by changing the lower edge of the dijet mass spectrum, a region can be found where the dijet fit functions are able to describe the background accurately. To find the largest region with a stable fit quality, the simulated dijet mass spectrum is fitted to using the 4 parameter dijet fit function with the lower edge of the dijet mass spectrum increased one bin at a time from 1100 to 1500 GeV. For each lower edge considered the  $p$ -value of the most discrepant excess is calculated using the BumpHunter algorithm as before, the  $p$ -value of the most discrepant deficit is calculated using the DeficitHunter algorithm, and an overall quality of fit is represented using a  $\chi^2$   $p$ -value. Figure 8.4 shows the distributions of the BumpHunter, DeficitHunter and  $\chi^2$   $p$ -values as the lower edge of the dijet mass spectra is increased for both  $b$ -tag categories. In both categories the background estimations are stable if the lower mass edge of the dijet mass spectrum is  $m_{jj} = 1378$  GeV or above. This demonstrates that at low mass there are features in the background dijet mass spectrum that are causing a poor fit quality, which can be removed by requiring that  $m_{jj} > 1378$  GeV.

Figure 8.3 shows the search phase applied to the dijet mass spectra of the simulated QCD dijet sample with a lower edge at  $m_{jj} = 1378$  GeV for both  $b$ -tag categories using the 4 parameter dijet fit function. The most discrepant excess, as found by the BumpHunter algorithm, is indicated by the blue lines and the  $p$ -value of the excess is shown on the plot. The study presented in this section motivates the requirement that  $m_{jj} > 1378$  GeV in the *Summer16\_HighMass* data-set event selection.

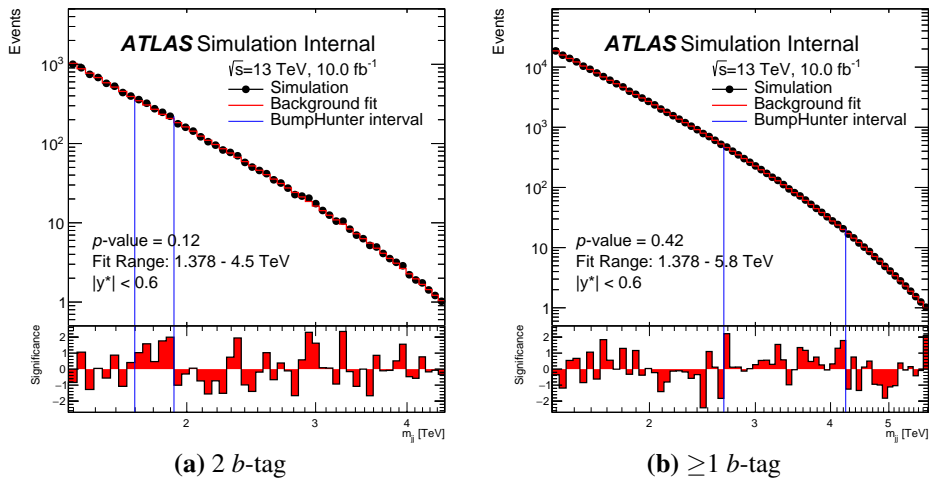


**Figure 8.3:** The scaled dijet mass spectrum from QCD dijet simulation for the (a) 2 and (b)  $\geq 1 b$ -tag category, fitted to using the 4 parameter dijet fit function, with the lower edge of the dijet mass spectrum at 1378 GeV. The most discrepant excess as found by the BumpHunter algorithm is indicated by the vertical blue lines and the  $p$ -value of this excess is printed on the plot. The *Summer16\_HighMass* data-set event selection has been applied.

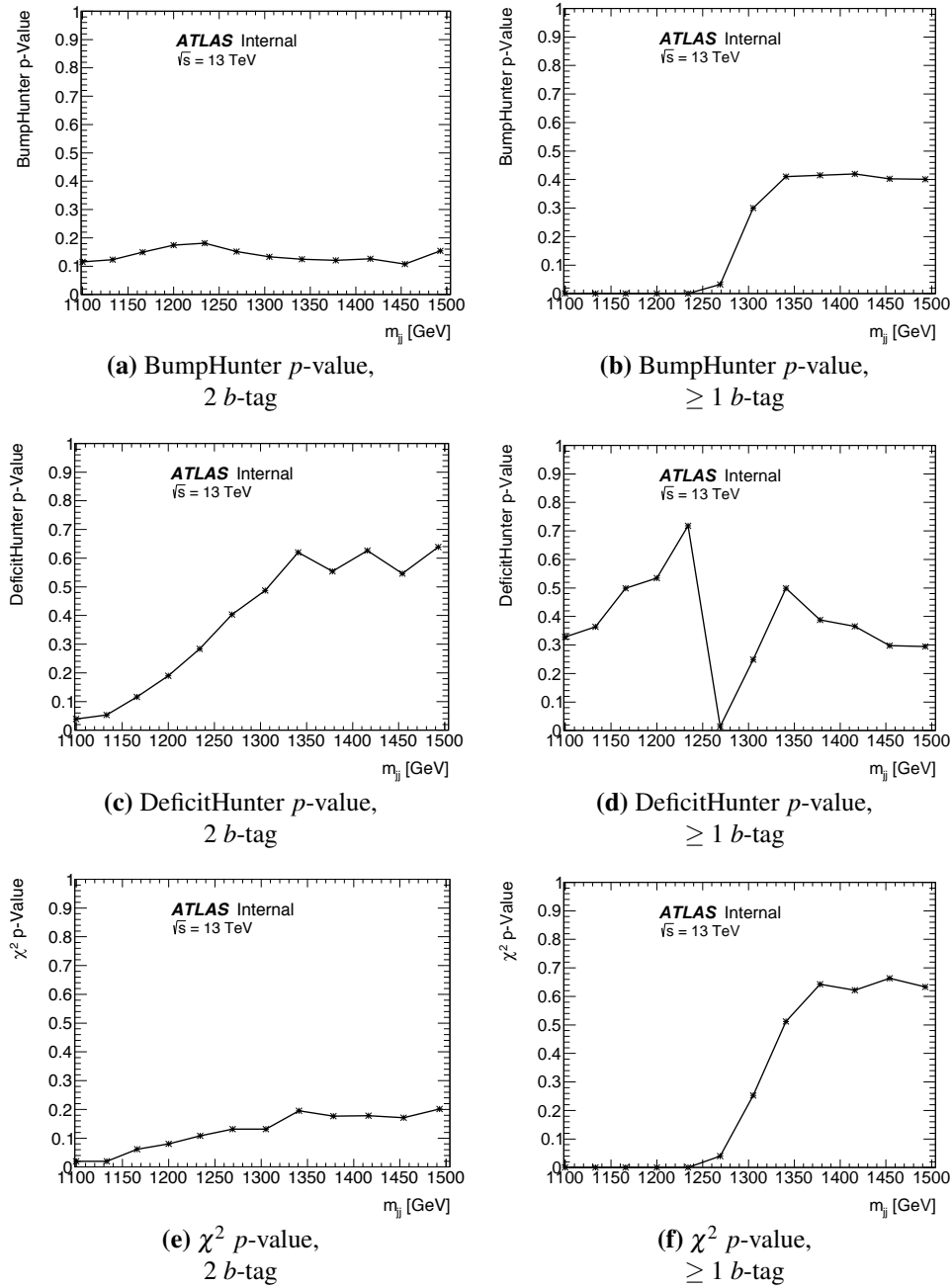


**Figure 8.4:** The BumpHunter (top row), DeficitHunter (middle row) and  $\chi^2$  (bottom row)  $p$ -values for search phases performed to the scaled dijet mass spectrum from QCD dijet simulation using the 4 parameter dijet fit function for the 2  $b$ -tag category (left column) and  $\geq 1 b$ -tag category (right column) as a function of the lower edge of the dijet mass ( $m_{jj}$ ) spectrum. The *Summer16\_HighMass* data-set event selection has been applied.

### 8.4.3 Fit Function Selection

With the range of the dijet mass spectrum selected using Monte-Carlo, shown in the previous section, the dijet fit function is then selected using the final dijet mass spectrum from data and the Wilks'  $p$ -value described in Section 8.2.2. The exact function selection procedure is as follows: using the dijet mass spectrum the Wilks'  $p$ -value is calculated with the 3 parameter dijet function as the nominal function and the 4 parameter dijet fit function as the alternate function. If the Wilks'  $p$ -value is less than 0.05, the nominal fit function is rejected and the alternate function becomes the nominal. The process is iteratively run until a dijet fit function with a Wilks'  $p$ -value  $> 0.05$  is selected.

For the *Summer16\_HighMass* data-set the choice of the dijet fit function was fixed using a  $8.8 \text{ fb}^{-1}$  subset of data. A subset was used such that the function choice could be finalised before the full data-set was collected; this meant that the analysis strategy and search phase validation studies could be scrutinised by other members of the ATLAS collaboration before the conference note publication. With hindsight, I think it would have been more rigorous to calculate Wilks'  $p$ -value on the full data-set.

Figure 8.5 shows the Wilks'  $p$ -value as a function of luminosity for the  $\geq 1$  and  $2$   $b$ -tag categories for the  $8.8 \text{ fb}^{-1}$  subset of data. For both categories the 3 parameter dijet fit function when compared to the 4 parameter dijet fit function has a Wilks'  $p$ -value  $> 0.05$ , therefore the 3 parameter dijet fit function is selected in both categories. Given that the 3 parameter dijet fit function adequately describes the dijet mass spectra of the majority of the data-set it is concluded that it has sufficient parameters to describe the dijet mass spectrum of the full data-set.

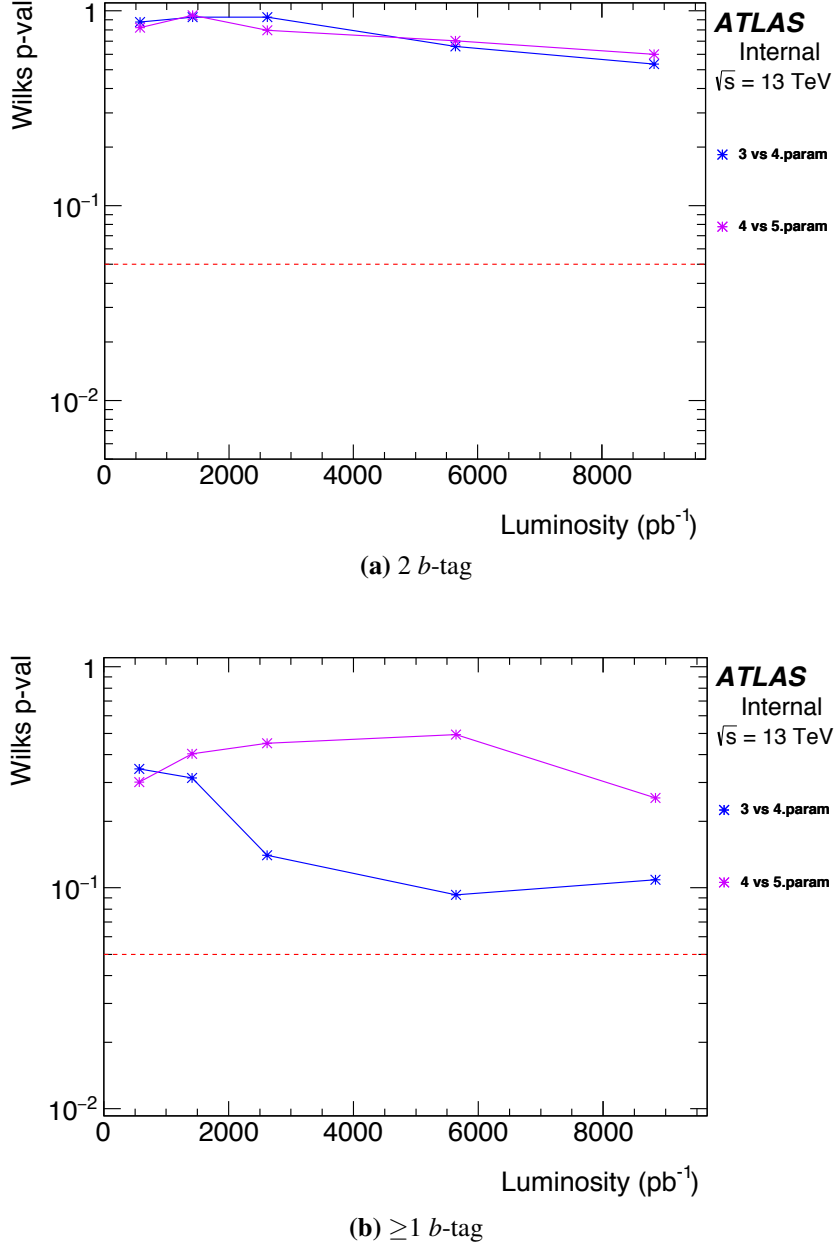


**Figure 8.5:** The Wilks'  $p$ -value as a function of luminosity in the case that the 3 parameter dijet fit function is the nominal and the 4 parameter is the alternate (blue) and the case where the 4 parameter dijet fit function is the nominal and the 5 parameter is the alternate (purple) for a  $8.8 \text{ fb}^{-1}$  subset of the *Summer16\_HighMass* data-set in the (a) 2 and (b)  $\geq 1 b$ -tag category [10].

#### 8.4.4 Validation Studies: Spurious Signal

If an inadequate background estimation is used fit biases can occur, where a fit bias is defined as a difference between the true background dijet mass spectrum and the background estimation. Fit biases that are large compared to the statistical fluctuations of the background can appear as false signal or could hide a true signal, the former is referred to as spurious signal. For the di-*b*-jet search to be able to observe a new particle with confidence it is important to demonstrate that spurious signal cannot occur.

To demonstrate that fit biases are not occurring for the 3 parameter dijet fit function the search phase is performed on the simulated QCD dijet sample, which is a background-only representative data-set. As described in Section 8.4.1, the simulated dijet mass spectrum contains smaller statistical fluctuations than are present in the final data-set. Therefore, to create a dijet mass spectrum representative of the one that is expected in data Poisson fluctuations are applied to the scaled spectrum to create ‘data-like’ dijet mass spectra; Figure 8.6 shows the scaled and effective entries spectra for both *b*-tag categories overlaid with a data-like spectrum in blue.

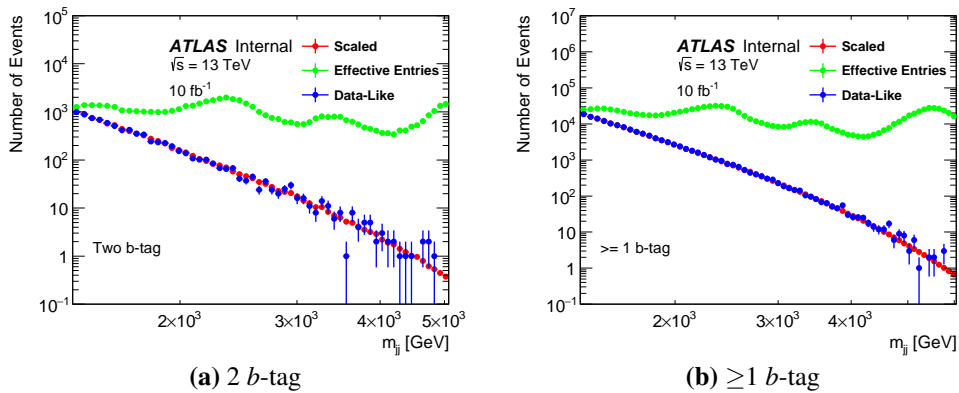


**Figure 8.6:** The scaled dijet mass spectrum (red) compared to the effective entries of the dijet mass spectrum (green) for the (a) 2 and (b)  $\geq 1$  *b*-tag categories. Overlaid is a data-like dijet mass spectrum (blue) created by applying Poisson fluctuations to the scaled spectrum. The *Summer16\_HighMass* data-set event selection has been applied.

The search phase is then applied to the data-like dijet mass spectra in both *b*-tag categories. Figure 8.7 shows the search phase using the 3 parameter dijet fit function applied to a data-like spectrum in both *b*-tag categories. Figure 8.8 illustrates the calculation of the BumpHunter *p*-value in the search phase. For this data-like dijet mass spectrum, in the 2 *b*-tag category the BumpHunter, DeficitHunter and  $\chi^2$  *p*-value are found to be 0.57, 0.80 and 0.39 respectively. Similarly, in the  $\geq 1$  *b*-tag category the BumpHunter, DeficitHunter and  $\chi^2$  *p*-values are 0.93, 0.77 and 0.86 respectively. Therefore, a valid background estimation has been found in both *b*-tag categories for this data-like dijet mass spectrum.

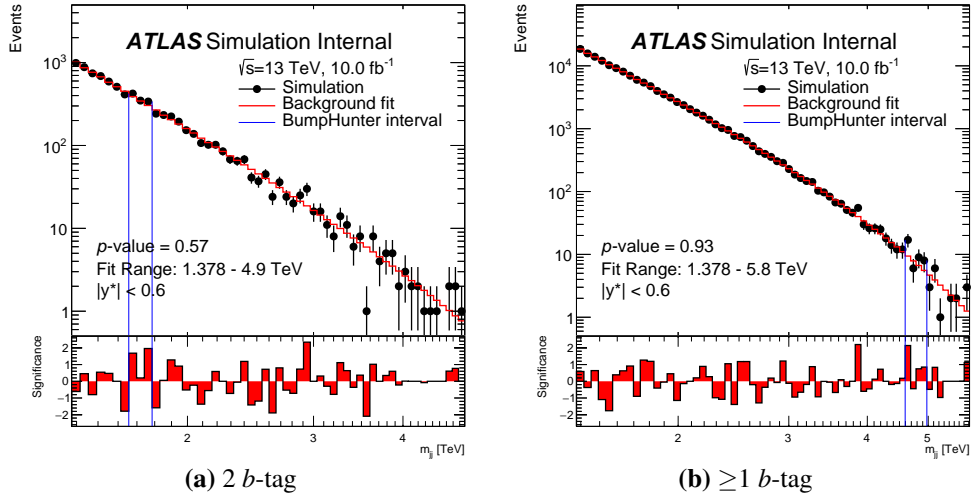


**Figure 8.7:** A data-like dijet mass spectrum from QCD dijet simulation for the (a) 2 and (b)  $\geq 1$   $b$ -tag category, fitted to using the 3 parameter dijet fit function. The most discrepant excess as found by the BumpHunter algorithm is indicated by the vertical blue lines and the  $p$ -value of this excess is printed on the plot. The *Summer16\_HighMass* data-set event selection has been applied.

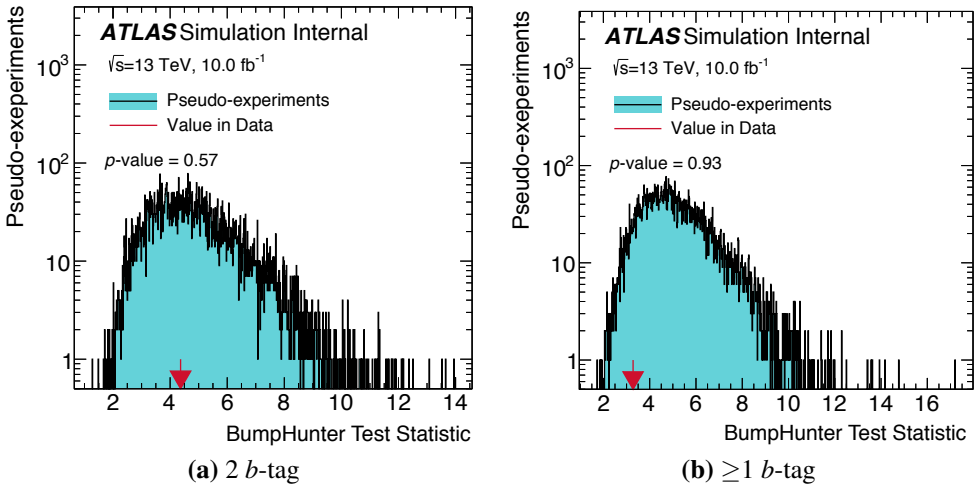


**Figure 8.8:** The observed BumpHunter test statistic (red arrow) when the search phase is applied to a data-like dijet mass spectrum from QCD dijet simulation compared to the distribution of the BumpHunter test statistic for 10,000 pseudo-experiments (blue area) taken from the background estimation for the (a) 2 and (b)  $\geq 1$   $b$ -tag categories. The fraction of pseudo-experiments with a BumpHunter test statistic greater than the observed value is the BumpHunter  $p$ -value. The *Summer16\_HighMass* data-set event selection has been applied.

However, one data-like dijet mass spectrum does not represent the full range of fluctuations that are possible. Therefore, the search phase is applied to an ensemble of data-like dijet mass spectra, each created using a different set of Poisson fluctuations. Figure 8.9 shows the distribution of the BumpHunter, DeficitHunter and  $\chi^2$   $p$ -values for 200 different data-like dijet mass spectra, for the 2 and  $\geq 1$   $b$ -tag category respectively. It can be

noted that there is no bias towards low BumpHunter  $p$ -values, which shows that there is no evidence that a fit bias could cause spurious signal. Similarly there is no bias towards low DeficitHunter  $p$ -values, which shows that there is no evidence that a fit bias could cause fake deficits. Furthermore, the distribution of the  $\chi^2$   $p$ -values also indicates that there is a good fit quality observed in both  $b$ -tag categories.

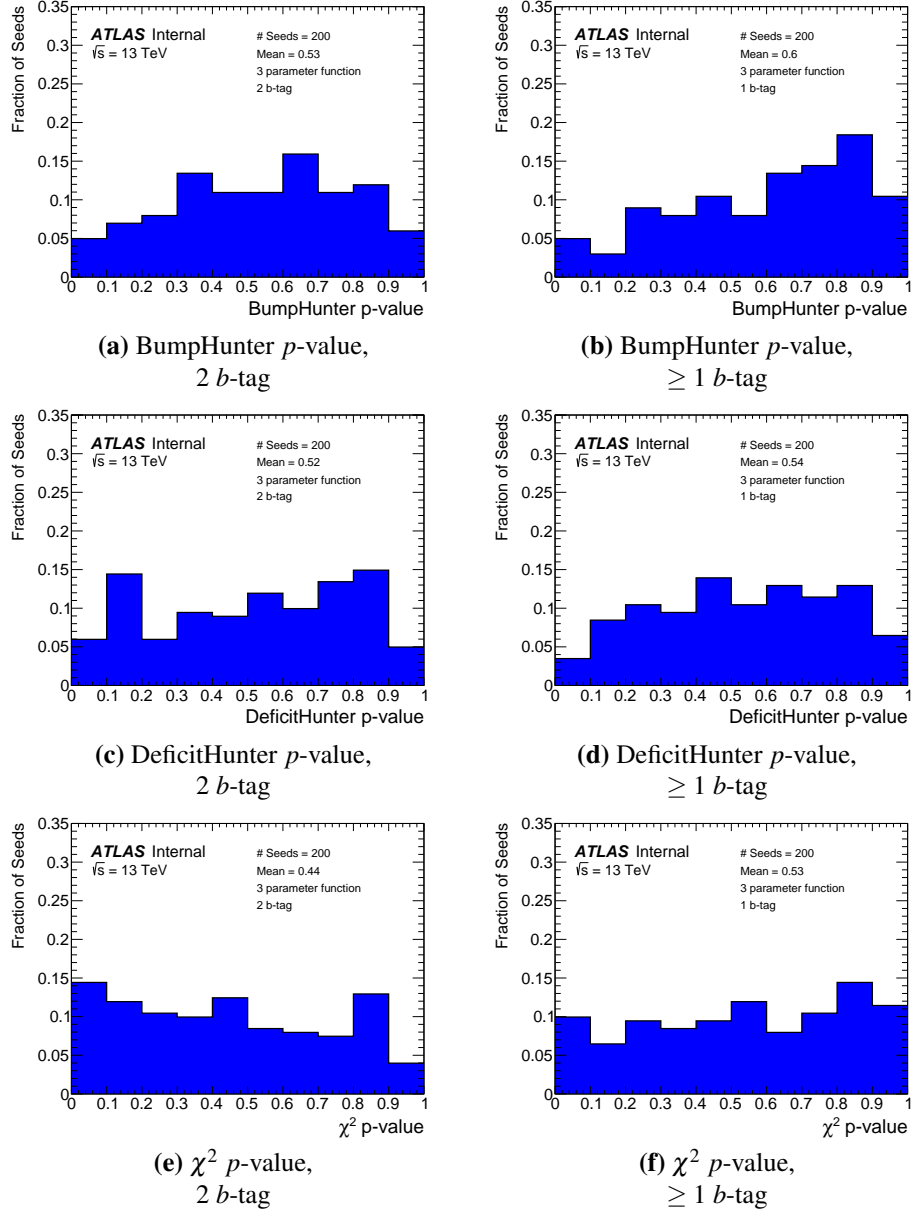


**Figure 8.9:** The normalised distributions of BumpHunter (top row), DeficitHunter (middle row) and  $\chi^2$  (bottom row)  $p$ -values for the search phase using the 3 parameter dijet fit function performed on 200 data-like dijet mass spectra from QCD dijet simulation for the 2  $b$ -tag category (left column) and  $\geq 1$   $b$ -tag category (right column). The *Summer16\_HighMass* data-set event selection has been applied.

### 8.4.5 Validation Studies: Signal Injection

If an excess with a BumpHunter  $p$ -value  $< 0.01$  is observed then the background estimation is performed again with an exclusion region applied. The exclusion region is defined as the mass range of the excess with one additional bin on the low mass side. The fit ignores all bins in the exclusion region, meaning that signal induced fit biases are removed.

It has been shown in previous iterations of the inclusive dijet and di- $b$ -jet searches at ATLAS [2, 12] that, using the region exclusion procedure, the 3 parameter dijet fit function is able to describe a data-like dijet mass spectrum taken from a simulated QCD dijet sample when a signal has been injected. This is because the parameters of the 3 parameter dijet fit function are highly constrained by the QCD background and the region exclusion procedure will remove any signal induced fit bias caused by a large signal. Hence, it is concluded that the search phase using the 3 parameter dijet fit function is robust against the presence of signal.

To conclude the search phase validation studies for the *Summer16\_HighMass* data-set analysis, it has been shown that the 3 parameter dijet fit function has a sufficient number of parameters to provide an adequate background and that there is no evidence that spurious signal can occur. It is also known that the search phase using the 3 parameter dijet fit function will not produce large signal induced fit biases. Hence, the 3 parameter dijet fit function provides a valid background estimation in both  $b$ -tag categories.

### 8.4.6 Search Phase Results

Figure 8.10 shows the dijet mass spectrum of the *Summer16\_HighMass* data-set and the background estimate created using the 3 parameter dijet fit function in the 2 and  $\geq 1$   $b$ -tag categories. The upper panel shows the data compared to the background estimation, in addition the benchmark signal models with enhanced cross sections have been overlaid. The lower panel shows the significance of the difference between the data and background estimate.

In both cases the BumpHunter algorithm has identified the most discrepant excess indicated in the figure using vertical blue lines; the BumpHunter  $p$ -value has been calculated using 10,000 pseudo-experiments. The BumpHunter  $p$ -value is 0.60 in the 2  $b$ -tag category and 0.44 in the  $\geq 1$   $b$ -tag category; this shows that no significant excess is found in either  $b$ -tag category and it is therefore concluded that there is no evidence of a BSM resonance in the *Summer16\_HighMass* data-set. As no significant excess is found, limits on the benchmark signal models are set using the *Summer16\_HighMass* data-set, which will be shown in Chapter 9.

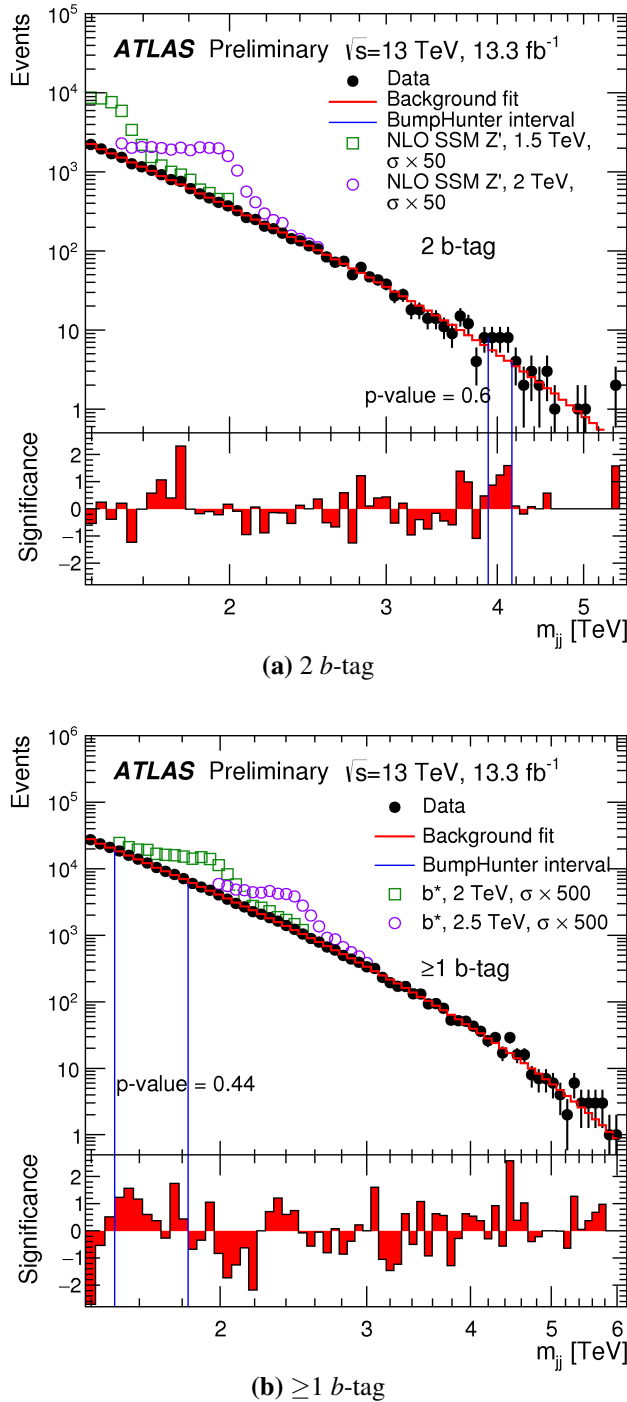


**Figure 8.10:** The dijet mass spectrum of the *Summer16\_HighMass* data-set in the (a) 2 and (b)  $\geq 1$   $b$ -tag category compared to the background estimation created using the 3 parameter dijet fit function. The upper panel shows the data compared to the background estimate, benchmark signal models with enhanced cross sections are overlaid. The lower panel shows the significance of the difference between the data and the background estimate. The most discrepant excess as found by the BumpHunter algorithm is indicated by the vertical blue lines and the  $p$ -value of this excess is printed on the plot [10].

## 8.5 Full16\_LowMass Search Phase

This section presents the search phase for the *Full16\_LowMass* data-set: Section 8.5.1 describes the background-only samples used for the search phase validation studies. Section 8.5.2 demonstrates that the global fit strategy is not a valid strategy for the *Full16\_LowMass* data-set. Section 8.5.3 introduces an alternative background estimation strategy called the Sliding Window Fit (SWiFt) and Section 8.5.4 describes the strategy used for selecting the parameters of the SWiFt background estimation. Sections 8.5.5 – 8.5.7 show validation studies of the search phase performed using the SWiFt background estimation. Sections 8.5.8 – 8.5.9 presents the results of the search phase using the *Full16\_LowMass* data-set.

### 8.5.1 Background-Only Samples

To perform the validation studies of the *Full16\_LowMass* search phase a dijet mass spectrum that represents the shape of the background with no signal contamination is required. In the *Summer16\_HighMass* data-set analysis Monte-Carlo simulation was used, as described in Section 8.4.1. However, as the *Full16\_LowMass* data-set contains  $24.3 \text{ fb}^{-1}$  of data, Monte-Carlo simulation cannot be produced with a large enough statistical precision to perform an adequate test of the background estimation strategy.

Instead two background representative data-sets are used: a  $3 \text{ fb}^{-1}$  subset of data and a high statistical precision fit control region. The  $3 \text{ fb}^{-1}$  subset of data is created from events drawn at random from the final data spectrum. Figure 8.11 shows the dijet mass spectrum of the  $3 \text{ fb}^{-1}$  subset and the full *Full16\_LowMass* data-set. The dijet mass spectrum of the subset represents the shape of the dijet mass spectrum in full data-set, except with a lower statistical precision. The luminosity of the subset of data was chosen to be similar to that of a previous low mass di-*b*-jet search in an equivalent mass range [13], such that this subset of data is known not to be sensitive to signal.

To create the *Full16\_LowMass* fit control region, the dijet mass spectrum of events that have passed the *Full16\_LowMass* event-selection except offline *b*-tagging selection is used, this is referred to as the 0-tag dijet mass spectrum. This dijet mass spectrum contains more events than the final dijet mass spectrum and will have a similar shape as most of the event selection, including online *b*-tagging, has been applied.

To account for the effect of offline *b*-tagging in the fit control region, the 0-tag data must be multiplied by the event-level offline *b*-tagging efficiency with respect to online *b*-tagging,  $\varepsilon_b^{\text{offline}}$ , which is defined as the fraction of events that pass offline *b*-tagging re-

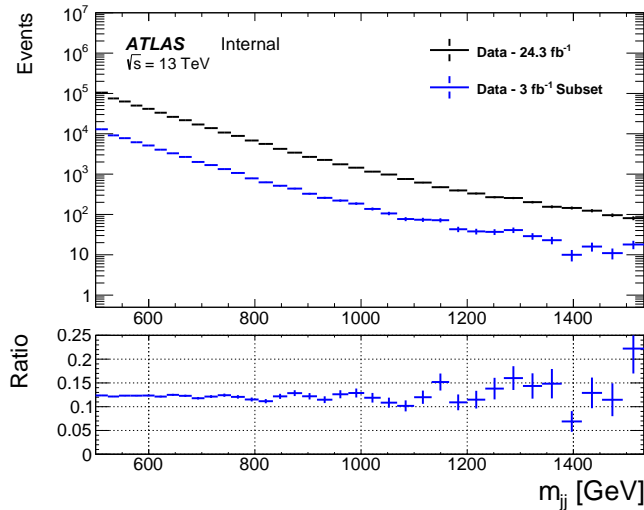


**Figure 8.11:** The dijet mass ( $m_{jj}$ ) spectrum of the full *Full16\_LowMass* data-set and a  $3\text{ fb}^{-1}$  subset of *Full16\_LowMass* data. The lower panel shows a ratio.

quirements given that the events have passed all other requirements of the *Full16\_LowMass* event selection, including online  $b$ -tagging.  $\epsilon_b^{\text{offline}}$  is estimated using the ratio of the dijet mass spectrum from the 0-tag data to the  $3\text{ fb}^{-1}$  subset of data; Figure 8.12(a) shows the two dijet mass spectra and the ratio. The ratio is then scaled by  $24.3/3$  to account for the lower luminosity of the subset of data, and is smoothed using the five parameter dijet fit function. Figure 8.12(b) shows the luminosity adjusted ratio (black points) and the fit (red line). The goodness of fit is estimated by comparing the  $\chi^2$  test statistic to a  $\chi^2$  distribution with the same number of degrees of freedom; a  $\chi^2$   $p$ -value of 0.053 is observed indicating a reasonable fit quality.

The 0-tag spectrum is then scaled by the smoothed estimation of  $\epsilon_b^{\text{offline}}$  to create the dijet mass spectrum of the fit control region. Figure 8.12(c) shows the dijet mass spectrum from the full *Full16\_LowMass* data-set and the fit control region, showing that the fit control region gives a reasonable background-only sample for search phase validation studies.

Two types of dijet mass spectra are created using the fit control region for the search phase validation studies. The first is a ‘smooth’ dijet mass spectrum, where the uncertainties on the fit control region are set to be Poisson like, which means that the uncertainty is the square root of the number of events. This is done such that the uncertainties represent the size of statistical fluctuations expected in the full *Full16\_LowMass* data-set. The second type of dijet mass spectrum is a ‘*data-like*’ dijet mass spectrum, where a random set of Poisson fluctuations are applied to the fit control region, to represent the statistical fluctuations that are observed in data. Many *data-like* dijet mass spectra can be made, each representing a different set of random fluctuations. Figure 8.12(d) shows the comparison of the smooth spectrum and a *data-like* spectrum.

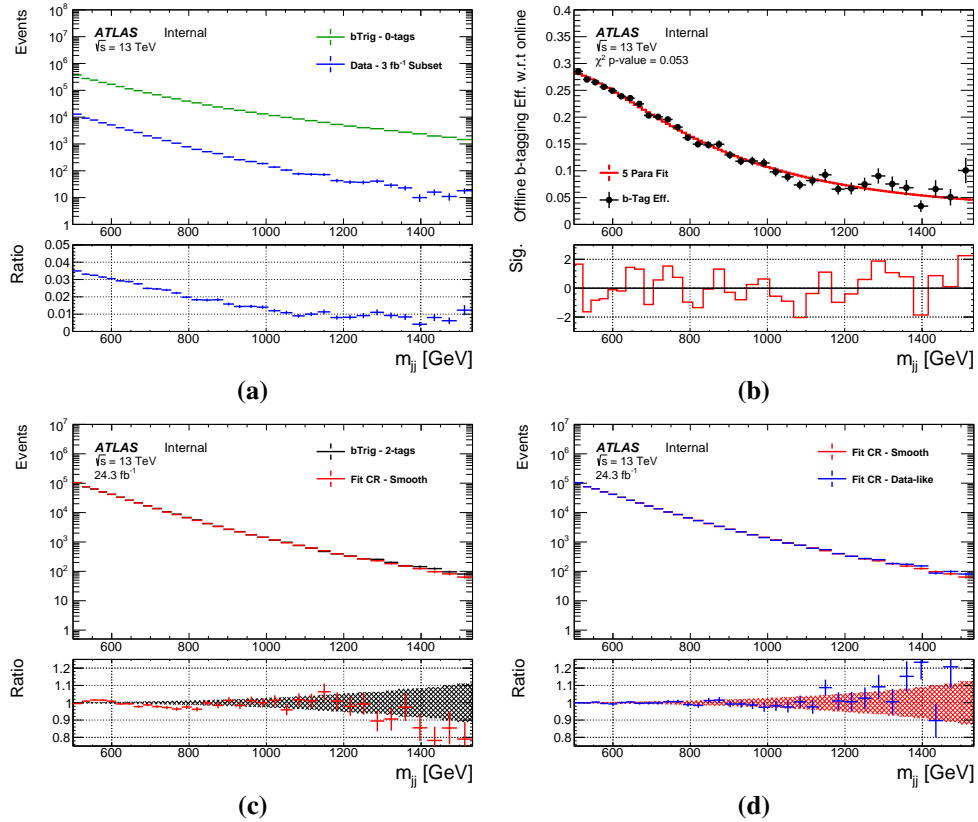


**Figure 8.12:** A figure showing the process of obtaining the fit control region dijet mass ( $m_{jj}$ ) spectrum used for the *Full16\_LowMass* data-set fit studies. Panel (a) shows the dijet mass spectrum of events before  $b$ -tagging is applied (0-tag) and of a  $3 \text{ fb}^{-1}$  subset of *Full16\_LowMass* data. Panel (b) shows the offline  $b$ -tagging efficiency with respect to online  $b$ -tagging estimated using the luminosity adjusted ratio of the two spectra in plot (a), the lower panel shows the significance of difference between the luminosity adjusted ratio and the fit. Panel (c) shows the dijet mass spectrum of the fit control region and the full *Full16\_LowMass* data-set. Panel (d) shows the smooth and data-like dijet mass spectra from the fit control region.

As no offline  $b$ -tagging is applied, the 0-tag data contains larger light jet and  $c$ -jet impurities than the full *Full16\_LowMass* data-set and hence is considered insensitive to signal. As has been discussed above, the  $3 \text{ fb}^{-1}$  subset of data will not be sensitive to signal. Therefore the fit control region is insensitive to signal and can be considered a background-only spectrum.

All search phase validation studies for the *Full16\_LowMass* data-set are performed in the mass region outlined by the *Full16\_LowMass* event selection, 566–1533 GeV. However, the fit control region is created in the dijet mass region 500–1533 GeV because the fit control region was created before the bias due to non-leading jets, described in Section 7.3.1, was observed. As the fit control region is created by applying a smoothed efficiency to each independent dijet mass bin, the bias will not affect events with  $m_{jj} > 566 \text{ GeV}$ .

The use of the subset of data and the fit control region gives two complementary dijet mass spectra to perform search phase validation studies. The subset is representative of the same underlying dijet mass spectrum as the full *Full16\_LowMass* data-set but has lower precision. The fit control region, provides a high-statistic background-only spectra with a similar shape to the dijet mass spectrum of the full *Full16\_LowMass* data-set.

### 8.5.2 Global Fit Strategy

Using a single dijet fit function to model the full mass range considered is known as the global fit strategy. Previous di-*b*-jet searches have used a global fit strategy [12], including the *Summer16\_HighMass* analysis described above.

Figure 8.13 shows the smooth dijet mass spectrum from the fit control region fitted to using the global fit strategy with the 3, 4 and 5 parameter dijet fit functions. The lower panel shows the significance of the difference between the data and the various fits. One would expect an excellent fit quality when an appropriate background estimation is used to model the smooth spectrum as the uncertainties are larger than the true statistical fluctuations present. The 3 parameter dijet fit function has a  $\chi^2/n.d.f. = 3.65$ , where *n.d.f.* represents the number of degrees of freedom, demonstrating an extremely poor fit quality; hence, the 3 parameter dijet fit function is rejected. Further to this, there is a fit bias present for all dijet fit functions, where a fit bias is defined as a difference between the background estimation and the true underlying dijet mass spectrum of the background. The bias is observed as a set of peaks and troughs in the significance plot. A fit bias that is similar in size to the statistical fluctuations may cause a peak to be falsely interpreted as signal or for a trough to mask true signal.

To further quantify the effect of the fit biases in the 4 and 5 parameter case, Figure 8.14 shows the two global fits after the BumpHunter algorithm has been performed. The BumpHunter algorithm assigns *p*-values of 0.418 and 0.513 to the largest excesses in the 4 parameter and 5 parameter case respectively. In the case of the smooth dijet mass spectrum, the BumpHunter *p*-value cannot be interpreted in the conventional way, as the smooth spectrum does not contain the Poisson fluctuations that are present in the pseudo-experiments it is being compared to. Instead, it provides an approximate estimation of the size of the largest fit bias to the size of the largest excesses expected in data due to statistical fluctuations. The fit biases in the global fit for the 4 and 5 parameter dijet fit functions are large relative to the size of statistical fluctuations expected. It is therefore concluded that neither fit function provides an adequate description of the background.

As a result, the global fit strategy is rejected and an alternative background modelling strategy is used. It is not unexpected that the global fit strategy is inadequate for large luminosities and wide mass ranges, as the resulting small statistical uncertainties and large fit ranges mean that any difference between the underlying shape of the QCD dijet mass spectrum and the dijet fit functions are significant.

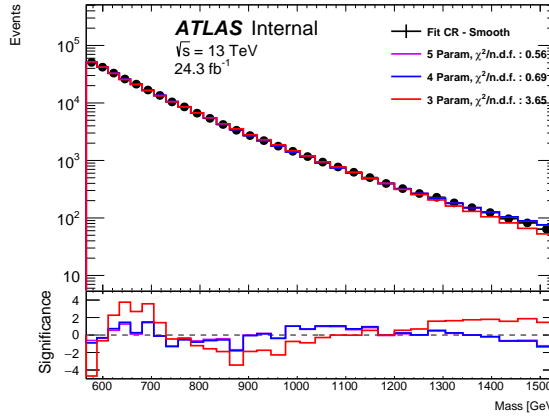


**Figure 8.13:** The smooth dijet mass spectrum from the *Full16\_LowMass* fit control region fitted to using the 3, 4 and 5 parameter global fits. The lower panel shows the significance of the difference between the data and the background fits.

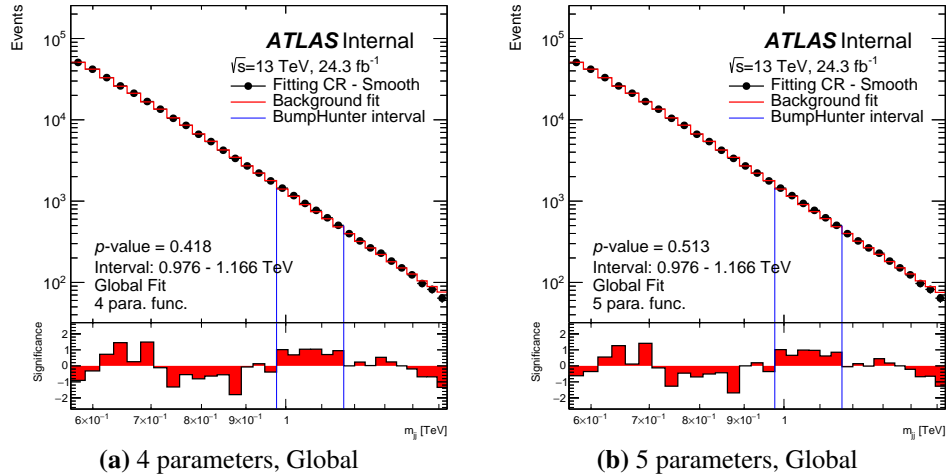


**Figure 8.14:** The global fit and BumpHunter algorithm procedure run on the smooth dijet mass spectrum from the *Full16\_LowMass* fit control region using the 4 and 5 parameter dijet fit functions. The upper panel shows the data compared to the background estimate and the lower panel shows the significance of the difference between the two. The most discrepant excess as found by the BumpHunter algorithm is indicated by the vertical blue lines and the  $p$ -value of this excess is printed on the plot.

### 8.5.3 Sliding Window Fit Background Estimation (SWiFt)

As the global fit strategy cannot provide a valid background estimation in the *Full16\_LowMass* fit control region, an alternate background modelling strategy must be used.

The Sliding Window Fit (SWiFt) background estimation divides the dijet mass spectrum into many overlapping windows, and performs a local fit in each window to provide one point in the dijet mass background estimate. This makes the SWiFt method more stable than the global fit at higher luminosities as the mass range of each fit is reduced. The SWiFt background estimation has been used in the inclusive dijet analysis on the full 2015+2016 ATLAS data-set [3].

The windows used by the SWiFt background estimate are centred at each of the bin boundaries defined by the dijet mass bins, which are shown in Appendix A. The window width is defined by fixing the number of bins below the window centre ( $n_{\text{Low}}$ ) and fixing the number of bins above the window centre ( $n_{\text{High}}$ ). For this analysis symmetric windows are used, defined by their window half-width ( $wHW$ ); i.e.  $n_{\text{Low}} = n_{\text{High}} = wHW$ . Windows are required to have a lower mass bound that is  $\geq 566$  GeV, which is the dijet mass requirement of the event-selection. Figure 8.15 shows the SWiFt windows used in the *Full16\_LowMass* data-set analysis for the window half-widths of 10, 12, 14 and 16.

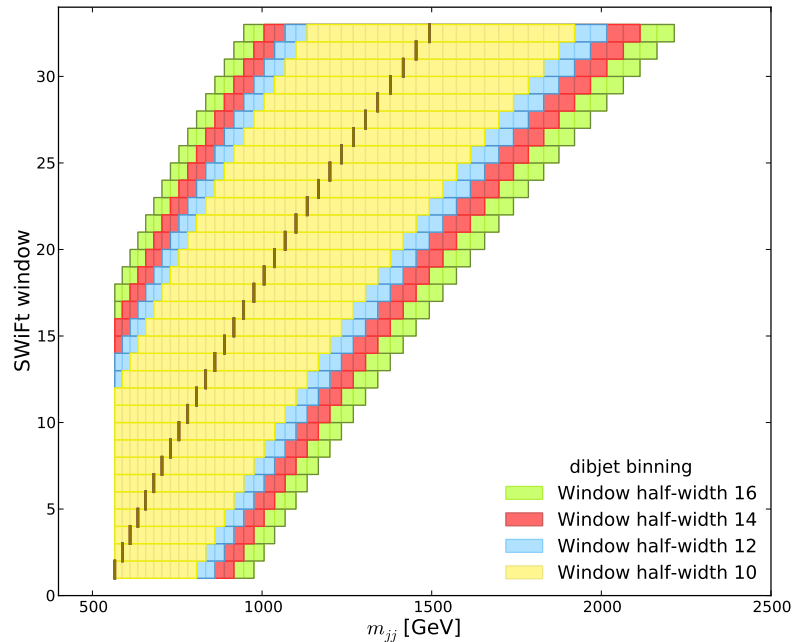


**Figure 8.15:** The windows used by the SWiFt background estimate in the *Full16\_LowMass* data-set analysis for a range of window half-widths. The bin centre is indicated by the black mark and the corresponding window is indicated by the coloured squares.

Windows symmetric in the number of dijet mass bins either side of the centre are chosen as this ensures that there will be an adequate side band on either side of the window centre where possible and reduces the number of parameters that have to be tested. For clarity, it should be noted that because the width of the dijet mass bins is not uniform, the windows used are not exactly symmetric with respect to dijet mass; this effect can be seen in Figure 8.15. Furthermore, it must be noted that enforcing the requirement that the lower mass bound is  $\geq 566$  GeV means that for the lowest mass windows  $n_{\text{Low}}$  is less than  $n_{\text{High}}$ ; again this effect can be clearly seen in Figure 8.15.

In each window a fit to the data is performed using one of the dijet fit functions listed in Table 8.1. The same function is used in all windows, with parameters initially seeded from a configuration file and then from the previous fit. Each of the fits are evaluated at the dijet mass bin which is at the centre of the window, the value is the background estimation for that bin. The SWiFt background estimation for the full dijet mass spectrum is constructed by combining the single bin background estimations from each of the window fits.

Once, a SWiFt background estimation is constructed, it is then compared to data using the BumpHunter algorithm which finds the most discrepant excess region and assigns a  $p$ -value to it. The combination of the SWiFt background estimation and BumpHunter algorithm is referred to as the SWiFt search phase. In the following SWiFt validation studies 1,000 pseudo-experiments are used to calculate the BumpHunter  $p$ -value.

#### 8.5.4 Window Selection Strategy

There are two key input parameters of the SWiFt background estimation:

**1. The window width:**

In this analysis symmetric windows are used, therefore the width of the windows is defined by the window half-width ( $wHW$ ) parameter.

**2. Fit function:**

The dijet fit functions are used, as used in the global fit strategy.

The functions are listed in Table 8.1.

The chosen window half-width and fit function is referred to as the SWiFt configuration. The best sensitivity to signal is achieved by using the largest window width and the dijet fit function with the fewest number of parameters, whilst still obtaining sufficient fit quality. Sensitivity studies that demonstrate this statement are shown below in Section 8.5.7.

To define ‘sufficient fit quality’ the following fit quality criteria are used:

- **Global  $\chi^2$   $p$ -value > 0.05:**

The  $\chi^2$  test statistic is calculated by comparing the data to the SWiFt background estimate. The global  $\chi^2$   $p$ -value is then calculated by comparing the test statistic to a  $\chi^2$  distribution with the number of degrees of freedom equal to the number of bins minus the number of parameters of the fit function.

- **Number of windows with Wilks’  $p$ -value < 0.1 must be  $\leq 10$ :**

The Wilks’  $p$ -value is used to test if an additional parameter is required in the fit function to provide an adequate description of the data, as described in 8.2.2. However, it is not appropriate to require that every window fit passes the Wilks’  $p$ -value  $> 0.05$  criteria used in the global fit strategy, as this does not account for the fact that many fits are performed and it is expected that by chance some fits would fail this requirement. Instead, a requirement is placed that the large majority of windows pass a tighter requirement on the Wilks’  $p$ -value ( $> 0.1$ ), as this indicates that the correct functional form is being used.

To select the optimal SWiFt configuration, a predefined iterative window selection procedure is performed on the full *Full16\_LowMass* data-set. A predefined procedure is used as this means that the most sensitive SWiFt configuration that provides an adequate fit to the final data-set can be selected in a manner in which no personal bias can be introduced.

In the *Full16\_LowMass* data-set, the mass range is 566 – 1533 GeV. This contains 32 bins, which in turn requires 32 windows and 32 fits. A window half-width of 16 is the widest window that is considered, as this configuration is similar to the size of the dijet mass spectrum. A window half-width of 10 is the narrowest window considered for the purposes of the SWiFt search phase validation studies, as at this point the windows are becoming excessively narrow. Figure 8.15 shows the SWiFt windows when the window half-width is 16, 14, 12 and 10.

The 5 parameter dijet fit function is used for the SWiFt background estimation. The 3 parameter dijet fit function was not considered due to its exceptionally poor performance in the global fit, as noted in Section 8.5.2. The 4 parameter dijet fit function was rejected for two reasons. Firstly, the SWiFt background estimation using the 4 parameter dijet fit function shows evidence of spurious signal for most window widths, as will be demonstrated below in Section 8.5.6. Secondly, the SWiFt background estimate for the 4 parameter dijet fit function is less sensitive to signal than using the SWiFt background procedure with the 5 parameter dijet fit function and wider windows, as is demonstrated in Section 8.5.7.

Given the quality requirements outlined above, the strategy for selecting a window width is:

1. Perform the SWiFt background estimate using a window half-width of 16.
2. Use the BumpHunter algorithm to search for any significant excesses ( $p$ -value  $< 0.01$ ), if one is found then a region exclusion procedure is applied.
3. If the fit quality criteria outlined above are passed, select this window width.
4. If not then drop the window half-width by 2, and repeat step (2).

This procedure is repeated until a window half-width is found where the fit quality criteria are passed.

The region exclusion procedure is introduced if the BumpHunter  $p$ -value  $< 0.01$  as a large signal can cause a signal induced fit bias. To remove this bias the region containing the excess is excluded when creating the SWiFt background estimation. The exact region exclusion procedure is outlined in Section 8.5.7. A threshold of 0.01 is used as this signifies an excess that is greater than  $2\sigma$  in significance, and is consistent with the threshold used in previous dijet searches [22]. Therefore, the observation of a BumpHunter  $p$ -value of 0.01 becomes a critical point in this analysis, and as such will be considered as the point at which signal becomes significant for the purposes of the following SWiFt search phase validation studies.

The results of the window selection procedure applied to the full data-set are shown in Section 8.5.8; after the SWiFt search phase validation studies are presented.

### 8.5.5 SWiFt Validation Studies: Window Selection

The SWiFt window selection strategy, described in Section 8.5.4, has been tested in the fitting test data-sets, described in Section 8.5.1.

Firstly, let's examine the results from the SWiFt window selection procedure applied to 100 different data-like spectra from the fit control region when a range of window half-widths and the 5 parameter dijet fit function are used. Table 8.2 shows the fraction of data-like spectra that pass the two fit quality criteria used in the window selection procedure. It is shown that in 99% of cases a window half-width in the range considered would pass the Wilks'  $p$ -value requirement and that in  $> 80\%$  of cases a window half-width in the range considered would pass the global  $\chi^2$   $p$ -value requirement.

The window selection procedure is also tested using the  $3 \text{ fb}^{-1}$  subset of data. Figure 8.16 shows the fit quality measures used in the window width selection procedure, using a range of window half-widths of 16 to 10, for both the 4 and 5 parameter dijet fit function. According to the window selection procedure the 5 parameter dijet fit function with a win-

dow half-width of 16 would have been selected, although the 4 parameter dijet fit function with window half-width of 16 has also passed the fit quality criteria.

Fit Quality Criteria	Window Half-Width			
	16	14	12	10
Global $\chi^2$ $p$ -value $> 0.05$	0.82	0.79	0.83	0.84
Number of windows with Wilks' $p$ -value $< 0.1$ must be $\leq 10$	0.64	0.83	0.98	0.99

**Table 8.2:** The fraction of data-like spectra that pass the fit quality requirements when the SWiFt background estimation procedure is performed for 100 data-like dijet mass spectra taken from the *Full16\_LowMass* fit control region. The SWiFt procedure has been performed using the 5 parameter dijet fit function for the range of window half-widths of 10 to 16.

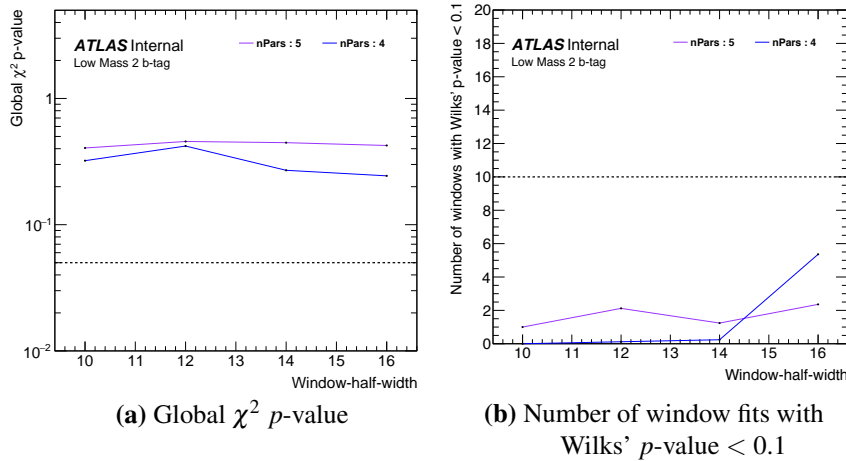


**Figure 8.16:** An illustration of the window selection procedure for a  $3 \text{ fb}^{-1}$  subset of *Full16\_LowMass* data. It shows the global  $\chi^2$   $p$ -value and number of window fits with Wilks'  $p$ -value  $< 0.1$  for the SWiFt background estimate using a range of window half-widths ( $wHW$ ) and number of parameters (nPars) of the dijet fit function. The dotted lines indicate thresholds that are used in the window selection procedure.

### 8.5.6 SWiFt Validation Studies: Spurious Signal

As described in Section 8.4.4, it is important to demonstrate that fit biases and spurious signal will not occur for the SWiFt background estimation strategy, where a fit bias is a difference between the background estimation and the true background dijet mass spectrum, and spurious signal is a false excess caused by a fit bias.

To demonstrate that fit biases are not occurring the SWiFt search phase is performed to background-only representative data-sets and the BumpHunter  $p$ -values are studied for evidence of spurious signal. The SWiFt configurations considered use the 4 and 5 parameter

dijet fit function and window half-widths of 10, 12, 14 and 16; giving 8 different configurations. Only SWiFt configurations that show no evidence of spurious signal are considered in the window selection procedure.

Firstly, we consider the results from the subset of data. Figure 8.17 shows the SWiFt search phase performed on the dijet mass spectrum of the  $3 \text{ fb}^{-1}$  data subset, for the 4 and 5 parameter dijet fit function for a window half-width of 16. The blue lines indicate the largest excess found by the BumpHunter algorithm and the  $p$ -value assigned is printed on the plot. In both cases the background is well modelled and there is no evidence of spurious signal; similar results are found for all window half-widths considered. However, searches for spurious signal using the subset of data are limited by the small statistical precision of the subset relative to the final data-set.

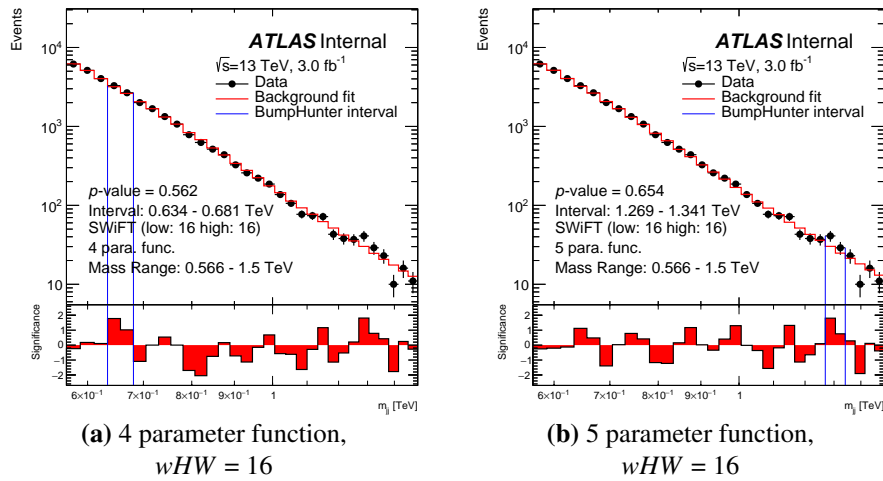


**Figure 8.17:** The SWiFt search phase run on a  $3 \text{ fb}^{-1}$  subset of the *Full16\_LowMass* data-set using the 4 and 5 parameter dijet fit function for a window half-width ( $wHW$ ) of 16. The upper panel shows the data compared to the background estimate and the lower panel shows the significance of the difference between the two. The most discrepant excess as found by the BumpHunter algorithm is indicated by the vertical blue lines and the  $p$ -value of this excess is printed on the plot.

Next, the SWiFt search phase is applied to the smooth dijet mass spectrum from the fit control region where the uncertainties are set to be Poisson like, as described in Section 8.5.1. Performing the SWiFt search phase to the smooth dijet mass spectra gives a direct comparison of any fit biases relative to the background fluctuations expected in data. Figure 8.18 shows the SWiFt search phase performed on the smooth dijet mass spectrum taken from the fit control region, for a SWiFt configuration using the 4 and 5 parameter dijet fit functions and a window half-width of 16 and 10; the full set of plots for all SWiFt configurations considered are in Appendix C.

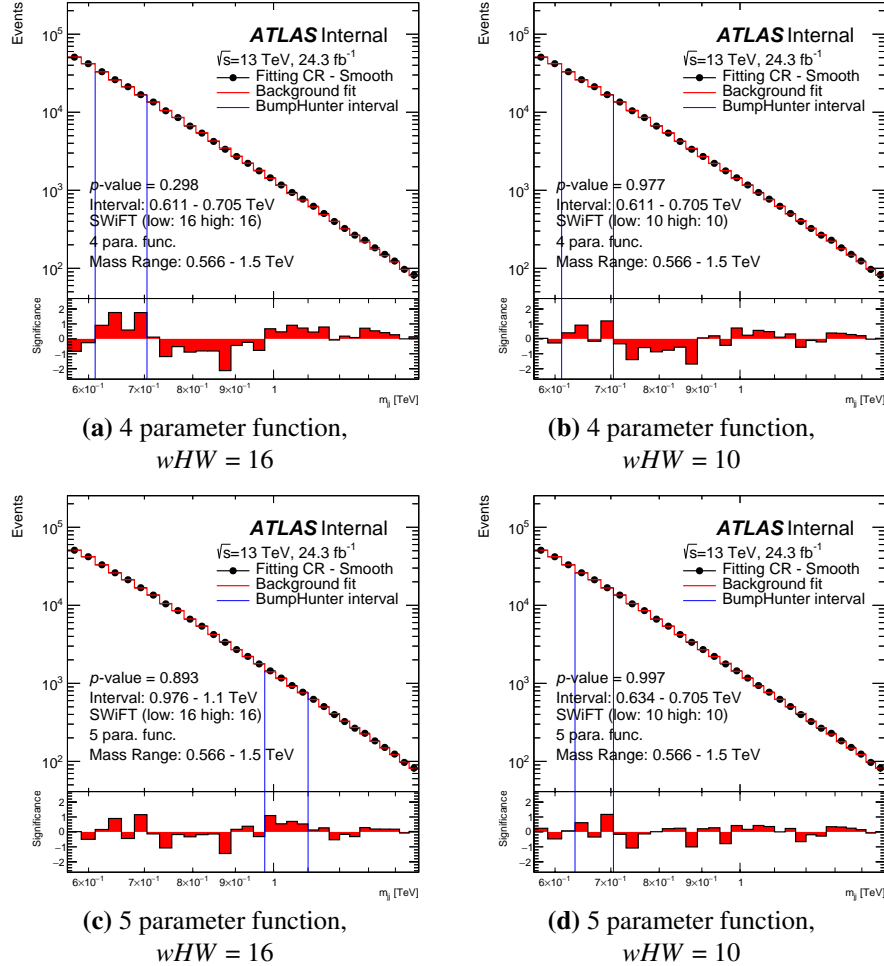


**Figure 8.18:** The SWiFT search phase run on the smooth dijet mass spectrum from the *Full16\_LowMass* fit control region using the 4 and 5 parameter dijet fit function for a window half-width ( $wHW$ ) of 10 and 16. The upper panel shows the data compared to the background estimate and the lower panel shows the significance of the difference between the two. The most discrepant excess as found by the BumpHunter algorithm is indicated by the vertical blue lines and the  $p$ -value of this excess is printed on the plot.

As was discussed in Section 8.5.2, in the case of the smooth spectrum the BumpHunter  $p$ -value provides an approximate estimation of the size of the largest fit bias relative to the size of the largest excesses expected in data due to statistical fluctuations, therefore a low  $p$ -value is an indication that a spurious signal can occur. For the 4 parameter dijet fit function with a window half-width of 16 a BumpHunter  $p$ -value of 0.298 is observed indicating that there is a fit bias which is large relative to the expected statistical fluctuations. It is also notable that for the 4 parameter dijet fit function there is a large deficit observed in the middle of the mass range for both window half-widths shown. In the 5 parameter dijet fit function BumpHunter  $p$ -values of 0.826 and 0.987 are observed in the window half-width of 16 and 10 respectively, which indicates that the largest fit bias is not larger than the size of the excesses expected from statistical fluctuations.

The SWiFt search phase performed on the smooth dijet mass spectrum provides a good visual representation and approximate size of possible fit biases. However, it is possible that fit biases could enhance statistical fluctuations to create spurious signal in data-sets containing Poisson fluctuations. To demonstrate that this is not occurring, the SWiFt search phase is applied to many data-like dijet mass spectra, where Poisson fluctuations are applied to the fit control region as described in Section 8.5.1. Figure 8.19 shows an example of the SWiFt search phase performed on a data-like dijet mass spectrum taken from the fit control region. The SWiFt configurations with a window half-width of 16 for the 4 and 5 parameter dijet fit function are shown, the full set can be found in Appendix C. The fit biases noted in Figure 8.18 are still visible in the 4 parameter case. In the 5 parameter case the BumpHunter algorithm has not identified a discrepant excess indicating there is no spurious signal for this particular data-like spectrum.

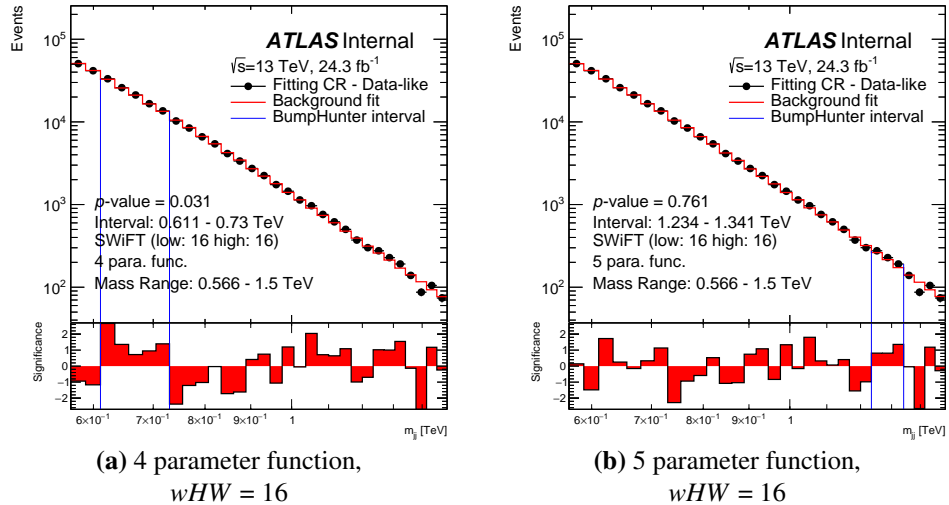


**Figure 8.19:** The SWiFt search phase run on a data-like dijet mass spectrum of the *Full16\_LowMass* fit control region. The SWiFt procedure has been run for the 4 and 5 parameter dijet fit function for a window half-width ( $wHW$ ) of 16. The upper panel shows the data compared to the background estimate and the lower panel shows the significance of the difference between the two. The most discrepant excess as found by the BumpHunter algorithm is indicated by the vertical blue lines and the  $p$ -value of this excess is printed on the plot.

The SWiFt search phase is performed on 100 data-like dijet mass spectra and the distribution of BumpHunter  $p$ -values is studied to search for evidence of spurious signal. 500 data-like spectra are used in the case of the 5 parameter fit for window half-widths of 14 and 16 as increased statistical precision is required to make the necessary conclusion for these configurations. Each data-like spectrum is referred to as a ‘seed’.

Figure 8.20 shows the normalised distribution of  $p$ -values for the ensemble of data-like dijet mass spectra for a subset of the SWiFt configurations considered, the full range of plots can be found in Appendix C. Table 8.3 shows the percentage of data-like spectra (or seeds) that have a BumpHunter  $p$ -value less than 0.05 and 0.01 for the full range of SWiFt configurations considered; in particular 0.01 is important as it is the threshold for an excess region to be considered significant enough to exclude from the background estimation procedure.

For the 4 parameter dijet fit function and a window half-width of 12, 14 and 16 there is a clear bias towards low BumpHunter  $p$ -values; in particular significantly more than 1% of seeds have a BumpHunter  $p$ -value of less than 0.01. Hence, it is concluded that all SWiFt configurations with the 4 parameter dijet fit function with window half-width greater than 10 show evidence of spurious signal. For the 4 parameter dijet fit function with a window half-width of 10, there is no evidence of spurious signal; however this SWiFt configuration is not used as it is less sensitive to signal than SWiFt configurations using the 5 parameter dijet function with wider windows, as will be shown in Section 8.5.7. In the case of all SWiFt configurations using the 5 parameter dijet fit function there is no significant bias towards low BumpHunter  $p$ -values, specifically the number of seeds with a BumpHunter  $p$ -value of less than 0.01 is consistent with expectations. There is a deficit of seeds with a BumpHunter  $p$ -value  $> 0.9$  for all SWiFt configurations; this is because the dijet mass spectrum of the fit control region is not perfectly smooth, as there are small statistical fluctuations present in the 0-tag dijet mass spectrum.

Therefore, it is concluded that for SWiFt configurations using the 5 parameter dijet fit function there is no evidence that spurious signal can occur in the window half-widths considered.

Dijet Fit Function	$wHW$	Fraction of Seeds with BH $p$ -value <		Number of Seeds
		0.05	0.01	
4 parameter	16	31% (26-35%)	7.0% (4-10%)	100
	14	13% (9-16%)	4.0% (2-6%)	100
	12	10% (7-13%)	4.0% (2-6%)	100
	10	2% (1-4%)	1.0% (0-3%)	100
5 parameter	16	4.0% (3.2-4.9%)	1.2% (0.8-1.8%)	500
	14	2.4% (1.8-3.1%)	0.8% (0.5-1.3%)	500
	12	1% (0-3%)	0.0% (0-1%)	100
	10	2% (1-4%)	1.0% (0-3%)	100

**Table 8.3:** The fraction of data-like dijet mass spectra (seeds) with a BumpHunter (BH)  $p$ -value less than 0.05 and 0.01, when the SWiFt search phase with the 4 and 5 parameter dijet fit function and various window half-widths ( $wHW$ ) is performed on an ensemble of data-like spectra taken from the *Full16\_LowMass* fit control region.  $1\sigma$  confidence interval on the fractions are shown in brackets. The number of seeds used for each SWiFt configuration is shown in the table.

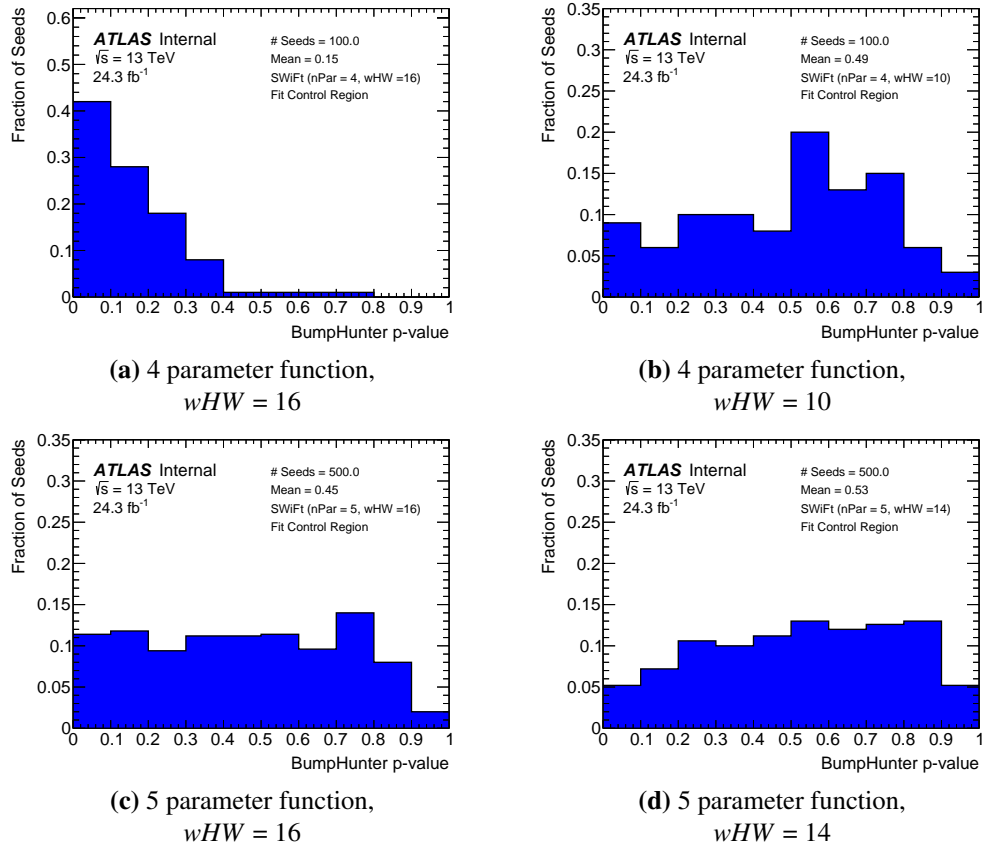


**Figure 8.20:** The normalised distributions of BumpHunter  $p$ -values from performing the SWiFt background estimate on an ensemble of data-like dijet mass spectra (seeds) from the *Full16\_LowMass* fit control region, shown for the 4 and 5 parameter dijet fit function for a selection of window half-widths ( $wHW$ ). The number of data-like spectra used is given on the plot.

### 8.5.7 SWiFt Validation Studies: Signal Injection

In the previous two subsections it is shown that the SWiFt background estimate procedure is effective in the case that there is no signal. However, it is also required to test the SWiFt search phase in the case that signal is present to show that signal can be identified and the remaining background estimate is valid.

To identify signal, the SWiFt search phase uses the BumpHunter algorithm to identify the most discrepant excess region and assigns that region a  $p$ -value. If the  $p$ -value is  $< 0.01$  then an exclusion region procedure is used to remove any signal induced fit bias in the background estimation. The exclusion region procedure is as follows.

1. Define an exclusion region as the discrepant excess region identified by the BumpHunter algorithm extended on the low mass side by including the dijet mass bin adjacent to the excess region. It has been shown that the additional dijet mass bin is required to remove signal induced fit bias [2].

2. Create an updated background estimate by performing the SWiFt fitting procedure to the dijet mass spectrum, ignoring the exclusion region in all fits and fit quality measures.
3. Identify an updated excess region, by performing the BumpHunter algorithm to the dijet mass spectrum using the updated background estimate created in Step 2. For this step the exclusion region is not ignored.
4. If the updated excess region is *not* contained within the initial exclusion region, then the procedure returns to Step 1 using the updated excess region. This step ensures that the full effect of the signal induced fit bias is removed.
5. If the updated excess region is contained within the initial exclusion region, the updated background estimate is tested using the fit quality criteria outlined in Section 8.5.4. If the fit quality criteria are passed, the updated background estimation is used. If the fit quality criteria are failed, then a narrower window is tested.

This process will be illustrated with an example below for clarity.

Signal injected dijet mass spectra are used to validate the SWiFt search phase in the case that signal is present. To create the signal injected spectra, the dijet mass signal templates, described in Section 6.3, are added to the data-like dijet mass spectrum taken from the background-only fit control region. The dijet mass signal templates of a sequential standard model (SSM)  $Z'$  boson with generated masses of 600, 800 and 1000 GeV are used in the following studies. The size of the signal is varied by applying a normalisation factor of 1, 2 or 3 to the simulated signal templates. Therefore the size of signal in these studies is given relative to the nominal simulated cross-section from PYTHIA8; for example ‘xs\*2’ means that a normalisation factor of 2 is used.

In the following section two studies with the signal injected spectra are shown:

### 1. Sensitivity Studies

Studies are performed to show that the SWiFt search phase is sensitive to signal, and to determine which choices of window half-width and fit function are most sensitive. In these studies the SWiFt search phase is applied to the signal injected spectra described above and the BumpHunter  $p$ -values for various SWiFt configurations are studied. A  $p$ -value  $< 0.01$  is considered significant in this study, as in these cases the region exclusion procedure would be applied. For comparing the sensitivity of two SWiFt configurations a comparison of the observed BumpHunter  $p$ -values is used, where a lower  $p$ -value indicates a better sensitivity.

### 2. Robustness of Window Selection Procedure

Studies are performed to show that, if signal is present, the window selection procedure is able to select a window and the SWiFt search phase can create an adequate description of

the background. In these studies, the region exclusion and window selection procedure described above is applied to SWiFt search phases that find a BumpHunter  $p$ -value  $< 0.01$  in the sensitivity studies.

As an example let's first consider the  $Z'$  boson with mass of 800 GeV. The SWiFt search phase is performed on a data-like dijet mass spectrum with an injected  $Z'$  boson with mass of 800 GeV and the nominal cross section. Figure 8.21 shows the results of the SWiFt search phase using the 5 parameter dijet fit function and a range of window half-widths of 16 to 10. For all window widths, the BumpHunter algorithm has correctly identified the signal region location and, in the case of the window half-width of 14 and 16, has assigned a significant  $p$ -value ( $< 0.01$ ).

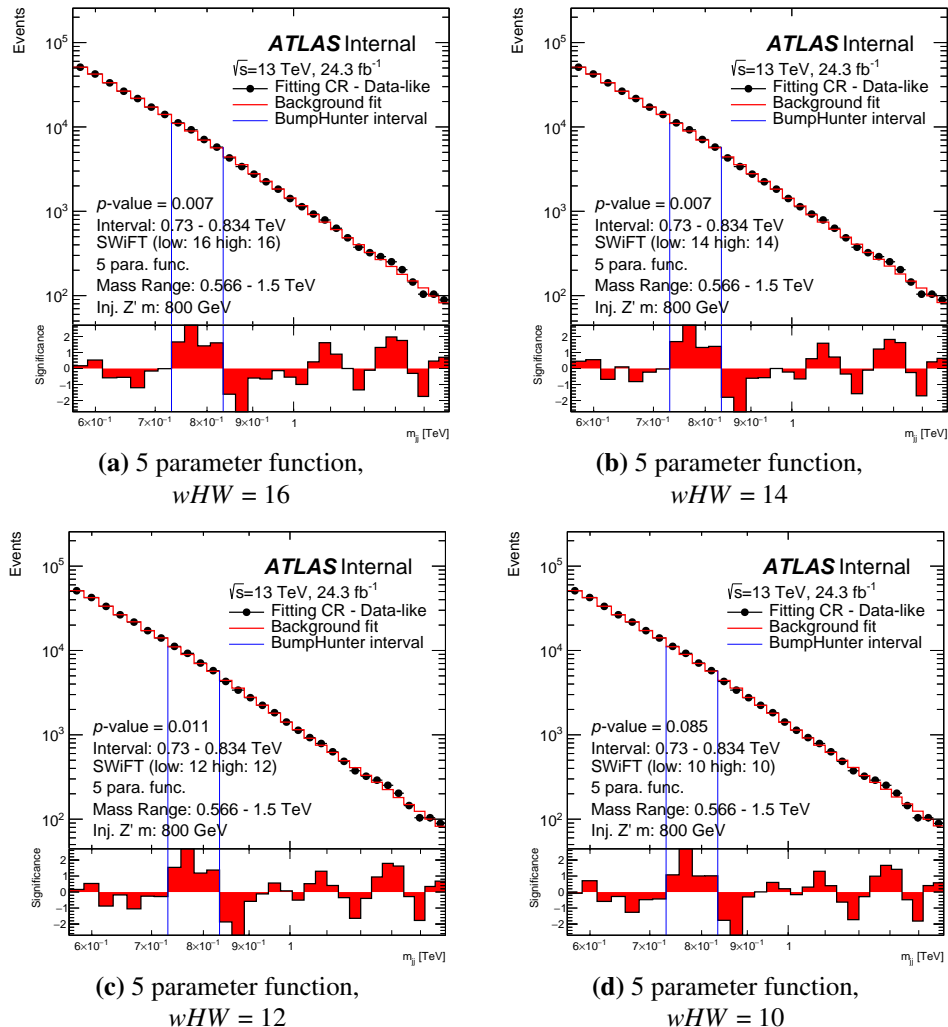


**Figure 8.21:** The SWiFt search phase run on a data-like dijet mass spectrum from the fit control region with a simulated SSM  $Z'$  boson of mass 800 GeV injected. The SWiFt procedure has been run for the 5 parameter dijet fit function for a window half-width ( $wHW$ ) range of 10 to 16.

Therefore, in the case of the window half-width of 14 and 16 the region exclusion procedure is applied. The region excluded is 705-834 GeV, derived by adding one bin on the low mass side of the excess region identified by the BumpHunter algorithm (730-834 GeV). Figure 8.22 shows the SWiFt search phase performed on the same spectrum when a region exclusion of 705-834 GeV is applied. The new excess found lies within the exclusion region which indicates that any signal induced fit bias has been removed and therefore the exclusion region does not need to be widened.

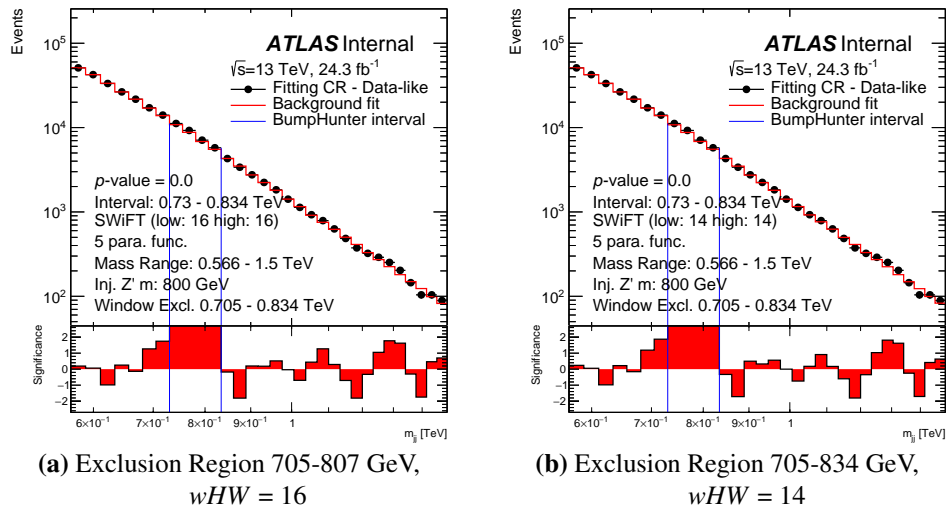


**Figure 8.22:** The SWiFt search phase run on a data-like dijet mass spectrum from the fit control region with a simulated SSM  $Z'$  boson of mass 800 GeV and the nominal cross-section injected. The SWiFt search phase is run for the 5 parameter dijet fit function for a window half-width ( $wHW$ ) of (a) 16 and (b) 14 with an exclusion region of 705-834 GeV.

Figure 8.23 shows the fit quality measures used in the window selection procedure after the region exclusion of 705-834 GeV is applied, for a window half-width of 14 and 16 for the 5 parameter dijet fit function. Only two window half-widths are considered as these are the only windows that had a significant enough  $p$ -value to trigger the region exclusion procedure in Figure 8.21. The window selection procedure would chose the SWiFt background estimate with the 5 parameter dijet fit function and a window half-width of 14.

Hence, it can be concluded that the SWiFt search phase and region exclusion procedure can identify a  $Z'$  boson with a mass of 800 GeV at the nominal cross-section. The BumpHunter  $p$ -value assigned after region exclusion is applied is  $< 0.001$  using 10,000 pseudo-experiments; this shows that the excess has a significance greater than  $3\sigma$ .

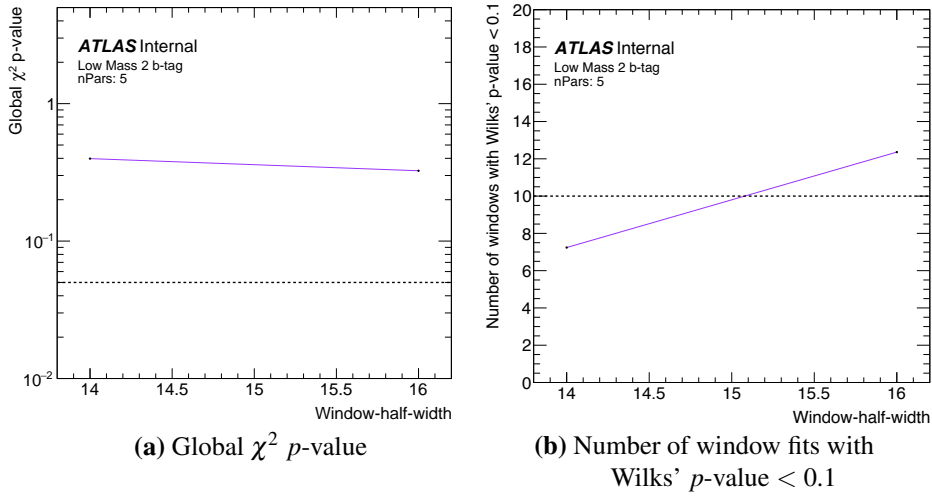


**Figure 8.23:** An illustration of the window selection procedure for a data-like dijet mass spectrum when a simulated SSM  $Z'$  boson of mass 800 GeV has been injected with the nominal cross-section, and a region of 705–834 GeV has been excluded from the SWiFt background estimation. The global  $\chi^2$  *p*-value and the number of window fits with Wilks' *p*-value  $< 0.1$  of the SWiFt background estimate are shown for a range of window half-widths ( $wHW$ ) and the 5 parameter dijet fit function. The procedure would have selected the 5 parameter dijet fit function with a window half-width of 14.

Similar tests are performed for a data-like dijet mass spectrum with a SSM  $Z'$  boson injected at masses of 600, 800 and 1000 GeV. The SWiFt configurations considered use the 4 and 5 parameter dijet fit function and window half-widths ranging from 10 to 16. The 4 parameter dijet fit function is also considered to compare the sensitivity of the two fit functions. Table 8.4 shows the BumpHunter *p*-value when performing the SWiFt search phase on each of the injected spectra for all SWiFt configurations considered with no region exclusion applied. A dash indicates that the largest excess found by the BumpHunter algorithm is not consistent with the mass of the injected signal. Bold text indicates that the SWiFt configuration has a BumpHunter *p*-value  $< 0.01$  and is selected by the window selection procedure after the region exclusion procedure has been applied.

There are four important conclusions that are taken from Table 8.4.

Firstly, all SWiFt configurations are able to obtain a BumpHunter *p*-value  $< 0.01$  if the cross-section is high enough. At 800 GeV the cross-section required is that of the nominal Monte-Carlo simulation, whilst for the 600 and 1000 GeV points the cross-section needs to be increased to 3 and 2 times respectively. For the  $Z'$  boson at 600 GeV, a large cross-section is required indicating that there is a signal induced fit bias in this case; this is due to the fact that the generated mass is close to the low mass edge of the dijet mass spectrum, meaning there is no side-band to constrain the background estimate at a dijet mass of 600 GeV.

Secondly, for all signals considered that trigger the region exclusion procedure a window width can be selected; this shows that the region exclusion and window selection procedure is robust in the case that signal is present.

Thirdly, SWiFt configurations that use large window half-widths are more sensitive to signal, this can be seen by comparing BumpHunter  $p$ -values for identical injected signals across SWiFt configurations in Table 8.4. Take for example the case when the simulated mass is 800 GeV, the signal normalisation is 1 and the 5 parameter dijet fit function is used; we see that the  $p$ -value observed for the widest window considered ( $wHW = 16$ ) is notably lower than the narrowest window considered ( $wHW = 10$ ), indicating that the wider window is more sensitive to signal. This case is particularly notable as only for the two widest widths considered ( $wHW = 16$  or 14) is the  $p$ -value below the threshold to trigger the window exclusion procedure. Furthermore, in all but one of the rows shown in Table 8.4 the widest window considered has a  $p$ -value  $< 0.01$ , which would trigger the exclusion region procedure, or has a  $p$ -value lower than the  $p$ -value of the narrowest window considered; this shows that overall the best sensitivity to signal is found by using a large window-half-width.

Simulated Mass [GeV]	Signal Norm.	nPars	Window Half-Width			
			10	12	14	16
600	2	4	0.061	0.071	-	-
		5	0.110	0.093	0.104	0.045
	3	4	$<0.001$	0.001	0.001	0.005
		5	0.003	0.001	0.001	<b>&lt;0.001</b>
800	1	4	0.100	0.069	-	-
		5	0.085	0.011	<b>0.007</b>	0.007
	2	4	$<0.001$	$<0.001$	$<0.001$	$<0.001$
		5	<b>&lt;0.001</b>	$<0.001$	$<0.001$	$<0.001$
1000	1	4	0.120	0.112	0.098	0.074
		5	-	-	0.107	0.093
	2	4	$<0.001$	$<0.001$	$<0.001$	$<0.001$
		5	$<0.001$	$<0.001$	$<0.001$	<b>0.001</b>

**Table 8.4:** The BumpHunter  $p$ -value when performing the SWiFt search phase with no region exclusion applied on a data-like dijet mass spectrum that has been injected with a sequential standard model  $Z'$  boson with a variety of generated masses when the cross-section has been multiplied by a normalisation factor 1, 2 or 3 (Signal Norm.). The SWiFt search phase has been performed using a window half-width range of 10 to 16 and the number of parameters used in the dijet fit function (nPars) are 4 or 5. A dash indicates that the largest excess found by BumpHunter algorithm is not consistent with the generated mass of the injected signal. Bold text indicates that the SWiFt configuration has a BumpHunter  $p$ -value  $< 0.01$  and is selected by the window selection procedure after the region exclusion procedure has been applied.

The fourth conclusion is that the SWiFt search phase with a 5 parameter dijet fit function and a window half-width of 16 provides better sensitivity than the SWiFt search phase with a 4 parameter dijet function and window half-width of 10. This can be concluded from Table 8.4 by noting that, for all signals considered, the 5 parameter dijet fit function and window half-width of 16 has a  $p$ -value that can trigger the exclusion region procedure ( $< 0.01$ ) or has a  $p$ -value lower than the  $p$ -value when using the 4 parameter dijet fit function and window half-width of 10. The final two conclusions are important factors in the development of the window selection procedure, described in Section 8.5.4.

It should also be noted that all BumpHunter  $p$ -values shown in Table 8.4 are before region exclusion is applied. The BumpHunter  $p$ -values are always smaller after region exclusion is applied as the effect of any signal induced fit bias in the background estimation has been removed; this has been shown in the case of the  $Z'$  boson at a mass of 800 GeV.

To conclude the search phase validation studies for the *Full16\_LowMass* data-set analysis, it has been shown the SWiFt search phase is able to provide an adequate background estimation and that there is no evidence that spurious signal can occur. It has also been shown that the SWiFt search phase is able to identify a  $Z'$  boson with a generated mass of 600, 800 and 1000 GeV if the cross-section is large enough.

### 8.5.8 Results of Window Selection Procedure

For the full *Full16\_LowMass* data-set a window half-width is chosen using the window selection procedure outlined in Section 8.5.4. The SWiFt background estimation is performed using the 5 parameter dijet fit function and a window half-width range of 16 to 10.

For each SWiFt configuration, Figure 8.24 shows the two fit quality measures used in the window selection procedure: the global  $\chi^2$   $p$ -value and the number of windows with a Wilks'  $p$ -value  $< 0.1$ . The requirements placed on each fit quality measure by the window selection procedure are indicated by dotted lines on the figure. A window half-width of 16 is selected as it is the widest window that passes the fit quality criteria.

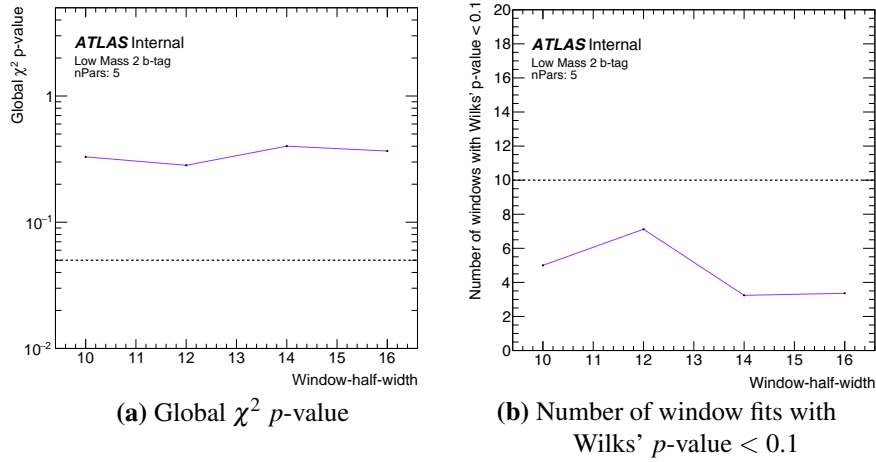


**Figure 8.24:** An illustration of the window selection procedure for the full *Full16\_LowMass* dataset. It shows the global  $\chi^2$  *p*-value and number of window fits with Wilks' *p*-value  $< 0.1$  for the SWiFt background estimate using a range of window half-widths and the 5 parameter dijet fit function. The dotted lines indicate the requirements used in the window selection procedure. A window half-width of 16 is selected.

Figure 8.25 shows the Wilks'  $p$ -value and  $\chi^2$   $p$ -value for fits in each of the windows as a function of the window centre for the SWiFt background estimation using the 5 parameter dijet fit function and a window half-width of 16, further showing that all fits used in the SWiFt background estimation are of good quality.

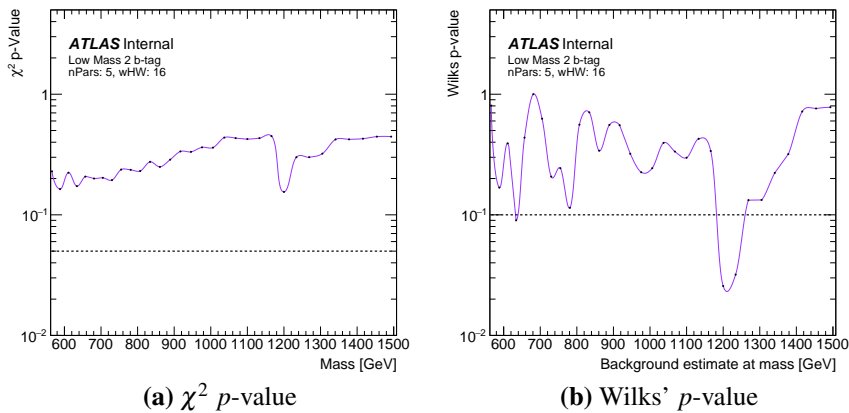


**Figure 8.25:** The  $\chi^2$  *p*-value and Wilks' *p*-value for each window fit in the SWiFt background estimate performed on the full *Full16\_LowMass* data-set, shown as a function of the window centre. The 5 parameter dijet fit function with a window half-width (*wHW*) of 16 is used as the SWiFt configuration. The dotted lines indicate thresholds that are used in the window selection procedure.

### 8.5.9 Search Phase Results

Figure 8.26 shows the dijet mass spectrum of the full *Full16\_LowMass* data-set and the SWiFt background estimation created using the 5 parameter dijet fit function and a window half-width of 16. The BumpHunter algorithm has identified the most discrepant excess, indicated in the figure using vertical blue lines, and assigned the excess a  $p$ -value of 0.603, which has been calculated using 10,000 pseudo-experiments.

The BumpHunter  $p$ -value is 0.603, showing that no significant excess is observed. Therefore it is concluded that there is no evidence of a BSM resonance in the *Full16\_LowMass* data-set. As no significant excess is found, the *Full16\_LowMass* data-set is used to set limits on the benchmark signal models, which will be described in Chapter 9.

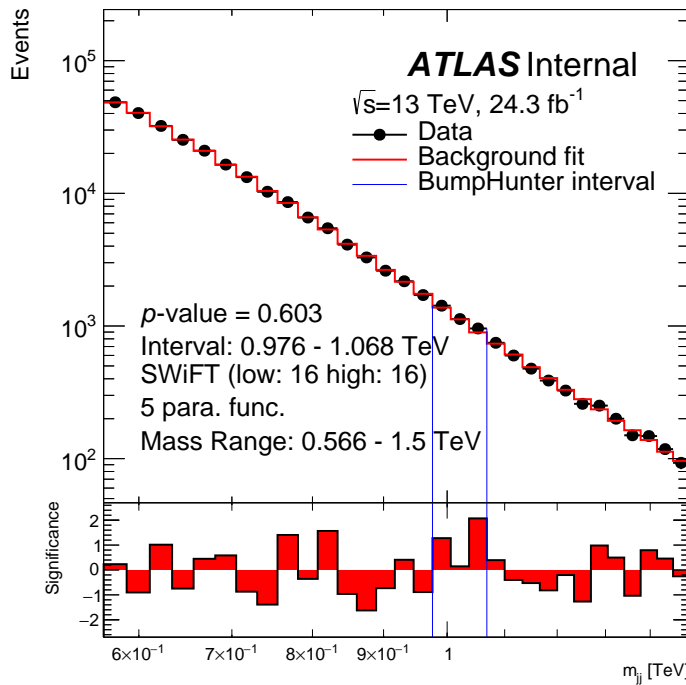


**Figure 8.26:** The dijet mass spectrum ( $m_{jj}$ ) of the *Full16\_LowMass* data-set and the SWiFt background estimation created using the 5 parameter dijet fit function and a window half-width ( $wHW$ ) of 16. The upper panel shows the data compared to the background estimate and the lower panel shows the significance of the difference between the two. The most discrepant excess found by the BumpHunter algorithm is indicated by the vertical blue lines and the  $p$ -value of this excess is printed on the plot.

## Chapter 9

# Di-*b*-Jet Search: Limit Setting Phase

In Chapter 8 it was shown that there is no evidence of new physics in the dijet mass spectra of the observed di-*b*-jet events <sup>1</sup>. However, it is also useful to quantify what this result means in the context of the signal models that are being searched for. Specifically, one can estimate the degree of belief that a signal model is true given the di-*b*-jet events that have been observed. If the degree of belief in a specific model is less than a certain threshold the model is excluded. This process is known as the limit setting phase.

In this Chapter, Section 9.1 will describe the limit setting methodology and Section 9.2 will discuss the systematic uncertainties considered. Then Sections 9.3 and 9.4 present the details and the results of the limit setting phase for the *Summer16\_HighMass* and *Full16\_LowMass* data-sets respectively.

### 9.1 Limit Setting Methodology

In this analysis a Bayesian limit setting approach is used [22, 112]. To set a limit on a particular model, one considers the hypothesis that the di-*b*-jet events are produced by a combination of the QCD background and the new physics process. A background template is produced using the background estimation procedures described in the previous chapter and the BSM physics model is described by a dijet mass signal template, normalised such that  $v$  di-*b*-jet events <sup>1</sup> are produced. This signal plus background hypothesis is denoted by the symbol  $H_v$ .

Now let us consider this hypothesis in the context of the data, denoted by  $D$ , which in this case is one of the observed dijet mass spectra. For the hypothesis,  $H_v$ , the probability of producing the data is known as the likelihood. In each dijet mass bin, labelled by the

---

<sup>1</sup> Defined as events that pass the di-*b*-jet event selection.

index  $i$ :  $n_i$  is the number of events observed in data and  $s_i(v)$  and  $b_i$  are the number of signal and background events predicted by  $H_v$ . Therefore, by only considering statistical uncertainties, the likelihood for a given value of  $v$  is given by:

$$\mathcal{L}(v, D) = P(D | v) = \prod_i \left( \frac{(s_i(v) + b_i)^{n_i} e^{-(s_i(v) + b_i)}}{n_i!} \right) \quad (9.1)$$

where the product is over all dijet mass bins and the notation  $P(A | B)$  represents the probability of event  $A$  occurring under the assumption of  $B$ .

Then, one can employ Bayes' theorem which states that

$$P(A | B) = \frac{P(B | A) P(A)}{P(B)} \quad (9.2)$$

to obtain the probability density function of  $v$  given the observed dijet mass spectrum,

$$P(v | D) = \frac{P(D | v) \Pi(v)}{\Pi(D)} \quad (9.3)$$

This quantity, known as the posterior, is an expression of the degree of belief in the hypothesis  $H_v$  for any particular value of  $v$ . The  $\Pi(v)$  term in the posterior is called the signal prior and gives the probability density of  $v$  before the experiment took place. A prior flat with respect to  $v$  is chosen<sup>2</sup> which represents ignorance to the size of the signal. The  $\Pi(D)$  term does not depend on  $v$  and as such can be considered as a normalisation term.

To accurately represent a true degree of belief in a model, one must consider the systematic uncertainties in the values of  $b_i$  and  $s_i$  in Equation 9.1. The sources of systematic uncertainty considered in this analysis are listed in Section 9.2. The systematic uncertainties are incorporated by explicitly considering  $s_i$  and  $b_i$  as a function of the parameters which are considered as sources of systematic uncertainty, the parameters are known as nuisance parameters. For example, the number of signal events in a dijet mass bin,  $s_i$ , is linearly dependant on luminosity ( $L$ ) such that  $s_i(L) \propto L$ . Luminosity is a source of systematic uncertainty, so is an example of a nuisance parameter.

Therefore, the likelihood can be expressed in terms of a set of nuisance parameters,  $\vec{\theta}$ :

$$\mathcal{L}(v, D, \vec{\theta}) = P(D | v, \vec{\theta}) = \prod_i \left( \frac{[s_i(v, \vec{\theta}) + b_i(\vec{\theta})]^{n_i} e^{-[s_i(v, \vec{\theta}) + b_i(\vec{\theta})]}]}{n_i!} \right) \quad (9.4)$$

---

<sup>2</sup> Flat from  $v = 0$  to the value of  $v$  where the likelihood has fallen to  $10^{-5}$  of the maximised value.

A prior probability is introduced for each of the nuisance parameters, given by  $\Pi(\vec{\theta})$ , that describes the systematic uncertainty on each of the nuisance parameters. By integrating over the nuisance parameters, one obtains the posterior for  $v$  that accounts for systematic uncertainties

$$P(v | D) \propto \int d\vec{\theta} \mathcal{L}(v, D, \vec{\theta}) \Pi(v) \Pi(\vec{\theta}) \quad (9.5)$$

One can calculate the likelihoods for the data, perform the integral over nuisance parameters and then normalise to calculate the probability density of  $v$ <sup>3</sup>. The process of integrating over nuisance parameters is known as marginalisation.

Using the posterior calculated from Equation 9.5, the 95% credibility level upper limit of  $v$ , denoted by  $v^{\text{up}}$ , is calculated using the expression

$$\int_0^{v^{\text{up}}} dv P(v | D) = 0.95 \quad (9.6)$$

Under the assumption of  $H_v$  there is a 95% probability that the value of  $v$  lies within the credibility interval defined as  $0 \leq v < v^{\text{up}}$ . Therefore, any model under the hypothesis  $H_v$  that predicts a  $v$  value above the upper limit,  $v^{\text{up}}$ , is excluded at the 95% credibility level.

In the di- $b$ -jet analysis, limits are set on the benchmark models for a range of generated mass points, the dijet mass signal templates used are described in Section 6.3. Upper limits are set on the product of cross-section, detector acceptance and tagging efficiency,  $\sigma \times A \times \epsilon$ , which is related to the parameter  $v$  used in the limit setting description<sup>4</sup>.  $A$  and  $\epsilon$  have been measured in Section 7.4 for the benchmark signal models.

Further to this, limits are set on a signal shape of a Gaussian distribution with a range of different signal widths, these limits are referred to as Gaussian limits. In Gaussian limits, it is assumed that, for an unspecified signal, when low-mass off-shell tails and non-perturbative effects are neglected the convolution of the signal shape, detector effects and PDF effects can be approximated by a Gaussian distribution. Using this assumption the Gaussian limits can be reinterpreted for a range of BSM models predicting resonances not explicitly considered by this analysis; a detailed method of how one can reinterpret the limits for a specific model is given in Appendix A of [113]. It is worth noting that in a previous ATLAS dijet search limits were set using a Breit-Wigner distribution convolved with PDF effects [114]; however this approach is not repeated here as it introduced dependencies on the choice of PDF model, meaning that the limits were not truly model independent.

<sup>3</sup> This integral is performed using a Markov chain Monte-Carlo using the Bayesian Analysis Toolkit. Full details on the implementation can be found in [22].

<sup>4</sup> Specifically  $v=L \times \sigma \times A \times \epsilon$ , where  $L$  is the luminosity.

The di- $b$ -jet analysis will present two limits. The first is the observed limit, which is set using the observed dijet mass spectra, as described above. The second is the expected limit, which is the upper limit that would be set if there is no signal present in the dijet mass spectrum; the expected limit represents the sensitivity of the limit setting phase. To calculate the expected limit, the limit setting phase is performed on pseudo-experiments created by varying the background estimate within the systematic uncertainties. This process is done for many pseudo-experiments; the median upper limit gives the expected limit and the 68% and 95% percentiles give the 1 and 2  $\sigma$  uncertainty bands on the expected limit.

In this analysis the Bayesian approach for limit setting is used, there is another widely used alternative known as the frequentist approach [115]. The Bayesian approach defines a credibility interval using the probability (or degree of belief) in a hypothesis given the observed data ( $P(v | D)$ ). On the other hand, the frequentist approach calculates the probability (or fraction of trials) of obtaining the data assuming a given signal model is true ( $P(D | v)$ ) and rejects models that produce a low probability. Both approaches are valid and logically consistent, but it is important that one states clearly which approach is being taken<sup>5</sup>.

## 9.2 Description of Systematic Uncertainties

The sources of systematic uncertainty in the di- $b$ -jet analysis are grouped into two categories. The first group are uncertainties on the dijet mass signal templates used in the limit setting phase, which are produced using Monte-Carlo simulations. The signal systematic uncertainties considered are:

- **Jet Energy Scale, Jet Energy Resolution and  $b$ -Jet Energy Scale (Signal)**

Jet energy scale (JES), jet energy resolution (JER) and  $b$ -jet energy scale ( $b$ JES) are uncertainties on the energy measurement of a  $b$ -jet. The JES and JER uncertainties used in this analysis were described in Section 4.2.4. The  $b$ JES uncertainty used is 2.6% for all jets, which, as described in Section 4.3.5, corresponds to the  $b$ JES uncertainty for jets with  $p_T > 60$  GeV, covering the jet- $p_T$  range considered in this thesis. The three jet energy uncertainties cause an uncertainty on the dijet mass of a simulated signal event.

- **$b$ -Tagging (Signal)**

The modelling of  $b$ -tagging in Monte-Carlo simulation is corrected to data using measured  $b$ -tagging scale factors; the scale factors and associated uncertainties are discussed in Section 4.3.4. The uncertainty on the  $b$ -tagging scale factors cause an uncertainty on the normalisation of each bin in the dijet mass signal template.

---

<sup>5</sup> As a side note the BumpHunter  $p$ -value uses the frequentist approach to calculate a  $p$ -value.

- ***b*-Jet Trigger (Signal)** - *Full16\_LowMass* data-set only

Similarly, when using the *b*-jet trigger, the modelling of the online *b*-tagging efficiency in simulation is corrected to data using *b*-jet trigger scale factors. The *b*-jet trigger scale factors and relevant uncertainties are derived in Section 5.3. The uncertainty on the *b*-jet trigger scale factors cause an uncertainty on the normalisation of each point in the dijet mass signal template. This systematic uncertainty is only used in the *Full16\_LowMass* data-set, as this is the only data-set using a *b*-jet trigger.

- **Luminosity (Signal)**

The luminosity uncertainty is determined using the methodology outlined in [116]. The luminosity uncertainties used are 2.9% in the *Summer16\_HighMass* data-set and 2.2% in the *Full16\_LowMass* data-set. The uncertainty on luminosity causes an uncertainty on the normalisation of the dijet mass signal template.

- **Parton Distribution Functions (PDFs) (Signal)**

The PDFs are important in calculating the cross-section of any process at the LHC. As shown in Section 2.2.3.2 there are uncertainties on the measurements of the PDFs which cause an uncertainty on the dijet mass signal template used. A flat 1% uncertainty on the normalisation of the dijet mass signal templates is applied, which has been found at previous dijet searches to conservatively cover the effect of the PDF uncertainties [2, 5].

The second group are systematic uncertainties on the background estimation. As the background estimate is data-driven, the set of uncertainties related to modelling in simulation are not required. The uncertainties on the background estimation model are:

- **Fit Function Parameters (Background)**

The parameters of the fit function are determined by maximising the likelihood with respect to the data-set. However, due to the statistical fluctuations in data the optimal parameters may not have been chosen. To estimate the uncertainty on the parameters of the fit function, the background estimation procedure is performed on pseudo-experiments created by applying Poisson fluctuations to the nominal background estimate. The root mean square of the difference between the nominal background estimate and those from the pseudo-experiments is taken as a symmetric uncertainty.

- **Fit Function Choice (Background)**

A different background estimation can be obtained if a different fit function is chosen. To obtain an uncertainty on the choice of fit function an alternate function is considered, which is the dijet fit function with one extra degree of freedom than the nominal function. The alternate function is then used to fit to the pseudo-experiments described in the previous bullet point. The mean of the difference between the nominal and alternate functions is taken as the uncertainty. This uncertainty is treated as a single-sided uncertainty mean-

ing that the nuisance parameter describing this uncertainty can only vary the background template created by the nominal function towards that of the alternate function; this is based on the assumption that it is unreasonable that the true background would lie outside of the envelope created by the two reliable descriptions of the background [2].

### 9.3 Summer16\_HighMass Data-Set Limits

Table 9.1 summarises the systematic uncertainties on the signal templates used in the *Summer16\_HighMass* data-set at three different dijet masses. Figure 9.1 shows the systematic uncertainties on the background estimate for both  $b$ -tagging categories as a function of dijet mass; the parameter uncertainty is shown as a dashed area representing that this is a two sided uncertainty whilst the function choice uncertainty is shown as a line representing that this is a one sided uncertainty.

Dijet Mass	Signal Systematic Uncertainties					
	JES	JER	$b$ JES	$b$ -Tagging ( $\geq 1 / 2$ $b$ -tags)	PDF	Lumi.
1.5 TeV	1.2%	1.0%	2.2%	20% / 10%	1%	2.9%
3 TeV	1.4%	0.7%	0.7%	50% / 60%	1%	2.9%
5 TeV	2.3%	0.3%	0.3%	50% / 70%	1%	2.9%

**Table 9.1:** The signal systematic uncertainties used in the *Summer16\_HighMass* data-set analysis. Jet Energy Scale (JES), Jet Energy Resolution (JER) and  $b$ -Jet Energy Scale ( $b$ JES) are uncertainties on the dijet mass of a simulated event, whilst  $b$ -tagging, PDF and luminosity are uncertainties on simulated event weight. Values taken from [10].

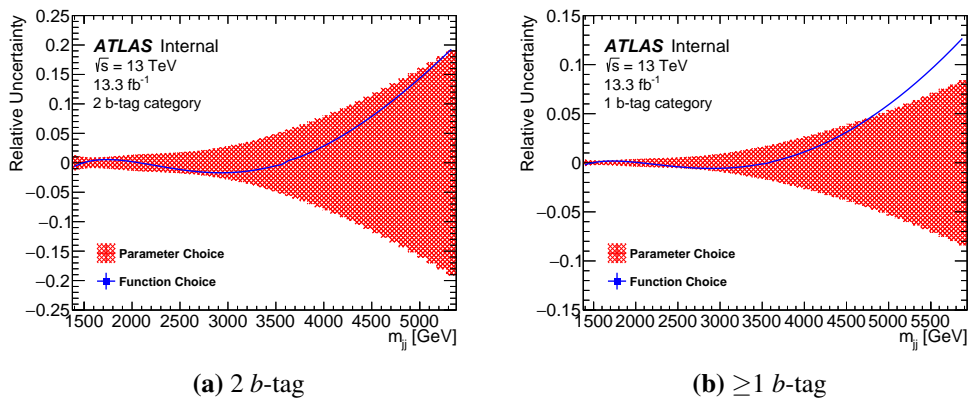


**Figure 9.1:** The relative background systematic uncertainties shown as a fraction for the (a) 2 and (b)  $\geq 1$   $b$ -tag categories as a function of dijet mass,  $m_{jj}$ , for the *Summer16\_HighMass* data-set analysis. The red shaded region shows the function parameter uncertainty and the blue line shows the function choice uncertainty.

Figure 9.2 shows the 95% credibility level upper limits set on  $\sigma \times A \times \epsilon$  as a function of generated mass for the  $Z'$  boson and  $b^*$  quark. The observed limit, the expected limit and the associated 1 and 2  $\sigma$  uncertainty bands on the expected limit are shown. The  $\geq 1$

$b$ -tag category is used for the  $b^*$  quark model and the 2  $b$ -tag category is used for the  $Z'$  boson models. Overlaid are theoretical predictions of  $\sigma \times A \times \epsilon$  for the benchmark models described in Section 6.3.

In the mass regions where the theoretical prediction of  $\sigma \times A \times \epsilon$  is larger than the upper limit, it can be concluded that the model is excluded at the 95% credibility level. Using the *Summer16\_HighMass* data-set, the  $b^*$  quark is excluded in the mass range of 1.4 – 2.3 TeV, the SSM  $Z'$  boson cannot be excluded, and the leptophobic  $Z'$  boson is excluded at a mass of 1.5 TeV.

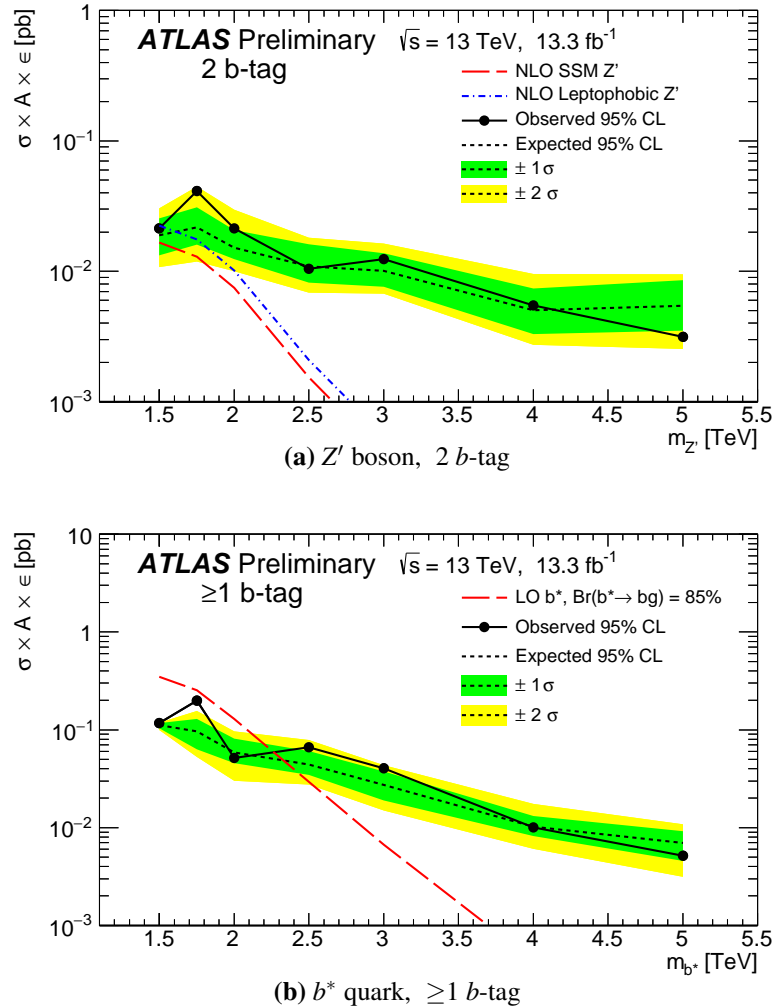


**Figure 9.2:** 95% credibility level upper limits on the product of cross-section, detector acceptance and tagging efficiency ( $\sigma \times A \times \epsilon$ ) for the (a)  $Z'$  boson and (b)  $b^*$  quark as a function of generated mass using the *Summer16\_HighMass* data-set in the 2 and  $\geq 1$   $b$ -tag category respectively. The observed limit is shown by the solid black line, the expected limit is shown by the dotted black line, and the associated 1 and 2  $\sigma$  uncertainty bands on the expected limit are shown by the green and yellow bands. The theoretical predictions of  $\sigma \times A \times \epsilon$  for the Sequential Standard Model (SSM) and leptophobic  $Z'$  boson and the  $b^*$  quark are overlaid [10].

To produce generic Gaussian limits, a signal template with a Gaussian shape in dijet mass is used. The Gaussian distributions are centred on a range of mass points between 1.4 and 6.0 TeV, the centre of the Gaussian distribution is referred to as the generated mass. The width of the Gaussian distributions are 15%, 10% and 7% of the generated mass in addition to a Gaussian with the width of the detector mass resolution. The detector mass resolution has been estimated at previous dijet searches [2] and varies from 3% at 1.5 TeV to 2% at 5 TeV. The sources of the systematic uncertainty considered for the Gaussian limits are the luminosity uncertainty, the background modelling uncertainties, and a 10% flat uncertainty to account for sources of experimental uncertainties related to signal modelling, such as jet energy scale.

Figure 9.3 shows the observed 95% credibility upper limits on the product of cross-section, detector acceptance, tagging efficiency and branching ratio,  $\sigma \times A \times \epsilon \times BR$ , for the full range of Gaussian signals described above in both  $b$ -tagging categories; where the branching ratio is defined as the fraction of decays of the proposed BSM particle to 2  $b$ -quarks in the 2  $b$ -tag category, or to a  $b$ -quark and a gluon in the  $\geq 1$   $b$ -tag category. For the *Summer16\_HighMass* data-set analysis an upper limit is set on the  $\sigma \times A \times \epsilon \times BR$  for a generic Gaussian signal ranging from 0.2 to 0.001 pb in the mass range 1.4 to 6 TeV.

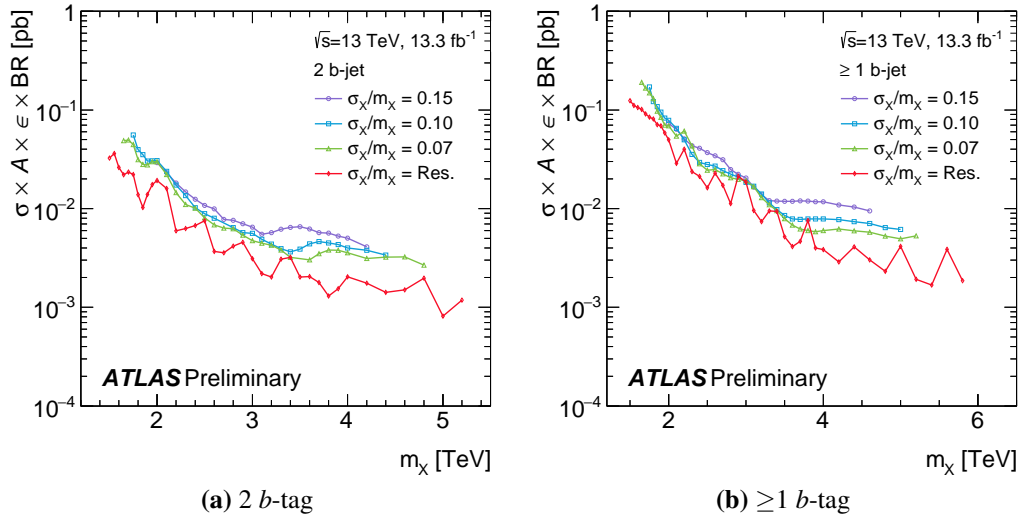


**Figure 9.3:** 95% credibility observed upper limits on the product of cross-section, detector acceptance, tagging efficiency and branching ratio,  $\sigma \times A \times \epsilon \times BR$ , for Gaussian signals in both  $b$ -tagging categories using the *Summer16\_HighMass* data-set. The signal templates are Gaussian in dijet mass with widths of 15%, 10% and 7% of the generated mass in addition to a Gaussian with the width of the detector mass resolution [10].

## 9.4 Full16\_LowMass Data-set Limits

### 9.4.1 Signal Morphing

The limit setting phase requires dijet mass signal templates as an input. For the *Full16\_LowMass* data-set analysis, simulated dijet mass signal templates of the SSM  $Z'$  boson are created at generated mass points of 600, 800, 1000 and 1250 GeV, as described in Section 6.3. To obtain dijet mass signal templates for intermediate points a signal morphing technique is used, first implemented in an inclusive dijet search at ATLAS [3].

A ‘Gaussian + reverse Landau’ fit is performed to the simulated dijet mass signal templates. The reverse Landau function is the transformation of the Landau function [117] under  $x \rightarrow -x$ . The Gaussian + reverse Landau fit function is therefore defined as:

$$f(x) = p_0 [p_1 \text{Gauss}(x, p_2, p_3) + (1 - p_1) \text{Landau}(-x, p_4, p_5)] \quad (9.7)$$

The Gaussian distribution models the convolution of a Breit-Wigner resonance distribution and detector mass resolution effects. The reverse Landau distribution provides a description of the off-shell contributions to the dijet mass signal templates which are enhanced at low mass by PDF effects. The parameters of the Gaussian + reverse Landau fits are interpolated to produce dijet mass signal templates at intermediary generated mass points in the range 600 to 1250 GeV with a separation of 50 GeV.

Figure 9.4 shows the simulated SSM  $Z'$  boson dijet mass signal templates compared to the dijet mass signal templates created using the signal morphing technique. The lower panel of Figure 9.4 shows the ratio of the simulated signal templates to the morphed signal templates; for clarity the ratios for each generated mass point are truncated such that only one point is shown for each dijet mass bin.

For each generated mass point considered it is shown that, in the mass region where the signal peak occurs, the simulated and morphed signal templates have reasonable agreement within the statistical uncertainties of the simulated dijet mass signal templates. For the generated mass point of 600 GeV, there is a large disagreement between the morphed and simulated signal templates at dijet masses greater than 650 GeV, however this does not impact the analysis as the fraction of events with a dijet mass greater than 650 GeV is small.

In the limit setting phase for the *Full16\_LowMass* data-set analysis the simulated signal dijet mass spectra are used at generated mass points of 600, 800, 1000 and 1250 GeV and morphed signal templates are created at generated mass points of 650, 700, 750, 850, 900, 950, 1050, 1100, 1150 and 1200 GeV.

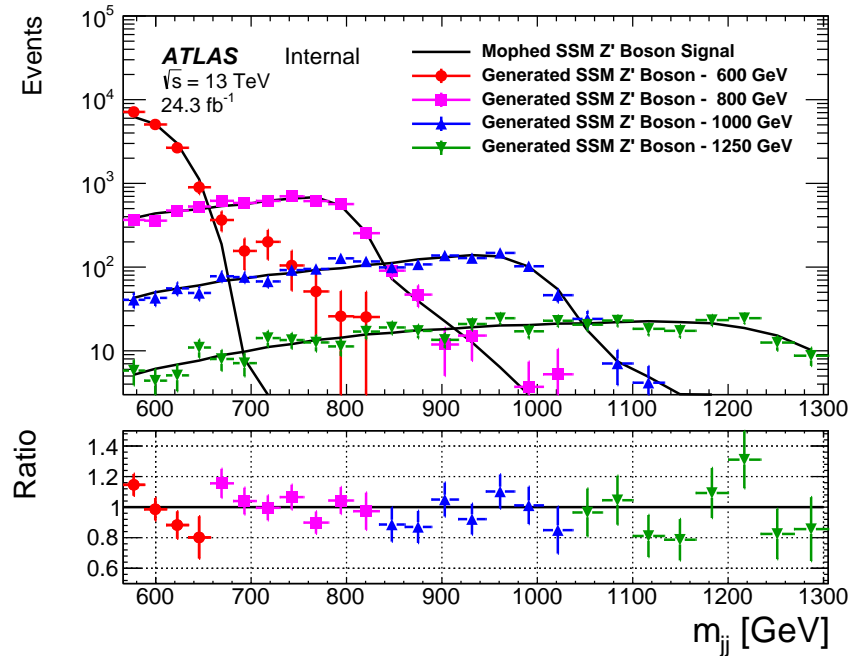


**Figure 9.4:** The simulated SSM  $Z'$  boson dijet mass ( $m_{jj}$ ) signal templates (coloured points) compared to the dijet mass signal templates created using the signal morphing technique (black lines) at generated mass points of 600, 800, 1000 and 1250 GeV. The error bars represent the statistical uncertainties on the simulated dijet mass signal templates. The *Full16\_LowMass* event selection has been applied. The lower panel shows the ratio of the generated to the morphed dijet mass signal template; the ratios for each mass point are truncated.

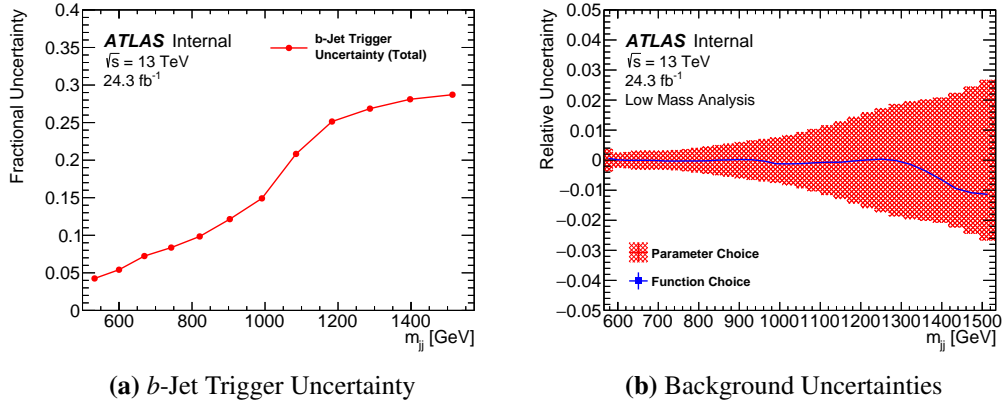
#### 9.4.2 Summary of Systematic Uncertainties

Table 9.2 summarises the systematic uncertainties considered for the signal templates used in the *Full16\_LowMass* data-set at three different dijet masses.

Dijet Mass	Signal Systematic Uncertainties						
	JES	JER	$b$ JES	$b$ -Tagging	$b$ -Jet Trigger	PDF	Lumi.
0.6 TeV	0.9%	1.4%	5%	5%	5.4%	1%	2.2%
1.0 TeV	0.8%	1.2%	3%	7%	15%	1%	2.2%
1.5 TeV	1.1%	1.0%	1.8%	10%	29%	1%	2.2%

**Table 9.2:** The signal systematic uncertainties used in the *Full16\_LowMass* data-set analysis for three different dijet mass ( $m_{jj}$ ) points. Jet Energy Scale (JES), Jet Energy Resolution (JER) and  $b$ -jet Energy Scale ( $b$ JES) are uncertainties on the dijet mass of a simulated event, whilst  $b$ -tagging,  $b$ -jet trigger, PDF and luminosity uncertainties are uncertainties on simulated event weight. All values except the  $b$ -jet trigger uncertainty are taken from [11].

Figure 9.5(a) shows the total  $b$ -jet trigger systematic uncertainty as a function of dijet mass; this includes both the jet-level and event-level uncertainties described in Section 5.3. Figure 9.5(b) shows the systematic uncertainties on the background estimate as a function of dijet mass; the two sided parameter uncertainty is represented by a dashed area whilst the one sided function choice uncertainty is represented by a line.



**Figure 9.5:** Panel (a) shows the total  $b$ -jet trigger systematic uncertainty as a fraction for the *Full16\_LowMass* data-set as a function of dijet mass ( $m_{jj}$ ). Panel (b) shows the relative background systematic uncertainties as a fraction for the *Full16\_LowMass* data-set as a function of dijet mass; the red shaded region shows the function parameter uncertainty and the blue line shows the function choice uncertainty.

### 9.4.3 Signal Subtracted Background Estimation

Section 8.5.3 described the SWiFt background estimation procedure used in the search phase of the *Full16\_LowMass* data-set, for clarity this will be referred to as the ‘*nominal SWiFt background estimation*’ in this section. The nominal SWiFt background estimation is model independent as there is no assumption of any signal models in the procedure. In Section 8.5.7 it was shown that there is a signal induced fit bias present when the nominal SWiFt background estimation is performed on a background-only test data-set with a SSM  $Z'$  boson injected. This is particularly notable for a SSM  $Z'$  boson with a generated mass of 600 GeV, as this is near the edge of the dijet mass spectrum considered.

To remove any signal induced fit bias in the limit setting phase, a signal plus background fit is performed for each signal point considered in the limit setting phase. The signal is modelled using the dijet mass signal templates described in Section 9.4.1 and the background is modelled using the 5 parameter dijet fit function. The signal plus background fit is performed in the SWiFt window in which the generated mass of the signal being considered is at the window centre, the fit does not use the full mass range as it has been shown in Section 8.5.2 that a global background fit is not reliable. A window half-width of 16 and

the 5 parameter dijet fit function are chosen to match the configuration used in the search phase results shown in Section 8.5.9. The normalisation of the signal template and the parameters of the background fit function are chosen to maximise the likelihood (defined in Equation 9.1), the signal normalisation is required to be greater or equal to zero.

The signal plus background fit provides an estimate of the number of signal and background events in the SWiFt window considered, however the framework used for the limit setting phase requires a background estimation for the full mass range considered. To extend the background estimate to the full range, the signal template, normalised by the signal plus background fit, is subtracted from the data. The SWiFt background estimation procedure is then performed to the signal subtracted data, using the 5 parameter dijet fit function and a window half-width of 16, which is again chosen to match the configuration used in the search phase. The resulting background estimation is known as the ‘*signal subtracted background estimation*’ (SSB). A signal subtracted background estimation is created for each generated mass point and is used as the background template in the limit setting phase for the *Full16\_LowMass* data-set analysis.

The signal subtracted background estimate is used as it provides a simple method of using the results of the signal plus background fit performed in a SWiFt window to create a background estimate for the full mass range. Furthermore, the signal subtracted background estimate is used by the most recent inclusive dijet search at ATLAS [3]. It is beneficial for related analyses at ATLAS to utilise similar background estimation techniques for three main reasons: it increases reliability as the technique is independently validated multiple times, shares framework development responsibilities between multiple analyses, and leads to greater consistency in the presentation of ATLAS results.

To demonstrate that the signal subtracted background estimation will remove the signal induced fit bias, the procedure is performed to a data-like dijet mass spectrum from the fit control region when a SSM  $Z'$  boson dijet mass signal template is injected. The same distributions were used in the signal injection studies presented in Section 8.5.7. The performance of the signal subtracted background estimation can be compared to that of the nominal SWiFt background estimation.

In Figure 9.6(a) the nominal SWiFt background estimate (red) and the signal subtracted background estimate (blue) for a data-like dijet mass spectrum from the fit control region with a SSM  $Z'$  boson injected at 600 GeV are shown as a ratio to the nominal SWiFt background estimation for the same data-like dijet mass spectrum when no signal is injected (black). This ratio is used to clearly show any signal induced fit biases. The signal injected dijet mass spectrum is shown by the green points and the grey area represents the

statistical uncertainty of the data. Figure 9.6(b) shows the same comparison using a SSM  $Z'$  boson injected at 1000 GeV. These two mass points are shown as the signal injection studies, presented in Section 8.5.7, found that the search phase would not produce a significant observation of a SSM  $Z'$  boson at these generated mass points.

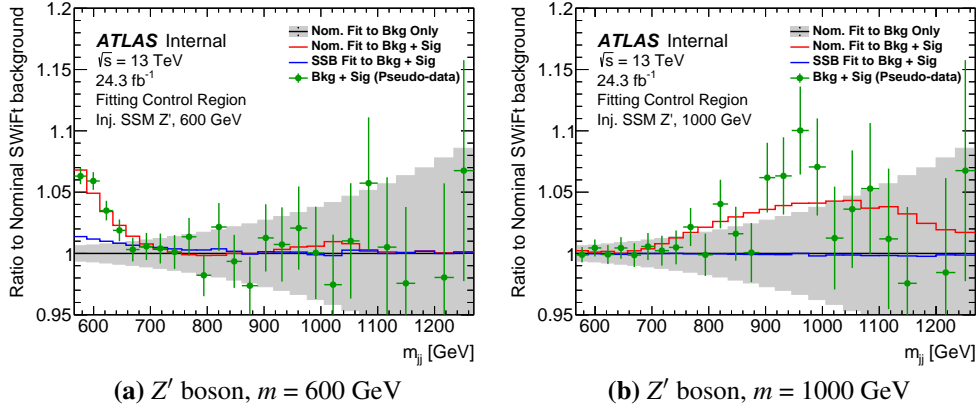


**Figure 9.6:** The nominal SWiFt background (red) and signal subtracted background (SSB) (blue) estimations for a data-like dijet mass ( $m_{jj}$ ) spectrum from the fit control region with a SSM  $Z'$  boson injected (green points) as a ratio to the nominal SWiFt background estimation performed on the same data-like dijet mass spectrum when no signal is injected. The grey area represents the statistical uncertainties of the data-set. The generated mass of the SSM  $Z'$  boson is (a) 600 GeV and (b) 1000 GeV. The nominal SWiFt background estimation procedure is used in the search phase, the signal subtracted background estimation procedure is used in the limit setting phase.

The nominal SWiFt background estimation has a large signal induced fit bias when a SSM  $Z'$  boson is injected, shown by the fact that the red line is significantly drawn towards the injected signal in Figure 9.6. The signal induced fit bias is especially notable in the case of a SSM  $Z'$  boson at 600 GeV. The signal induced fit bias of the signal subtracted background is small relative to the size of the injected signal, shown by the fact that the blue line lies close to one for all dijet masses. Therefore, the signal subtracted background estimation is used in the limit setting phase of the *Full16\_LowMass* data-set analysis, for both the  $Z'$  boson and generic Gaussian signals. A signal subtracted background estimate is created for each signal mass point using the dijet mass spectrum observed in data.

If the signal subtracted background estimates differ greatly from the nominal SWiFt background estimate, this is evidence that there may be a signal induced fit bias present in the search phase. Figure 9.7 shows the ratio of the signal subtracted background estimations to the nominal SWiFt background estimate (black) performed on the full *Full16\_LowMass* data-set<sup>6</sup>. The grey area represents the parameter choice uncertainty of the nominal SWiFt background estimation. Signal subtracted background estimations are created for

<sup>6</sup> The SWiFt background estimate for the full data-set is shown in comparison to the data in Figure 8.26.

all generated mass points considered, but for clarity only those at mass points of 600, 800, 1000 and 1250 GeV are shown in the figure.

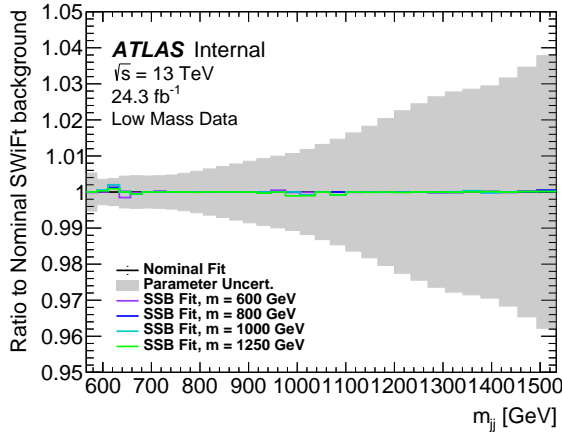


**Figure 9.7:** The ratio of signal subtracted background (SSB) estimations (coloured lines) and the nominal SWiFt background estimate (black) performed on the full *Full16\_LowMass* data-set. The parameter choice uncertainty on the background is shown by the grey area. The generated mass points used in the signal subtracted background estimations are indicated in the legend.

For all generated mass points, including those not shown in Figure 9.7, the signal subtracted background estimate is consistent with the nominal SWiFt background estimation within background uncertainties. Therefore, the background estimation used in the search phase and the limit setting phase are consistent. Furthermore, this shows that there is no signal induced fit bias due to a  $Z'$  boson in the nominal SWiFt background estimation performed to the *Full16\_LowMass* data-set.

The nominal SWiFt background estimate used in the search phase does not utilise a signal plus background fit as this would mean that the search phase result is not model independent. However, it is clear that the nominal SWiFt background estimation can be affected by a signal induced fit bias, as shown in Figure 9.6. As a result the sensitivity of the search phase is reduced to specific signal models relative to the results of the limit setting phase presented below; the reduced sensitivity is accepted to maintain model independence. In Chapter 10 I will discuss how a signal plus background fit could be employed differently to benefit both the search phase and the limit setting phase in future analyses.

#### 9.4.4 Results

For the *Full16\_LowMass* data-set analysis, limits are set on the product of cross-section and branching ratio ( $\sigma \times BR$ ) of the benchmark  $Z'$  boson models described in Section 6.3. Limits are set on  $\sigma \times BR$  by calculating limits for  $\sigma \times A \times \epsilon \times BR$ , using the same methodology used for the *Summer16\_HighMass* data-set result, and dividing by the  $A \times \epsilon$  shown in Figure 7.8(a).  $A \times \epsilon$  is corrected for such that limits set by the *Full16\_LowMass* and *Full16\_HighMass* data-set analyses can be shown on the same figure, even though different trigger and event selections are used [11]; the *Full16\_HighMass* data-set analysis result is not presented in this thesis<sup>7</sup>.  $BR$  is explicitly referred to for limits in the *Full16\_LowMass* data-set analysis to clearly identify that limits set on the SSM and leptophobic  $Z'$  models only consider decays to pairs of  $b$ -quarks, whilst for the DM  $Z'$  boson decays to pairs of  $u$ ,  $d$ ,  $s$ ,  $c$  or  $b$  quarks are considered.

Figure 9.8 shows the 95% credibility level upper limits set on  $\sigma \times BR$  for the (a) SSM and leptophobic  $Z'$  boson and the (b) DM  $Z'$  boson as a function of generated mass. The observed limit, expected limit, and the associated 1 and 2  $\sigma$  uncertainty bands on the expected limit are shown. Overlaid are theoretical predictions of  $\sigma \times BR$  for the  $Z'$  boson benchmark models.

The change in gradient of the observed and expected limits at  $m_{Z'} = 800$  GeV is a result of a reduction in the acceptance of the  $Z'$  boson for  $m_{Z'} < 800$  GeV caused by the requirement that the dijet mass of an event is greater than 566 GeV. This effect can be seen clearly in Figure 7.8(a).

Using the *Full16\_LowMass* data-set the SSM and leptophobic  $Z'$  boson are excluded in the generated mass range 0.6 – 1.25 TeV at the 95% credibility level. Additionally, the DM  $Z'$  boson is excluded in the generated mass range 0.6 – 1.0 TeV at the 95% credibility level.

It should be noted that the largest  $Z'$  boson mass considered in the limits for the *Full16\_LowMass* data-set is 1.25 TeV (as shown in Figure 9.8), whereas the largest dijet mass considered in the search phase results for the *Full16\_LowMass* data-set is 1.53 TeV (as shown in Section 8.5.9). The upper bound of the dijet mass spectrum was chosen to be 1.53 TeV such that there would be no gap in the limits set by the low-mass and high-mass di- $b$ -jet searches, as discussed in Section 7.2. However, the largest mass considered in the limits set by the *Full16\_LowMass* data-set analysis is 1.25 TeV because the

---

<sup>7</sup> Details of the *Full16\_HighMass* data-set are found in Section 6.2.

*Full16\_HighMass* data-set analysis<sup>8</sup>, to be published together with the *Full16\_LowMass* data-set analysis [11], is able to set stricter limits in the mass region 1.25 – 1.5 GeV than can be set using the *Full16\_LowMass* data-set analysis. Therefore, there is no gap in the limits set by the *Full16\_LowMass* and *Full16\_HighMass* data-set analyses in the mass region 0.6 – 5 TeV, as presented in [11].

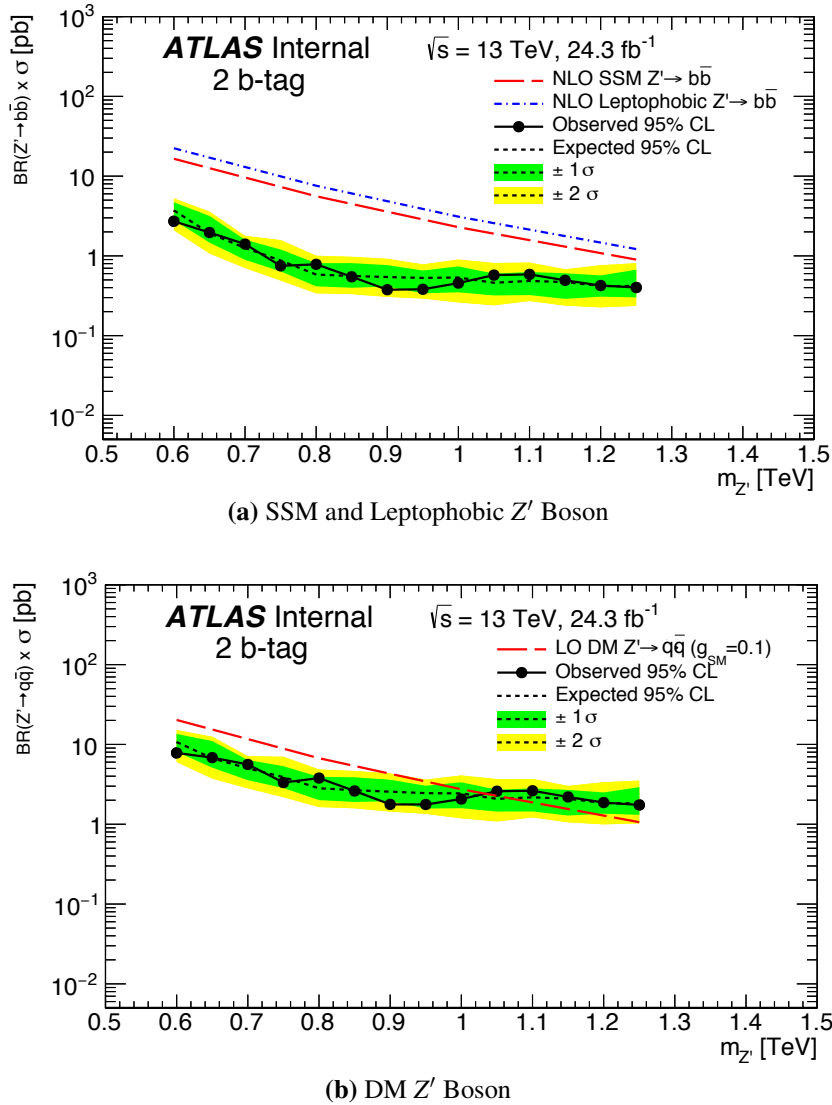


**Figure 9.8:** 95% credibility level upper limits on the product of cross-section and branching ratio ( $\sigma \times BR$ ) for (a) the Sequential Standard Model (SSM) and leptophobic  $Z'$  boson decaying to a pair of  $b$ -quarks and (b) the DM  $Z'$  boson decaying to a pair of  $u$ ,  $d$ ,  $s$ ,  $c$  or  $b$  quarks as a function of generated mass using the *Full16\_LowMass* data-set. The observed limit is shown by the solid black line, the expected limit is shown by the dotted black line and the associated 1 and 2  $\sigma$  uncertainty bands on the expected limit are shown by the green and yellow bands. The theoretical predictions of  $\sigma \times BR$  for the SSM, leptophobic and DM  $Z'$  models are overlaid [11].

---

<sup>8</sup>The *Full16\_HighMass* data-set analysis is not presented in this thesis.

For the generic Gaussian limit setting phase there is a significant difference with respect to the *Summer16\_HighMass* data-set analysis. In the *Summer16\_HighMass* data-set analysis a signal template with a Gaussian distribution in dijet mass is used; however, this approach relies on an assumption that the convolution of the signal shape and the detector response can be modelled by a Gaussian distribution. Therefore, for the *Full16\_LowMass* data-set analysis a new approach is taken, which was first used in [3]. In the *Full16\_LowMass* data-set analysis a signal template with a Gaussian distribution in the truth mass distribution is used, where the truth mass is defined as the invariant mass of the leading and subleading truth jets using the definition of truth jet from Section 4.2.3.

The Gaussian limit setting method used in the *Full16\_LowMass* data-set analysis is preferred, as in this approach the limits can be interpreted for a range of signal models without any assumption of the effect of the response of the detector on the signal shape. It should be noted that the *Full16\_LowMass* data-set analysis is to be published together with the *Full16\_HighMass* data-set analysis<sup>9</sup> in [11], and in this publication both analyses use the same generic Gaussian limit setting methodology.

The centre of the truth mass Gaussian distribution is referred to as the generated mass, the generated mass points used are in the range 0.65–1.45 TeV with a spacing of 0.05 TeV. The lowest generated mass considered by the Gaussian limits is 0.65 TeV, such that the majority of the signal events have a dijet mass above the 566 GeV requirement in the *Full16\_LowMass* data-set event selection. The width of the Gaussian distributions are 15%, 10%, 7%, 5%, 3% and 0% of the generated mass; a Gaussian distribution with a 0% width is a Dirac delta peak. The transformation of the signal templates from truth mass to dijet mass is performed using transfer matrices calculated in a Monte-Carlo simulated QCD dijet sample, following the procedure outlined in [3]. The Gaussian signal with a 0% width in truth mass will have a width of the mass resolution of the detector in dijet mass.

For the Gaussian limit setting phase, the sources of systematic uncertainties are the luminosity uncertainty, the background modelling uncertainties and a flat 5% uncertainty to cover the JES, JER and *b*JES systematic uncertainties. Other systematic uncertainties are not included in the limits, as these are found to have a small effect on the upper limit relative to the jet energy uncertainties. This is because the jet energy uncertainties cause uncertainties on the dijet mass of a simulated event and therefore can significantly affect the shape of the dijet mass signal template.

---

<sup>9</sup>The *Full16\_HighMass* data-set analysis is not presented in this thesis.

Figure 9.9 shows the observed 95% credibility upper limits set on the product of cross-section, detector acceptance, tagging efficiency and branching ratio,  $\sigma \times A \times \epsilon \times BR$ , for the full range of Gaussian signals described above. For the Gaussian signal with 0% width in truth mass, which corresponds to the detector resolution in dijet mass, the expected limits are shown by the dotted lines and the associated 1 and 2  $\sigma$  uncertainty bands are shown in green and yellow.

For the *Full16\_LowMass* data-set an upper limit is placed on the  $\sigma \times A \times \epsilon \times BR$  for a generic Gaussian signal ranging from 0.05 to 0.003 pb in the mass range 0.65 to 1.45 TeV.

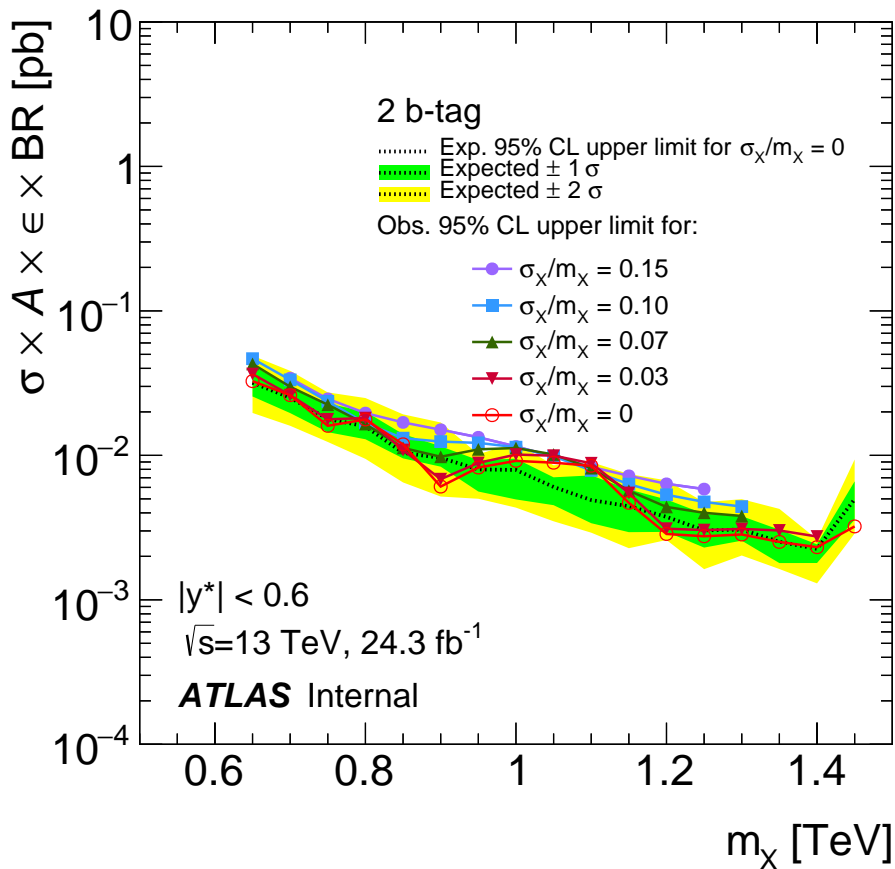


**Figure 9.9:** 95% credibility observed upper limits on the product of cross-section, detector acceptance, tagging efficiency and branching ratio,  $\sigma \times A \times \epsilon \times BR$ , for Gaussian signals using the *Full16\_LowMass* data-set as a function of generated mass ( $m_X$ ) are shown by the solid lines. The signal templates are a Gaussian distribution in truth mass with widths of 15%, 10%, 7%, 5%, 3% and 0% of the generated mass. The Gaussian distribution with 0% width in truth mass represents the width of the detector resolution in dijet mass. Also shown are the expected 95% credibility expected upper limit on the Gaussian signal shape with a 0% width (dotted line) and the associated 1 and 2  $\sigma$  uncertainty bands (green and yellow) [11].

## Chapter 10

# Future Prospects of Di-*b*-Jet Searches

This chapter will consider the future prospects of di-*b*-jet searches at ATLAS, including a discussion of possible improvements and developments of the analyses presented in this thesis.

## 10.1 Di-*b*-Jet Searches at Higher Luminosities

The LHC has been collecting 13 TeV  $pp$  collision data since May 2015 and is scheduled to continue until 2038 [118]. The di-*b*-jet searches presented in Chapters 6 – 9 used 13 TeV  $pp$  collision data collected in 2015 and 2016. It is expected that the integrated luminosity of  $pp$  collision data collected by the end of 2022 will be  $\sim 300 \text{ fb}^{-1}$  [118]. After 2022, significant upgrades to the LHC accelerator and ATLAS detector are planned such that data can be taken at a higher instantaneous luminosity, this is known as the High-Luminosity LHC. The High-Luminosity LHC is expected to collect 13 or 14 TeV  $pp$  collision data with an integrated luminosity of  $\sim 3000 \text{ fb}^{-1}$  by the end of 2038 [118].

Table 10.1 summarises the integrated luminosity of the data-sets used by di-*b*-jet searches at ATLAS and the expected integrated luminosities at the key points in the LHC schedule discussed above. All di-*b*-jet searches at ATLAS use 13 TeV  $pp$  collisions.

The sensitivity of the di-*b*-jet analysis can be estimated as  $S/\sqrt{B}$ , where  $S$  and  $B$  are the number of signal and background events passing the di-*b*-jet event selection in the mass region of the signal. This approximation assumes that a perfect background estimation model is used and that there is no change in the systematic uncertainties used. Therefore the estimated sensitivity of the di-*b*-jet analysis is proportional to the square root of the integrated luminosity. Using this approximation and the values in Table 10.1, it can be seen that the addition of data collected in 2016 increased the sensitivity of di-*b*-jet searches by a

End of Data Collection	Integrated Luminosity using a Single Jet Trigger	Integrated Luminosity using a Double $b$ -Jet Trigger
End of 2015	$3.2 \text{ fb}^{-1}$ [12]	$3.2 \text{ fb}^{-1}$ [13]
July 2016	$13.3 \text{ fb}^{-1}$ [10]	No analysis performed
End of 2016	$36.1 \text{ fb}^{-1}$ [11]	$24.3 \text{ fb}^{-1}$ [11] †
End of 2022	$\sim 300 \text{ fb}^{-1}$ ( <i>Projection</i> )	$\sim 300 \text{ fb}^{-1}$ ( <i>Projection</i> )
End of 2038	$\sim 3000 \text{ fb}^{-1}$ ( <i>Projection</i> )	$\sim 3000 \text{ fb}^{-1}$ ( <i>Projection</i> )

**Table 10.1:** A summary of the integrated luminosity of data-sets used by the di- $b$ -jet analyses performed at ATLAS and the expected integrated luminosities at key points in the LHC schedule [118]. All data-sets contain 13 TeV  $pp$  collision data collected since May 2015, with the exception of the ‘End of 2016’ data-set using a double  $b$ -jet trigger (†) which is collected from March 2016.

factor of  $\sim \sqrt{10}$ . The next analysis to obtain a similar gain in sensitivity must contain all  $pp$  collision data collected up to end of 2022, and then for the same increase again all data collected up to the end of 2038 must be included.

Therefore it can be seen that the increasing integrated luminosity of data collected by ATLAS will allow for di- $b$ -jet searches with increased sensitivity in the future, although the time intervals between similar improvements of sensitivity become large. Furthermore, at the Hi-Lumi LHC it is likely that there might be other limitations, for example  $b$ -tagging performance may decrease in the high track density environments expected at the Hi-Lumi LHC. Therefore, it is important to investigate other techniques to increase the sensitivity on a shorter time-scale.

## 10.2 Combination of $b$ -Tagging Categories

The *Summer16\_HighMass* data-set analysis presented in Chapters 6–9 uses two  $b$ -tag categories; the 2  $b$ -tag and  $\geq 1$   $b$ -tag category. The two categories are considered independently; the former is used to search for a  $Z'$  boson and the latter is used to search for a  $b^*$  quark. However, a  $Z'$  boson can sometimes have only one  $b$ -tag as a true  $b$ -jet may not be  $b$ -tagged. Similarly, a  $b^*$  quark can have two  $b$ -tags as a gluon can split into two  $b$ -quarks which can be tagged. The two features described above can be seen in Figure 7.7(b).

Hence, to increase the signal acceptance of the current analysis one could consider three exclusive  $b$ -tagging categories; where there are two jets that contain exactly 0, 1 or 2  $b$ -tags. Limits are then set on the benchmark models using a statistical combination of the three  $b$ -tagging categories. This would allow for limits to be set on each model using the

information from all three categories.

A di- $b$ -jet search using a combination of the three  $b$ -tagging categories has been performed by the CMS collaboration [9]. The CMS analysis uses 8 TeV  $pp$  collision data with an integrated luminosity of  $19.6 \text{ fb}^{-1}$  in the mass region  $m_{jj} > 1.1 \text{ TeV}$ . Table 10.2 shows a comparison of the 95% credibility-level observed upper mass limits set on the benchmark models by the *Summer16\_HighMass* data-set analysis and the CMS di- $b$ -jet search; the upper mass limit is the highest mass excluded. The *Summer16\_HighMass* data-set analysis sets a higher upper mass limit on the  $b^*$  quark than the CMS search; likely due to the larger centre-of-mass energy used. The improvement from combining categories is smaller for the  $b^*$  quark as the  $\geq 1$   $b$ -tag category is already used by the *Summer16\_HighMass* analysis. However, the CMS search is able to set a limit on the SSM  $Z'$  boson, where the *Summer16\_HighMass* data-set analysis cannot.

It should be noted that the direct comparison of limits is not perfect as the CMS detector, object reconstruction and analysis structure is different to those at ATLAS and different luminosities and centre-of-mass energies have been used. That said, the comparison does suggest that a combination of categories could lead to a significant improvement of the sensitivity to the  $Z'$  boson signal models in future ATLAS di- $b$ -jet analyses and should be investigated.

<b>Analysis</b>	$\sqrt{s}$	<b>Integrated Luminosity</b>	<b>95% CL Observed Upper Mass Limit</b>	
			SSM $Z'$ boson	$b^*$ quark
ATLAS [10]	13 TeV	$13.3 \text{ fb}^{-1}$	-	2.3 TeV
CMS [9]	8 TeV	$19.6 \text{ fb}^{-1}$	1.7 TeV	1.5 TeV

**Table 10.2:** A comparison of the observed 95% credibility level (CL) upper mass limits set on the Sequential Standard Model  $Z'$  boson and  $b^*$  quark by the *Summer16\_HighMass* data-set analysis at ATLAS and a di- $b$ -jet search performed by the CMS collaboration [9]. The upper mass limit represents the highest mass excluded by the analysis on the two benchmark models considered. A dash indicates that no limit was set.

## 10.3 Improvement of $b$ -Jet Trigger Efficiency Measurement

In Section 9.4 it was shown that in the *Full16\_LowMass* data-set analysis there is a large systematic uncertainty at high dijet mass due to the measurement of the  $b$ -jet trigger efficiency, the details of which are described in Chapter 5. Tables 5.3 and 5.5 show that the largest sources of uncertainty on the measurement of the  $b$ -jet trigger efficiency are caused by non- $b$ -jet impurities and the high- $p_T$  extrapolation process required due to the low number of high- $p_T$  jets in di-lepton  $t\bar{t}$  events.

Techniques have been developed to reduce the same sources of systematic uncertainties in measurements of the offline <sup>1</sup>  $b$ -tagging efficiency [79, 80], described in Section 4.3.4. For example, a Boosted Decision Tree (BDT) is used to increase the  $b$ -jet purity of the selected jets and di-lepton  $t\bar{t}$  events containing two electrons or two muons are included to increase the number of di-lepton  $t\bar{t}$  events. Such techniques can be used to improve the  $b$ -jet trigger efficiency measurements.

A possible future development is to combine the frameworks used by the  $b$ -jet trigger and offline  $b$ -tagging efficiency measurements. This would allow for a combined offline plus online  $b$ -tagging efficiency measurement using the improved techniques from the offline  $b$ -tagging measurement described above.

## 10.4 Signal Plus Background Fit in the Search Phase

In Figure 9.6 it was shown that, for the *Full16\_LowMass* data-set analysis, there is a signal induced fit bias when the nominal background estimate is applied to a background-only dijet mass spectrum injected with a dijet mass signal template of a SSM  $Z'$  boson. This could be because higher order dijet fit functions and more complex fitting models, such as SWiFt, are required to estimate the background from QCD dijet production at high luminosity. The signal induced fit bias is removed when a technique employing a signal plus background fit is applied. The signal plus background fit is not used in the search phase of the *Full16\_LowMass* analysis such that model independence can be maintained.

Therefore, to improve the sensitivity of the search phase in future analyses a signal plus background fit should be considered, such that the signal induced fit biases are removed. To reduce the dependence of such a search phase on any signal model, a large range of signal widths should be considered. A similar approach has been used in a search for resonances decaying into a pair of photons at ATLAS [119].

Furthermore, an analysis based around the signal plus background fit could be developed such that same signal plus background fit is used in the search phase and limit setting phase. This would simplify the analysis structure as the same background estimate would be used in the search phase and limit setting phase.

---

<sup>1</sup>Offline refers to objects reconstructed after events have passed the trigger at the data-processing level and online refers to reconstructed objects used in the trigger decision. From the definition in Section 5.3.

## Chapter 11

# Conclusions

Two searches for Beyond Standard Model (BSM) resonances in the invariant mass of pairs of jets, where at least one or both jets contain a  $b$ -quark, have been performed using 13 TeV  $pp$  collision data collected by the ATLAS detector. Such searches are sensitive to BSM resonances that preferentially decay to one or two  $b$ -quarks, such as the excited  $b^*$  quark and the  $Z'$  boson.

A high-mass di- $b$ -jet search probes the mass region 1.4 – 6 TeV using data collected in 2015-16 with an integrated luminosity of  $13.3 \text{ fb}^{-1}$ . No evidence of a BSM resonance is found. The excited  $b^*$  quark with a mass in the interval 1.4 – 2.3 TeV and the leptophobic  $Z'$  boson with a mass of 1.5 TeV are excluded at the 95% credibility level. 95% credibility level upper limits on  $\sigma \times A \times \epsilon \times BR$  are set in the range 0.2 to 0.001 pb for generic Gaussian signals with widths from 15% to 3% and masses in the interval 1.4 – 6 TeV. This di- $b$ -jet search has been published as a conference note [10].

A low-mass di- $b$ -jet search probes the mass region 0.6 – 1.5 TeV using data collected using the ATLAS  $b$ -jet trigger in 2016 with an integrated luminosity of  $24.3 \text{ fb}^{-1}$ . No evidence of a BSM resonance is found. The sequential standard model and leptophobic  $Z'$  boson models with a mass in the interval 0.6 – 1.25 TeV and a dark matter inspired  $Z'$  boson model with a mass in the interval 0.6 – 1.0 TeV are excluded at the 95% credibility level. 95% credibility level upper limits on  $\sigma \times A \times \epsilon \times BR$  in the range 0.05 to 0.003 pb are set for generic Gaussian signals with widths from 15% to 0% and masses in the interval 0.65 – 1.4 TeV. This di- $b$ -jet search has been submitted to Phys. Rev. D. [11].

The low-mass di- $b$ -jet search uses the ATLAS  $b$ -jet trigger; therefore a detailed understanding of the  $b$ -jet trigger performance is required. It was identified that some regions of data collected by the ATLAS  $b$ -jet trigger in 2016 were defective and a strategy was developed to mitigate the observed issues. Then, a measurement of the  $b$ -jet trigger efficiency

in 2016 data was performed. The  $b$ -jet trigger studies and efficiency measurement presented in this thesis will be used by a number of ATLAS analyses, such as a proposed update to a search for resonances decaying to 4  $b$ -quarks via a pair of Higgs bosons [120] using 2016 data.

The outlook for future di- $b$ -jet searches at the ATLAS detector has been considered, including a summary of the prospects for di- $b$ -jet searches at high luminosities and a discussion of possible future developments to further improve the analyses presented in this thesis.

## Appendix A

# Dijet Mass Binning

The dijet mass binning used in the di-*b*-jet analyses, given in units of GeV:

203, 216, 229, 243, 257, 272, 287, 303, 319, 335, 352, 369,  
387, 405, 424, 443, 462, 482, 500, 523, 544, 566, 588, 611,  
634, 657, 681, 705, 730, 755, 781, 807, 834, 861, 889, 917,  
946, 976, 1006, 1037, 1068, 1100, 1133, 1166, 1200, 1234,  
1269, 1305, 1341, 1378, 1416, 1454, 1493, 1533, 1573, 1614,  
1656, 1698, 1741, 1785, 1830, 1875, 1921, 1968, 2016, 2065,  
2114, 2164, 2215, 2267, 2320, 2374, 2429, 2485, 2542, 2600,  
2659, 2719, 2780, 2842, 2905, 2969, 3034, 3100, 3167, 3235,  
3305, 3376, 3448, 3521, 3596, 3672, 3749, 3827, 3907, 3988,  
4070, 4154, 4239, 4326, 4414, 4504, 4595, 4688, 4782, 4878,  
4975, 5074, 5175, 5277, 5381, 5487, 5595, 5705, 5817, 5931,  
6047, 6165, 6285, 6407, 6531, 6658, 6787, 6918, 7052, 7188,  
7326, 7467, 7610, 7756, 7904, 8055, 8208, 8364, 8523, 8685,  
8850, 9019, 9191, 9366, 9544, 9726, 9911, 10100, 10292,  
10488, 10688, 10892, 11100, 11312, 11528, 11748, 11972,  
12200, 12432, 12669, 12910, 13156

## Appendix B

# Single Jet Trigger Threshold $p_T$ Fit

The trigger plateau is defined as the kinematic region where all events that pass the offline jet- $p_T$  selection also pass the online jet- $p_T$  selection at the trigger level. To be on the trigger plateau of a single jet trigger the offline jet- $p_T$  must be above some threshold value, which is referred to as the threshold jet- $p_T$ .

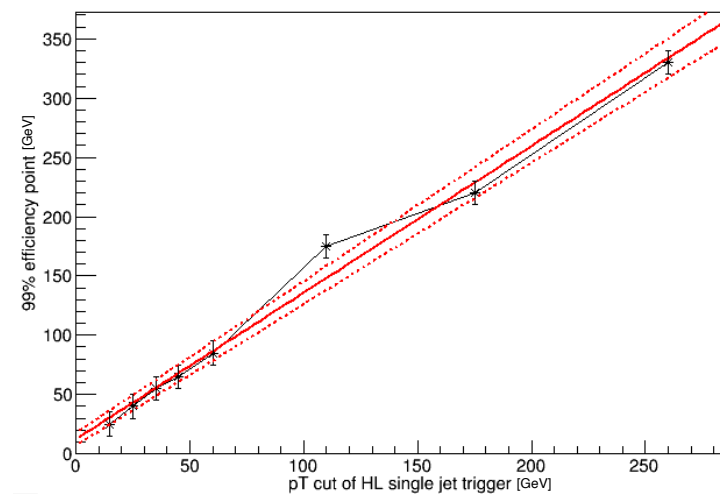
For single jet triggers it is found that the threshold offline jet- $p_T$  follows a linear behaviour with respect to the online jet- $p_T$  requirements at the trigger level. Therefore a linear fit can be used to predict the threshold jet- $p_T$  of any single jet trigger from considering a small number of single jet triggers. The single jet triggers considered require that there is an online jet with  $p_T$  above 15, 25, 35, 45, 60, 110, 175, 260 and 360 GeV respectively.

Figure B.1 shows the threshold jet- $p_T$  at which a trigger is 99% efficient with respect to a lower- $p_T$  benchmark trigger as a function of the jet- $p_T$  requirement of the single jet trigger. A linear fit is performed, as shown by the red line. The  $1\sigma$  error band on the fit slope is shown by the dotted lines [121].

The resulting linear fit has a normalisation of 12.3 and a slope of 1.24. Applying the fit to the trigger level jet requirements of the double  $b$ -jet trigger we obtain:

- Trigger level jet  $p_T > 150$  GeV, Threshold offline jet  $p_T > 198$  GeV
- Trigger level jet  $p_T > 50$  GeV, Threshold offline jet  $p_T > 74.1$  GeV

The values are rounded up in the analysis to give a safety margin.



**Figure B.1:** A plot showing the threshold offline jet- $p_T$  at which a trigger is 99% efficient with respect to a lower- $p_T$  benchmark trigger as a function of the trigger-level  $p_T$  requirements of the single jet trigger. A linear fit is performed, as shown by the red line. The  $1\sigma$  error band on the fit slope is shown by the dotted lines [121].

## Appendix C

# Additional Plots for *Full16\_LowMass* Data-Set Fit Validation Studies

### C.1 Figure 8.20 for all SWiFt configurations

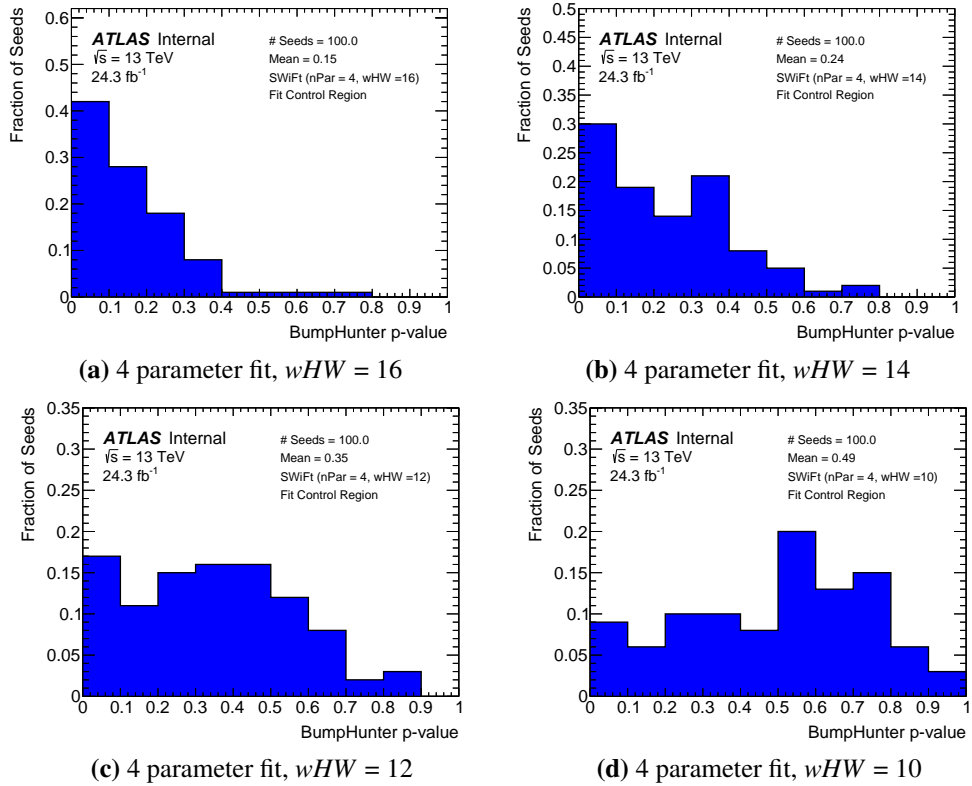


**Figure C.1:** Figure 8.20 for all SWiFt configurations using the 4 parameter dijet fit function. This figure shows the normalised distribution of BumpHunter  $p$ -values from performing the SWiFt background estimate on an ensemble of data-like dijet mass spectra taken from the fit control region for the *Full16\_LowMass* data-set. The SWiFt configurations shown use the 4 parameter dijet fit function for a window half-width ( $wHW$ ) range of 10 to 16.

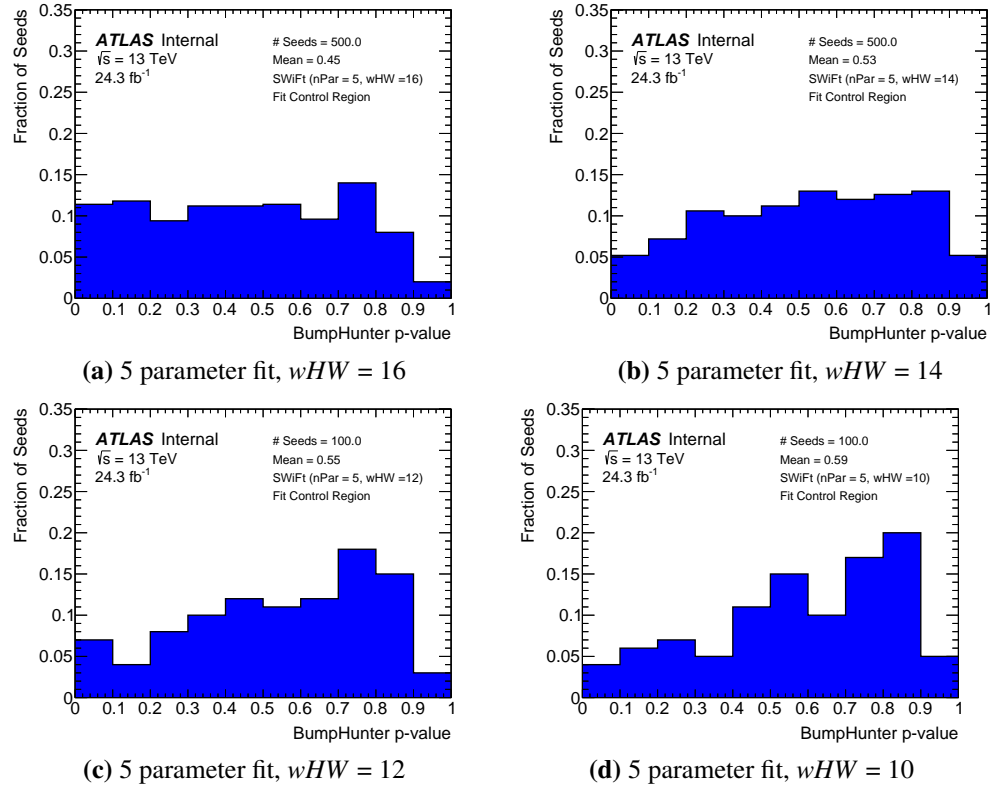


**Figure C.2:** Figure 8.20 for all SWiFt configurations using the 5 parameter dijet fit function. This figure shows the normalised distribution of BumpHunter  $p$ -values from performing the SWiFt background estimate on an ensemble of data-like dijet mass spectra taken from the fit control region for the *Full16\_LowMass* data-set. The SWiFt configurations shown use the 5 parameter dijet fit function for a window half-width ( $wHW$ ) range of 10 to 16.

## C.2 Figure 8.18 for all SWiFt configurations

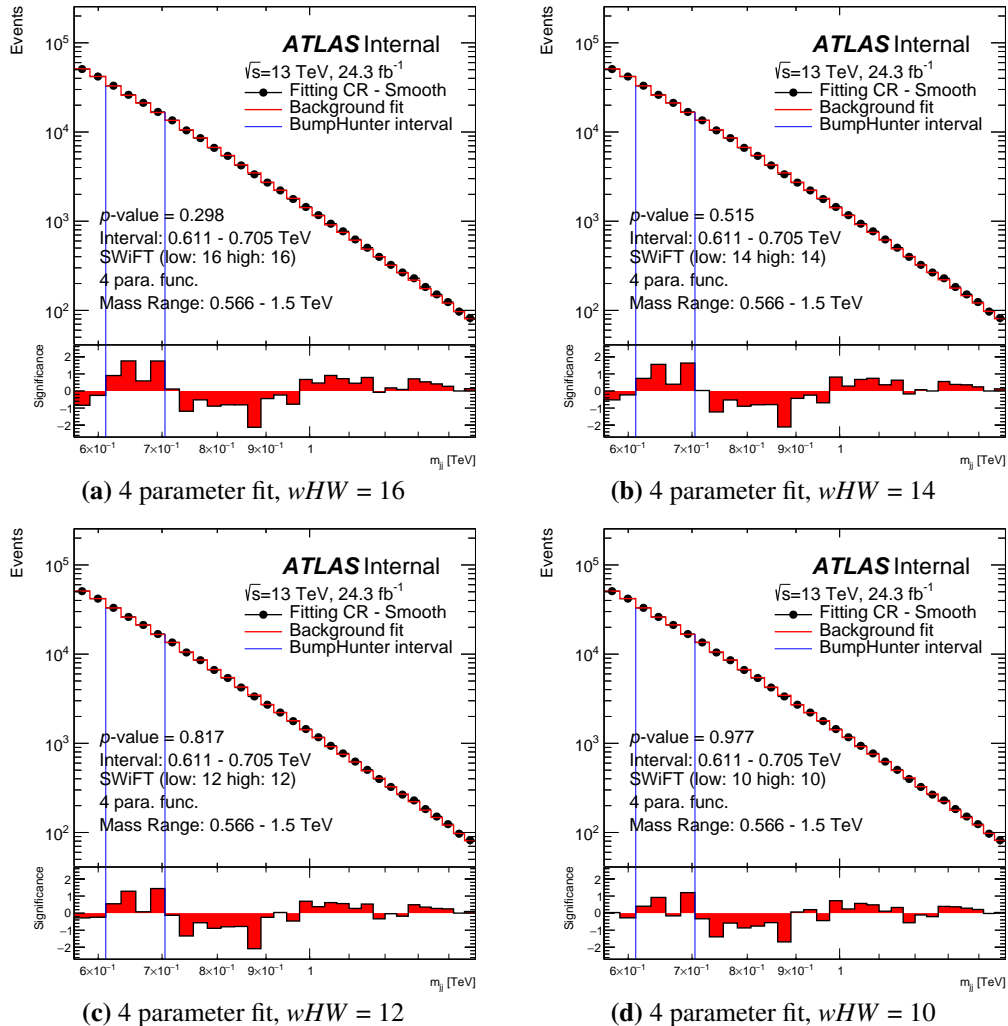


**Figure C.3:** Figure 8.18 for all SWiFt configurations using the 4 parameter dijet fit function. The SWiFt search phase run on the smooth dijet mass spectrum from the fit control region for the *Full16\_LowMass* data-set. The SWiFt configurations shown use the 4 parameter dijet fit function for a window half-width ( $wHW$ ) range of 10 to 16.

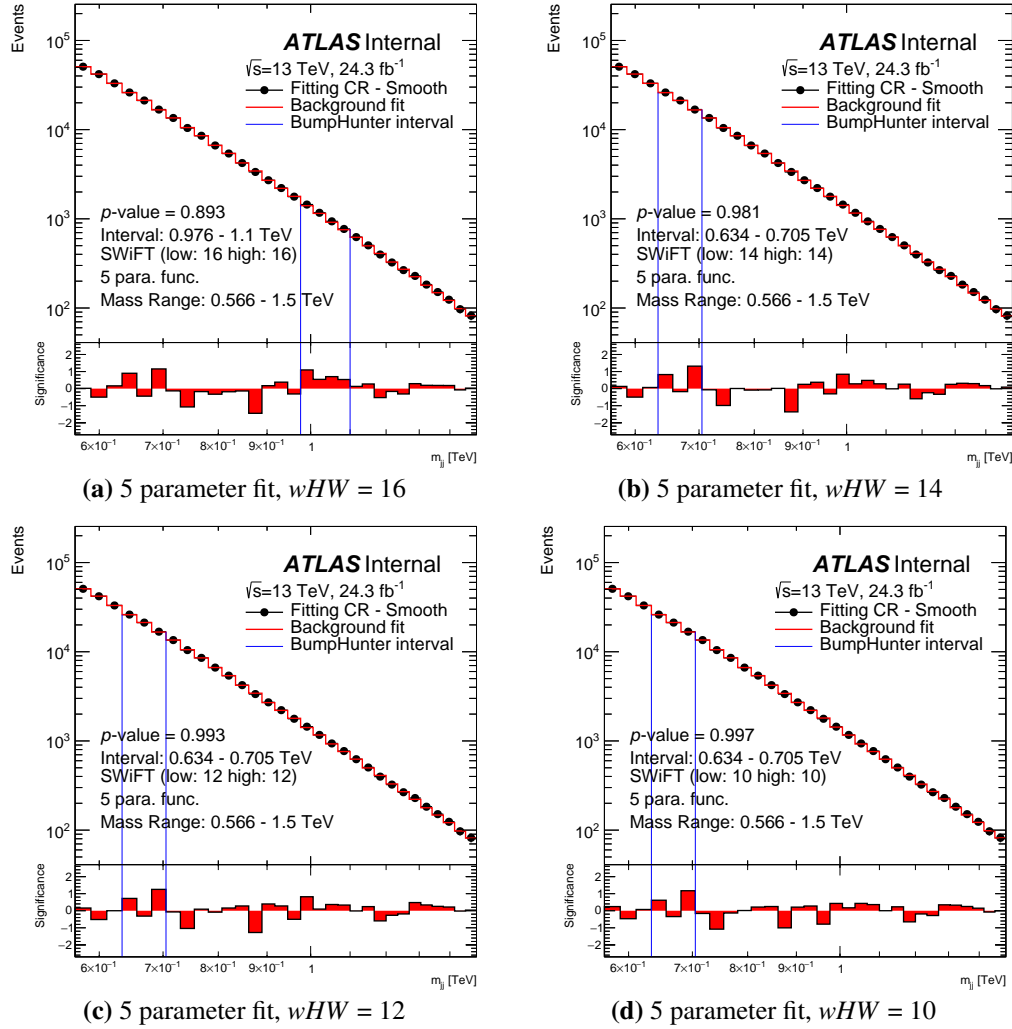


**Figure C.4:** Figure 8.18 for all SWiFt configurations using the 5 parameter dijet fit function. The SWiFt search phase run on the smooth dijet mass spectrum from the fit control region for the *Full16\_LowMass* data-set. The SWiFt configurations shown use the 5 parameter dijet fit function for a window half-width ( $wHW$ ) range of 10 to 16.

### C.3 Figure 8.19 for all SWiFt configurations

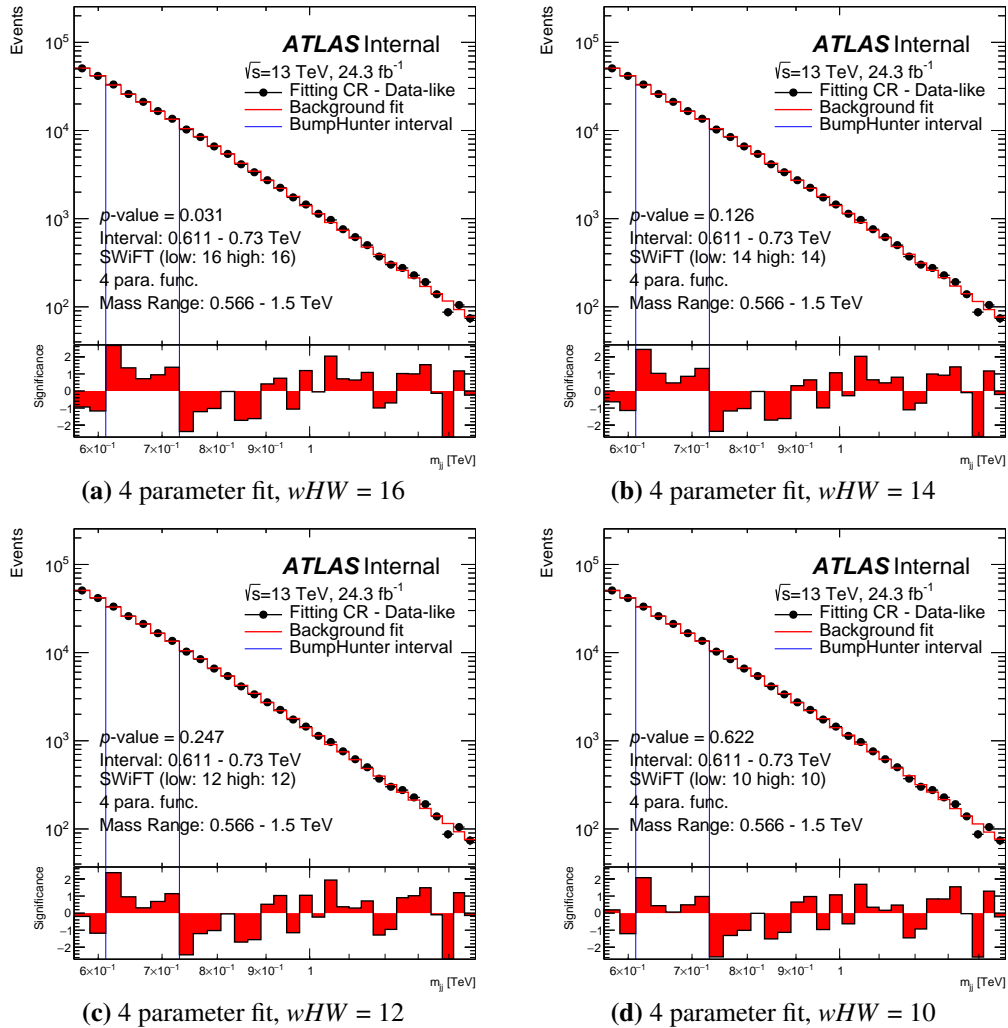


**Figure C.5:** Figure 8.19 for all SWiFt configurations using the 4 parameter dijet fit function. The SWiFt search phase run on a data-like dijet mass spectrum from the fit control region for the *Full16\_LowMass* data-set. The SWiFt configurations shown use the 4 parameter dijet fit function for a window half-width ( $wHW$ ) range of 10 to 16.

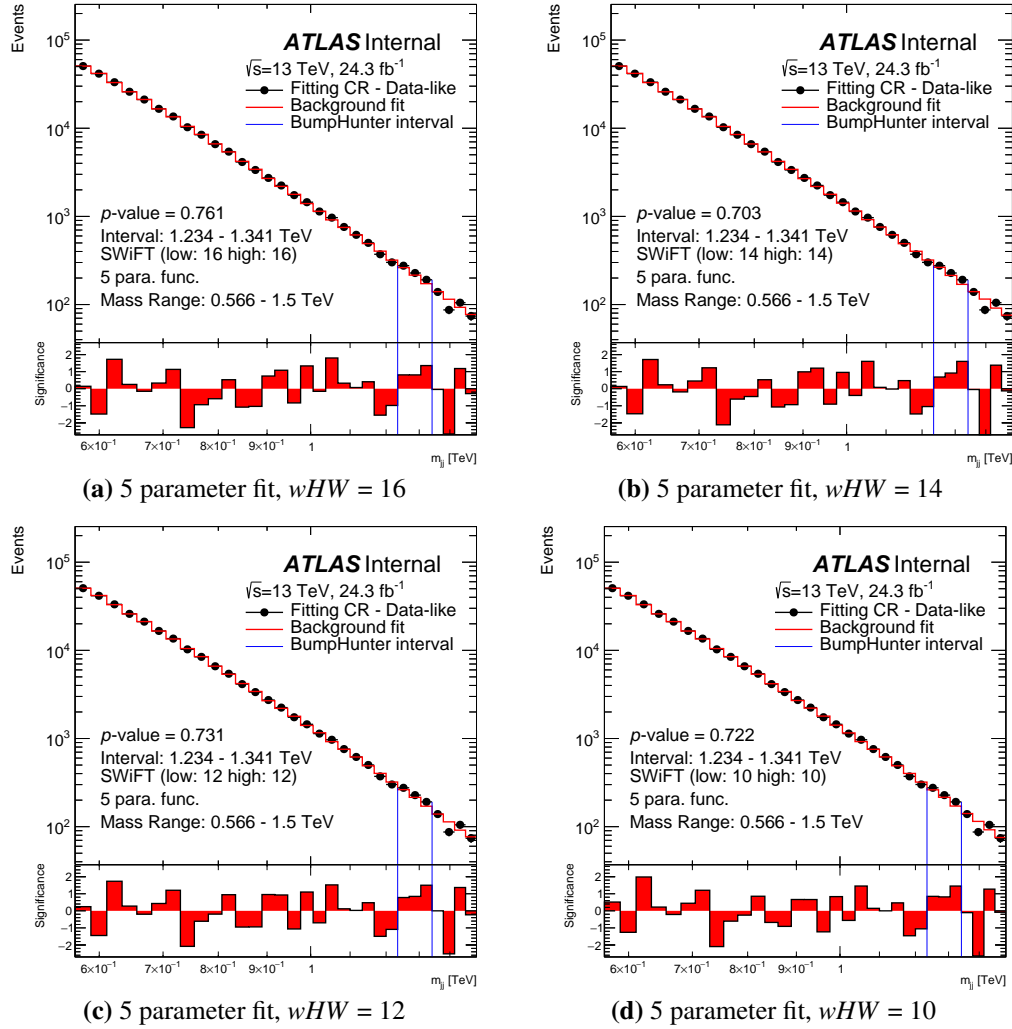


**Figure C.6:** Figure 8.19 for all SWiFt configurations using the 5 parameter dijet fit function. The SWiFt search phase run on a data-like dijet mass spectrum from the fit control region for the *Full16\_LowMass* data-set. The SWiFt configurations shown use the 5 parameter dijet fit function for a window half-width ( $wHW$ ) range of 10 to 16.

## C.4 Figure 8.21 for all SWiFt configurations.

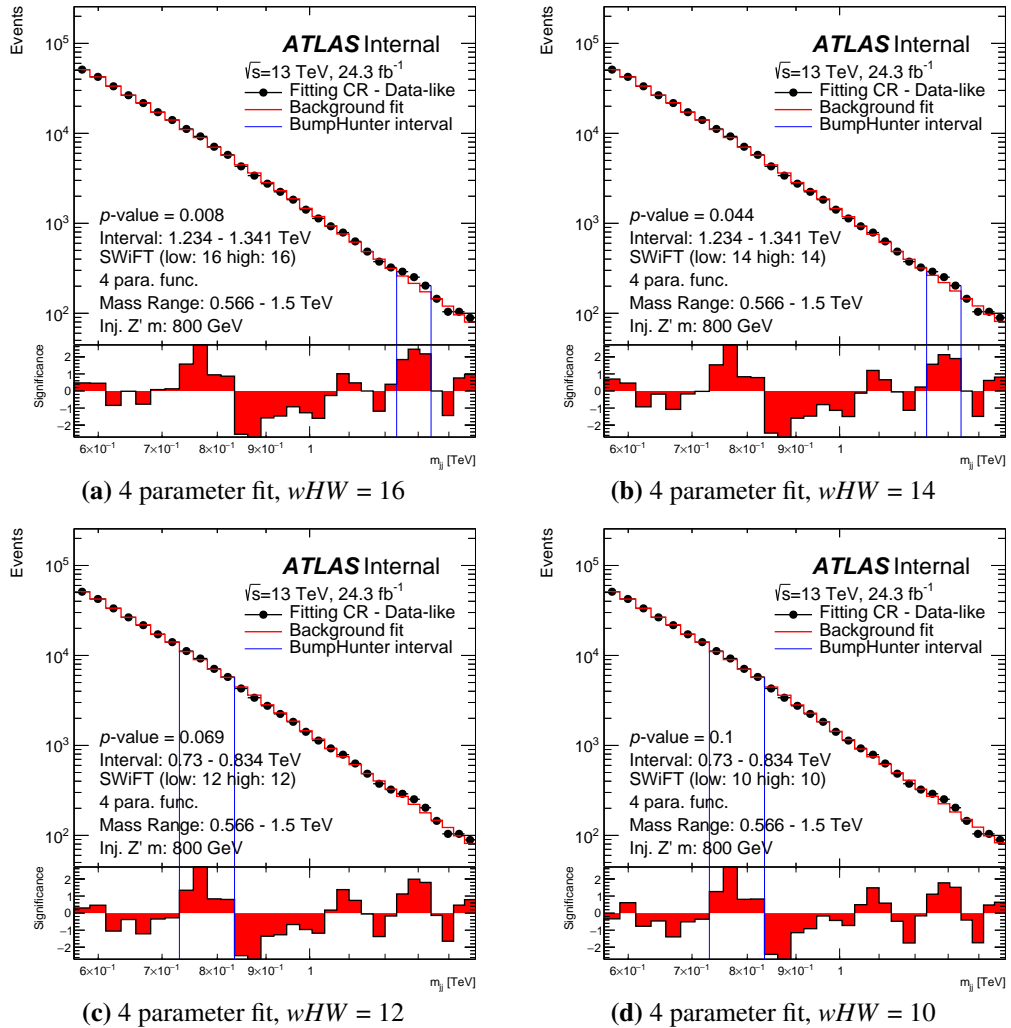


**Figure C.7:** Figure 8.21 for all SWiFt configurations using the 4 parameter dijet fit function. The SWiFt search phase run on a data-like dijet mass spectrum from the fit control region with a SSM  $Z'$  of mass 800 GeV injected. The SWiFt configurations shown use the 4 parameter dijet fit function for a window half-width ( $wHW$ ) range of 10 to 16.

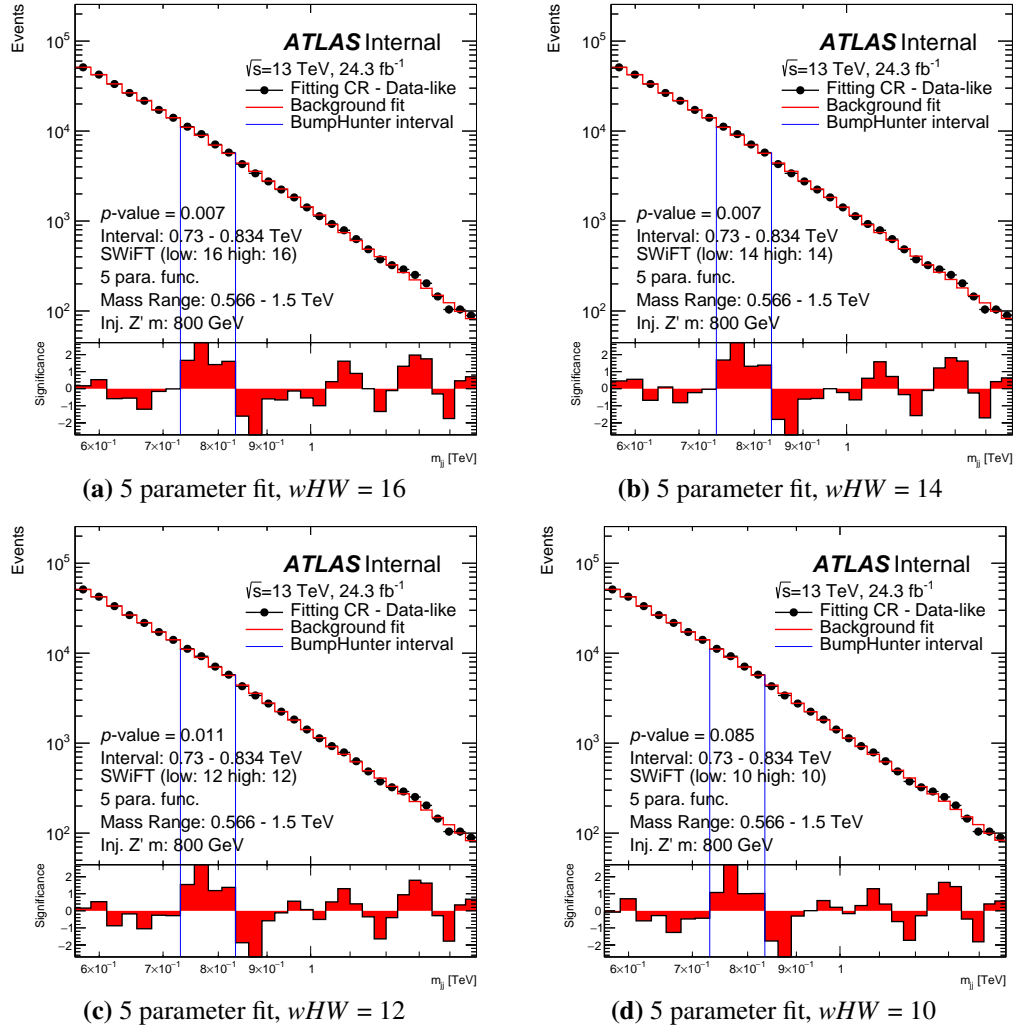


**Figure C.8:** Figure 8.21 for all SWiFt configurations using the 5 parameter dijet fit function. The SWiFt search phase run on a data-like dijet mass spectrum from the fit control region with a SSM  $Z'$  of mass 800 GeV injected. The SWiFt configurations shown use the 5 parameter dijet fit function for a window half-width ( $wHW$ ) range of 10 to 16.

# Bibliography

- [1] R. M. Harris and K. Kousouris, *Searches for Dijet Resonances at Hadron Colliders*, Int. J. Mod. Phys. **A26** (2011) 5005–5055, arXiv:1110.5302 [hep-ex].
- [2] ATLAS Collaboration, *Search for new phenomena in dijet mass and angular distributions from pp collisions at  $\sqrt{s} = 13$  TeV with the ATLAS detector*, Phys. Lett. **B754** (2016) 302–322, arXiv:1512.01530 [hep-ex].
- [3] ATLAS Collaboration, *Search for new phenomena in dijet events using  $37\text{ fb}^{-1}$  of pp collision data collected at  $\sqrt{s} = 13$  TeV with the ATLAS detector*, Phys. Rev. **D96** (2017) no. 5, 052004, arXiv:1703.09127 [hep-ex].
- [4] CMS Collaboration, *Search for dijet resonances in proton-proton collisions at  $\sqrt{s} = 13$  TeV and constraints on dark matter and other models*, Phys. Lett. **B769** (2017) 520–542, arXiv:1611.03568 [hep-ex]. [Erratum: Phys. Lett.B772,882(2017)].
- [5] ATLAS Collaboration, *Search for new light resonances decaying to jet pairs and produced in association with a photon or a jet in proton-proton collisions at  $\sqrt{s} = 13$  TeV with the ATLAS detector*, Tech. Rep. ATLAS-CONF-2016-070, CERN, Geneva, Aug, 2016. <https://cds.cern.ch/record/2206221>.
- [6] ATLAS Collaboration, *Search for light dijet resonances with the ATLAS detector using a Trigger-Level Analysis in LHC pp collisions at  $\sqrt{s} = 13$  TeV*, Tech. Rep. ATLAS-CONF-2016-030, CERN, Geneva, Jun, 2016. <https://cds.cern.ch/record/2161135>.
- [7] CMS Collaboration, *Search for Low Mass Vector Resonances Decaying to Quark-Antiquark Pairs in Proton-Proton Collisions at  $\sqrt{s} = 13$  TeV*, Phys. Rev. Lett. **119** (2017) no. 11, 111802, arXiv:1705.10532 [hep-ex].
- [8] CDF Collaboration, *Search for New Particles Decaying to  $b\bar{b}$  in  $p\bar{p}$  Collisions at  $\sqrt{s} = 1.8$  TeV*, Phys. Rev. Lett. **82** (1999) 2038–2043, arXiv:hep-ex/9809022 [hep-ex].

- [9] CMS Collaboration, *Search for Heavy Resonances Decaying into bb and bg Final States in pp Collisions at  $\sqrt{s} = 8 \text{ TeV}$* , Tech. Rep. CMS-PAS-EXO-12-023, CERN, Geneva, 2013. <https://cds.cern.ch/record/1542405>.
- [10] ATLAS Collaboration, *Search for resonances in the mass distribution of jet pairs with one or two jets identified as b-jets with the ATLAS detector with 2015 and 2016 data*, Tech. Rep. ATLAS-CONF-2016-060, CERN, Geneva, Aug, 2016. <https://cds.cern.ch/record/2206175>.
- [11] ATLAS Collaboration, *Search for resonances in the mass distribution of jet pairs with one or two jets identified as b-jets in proton-proton collisions at  $\sqrt{s} = 13 \text{ TeV}$  with the ATLAS detector*, Submitted to Phys. Rev. D. (2018) , arXiv:1805.09299 [hep-ex].
- [12] ATLAS Collaboration, *Search for resonances in the mass distribution of jet pairs with one or two jets identified as b-jets in proton–proton collisions at  $\sqrt{s} = 13 \text{ TeV}$  with the ATLAS detector*, Phys. Lett. **B759** (2016) 229–246, arXiv:1603.08791 [hep-ex].
- [13] ATLAS Collaboration, *Search for resonances below 1.2 TeV from the mass distribution of b-jet pairs in proton-proton collisions at  $\sqrt{s}=13 \text{ TeV}$  with the ATLAS detector*, Tech. Rep. ATLAS-CONF-2016-031, CERN, Geneva, Jun, 2016. <https://cds.cern.ch/record/2161136>.
- [14] G. Altarelli and M. W. Grunewald, *Precision electroweak tests of the standard model*, Phys. Rept. **403-404** (2004) 189–201, arXiv:hep-ph/0404165 [hep-ph].
- [15] C. Patrignani et al., *Review of Particle Physics*, Chin. Phys. **C40** (2016) no. 10, 100001.
- [16] S. L. Glashow, *Partial Symmetries of Weak Interactions*, Nucl. Phys. **22** (1961) 579–588.
- [17] P. W. Higgs, *Broken Symmetries and the Masses of Gauge Bosons*, Phys. Rev. Lett. **13** (1964) 508–509.
- [18] F. Englert and R. Brout, *Broken Symmetry and the Mass of Gauge Vector Mesons*, Phys. Rev. Lett. **13** (1964) 321–323.
- [19] T. Gershon, *Overview of the CKM Matrix*, Pramana **79** (2012) 1091–1108, arXiv:1112.1984 [hep-ex].

- [20] ATLAS Collaboration, *Observation of a new particle in the search for the Standard Model Higgs boson with the ATLAS detector at the LHC*, Phys. Lett. B **B716** (2012) 1–29, arXiv:1207.7214 [hep-ex].
- [21] CMS Collaboration, *Observation of a new boson at a mass of 125 GeV with the CMS experiment at the LHC*, Phys. Lett. B **B716** (2012) 30–61, arXiv:1207.7235 [hep-ex].
- [22] K. Pachal, *Search for new physics in the dijet invariant mass spectrum at 8 TeV*. PhD Thesis, Jan, 2015, Presented 01 Jun 2015.  
<http://cds.cern.ch/record/2063032>.
- [23] A. Zee, *Quantum field theory in a nutshell*. Princeton Univ. Press, Princeton, NJ, 2003.
- [24] B. Andersson, G. Gustafson, G. Ingelman, and T. Sjostrand, *Parton Fragmentation and String Dynamics*, Phys. Rept. **97** (1983) 31–145.
- [25] B. R. Webber, *A QCD Model for Jet Fragmentation Including Soft Gluon Interference*, Nucl. Phys. **B238** (1984) 492–528.
- [26] J. Butterworth, *This is not a measurement*, Guardian newspaper, 2015.  
<https://www.theguardian.com/science/life-and-physics/2015/jan/10/this-is-not-a-measurement>.
- [27] C. A. Aidala, S. D. Bass, D. Hasch, and G. K. Mallot, *The Spin Structure of the Nucleon*, Rev. Mod. Phys. **85** (2013) 655–691, arXiv:1209.2803 [hep-ph].
- [28] C. C. Tully, *Elementary particle physics in a nutshell*. Princeton Univ. Press, Princeton, NJ, 2011. <https://cds.cern.ch/record/1417476>.
- [29] ZEUS, H1 Collaboration, *Combined Measurement and QCD Analysis of the Inclusive  $e^- + p$  Scattering Cross Sections at HERA*, JHEP **01** (2010) 109, arXiv:0911.0884 [hep-ex].
- [30] L. A. Harland-Lang, A. D. Martin, P. Motylinski, and R. S. Thorne, *Parton distributions in the LHC era: MMHT 2014 PDFs*, Eur. Phys. J. **C75** (2015) no. 5, 204, arXiv:1412.3989 [hep-ph].
- [31] CDF Collaboration, *Observation of Single Top Quark Production and Measurement of  $|V_{tb}|$  with CDF*, Phys. Rev. **D82** (2010) 112005, arXiv:1004.1181 [hep-ex].

- [32] M. E. Peskin, *Dark matter and particle physics*, J. Phys. Soc. Jap. **76** (2007) 111017, arXiv:0707.1536 [hep-ph].
- [33] M. Roos, *Dark Matter: The evidence from astronomy, astrophysics and cosmology*, arXiv:1001.0316 [astro-ph.CO].
- [34] J. L. Feng, *Dark Matter Candidates from Particle Physics and Methods of Detection*, Ann. Rev. Astron. Astrophys. **48** (2010) 495–545, arXiv:1003.0904 [astro-ph.CO].
- [35] C. Csaki and P. Tanedo, *Beyond the Standard Model*, in *Proceedings, 2013 European School of High-Energy Physics (ESHEP 2013): Paradfurdo, Hungary, June 5-18, 2013*, pp. 169–268. 2015. arXiv:1602.04228 [hep-ph].
- [36] S. P. Martin, *A Supersymmetry primer*, pp. 1–98. World Scientific Publishing Co, 1998. arXiv:hep-ph/9709356 [hep-ph].
- [37] C. P. Yuan, *Top quark and electroweak symmetry breaking mechanism*, in *Quarks. Proceedings, 10th International Seminar on High Energy Physics, QUARKS'98, Suzdal, Russia, May 18-24, 1998*. 1998. arXiv:hep-ph/9809536 [hep-ph].
- [38] P. Langacker, *The Physics of Heavy Z' Gauge Bosons*, Rev. Mod. Phys. **81** (2009) 1199–1228, arXiv:0801.1345 [hep-ph].
- [39] ATLAS Collaboration, *Search for new high-mass phenomena in the dilepton final state using  $36\text{ fb}^{-1}$  of proton-proton collision data at  $\sqrt{s} = 13\text{ TeV}$  with the ATLAS detector*, JHEP **10** (2017) 182, arXiv:1707.02424 [hep-ex].
- [40] C.-W. Chiang, T. Nomura, and K. Yagyu, *Phenomenology of E<sub>6</sub>-Inspired Leptophobic Z' Boson at the LHC*, JHEP **05** (2014) 106, arXiv:1402.5579 [hep-ph].
- [41] A. Albert et al., *Recommendations of the LHC Dark Matter Working Group: Comparing LHC searches for heavy mediators of dark matter production in visible and invisible decay channels. Recommendations of the LHC Dark Matter Working Group: Comparing LHC searches for heavy mediators of dark matter production in visible and invisible decay channels*, Tech. Rep. CERN-LPCC-2017-01, Mar, 2017. <https://cds.cern.ch/record/2256144>.
- [42] D. A. Demir, G. L. Kane, and T. T. Wang, *The Minimal U(1)' extension of the MSSM*, Phys. Rev. **D72** (2005) 015012, arXiv:hep-ph/0503290 [hep-ph].

- [43] U. Baur, I. Hinchliffe, and D. Zeppenfeld, *Excited Quark Production at Hadron Colliders*, Int. J. Mod. Phys. **A2** (1987) 1285.
- [44] UA1 Collaboration, *Experimental Observation of Isolated Large Transverse Energy Electrons with Associated Missing Energy at  $s^{1/2} = 540 \text{ GeV}$* , Phys. Lett. **122B** (1983) 103–116. [,611(1983)].
- [45] UA1 Collaboration, *Experimental Observation of Lepton Pairs of Invariant Mass Around  $95\text{-GeV}/c^2$  at the CERN SPS Collider*, Phys. Lett. **126B** (1983) 398–410.
- [46] UA2 Collaboration, *Observation of Single Isolated Electrons of High Transverse Momentum in Events with Missing Transverse Energy at the CERN anti- $p\ p$  Collider*, Phys. Lett. **122B** (1983) 476–485.
- [47] UA2 Collaboration, *Evidence for  $Z_0 \rightarrow e^+e^-$  at the CERN anti- $p\ p$  Collider*, Phys. Lett. **129B** (1983) 130–140.
- [48] CDF Collaboration, *Observation of top quark production in  $\bar{p}p$  collisions*, Phys. Rev. Lett. **74** (1995) 2626–2631, arXiv:hep-ex/9503002 [hep-ex].
- [49] D0 Collaboration, *Observation of the top quark*, Phys. Rev. Lett. **74** (1995) 2632–2637, arXiv:hep-ex/9503003 [hep-ex].
- [50] ATLAS Collaboration, *Luminosity Public Results Run-2*, Atlas public website.  
<https://twiki.cern.ch/twiki/bin/view/AtlasPublic/LuminosityPublicResultsRun2>.
- [51] ATLAS Collaboration, *Simulation of Pile-up in the ATLAS Experiment*, J. Phys. Conf. Ser. **513** (2014) 022024.
- [52] ATLAS Collaboration, *The ATLAS Experiment at the CERN Large Hadron Collider*, JINST **3** (2008) S08003.
- [53] ATLAS Collaboration, *ATLAS detector and physics performance: Technical Design Report, 1.* Technical Design Report ATLAS. CERN, Geneva, 1999.  
<https://cds.cern.ch/record/391176>.
- [54] ATLAS Collaboration, *Performance of the ATLAS Detector using First Collision Data*, JHEP **09** (2010) 056, arXiv:1005.5254 [hep-ex].
- [55] ATLAS Collaboration, *The alignment of the ATLAS Inner Detector in Run 2*, Tech. Rep. ATL-INDET-PROC-2016-003, CERN, Geneva, Sep, 2016.  
<https://cds.cern.ch/record/2213441>.

- [56] ATLAS Collaboration, *Performance of the ATLAS Track Reconstruction Algorithms in Dense Environments in LHC Run 2*, Eur. Phys. J. **C77** (2017) no. 10, 673, arXiv:1704.07983 [hep-ex].
- [57] B. Mindur et al., *Gas gain stabilisation in the ATLAS TRT detector*, JINST **11** (2016) no. 04, P04027.
- [58] ATLAS Collaboration, *Particle Identification Performance of the ATLAS Transition Radiation Tracker*, Tech. Rep. ATLAS-CONF-2011-128, CERN, Geneva, Sep, 2011. <https://cds.cern.ch/record/1383793>.
- [59] C. Leroy and P. G. Rancoita, *Principles of Radiation Interaction in Matter and Detection*. World Scientific, 2016.
- [60] M. Livan and R. Wigmans, *Misconceptions about Calorimetry*, Instruments **1** (2017) no. 1, 3, arXiv:1704.00661 [physics.ins-det].
- [61] L. Bryngemark, *Search for new phenomena in dijet angular distributions at  $\sqrt{s} = 8$  and 13 TeV*. PhD Thesis, Feb, 2016, Presented 18 Mar 2016. <https://cds.cern.ch/record/2131851>.
- [62] J. J. Goodson and R. McCarthy, *Search for Supersymmetry in States with Large Missing Transverse Momentum and Three Leptons including a Z-Boson*. PhD Thesis, May, 2012, Presented 17 Apr 2012. <https://cds.cern.ch/record/1449722>.
- [63] S. Boutle et al., *Primary vertex reconstruction at the ATLAS experiment*, J. Phys. Conf. Ser. **898** (2017) no. 4, 042056.
- [64] J. M. Butterworth, G. Dissertori, and G. P. Salam, *Hard Processes in Proton-Proton Collisions at the Large Hadron Collider*, Ann. Rev. Nucl. Part. Sci. **62** (2012) 387–405, arXiv:1202.0583 [hep-ex].
- [65] ATLAS Collaboration, *Search for heavy resonances decaying to a W or Z boson and a Higgs boson in final states with leptons and b-jets in  $36.1 \text{ fb}^{-1}$  of pp collision data at  $\sqrt{s} = 13 \text{ TeV}$  with the ATLAS detector*, Tech. Rep. ATLAS-CONF-2017-055, CERN, Geneva, Jul, 2017. <https://cds.cern.ch/record/2273871>.
- [66] ATLAS Collaboration, *Topological cell clustering in the ATLAS calorimeters and its performance in LHC Run 1*, Eur. Phys. J. **C77** (2017) 490, arXiv:1603.02934 [hep-ex].
- [67] G. P. Salam, *Towards Jetography*, Eur. Phys. J. **C67** (2010) 637–686, arXiv:0906.1833 [hep-ph].

- [68] UA1 Collaboration, *Hadronic Jet Production at the CERN Proton - anti-Proton Collider*, Phys. Lett. **132B** (1983) 214.
- [69] M. Cacciari, G. P. Salam, and G. Soyez, *The Anti- $k_t$  jet clustering algorithm*, JHEP **04** (2008) 063, arXiv:0802.1189 [hep-ph].
- [70] ATLAS Collaboration, *Jet Calibration and Systematic Uncertainties for Jets Reconstructed in the ATLAS Detector at  $\sqrt{s} = 13$  TeV*, Tech. Rep. ATL-PHYS-PUB-2015-015, CERN, Geneva, Jul, 2015.  
<http://cds.cern.ch/record/2037613>.
- [71] ATLAS Collaboration, *Jet energy scale measurements and their systematic uncertainties in proton-proton collisions at  $\sqrt{s} = 13$  TeV with the ATLAS detector*, Phys. Rev. **D96** (2017) no. 7, 072002, arXiv:1703.09665 [hep-ex].
- [72] ATLAS Collaboration, *Search for diboson resonances with boson-tagged jets in pp collisions at  $\sqrt{s} = 13$  TeV with the ATLAS detector*, Phys. Lett. **B777** (2018) 91–113, arXiv:1708.04445 [hep-ex].
- [73] ATLAS Collaboration, *Data-driven determination of the energy scale and resolution of jets reconstructed in the ATLAS calorimeters using dijet and multijet events at  $\sqrt{s} = 8$  TeV*, Tech. Rep. ATLAS-CONF-2015-017, CERN, Geneva, Apr, 2015. <https://cds.cern.ch/record/2008678>.
- [74] ATLAS Collaboration, *Measurements of top-quark pair differential cross-sections in the  $e\mu$  channel in pp collisions at  $\sqrt{s} = 13$  TeV using the ATLAS detector*, Eur. Phys. J. **C77** (2017) no. 5, 292, arXiv:1612.05220 [hep-ex].
- [75] ATLAS Collaboration, *Evidence for the  $H \rightarrow b\bar{b}$  decay with the ATLAS detector*, JHEP **12** (2017) 024, arXiv:1708.03299 [hep-ex].
- [76] ATLAS Collaboration, *Expected performance of the ATLAS b-tagging algorithms in Run-2*, Tech. Rep. ATL-PHYS-PUB-2015-022, CERN, Geneva, Jul, 2015.  
<https://cds.cern.ch/record/2037697>.
- [77] ATLAS Collaboration, *Optimisation of the ATLAS b-tagging performance for the 2016 LHC Run*, Tech. Rep. ATL-PHYS-PUB-2016-012, CERN, Geneva, Jun, 2016.  
<https://cds.cern.ch/record/2160731>.
- [78] B. P. Roe and all., *Boosted decision trees, an alternative to artificial neural networks*, Nucl. Instrum. Meth. **A543** (2005) no. 2-3, 577–584, arXiv:physics/0408124 [physics].

- [79] ATLAS Collaboration, *Calibration of b-tagging using dileptonic top pair events in a combinatorial likelihood approach with the ATLAS experiment*, Tech. Rep. ATLAS-CONF-2014-004, CERN, Geneva, Feb, 2014.  
<https://cds.cern.ch/record/1664335>.
- [80] ATLAS Collaboration, *b-tagging calibration plots using dileptonic  $t\bar{t}$  events produced in pp collisions at  $\sqrt{s} = 13$  TeV and a combinatorial likelihood approach*, Atlas public website, 2016. <http://atlas.web.cern.ch/Atlas/GROUPS/PHYSICS/PLOTS/FTAG-2016-003/>.
- [81] G. Watts, F. Filthaut, and G. Piacquadio, *Extrapolating Errors for b-tagging*, Tech. Rep. ATL-COM-PHYS-2015-711, CERN, Geneva, Jul, 2015.  
<https://cds.cern.ch/record/2034234>.
- [82] ATLAS Collaboration, *Electron efficiency measurements with the ATLAS detector using the 2015 LHC proton-proton collision data*, Tech. Rep. ATLAS-CONF-2016-024, CERN, Geneva, Jun, 2016.  
<https://cds.cern.ch/record/2157687>.
- [83] ATLAS Collaboration, *Technical Design Report for the Phase-I Upgrade of the ATLAS TDAQ System*, Tech. Rep. CERN-LHCC-2013-018. ATLAS-TDR-023, Sep, 2013. <https://cds.cern.ch/record/1602235>. Final version presented to December 2013 LHCC.
- [84] Y. Nakahama, *The ATLAS Trigger System: Ready for Run-2*, J. Phys. Conf. Ser. **664** (2015) no. 8, 082037.
- [85] ATLAS Collaboration, *Performance of the ATLAS Trigger System in 2015*, Eur. Phys. J. **C77** (2017) no. 5, 317, arXiv:1611.09661 [hep-ex].
- [86] R. Achenbach et al., *The ATLAS level-1 calorimeter trigger*, JINST **3** (2008) P03001. <https://cds.cern.ch/record/1080560>.
- [87] ATLAS Collaboration, *2015 start-up trigger menu and initial performance assessment of the ATLAS trigger using Run-2 data*, Tech. Rep. ATL-DAQ-PUB-2016-001, CERN, Geneva, Mar, 2016.  
<https://cds.cern.ch/record/2136007>.
- [88] A. Coccaro, *Track Reconstruction and b-Jet Identification for the ATLAS Trigger System*, J. Phys. Conf. Ser. **368** (2012) 012034, arXiv:1112.0180 [hep-ex].
- [89] ATLAS Collaboration, *Measurement of the  $t\bar{t}$  production cross-section using  $e\mu$  events with b-tagged jets in pp collisions at  $\sqrt{s}=13$  TeV with the ATLAS detector*,

- Phys. Lett. **B761** (2016) 136–157, arXiv:1606.02699 [hep-ex]. [Erratum: Phys. Lett.B772,879(2017)].
- [90] S. Alioli, P. Nason, C. Oleari, and E. Re, *A general framework for implementing NLO calculations in shower Monte Carlo programs: the POWHEG BOX*, JHEP **06** (2010) 043, arXiv:1002.2581 [hep-ph].
- [91] H.-L. Lai et al., *New parton distributions for collider physics*, Phys. Rev. **D82** (2010) 074024, arXiv:1007.2241 [hep-ph].
- [92] T. Sjostrand, S. Mrenna, and P. Z. Skands, *PYTHIA 6.4 Physics and Manual*, JHEP **05** (2006) 026, arXiv:hep-ph/0603175.
- [93] J. Pumplin et al., *New generation of parton distributions with uncertainties from global QCD analysis*, JHEP **07** (2002) 012, arXiv:hep-ph/0201195 [hep-ph].
- [94] P. Z. Skands, *Tuning Monte Carlo Generators: The Perugia Tunes*, Phys. Rev. **82** (2010) 074018, arXiv:1005.3457 [hep-ph].
- [95] D. J. Lange, *The EvtGen particle decay simulation package*, Nucl. Instrum. Meth. **A462** (2001) 152–155.
- [96] J. Cogan, R. Bartoldus, E. Strauss, and E. Miller, *ATLAS Online Determination and Feedback of the LHC Beam Parameters*, Tech. Rep. ATL-DAQ-PROC-2011-027, CERN, Geneva, Oct, 2011. <https://cds.cern.ch/record/1389903>.
- [97] G. Choudalakis, *On hypothesis testing, trials factor, hypertests and the BumpHunter*, in *Proceedings, PHYSTAT 2011 Workshop on Statistical Issues Related to Discovery Claims in Search Experiments and Unfolding*, CERN, Geneva, Switzerland 17-20 January 2011. 2011. arXiv:1101.0390 [physics.data-an].
- [98] T. Sjostrand, S. Mrenna, and P. Z. Skands, *A Brief Introduction to PYTHIA 8.1*, Comput. Phys. Commun. **178** (2008) 852, arXiv:0710.3820 [hep-ph].
- [99] ATLAS Collaboration, *ATLAS Run 1 Pythia8 tunes*, Tech. Rep. ATL-PHYS-PUB-2014-021, CERN, Geneva, Nov, 2014. <https://cds.cern.ch/record/1966419>.
- [100] R. D. Ball et al., *Parton distributions with LHC data*, Nucl. Phys. **B867** (2013) 244–289, arXiv:1207.1303 [hep-ph].

- [101] ATLAS Collaboration, *The ATLAS Simulation Infrastructure*, Eur. Phys. J. **C70** (2010) 823–874, arXiv:1005.4568 [physics.ins-det].
- [102] J. Gao, C. S. Li, B. H. Li, C.-P. Yuan, and H. X. Zhu, *Next-to-leading order QCD corrections to the heavy resonance production and decay into top quark pair at the LHC*, Phys. Rev. **D82** (2010) 014020, arXiv:1004.0876 [hep-ph].
- [103] J. Alwall et al., *MadGraph 5 : Going Beyond*, JHEP **06** (2011) 128, arXiv:1106.0522 [hep-ph].
- [104] J. Alwall et al., *The automated computation of tree-level and next-to-leading order differential cross sections, and their matching to parton shower simulations*, JHEP **07** (2014) 079, arXiv:1405.0301 [hep-ph].
- [105] ATLAS Collaboration, *Selection of jets produced in 13 TeV proton-proton collisions with the ATLAS detector*, Tech. Rep. ATLAS-CONF-2015-029, CERN, Geneva, Jul, 2015. <https://cds.cern.ch/record/2037702>.
- [106] ATLAS Collaboration, *Tagging and suppression of pileup jets with the ATLAS detector*, Tech. Rep. ATLAS-CONF-2014-018, CERN, Geneva, May, 2014. <https://cds.cern.ch/record/1700870>.
- [107] T. H. Kittelmann, V. Tsulaia, J. Boudreau, and E. Moyse, *The virtual point 1 event display for the ATLAS experiment*, J. Phys. Conf. Ser. **219** (2010) 032012.
- [108] ATLAS Collaboration, *Observation of a new particle in the search for the Standard Model Higgs boson with the ATLAS detector at the LHC*, Phys. Lett. **B716** (2012) 1–29, arXiv:1207.7214 [hep-ex].
- [109] CDF Collaboration, *Search for new particles decaying to dijets in  $p\bar{p}$  collisions at  $\sqrt{s} = 1.8 \text{ TeV}$* , Phys. Rev. Lett. **74** (1995) 3538–3543, arXiv:hep-ex/9501001 [hep-ex].
- [110] CDF Collaboration, *Search for new particles decaying into dijets in proton-antiproton collisions at  $s^{**}(1/2) = 1.96\text{-TeV}$* , Phys. Rev. **D79** (2009) 112002, arXiv:0812.4036 [hep-ex].
- [111] S. S. Wilks, *The Large-Sample Distribution of the Likelihood Ratio for Testing Composite Hypotheses*, Annals Math. Statist. **9** (1938) no. 1, 60–62.
- [112] J. Heinrich et al., *Interval estimation in the presence of nuisance parameters. 1. Bayesian approach*, arXiv:physics/0409129 [physics].

- [113] ATLAS Collaboration, *Search for new phenomena in the dijet mass distribution using  $p - p$  collision data at  $\sqrt{s} = 8$  TeV with the ATLAS detector*, Phys. Rev. **D91** (2015) no. 5, 052007, arXiv:1407.1376 [hep-ex].
- [114] ATLAS Collaboration, *Search for new phenomena in the dijet mass distribution using  $p - p$  collision data at  $\sqrt{s} = 8$  TeV with the ATLAS detector*, Phys. Rev. **D91** (2015) no. 5, 052007, arXiv:1407.1376 [hep-ex].
- [115] G. Cowan, K. Cranmer, E. Gross, and O. Vitells, *Asymptotic formulae for likelihood-based tests of new physics*, Eur. Phys. J. **C71** (2011) 1554, arXiv:1007.1727 [physics.data-an]. [Erratum: Eur. Phys. J.C73,2501(2013)].
- [116] ATLAS Collaboration, *Luminosity determination in  $pp$  collisions at  $\sqrt{s} = 8$  TeV using the ATLAS detector at the LHC*, Eur. Phys. J. **C76** (2016) no. 12, 653, arXiv:1608.03953 [hep-ex].
- [117] L. Landau, *On the energy loss of fast particles by ionization*, J. Phys.(USSR) **8** (1944) 201–205. <https://cds.cern.ch/record/216256>.
- [118] G. Apollinari, I. Bjar Alonso, O. Brning, M. Lamont, and L. Rossi, *High-Luminosity Large Hadron Collider (HL-LHC): Preliminary Design Report*. CERN Yellow Reports: Monographs. CERN, Geneva, 2015. <https://cds.cern.ch/record/2116337>.
- [119] ATLAS Collaboration, *Search for new phenomena in high-mass diphoton final states using  $37\text{ fb}^{-1}$  of proton–proton collisions collected at  $\sqrt{s} = 13$  TeV with the ATLAS detector*, Phys. Lett. **B775** (2017) 105–125, arXiv:1707.04147 [hep-ex].
- [120] ATLAS Collaboration, *Search for pair production of Higgs bosons in the  $b\bar{b}b\bar{b}$  final state using proton–proton collisions at  $\sqrt{s} = 13$  TeV with the ATLAS detector*, Phys. Rev. **D94** (2016) no. 5, 052002, arXiv:1606.04782 [hep-ex].
- [121] O. Nackenhorst. Personal communication.